Simulation of Flow around Bluff Bodies and Bridge Deck Sections using CFD

Kai Fan Liaw

Thesis submitted to the University of Nottingham for the degree of Doctor of Philosophy

June 2005

University of Nottingham
Schoolof Civil Engineering

Abstract

This thesis focuses on the simulation of flow around bluff bodies and bridge deck sections, in which unsteady nature and vortex shedding of flow are commonly found, using computational fluid dynamics (CFD). Various turbulence models have been tested to develop understanding and proper modelling techniques for the flow around such bodies.

Throughout the thesis, the turbulence models employed, mainly large eddy simulation (LES) and detached eddy simulation (DES), have been validated through comparative study with experimental work. The major part of the work discusses flow around bluff bodies ranging from a simple circular cylinder, a square cylinder to rectangular sections with various aspect ratios (*1:2* to *1:8*).

The research section concentrates on modelling flow characteristics around bluff bodies to investigate the impact of fluid flow on them. This aids in the understanding of a more complex flow around bridge deck sections. The thesis combines investigation and discussion of the vortex shedding nature on the flow around bluff bodies, in which the simulations are done using advanced modelling techniques on high performance computing system.

Work also includes a sectional wind tunnel test of the bridge deck section for the comparative study with the numerical solution. Finally, the conclusions outline the achievements and findings of the work done in this thesis and give recommendations for further research on the topic.

Acknowledgements:

I would like to thank the following people:

My supervisors, Dr Nigel Wright and Dr John Owen for their help, advice and support in making the PhD study such a rewarding experience.

Dr Dongke Sun for his contribution and encouragement throughout the research project.

Dr Hervé Morvan for his knowledge on CFD and his useful advice.

Wind tunnel team from the Nanyang Technological University for their contribution on the bridge sectional test.

All my colleagues for their useful discussions and support during the research period.

My sincere appreciation goes to my family for their understanding and encouragement during my study.

Finally, my girlfriend Tuang Li for her endless patience, support and love when most required.

List of figures:

List of tables:

1 INTRODUCTION

The topic of this thesis is the simulation of flow around bluff bodies and bridge deck sections using computational fluid dynamics (CFD). CFD calculates numerical solutions to the equations governing fluid flow. Bluff bodies are structures with shapes that significantly disturb the flow around them, as opposed to flow around a streamlined body. Examples of bluff bodies include circular cylinders, square cylinders and rectangular cylinders. Deck sections of long span bridges are another type of such a body that show similar flow characteristics as they are usually elongated with sharp corners which make flow around them very complicated.

Bridges provide link across river, valley or other physical obstacles. The study of the flow around bluff bodies and bridge deck sections is important in terms of the effects of wind on such bodies. Due to the increasing demand to connect people and for the transportation of goods, the latest development and design of long span bridges have entered the era of crossing sea straits such as the Messina Strait Bridge and the Gibraltar Crossing with main span exceeding *3000m*. Long span bridges are susceptible to wind loads excitation due to the shape of the deck and their flexibility. The adequacy and safety of the structures are vital when exposed to wind action. The collapse of the Tacoma Narrow in *1940* marked the beginning of the quantitative consideration of the aeroelastic instabilities of long span bridges, which were thought to be the cause of the disaster. Aeroelastic instabilities are concerned with the effects of the aerodynamic and elastic forces of a flexible solid body immersed in fluid, which might result in structure failure under certain circumstances. These phenomena were neglected during the design of the Tacoma Narrow.

Since then, investigation on the aeroelastic instabilities of long span bridges such as flutter, buffeting, galloping, divergence and vortex shedding has been carried out based on the combination of analytical, numerical and experimental approaches. Flutter could lead to catastrophic collapse as the bridge deck responded exponentially due to the oscillatory instabilities induced when the flow exceeds a particular critical wind speed. Buffeting is the random response of a structure that is occasioned by turbulence induced aerodynamic forces. This is common for long span bridges in gusty wind area, for instance bridges built across mountainous terrain. Galloping is common in asymmetry or irregular sections such as ice coated bridge cables, the associated asymmetry induced unbalance lift force that triggers the vibration. Divergence is a static instability that occurs at high wind speed cause by twisting moment of the bridge

deck which depends on the angle of incidence of the wind. The above-mentioned instabilities posted a challenge to the design of longer, lighter and most importantly, safer bridges. These considerations are vital in the design of long span bridges to avoid disaster like the Tacoma Narrow.

The Kessock Bridge is a cable stayed bridge located in Scotland, UK, which has been known to exhibit wind induced vibration. Investigation of the response of the bridge concluded that the vibration is caused by vortex shedding [98]. In the light of this, various simulations of the flow around bluff bodies have been done since these flows are characterised by flow separation and vortex shedding phenomena. This study provides fundamental knowledge for the investigation of the flow around bridge deck sections and aids in the understanding of the vibration of the bridge under wind effect.

To appropriately simulate these flow characteristics, turbulence models in CFD are used. Turbulence models are equations that account for turbulence of flow based on some assumptions, since it is computationally not practical to thoroughly represent all the physical characteristics of a flow using the current available computer power.

The simulations start with the application of various turbulence models to flow around bluff bodies, starting from the basic circular cylinder to square ones followed by rectangular cylindrical bodies with increasing aspect ratio. Advantages and disadvantages of each turbulence model are identified based on comparative studies with experimental results. Modelling of the more complex flow around a bridge deck section is then carried out based on the findings from the study of the flow around bluff bodies.

1.1 AIM OF WORK

The work in this thesis aims to develop proficient and advanced numerical modelling methodologies for the simulation of flow around bluff bodies using CFD with different turbulence models through comparative study between numerical solutions and experimental results. The suitable models are then used for simulation of flow around the Kessock Bridge deck section to study the effect of wind on long span bridges.

1.2 OBJECTIVES OF WORK

To achieve the aim of this project, three main objectives have been set:

- Investigate the flow around a circular cylinder, which is sensitive to changes of Reynolds number. Various Reynolds numbers (*250*< Re< *10,000*) have been tested using steady and unsteady turbulence models. The study includes the simulation of vortex shedding phenomenon, force coefficient and pressure distribution of the flow. For the validation of the advanced modelling approches (LES and DES) employed in the simulation, comparison with experimental data has been done at Reynolds number of *3,900*.
- Simulate the flow around a square and rectangular sections (*B/H=2, 3, 4, 5, 6, 7,* and *8*) within Reynolds number of *500* to *100,000*. Apart from investigating the flow characteristics around these sections, especially the changes of the shedding frequency and drag coefficient with the increase of aspect ratio, these simulations also involve verification and validation of LES and DES models for flow at higher Reynolds number (*Re 14,000*) compared to the flow around a circular cylinder. This work also aims to investigate the effect of vortical structure and pressure distribution around the sections, which aids in the understanding of the aerodynamic characteristics of the flow around a bridge deck section with similar aspect ratio.
- Investigate the effect of wind on the flow around a bridge deck section experimentally and numerically. The experimental aspect involves the wind tunnel test of a *1:40* scale Kessock Bridge sectional model to measure flow parameters such as the drag, lift and moment coefficients. For numerical investigation, DES is employed to simulate the flow around the Kessock Bridge deck section for comparative study with the wind tunnel test results.

1.3 METHODOLOGY OF WORK

To achieve the above-mentioned objectives, the work is split into various stages. Initially, modelling of the flow around a circular cylinder within range of Reynolds numbers (*Re250-Re10,000*) is done by using basic steady state simulation methods. This is done as a pilot study for the further application of CFD on the computation of a more complex flow using advanced CFD techniques at a later stage of the work.

The next stage is the simulation using the unsteady and more advanced LES model on the flow around a circular cylinder to study the vortex shedding phenomenon in the wake region of the flow. This acts as a first step towards the investigation of the effect of vortices on bluff body flow, which has been identified as the cause of the vibration

observed on the Kessock Bridge [98]. Following this, the validation of the turbulence models (LES and DES) employed in the simulation are performed at Reynolds number of *3,900* through comparative study with experimental results [64, 96].

Since the Reynolds number for the wind tunnel test for the flow around a bridge deck section is much higher compared to the flow around a circular cylinder, the flow around a square and rectangular sections with various aspect ratios has been simulated with Reynolds number between *500* and *100,000*. The simulation of flow around rectangular sections investigates the changes of Strouhal number and the drag coefficient with the increase in aspect ratio. Apart from that, validation of the turbulence models (LES and DES) at higher Reynolds number of *14,000* for the flow around a square cylinder is conducted. This ensures that the turbulence models are capable of capturing the flow characteristics accurately not only at low Reynolds number. The work on the simulation of flow around rectangular cylinders provides a general idea of the flow patterns and the expected outcomes on the flow around the bridge deck section of similar aspect ratio.

Based on the findings of the study of the flow around a circular cylinder and the rectangular sections, numerical modelling techniques of the simulation are then applied on the flow around a bridge deck section to investigate the wind effect on the bridge. A geometrically similar sectional model of the Kessock Bridge is simulated using DES to predict the flow parameters such as force and velocity distribution around the deck section. Evaluated drag, lift and moment coefficients are then compared to the measurement from the *1:40* scale sectional wind tunnel test of the bridge. Work done in this chapter then progresses to the investigation and development on the Fluid Structure Interaction (FSI) study of wind effect on long span bridges as discussed in Chapter Seven.

Current work imposes significant impact on the development of the FSI capability on long bridges within the research group. Findings and observation from the work contributes to the computational aspects of the FSI investigation on various similar projects within the group.

1.4 THESIS STRUCTURE

This chapter consists of the aim, the objectives and the methodology of the research work. The reader is then introduced to the main content of the following chapters.

Chapter Two discusses the principles of the computational fluid dynamics (CFD) and its numerical treatment of turbulent flow. Basic equations describing fluid motion are introduced, followed by the explanation on how CFD formulates these equations and solves them computationally. Three basic methodologies for solving the fluid flow equations, the finite difference method (FDM), the finite element method (FEM) and the finite volume method (FVM) are described. Different turbulence models such as the large eddy simulation (LES), the Reynolds Averaged Navier-Stokes (RANS) method and the detached eddy simulation (DES) are explained with the suitability of each model in the applications of the flow around bluff bodies and bridge deck sections discussed.

Chapter Three contains work done on the flow around a circular cylinder using RANS and LES methods at various Reynolds numbers. Pressure distribution from the prediction of RANS models are compared to experiment data. The chapter then focuses mainly on the verification and validation of LES and DES models on the flow around a circular cylinder. Detailed comparisons of the velocity profiles and Reynolds stress components at various locations in the wake region of the flow with experimental data are shown, as well as the comparison of the Strouhal number and the drag coefficient of the flow.

Chapter Four discusses the verification and validation of the turbulence models for the flow around a square cylinder at a higher Reynolds number of *14,000* compared to the flow around a circular cylinder in Chapter Three. Similar to the flow around a circular cylinder, current validation involves direct comparison of the velocity profiles and the Reynolds stress components of the flow with experimental findings.

Chapter Five contains the simulation of the flow around rectangular sections (*B/H=2* to *B/H=8*). These simulations focus on the changes of Strouhal number and drag coefficient under the effect of increasing the aspect ratio, including flow at high Reynolds numbers (*Re 42,800* and *Re 100,000*). The final section of the chapter discusses the analysis of the pressure distribution around the rectangular sections using the mathematical technique known as Principal Component Analysis (PCA).

In chapter Six, the design of the *1:40* scale sectional wind tunnel model of Kessock Bridge is outlined with the set up of the experiment described. The measurement of the wind tunnel test such as the wind speed and the frequencies when the vibration occurs are compared to the full scale observations of the Kessock Bridge. The second part of the chapter discusses the simulation of the flow around the Kessock

Bridge deck section using DES, followed by the comparative study between the simulated result and the wind tunnel test measurement. These include the force coefficients, the Strouhal number and the pressure distribution comparison.

Chapter Seven of the thesis is a short discussion chapter relating the fluid structure interaction study (FSI) on the flow around bridge deck sections to the work done in this thesis. This is to provide a link that relates the simulation of the flow around bluff bodies and a static bridge deck section to the simulation of a moving deck section.

Chapter Eight draws conclusions on the work done on the research. This focuses on the objectives of the work and how they are achieved throughout the thesis. The second part of Chapter Eight provides suggestions and recommendations on further work for the simulation of the flow around bluff bodies and bridge deck sections using CFD.

The references in the chapters are then listed following Chapter Eight. In the thesis, the figures are shown at the end of each chapter. This thesis is accompanied by a CD of the animation of the flow around bluff bodies and bridge deck sections. The next chapter discusses aspects of CFD and the turbulence models employed for the simulations in the current work.

2 COMPUTATIONAL FLUID DYNAMICS (CFD)

This chapter introduces the background theories of CFD and the techniques for solving fluid flow problems. Understanding CFD is important in investigating the influences and impacts of fluid flow. This refers particularly to engineering practice, such as the wind effects on tall buildings, chimneys or long span bridges.

The chapter consists of two main sections, the first section outlines the mathematical equations describing fluid flow and methods for solving the equations. The section also describes the background and roles of CFD in the study of fluid flow. The second section, which is the major part of this chapter, discusses the turbulence models that have been employed for the study of the flow around bluff bodies and the bridge deck sections in this thesis.

2.1 OVERVIEW

Flow can be laminar or turbulent depending on the Reynolds number. For engineering applications, most flows are turbulent in nature. Turbulence is the chaotic nature of flow in motion showing random variation in space and time. Turbulent flow is characterized by its irregularity, three-dimensionality and dissipative nature.

Turbulence contains eddies with different sizes which are always rotational in motion. Different scales of eddies are found in a flow. Large scale eddies are responsible for the carrying of energy and transfer of momentum in the flow. On the other hand, the smaller scale eddies, where dissipation of energy occurs are known as the Kolmogorov scale eddies. The large eddies extract energy from the mean flow and transfer it to the smallest eddies where energy is taken out of the flow through viscosity. This is known as the cascade (Figure 2.1) process in the study of fluid dynamics.

2.1.1 Equations describing fluid flow

In mid 18^{th} century, the French engineer Claude Navier and the Irish mathematician George Stokes derived the well-known equations of fluid motion, known as the Navier-Stokes equations. These equations have been derived based on the fundamental governing equations of fluid dynamics, called the continuity, the momentum and the energy equations, which represent the conservation laws of physics.

- Continuity equation: Equation based on the law of conservation of mass. Applying this concept to fluid flow, we ensure that the change of mass in a control volume is equal to the mass that enters through its faces minus the total mass leaving its faces.
- Momentum equation: By applying Newton's Second Law of Motion, the momentum equation is expressed in terms of the pressure and viscous stresses acting on a particle in the fluid. This ensures that the rate of change of momentum of the fluid particles is equal to the total force due to surface stresses and body forces acting in an aligned direction of a chosen co-ordinate axis.
- Energy equation: Based on the First Law of Thermodynamics, the rate of change of energy of a fluid particle is taken to be equal to the net rate of work done on that particle due to surface forces, heat and body forces such as gravitational force. The energy equation describes the transport of heat energy through a fluid and its effects.

2.1.1.1 Navier-Stokes equations

Combining these fundamental principles, the physics of fluid flow is expressed in terms of a set of partial differential equations known as the Navier-Stokes equations. By solving these equations, the pressure and velocity of the fluid can be predicted throughout the flow. For more explanation on the derivation of Navier-Stokes equations, see Versteeg and Malalasekera (1995) [134]. Assuming that the flow is incompressible, the following equations can be used to describe the fluid flow,

- Navier-Stokes Equations: (conservation of momentum),

$$\frac{\partial u_i}{\partial t} + u_j \frac{\partial u_i}{\partial x_j} = -\frac{1}{\rho}\frac{\partial p}{\partial x_i} + \frac{\partial}{\partial x_j}\left(\nu \frac{\partial u_i}{\partial x_j}\right) \qquad \text{Eq 2.1}$$

- The continuity equation: (conservation of mass),

$$\frac{\partial u_i}{\partial x_j} = 0 \qquad \text{Eq 2.2}$$

where u is the velocity in the streamwise direction, p is the pressure, ρ is the fluid density and υ is the kinematic viscosity of the flow.

2.1.2 Computational Fluid Dynamics (CFD)

CFD solves the Navier-Stokes Equations numerically for fluid flow using computers. All CFD codes contain three main elements: the pre-processor, the solver and the post-processor.

- Pre-processor: employed to fully specify a CFD flow problem in a form suitable for the use of the solver. The region of fluid to be analysed is called the computational domain and it is made up of a number of discrete elements called the mesh. The users need to define the properties of fluid acting on the domain before the analysis is begun; these include external constraints or boundary conditions, like pressure and velocity to implement realistic situations.
- Solver: a program that calculates the solution of the CFD problem. Here the governing equations are solved. This is usually done iteratively to compute the flow parameters of the fluid as time elapses. Convergence is important to produce an accurate solution of the partial differential equations.
- Post-processor: used to visualise and quantitatively process the results from the solver. In a contemporary CFD package, the analysed flow phenomena can be presented in vector plots or contour plots to display the trends of velocity, pressure, kinetic energy and other properties of the flow.

The advances in computer technology over the past decade enables CFD to be applied to complex flow field and has become a vital tool in applications on wind engineering study.

In CFD study, another aspect of consideration of a simulation is the residual of the solutions. The equations describing fluid flow are solved iteratively so residuals appear. In engineering application, a residual is usually targeted between four to six orders of magnitude of the actual values [119] to achieve convergence of the solution to an acceptable level.

2.1.3 Discretisation

When solving fluid flow problems numerically, the surfaces, boundaries and spaces around and between the boundaries of the computational domain have to be represented in a form usable by computer. This can be achieved by some arrangement of regularly and irregularly spaced nodes around the computational domain known as the mesh. Basically, the mesh breaks up the computational domain spatially; so that calculations can be carried out at regular intervals to simulate the passage of time, as numerical solutions can give answers only at discrete points in the domain at a specified time. The process of transforming the continuous fluid flow problem into discrete numerical data which are then solved by the computer is known as discretisation. Generally, there are three major parts of discretisation in solving fluid flow:

- Equation discretisation
- Spatial discretisation
- Temporal discretisation

Figure 2.2 shows the procedures of performing discretisation on a typical fluid flow problem.

2.1.3.1 Equation discretisation

As mentioned in section 2.1.2, the governing equations consist of partial differential equations. Equation discretisation is the translation of the governing equations into a numerical analogue that can be solved by computer. In CFD, equation discretisation is usually performed by using the finite difference method (FDM), the finite element method (FEM) or the finite volume method (FVM).

The FDM employs the concept of Taylor expansion [123] to solve the second order partial differential equations (PDE) in the governing equations of fluid flow. This method is straightforward, in which the derivatives of the PDE are written in discrete quantities of variables resulting in simultaneous algebraic equations with unknowns defined at the nodes of the mesh. FDM is famous for its simplicity and ease in obtaining higher order accuracy discretisation. However, FDM only applies to simple geometries because it employs a structured mesh.

Unlike FDM, unstructured mesh is usually used in FEM. The computational domain is subdivided into a finite number of elements. Within each element, a certain number of nodes are defined where numerical values of the unknowns are determined. In FEM, the discretisation is based on an integral formulation obtained using the method of weighted residuals, which approximates the solutions to a set of partial differential equations using interpolation functions. FEM is famous for its application around complex geometries because of the application of unstructured grid. But numerically, it requires higher computer power compared to FDM. So the finite volume method (FVM), which is mathematically similar to FEM in certain applications, but requires less computer power, is the next consideration in CFD applications.

In FVM, the computational domain is separated into a finite number of elements known as control volumes. The governing equations of fluid flow are integrated and solved iteratively based on the conservation laws on each control volume. The discretisation process results in a set of algebraic equations that resolve the variables at a specified finite number of points within the control volumes using an integration method. Through the integration on the control volumes, the flow around the domain can be fully modelled. FVM can be used both for the structured and unstructured meshes. Since this method involves direct integration, it is more efficient and easier to program in terms of CFD code development. Hence, FVM is more common in recent CFD applications compared to FEM and FDM.

2.1.3.2 Spatial discretisation

Spatial discretisation divides the computational domain into small sub-domains making up the mesh. The fluid flow is described mathematically by specifying its velocity at all points in space and time. All meshes in CFD comprise nodes at which flow parameters are resolved. Three main types of meshes commonly used in computational modelling are structured, unstructured and multi-block structured mesh.

A structured mesh is built on a coordinate system, which is common in bodies with a simple geometry such as square or rectangular sections. This method enables the accessing of neighbouring points easily and quickly, just by adding or subtracting an integer value. For slightly more flexibility, the mesh can also be generated following the boundaries of the computational space using a curvilinear or body-fitted mesh. The advantage of the curvilinear method over traditional structured mesh is that flow near the boundary can be accurately represented especially in the case of shear layers flow

along solid bodies. However, a structured mesh performs badly when the geometry is complex, which is quite common in industrial applications. In the view of this, unstructured meshes were introduced.

In an unstructured mesh, the nodes can be placed accordingly within the computational domain depending on the shape of the body, such that different kinds of complex computational boundaries and geometries can be simulated. Since the arrangement of nodes has no particular order, neighbouring points cannot be directly identified. A numerical approach has to be imposed to describe how each node is connected to the control volumes. An unstructured mesh works well around complex geometries but this requires more elements for refinement compared to a structured mesh on the same geometry, leading to higher computing cost. To compensate between computing cost and flexibility, we turn our attention to the multi-block structured mesh.

In a multi-block structured mesh, the computational domain is subdivided into different blocks, which consists of a structured mesh (Figure 3.22). The purpose is to avoid sharp changes in the grid direction around complex boundaries, which might reduce the accuracy of the results. A multi-block structured mesh is more complicated to generate compared to a structured and an unstructured mesh but it combines the advantages of both. It is more computer efficient than an unstructured mesh and yet provides ease of control in specifying refinement needed along certain surfaces or walls, especially for meshing around complex geometries.

2.1.3.3 Temporal discretisation

The third category of discretisation is the temporal or time discretisation. Generally, temporal discretisation splits the time in the continuous flow into discrete time steps. In time-dependent formulations, we have an additional time variable t in the governing equations compared to the steady state analysis. This leads to a system of partial differential equations in time, which comprise unknowns at a given time as a function of the variables of the previous time step. Thus, unsteady simulation normally requires longer computational time compared to a steady case due to the additional step between the equation and spatial discretisation.

Either explicit or implicit method can be used for unsteady time-dependent calculation. In an explicit calculation, a forward difference in time is taken when calculating the time t^{n+1} by using the previous time step value (n denotes state at time t and $n+1$ at time $t+\Delta t$) [120]. An explicit method is straight forward, but each time step

has to be kept to a minimum to maintain computation stability and convergence. On the other hand, implicit method computes values of time step t^{n+1} at the same time level in a simulation at different nodes based on a backward difference method. This results in a larger system of linear equations where unknown values at time step t^{n+1} have to be solved simultaneously.

The principal advantage of implicit schemes compared to explicit ones is that significantly larger time steps can be used, whilst maintaining the stability of the time integration process [13]. A smaller time step Δt in an explicit method implies longer computational running time but it is relatively more accurate.

2.1.4 Direct Numerical Simulation (DNS)

From this section onward, the numerical models for fluid flow will be discussed. It is worth reminding the reader that the discussion has been done in reverse chronological order, starting with the most advanced and up to date models currently available to the time averaging methods developed since the emergence of CFD back in the beginning of *70s*. This is to provide the readers with a clearer overview of the state of the art development of numerical modelling for easier representation and understanding on the solution of fluid flow. This is because earlier CFD software only provided a general view of the fluid motion without detail on the dynamic and time dependent properties of flow.

The simplest and most straight forward way to describe a flow is to solve the Navier Stokes equations directly, without any approximations applied in the calculation. This method is known as the direct numerical simulation (DNS). DNS numerically resolves all the significant scales of motion in a flow down to the Kolmogorov scales, corresponding to the scales responsible for the dissipation of energy in the flow. To achieve this, Blazek (2001) [13] pointed out that a sufficient spatial resolution and CPU time requirement for DNS is proportional to $Re^{9/4}$ and Re^3 (Re-Reynolds number) respectively. This agreed with the investigation of Frolich *et al.* (1998) [36] in determining the required resolution for DNS. Thus, it is still not practical to accurately resolve the non-linear nature and three dimensional characteristics of turbulence at high speed flow using DNS with the currently available computer technology.

DNS has been widely applied by researchers due to its high accuracy. Tremblay (2001) [131] successfully applied DNS on the flow around a circular cylinder at a Reynolds number of *3,900*. Very good agreement of the mean velocity profiles and

pressure distribution has been observed compared to experimental data. The result of Tremblay's work has been included in the comparison study of the flow around a circular cylinder in the next chapter, which provides a very good reference between the experimental findings and simulated solution. In an attempt to resolve flow at higher Reynolds number of *10,000* using DNS, Tremblay concluded that the simulation needs about *80* computing days running on a *32* processor parallel computer system. This could mean that DNS is still not practical for engineering applications and for the time being, applications are restricted to lower Reynolds number. In fact, Spalart (2000) [115] estimated that *80* years is needed for computer power to develop to an extent that DNS is able to simulate flow at Reynolds numbers of engineering interest, assuming that computer power increases by *100%* every year.

2.2 TURBULENCE MODELS

Turbulent flow is highly unsteady and irregular. As shown above, currently available computer power is not yet sufficient to represent all the eddies from the smallest scale corresponding to the dissipative motions, to the largest dimension responsible for most of the momentum transport in a high speed flow. So turbulence models are used to describe turbulence based on some simplified assumptions.

Figure 2.3 presents the overview of turbulence models commonly available in CFD. Generally, simulations of flow can be done by filtering or averaging the Navier-Stokes equations. The latter are usually referred as the Reynolds Averaged Navier Stokes (RANS) models (section 2.2.2), where the unsteadiness of the flow is averaged out. In the RANS model, all aspects of turbulence are modelled. On the contrary, the space filtering method resolves a major portion of the turbulent scales numerically and models only the small scales eddies, enabling the dynamic features of the flow to be captured.

In all CFD simulations, a mesh independence test is important in order to achieve a statistically accurate and converged solution. This means changes of mesh will not affect the numerical solutions significantly. A mesh independence test is usually done by refining the mesh resolution of the simulations gradually to achieve a constant solution. In other words, a mesh independence test is to check the convergence of the computation with respect to spatial resolution.

2.2.1 Large Eddy Simulation (LES)

Large eddy simulation (LES) is classified as a space filtering method in CFD. LES directly computes the large-scale turbulent structures which are responsible for the transfer of energy and momentum in a flow while modelling the smaller scale of dissipative and more isotropic structures.

In order to distinguish between the large scales and small scales, a filter function is used in LES. A filter function dictates which eddies are large by introducing a length scale, usually denoted as Δ in LES, the characteristic filter width of the simulation. All eddies larger than Δ are resolved directly, while those smaller than Δ are approximated.

2.2.1.1 Filtering of Navier-Stokes equations

In LES, the flow velocity U is separated into a filtered, resolved part $\overline{U}$ and a sub-filter, unresolved part, u',

$$U = \overline{U} + u' \qquad \text{Eq. 2.3}$$

The filter discretises the flow spatially. Applying the filter function to Eq. 2.3, we have,

$$\overline{U}(x) = \int G(x, x')U(x')dx' \qquad \text{Eq. 2.4}$$

As mentioned, the filter function dictates the large and small eddies in the flow. This is done by the localized function *G (x,x')*. This function determines the size of the small scales [13],

$$G = \begin{cases} 1/\Delta, & if\,|x - x'| \le \Delta/2 \\ 0, & otherwise \end{cases} \qquad \text{Eq. 2.5}$$

Various filtering methods exist, the top hat filter is common in LES. The function represents Eq. 2.5. Figure 2.4 depicts the top hat filter.

By imposing the filter function in the continuity and the Navier-Stokes equations, one obtains the filtered equations governing the fluid flow in LES,

$$\frac{\partial \overline{u}_i}{\partial x} = 0 \qquad \text{Eq 2.6}$$

$$\frac{\partial \overline{u}_i}{\partial t} + \frac{\partial \overline{u_i u_j}}{\partial x_j} = -\frac{1}{\rho}\left(\frac{\partial \overline{p}}{\partial x_i}\right) + \frac{\mu}{\rho}\left(\frac{\partial^2 \overline{u}_i}{\partial x_i \partial x_j}\right) \qquad \text{Eq. 2.7}$$

The over bar denotes the space filtered quantities. ρ, p and μ represent the air density, pressure and dynamic viscosity of the flow respectively. In fluid flow around an immersed object, shear stress occurs because not all the fluid exerts forces tangentially to the wall of the object. This results in the appearance of the stress terms in the equations governing fluid flow. After dividing the Navier-Stokes Equation into filtered and sub-filter components, the unknown stress term $\overline{u_i u_j}$ arises due to the non-linearity of the equations and the shear stress of the flow. This term needs to be approximated to solve the filtered Navier-Stokes Equations.

$$\overline{u_i u_j} = \overline{(\bar{u}_j + u'_j)(\bar{u}_i + u'_i)} = \overline{\bar{u}_i \bar{u}_j} + \overline{\bar{u}_i u'_j} + \overline{u'_i \bar{u}_j} + \overline{u'_i u'_j} \qquad \text{Eq 2.8}$$

The unknown term $\overline{u_i u_j}$ comprises the resolvable scale component $\overline{u_i}$ and the small scale component *u'* of the flow. Thus, a relationship based on the interaction among components of various scales in the flow has been derived to estimate the unknown. This is written as [26],

$$\tau_{ij} = \left(\overline{\bar{u}_i \bar{u}_j} - \overline{u_i}\,\overline{u_j}\right) + \left(\overline{\bar{u}_i u'_j} + \overline{u'_i \bar{u}_j}\right) + \overline{u'_i u'_j} \qquad \text{Eq. 2.9}$$

The term τ_{ij} is known as the subgrid scale (SGS) Reynolds Stress. Physically, the right hand side of Eq. 2.9 represents the large scale momentum flux due to turbulence motion [31]. Individually, these terms are explained as follow:

- $\overline{\bar{u}_i \bar{u}_j} - \overline{u_i}\,\overline{u_j}$ are the Leonard stresses which represent the interaction between two resolved scale eddies to produce small scale turbulence.
- $\overline{\bar{u}_i u'_j} + \overline{u'_i \bar{u}_j}$ are the cross-stress terms that describe the interaction between resolved eddies and small-scale eddies.
- $\overline{u'_i u'_j}$ is the subgrid scale stress that represents the interactions between two small scale eddies

2.2.1.2 Smagorinsky model

To approximate the SGS Reynolds stress τ_{ij}, a SGS model can be employed. The most commonly used SGS models in LES is the Smagorinsky model. In a flow, it is the shear stress and the viscosity of the flow that cause the chaotic and random nature of the fluid motion. Thus, in the Smagorinsky model, the effects of turbulence are represented by the eddy viscosity based on the well known Boussinesq hypothesis [15]. The Boussinesq hypothesis relates the Reynolds stress to the velocity gradients and the

turbulent viscosity of the flow (with reference to [25, 145]). It is therefore assumed that the SGS Reynolds stress τ_{ij} is proportional to the modulus of the strain rate tensor of the resolve eddies,

$$\tau_{ij} - \frac{1}{3}\tau_{kk} = -2\nu_{SGS} \cdot \overline{S}_{ij} = \nu_{SGS} \cdot \left| \frac{\partial \overline{u}_i}{\partial x_j} + \frac{\partial \overline{u}_j}{\partial x_i} \right| \qquad \text{Eq. 2.10}$$

where ν_{SGS} is the SGS eddy viscosity and $\overline{S}$ is the strain rate tensor,

$$\left|\overline{S}\right| = \left[2\overline{S}_{ij}\overline{S}_{ij}\right]^{\frac{1}{2}} \qquad \text{Eq. 2.11}$$

The SGS eddy viscosity ν_{SGS} needs to be approximated in order to solve Eq. 2.10. Based on dimensional analysis, the following relationship has been obtained [131],

$$\nu_{SGS} \propto l q_{SGS} \qquad \text{Eq. 2.12}$$

where l is the characteristic length scale of the unresolved motion that usually takes the value of the filter width $\Delta = \left(\Delta_x \Delta_y \Delta_z\right)^{\frac{1}{3}}$. Δ_x, Δ_y and Δ_z are the grid spacings in the x, y and z direction respectively [26]. By relating the velocity scale of the unresolved motion q_{SGS} to the gradients of the filtered velocity based on an analogy of the mixing length model [145], the SGS viscosity is written as [131],

$$\nu_{SGS} = \left(C_s \Delta\right)^2 \left|\overline{S}\right| \qquad \text{Eq. 2.13}$$

where C_s is the Smagorinsky constant that changes depending on the type of flow. For isotropic turbulent flow, the C_s value is usually around *0.18* to *0.20*.

Basically, the Smagorinsky SGS model simulates the energy transfer between the large and the subgrid-scale eddies. Energy is transferred from the large to the small scales but backscatter (reverse of cascade process) sometimes occurs where flow becomes highly anisotropic, usually near to the wall. To account for backscattering, the length scale of the flow can be modified using Van Driest damping [68],

$$\left(C_s \Delta\right) = C_s \Delta\left(1 - e^{-y^+/25}\right) \qquad \text{Eq. 2.14}$$

where y^+ is the dimensionless distance of grid points from the wall (section 3.2.1.1). Van Driest damping accounts for the reduced growth of the small scales near the wall which gives a smaller value of SGS viscosity in order to represent the flow more accurately.

The Smagorinksy model has been successfully applied to various flows as it is relatively stable and demands less computational resources among the SGS models. But some disadvantages of the model have been reported [13],

- Too dissipative in laminar regions.
- Requires special near wall treatment and laminar turbulent transition.
- C_s is not uniquely defined.
- Backscatter of flow is not properly modelled.

From Ferziger's (1993) [30] investigation, it has been pointed out that C_s is not constant in a flow and it is a function of the subgrid scale eddies and Reynolds number. The value of C_s varies between *10%-20%* depends on the regimes of flow (wall bounded flow or transition flow) to achieve optimum flow prediction. Hence, the dynamic SGS model has been introduced.

This model employs a similar concept as the Smagorinsky model, with the Smagorinsky constant C_s replaced by the dynamic parameter C_{dym}. The parameter C_{dym} is computed locally as a function of time and space, which automatically eliminates the problem of using constant C_s. In the dynamic SGS model, another filter is introduced which takes into account of the energy transfer in the dissipation range. Performing the double filtering allows the subgrid coefficient to be calculated locally based on the energy drain in the smallest scales. For a more complete mathematical explanation of the dynamic SGS model, see Blazek (2001) [13].

Various researchers have employed both the dynamic and Smagorinksy SGS models in LES. Generally, the dynamic model predicted better agreement with experimental work in region of transition flow and the near wall region. Some advantages of the dynamic model over the Smagorinsky models are [31],

- Dynamic SGS automatically uses a smaller model parameter in isotropic flows.
- Near the wall, the model parameters need to be reduced; the dynamic SGS model adapts these parameters accordingly.

- Definition of length scale is always an issue in LES, the dynamic model compensates for the error in length scale by changing the value of the parameters used.

In terms of the equation discretisation in LES, the central difference scheme is employed throughout the work in this thesis. Central difference in LES with SGS model predicts better results compared to upwinding scheme [11]. The latter introduces larger error comparatively while solving the Navier-Stokes equations, leading to a situation where the errors are large enough to take over the subgrid scale model in LES due to the generation of artificial diffusion in the flow. This could be avoided by using high order accuracy upwinding scheme such as the fifth or seventh order discretisation in solving the equations but this would increase the computer requirement for the simulation.

The influence of turbulence is well captured in LES with a more realistic prediction of flow but this indicates a significant increase of computational requirement to capture the unsteady motion of the flow. In terms of the mesh requirement for LES, Blazek (2001) [13] pointed out that the number of elements require for LES near to the viscous sublayer is at $Re^{1.8}$, which decreases to $Re^{0.4}$ away from the wall.

2.2.2 Reynolds Averaged Navier-Stokes (RANS)

Flow is separated into mean and fluctuating components in the RANS approach to turbulence,

$$U = \overline{U} + u' \qquad \text{Eq. 2.15}$$

Physically, this is represented in Figure 2.5. The time averaging velocity component is defined as,

$$\overline{U} = \frac{1}{T}\int_0^T U dt \qquad \text{Eq. 2.16}$$

where T is the averaging time of the simulation, usually chosen to be large compared to the typical timescale of turbulent fluctuation.

Substituting Eq. 2.15 into the Navier-Stokes equations for time averaging, one obtains the time averaged Navier-Stokes equations,

$$\frac{\partial \overline{u}_i}{\partial t} + \overline{u}_j \frac{\partial \overline{u}_i}{\partial x_j} = -\frac{1}{\rho}\frac{\partial \overline{p}}{\partial x_i} + \frac{\partial}{\partial x_j}\left(\nu \frac{\partial \overline{u}_i}{\partial x_j} - \overline{u_i u_j}\right) \qquad \text{Eq. 2.17}$$

where ρ, p and υ represent the air density, pressure and kinematic viscosity of the flow respectively.

The statistical averaging of the Navier-Stokes equations give rises to the unknown term $\overline{u_i u_j}$, which are the correlation between the fluctuating velocity components and is known as the Reynolds Stress term. The existence of the Reynolds stress means there is no longer a closed set of equations, and turbulence model assumptions are needed to estimate the unknowns to solve this closure problem.

RANS models have been developed based on the concept that a velocity scale and a length scale is sufficient to describe the effect of turbulence in a flow [134]. For instance, one of the earliest turbulence models, the eddy viscosity model, estimates the velocity and length scales of the flow from the local mean flow quantities. This is done by relating the turbulent viscosity to the mean velocity gradient of the flow [15]. But this simple isotropic model fails to simulate more complex flow.

At the other end of the spectrum, the Reynolds stress model (RSM) [61] is used. This model copes with more complex flow by taking into account the anisotropic features of turbulence that the eddy viscosity model fails to predict. In this model, the Reynolds stresses are expressed in term of known mean flow quantities to solve the fluid governing equations in the turbulence models. The mean flow quantities usually involve the convective and diffusive nature of turbulence, known as the transport of turbulent flow. The transport nature of the flow involves transfer of energy and is dealt with by solving differential transport equations which take into account the effects of the dynamics of turbulence. These transport equations are then combined with the Navier-Stokes equations in order to solve the flow in a closed set of differential equations. RSM gives more accurate solutions since it simulates the anisotropic nature of turbulence more realistically. However, this model is computationally more demanding among the RANS models.

On the other hand, the two equation models, which require less computer power compared to RSM, are common in industrial and engineering applications. These models involve the effect of the transport of turbulence quantities by considering the energy transfer in the flow. Apart from the transport of energy, the calculation of an empirical length scale from a second transport equation is also involved. Thus, these

techniques are known as the two equations models. In CFD, k-ε and k-ω are the two most widely used models in this category.

2.2.2.1 k-ε turbulence model

The k-ε turbulence model solves the flow based on the assumption that the rate of production and dissipation of turbulent flows are in near-balance in energy transfer. The dissipation rate, ε of the energy is written as,

$$\varepsilon = \frac{k^{3/2}}{L} \qquad \text{Eq. 2.18}$$

where k is the kinetic energy of the flow and L is the length scale involved. This is then related to the turbulent viscosity μ_t based on the Prandtl mixing length model [145],

$$\mu_t = \rho C_\mu \frac{k^2}{\varepsilon} \qquad \text{Eq. 2.19}$$

where C_μ is an empirical constant and ρ is the density of the flow. Applying this to the equations governing fluid flow, the k equation of the k-ε model is written as,

$$\underbrace{\frac{\partial(\rho k)}{\partial t}}_{\text{Convection term}} + \underbrace{U_i \frac{\partial(\rho U_j k)}{\partial x_j}}_{\text{Diffusion term}} = \underbrace{\frac{\partial}{\partial x_j}\left(\frac{\mu_t}{\sigma_\varepsilon}\frac{\partial k}{\partial x_j}\right)}_{\text{Production term}} + \underbrace{\mu_t \frac{\partial U_i}{\partial x_j}\left(\frac{\partial U_i}{\partial x_j} + \frac{\partial U_j}{\partial x_i}\right)\frac{\partial U_i}{\partial x_j}}_{\text{Destruction term}} - \rho\varepsilon \qquad \text{Eq. 2.20}$$

and the ε equation,

$$\frac{\partial(\rho\varepsilon)}{\partial t} + \frac{\partial(\rho U_j \varepsilon)}{\partial x_j} = \frac{\partial}{\partial x_j}\left(\frac{\mu_t}{\sigma_\varepsilon}\frac{\partial \varepsilon}{\partial x_j}\right) + C_{\varepsilon 1}\frac{\varepsilon}{k}\mu_t \frac{\partial U_i}{\partial x_j}\left(\frac{\partial U_i}{\partial x_j} + \frac{\partial U_j}{\partial x_i}\right) - \rho C_{\varepsilon 2}\frac{\varepsilon^2}{k} \qquad \text{Eq. 2.21}$$

Physically, the rate of change of kinetic energy (first term in Eq. 2.20) is related to the convection and diffusion of the mean motion of the flow. The diffusion term can be modelled by the gradient diffusion assumption as turbulent momentum transport is assumed to be proportional to mean gradients of velocity [15]. The production term, which is responsible for the transfer of energy from the mean flow to the turbulence, is counterbalanced by the interaction of the Reynolds stresses and mean velocity gradient. The destruction term deals with the dissipation of energy into heat due to viscous nature of the flow.

Based on extensive examination of a wide range of turbulent flows, the constant parameters used in the equations take the following values [106],

$$C_{\mu} = 0.09;\ C_{\varepsilon 1} = 1.44;\ C_{\varepsilon 2} = 1.92;\ \sigma_k = 1.0 \text{ and } \sigma_{\varepsilon} = 1.3$$

The k-ε model has gained popularity among RANS models due to the following [134]:

- Robust formulation
- One of the earliest two-equation models, widely documented, reliable and affordable
- Lower computational overhead

However, the model encounters some difficulties in:

- Over prediction of turbulence near stagnation point
- Length scale is too large in adverse pressure gradient flow
- Fails to resolve flows with large strains such as swirling flows and curved boundary layers flow

Thus other two equation models have been developed to improve the performance on the above-mentioned areas.

2.2.2.2 k-ω turbulence model

Wilcox (1993) [141] developed the k-ω two equation model as an alternative to cope with the deficiencies of the k-ε model at the walls. The k-ω model is very similar in structure to the k-ε model but the variable ε is replaced by the dissipation rate per unit kinetic energy, ω. The k equations in the k-ω model are written as,

$$\frac{\partial(\rho k)}{\partial t} + U_i \frac{\partial(\rho U_j k)}{\partial x_j} = \frac{\partial}{\partial x_j}\left(\frac{\mu_t}{\sigma_{\varepsilon}} \frac{\partial k}{\partial x_j}\right) + \mu_t \frac{\partial U_i}{\partial x_j}\left(\frac{\partial U_i}{\partial x_j} + \frac{\partial U_j}{\partial x_i}\right)\frac{\partial U_i}{\partial x_j} - \rho k \omega \quad \text{Eq. 2.22}$$

and the ω equation,

$$\frac{\partial(\rho\omega)}{\partial t}+\frac{\partial(\rho U_j\omega)}{\partial x_j}=\frac{\partial}{\partial x_j}\left(\frac{\mu_t}{\sigma_\omega}\frac{\partial\omega}{\partial x_j}\right)+\alpha\frac{\omega}{k}\mu_t\frac{\partial U_i}{\partial x_j}\left(\frac{\partial U_i}{\partial x_j}+\frac{\partial U_j}{\partial x_i}\right)-\beta\rho\omega^2 \quad \text{Eq. 2.23}$$

The replacement with the variable ω allows better treatment in solving the flow near wall. Near to the wall, the boundary layer is affected by viscous nature of the flow. A very refined mesh is necessary to appropriately resolve the flow. The *k*-ε model avoids using fine mesh near wall by employing empirical formula to predict the flow in order to save computational power (see section 3.2.1.1).

Although the near wall treatment of *k*-ε model saves a vast amount of computer power, it is not sufficient to represent complex flow accurately. In the *k*-ω formulation, the flow near wall is resolved directly through the integration of the ω equation. The advantage of the *k*-ω model compared to the *k*-ε model is that the ω equation is more robust and easier to integrate compared to the ε equation without the need of additional damping functions. Wilcox (1993) [141] studied the performance of both models on the prediction of the reattachment length of flow. The *k*-ω model gave very good comparison to experimental data while the *k*-ε model predicted a significantly shorter length. However, the *k*-ω model over predicted the spreading rates around free shear layer due to inaccurate prediction of eddy viscosity value [80].

Both the *k*-ε and the *k*-ω models have been tested on various flow fields, the performance of the models in different regions of flow are summarised below,

Table 2.1 Comparison between the *k*-ε model and the *k*-ω model.

	k-ω model	*k*-ε model
Sub layer	• Robust • Accurate • Simple	• Stiff • Less accurate • Complex
Log layer	• Accurate	• Length scale too large
Free stream	• Inaccurate near free shear layers	• Well defined

From the table, it is observed that the k-ε model performed well in the shear layer flow while the k-ω model is excellent near to the wall. This led to the development of the Shear Stress Transport (SST) model which aims to combine the advantages of these two models.

2.2.2.3 Shear Stress Transport (SST) model

In order to overcome the problem of free-stream dependency of the k-ω model and to prevent the over-prediction of length scales near the wall by the k-ε model, Menter (1994) [74] introduced the SST model, which combines the positive features of both models. The idea is to employ the k-ω model near wall and the k-ε model near the boundary layer edge. To achieve this, the k-ω model is multiplied by a blending function F_1 and the k-ε model by (1- F_1) such that F_1 has a value of one near wall region and switches to zero at the boundary layer where k-ε model is recovered [74].

The SST model also accounts for the transport of the turbulent shear stress inside boundary layers by modifying the turbulent eddy-viscosity function. The purpose is to improve the accuracy of prediction of flows with strong adverse pressure gradient, as well as flow with pressure-induced boundary layer separation. SST [3] has been shown to predict better flow separation compared to both k-ε and k-ω models.

Although the two equation models provide a good compromise between complexity and accuracy among RANS models, the applications are restricted to steady type of flow. Thus, solution is sought to achieve both computational efficiency and the capability of predicting the chaotic nature of flow such as vortex shedding. This leads to the hybrid of the LES and RANS models, known as the detached eddy simulation (DES).

2.2.3 Detached Eddy Simulation (DES)

Perhaps the solution to the restriction of computer resources on CFD at high Reynolds number relies on DES for the time being. DES employs the RANS models near to the wall and LES in the wake region of a flow where unsteady and chaotic motion of flow is usually found (Figure 4.22).

In DES, RANS model is used away from the wake region of the flow to save computational time compared to the usage of LES in the whole computational domain.

In the wake region of the flow, DES computes the eddies and vortices based on the LES formulation to maintain the dynamic features of the flow.

DES has been studied by various groups of researchers, among these is the Boeing Commercial Airplane Group lead by Spalart (2000) [115] and researchers at ANSYS-CFX [76]. The major difference between these two studies is the implementation of the RANS models in DES. Spalart (2000) [115] employs a one-equation turbulence model, the Spalart-Allmaras model (1994) [116] in the DES while Menter (1994) [76] uses the SST model [74] in the formulation of the DES approach in CFX. The one-equation model is computationally undemanding compared to other more complex RANS models. Simulations performed on the flow past a blunt trailing edge body and test on shock-induced separation using the one-equation model gives satisfactory results [116]. But the shortcoming of the model is the prediction of the reattachment of flow near adverse pressure gradient region. On the other hand, the SST model performs well in the prediction of flows with adverse pressure gradient and pressure-induced boundary layer separation [75].

Basically, DES uses a turbulent length scale, L_t to dictate which approach to use during a simulation. DES starts with the SST model at the inlet boundary, the formulation is the same as the standard SST model apart from the length scale used in the computation of the dissipation rate. This is replaced by a local grid spacing, Δ. If the turbulent length scale is greater than the grid spacing, which is common in regions with large eddies and chaotic flow nature, LES is activated in the DES formulation.

The activation of LES or the switching to SST model in DES is controlled by a blending factor. Generally, this factor takes the form,

$$F = \frac{L_t}{C_{DES}\Delta} \qquad \text{Eq. 3.15}$$

where C_{DES} is a constant.

In the studies of the applications of DES based on the Spalart-Allmaras model, test cases on the flows around a rounded-corner square, circular cylinder and landing gear have been done. Generally, good agreement has been observed compared to experimental data [118].

However, Menter (1994) [76] pointed out that the DES model faces challenges on the prediction of flow past a smooth surface where the mesh is usually refined in order to resolve the velocity profiles. The fine mesh suggests that the local grid spacing might be less than the boundary layer thickness, which is treated as the length scale of the flow

in this case. This creates a false signal on the DES formulation to trigger LES and thus resulted in the prediction of vortical flow or flow separation near the smooth wall surface, which defeats the purpose of DES. The SST-DES model developed by Menter (1994) [76] has taken this situation into account. In this model, another extra blending factor is introduced in the formulation near to the wall to prevent the activation of LES. This blending factor only allows the switching between the k-ε and the k-ω models in the SST, while shielding LES from activating around the wall region (see [76] for details of the formulation). The developed SST-DES model has been tested on the flow past a circular cylinder, a cube mounted in a channel and a car body shape known as the Ahmed Car Body.

Test on the flow past the car body investigated the prediction of flow at the slant surface near the back of the car with $25°$ and $35°$ angles (Figures 2.6 and 2.7). This is challenging due to the different flow patterns such as the flow separation and reattachment imposed by different slanting angles. The SST-DES predictions have been compared to experimental works and solutions from pure RANS models. The work concluded that SST-DES model gave closest solutions to the experimental work, especially in predicting the flow separation and reattachment on the slant surface [76]. Besides, the vortex structures and the unsteadiness of the flow fields from the SST-DES model agreed well with the experiment's flow topology.

In the study of the flow past a cube mounted in a channel using the SST-DES model at a Reynolds number of *40,000*, the velocity profiles in the flow recovery region downstream of the cube have been well captured [76]. LES predicted vortices and the three-dimensional nature of the flow in the wake region similar to experimental data.

From the above-mentioned works, it is obvious that the SST-DES offers great potential in the applications of simulations for a large class of flows. This refers to flows at high Reynolds numbers with chaotic and highly three-dimensional nature in wake regions. Comparing to pure LES, DES is more practical considering the available computer resources at this time.

2.3 SUMMARY

The background of CFD and the mathematical aspects of numerical simulation discussed in this chapter provide the reader with basic knowledge for understanding the simulated results presented in the next three chapters. A wide range of turbulence

models exist in CFD but current work focuses on the SST-RANS model and the space filtering LES model, with the SST-DES model as a combination of the two.

The time averaging (RANS) models and the space filtering (LES) model take on two different approaches. LES solves the equations governing fluid flow spatially by computing the large scales eddies of the flow while RANS model averages out the unsteadiness of the flow as time elapses. Comparatively, RANS models save a vast amount of computational time. Although LES tends to be computationally more demanding, researchers' investigation demonstrated that LES is capable of capturing the dynamic characteristics of flow very well and has become a vital tool in the simulation of complex flow.

On the other hand, the SST-DES model has shown good result on the simulation at high Reynolds number at reasonable computing cost. The Reynolds number simulated is far higher than those accessible to DNS and yet it is capable of capturing the dynamic characteristics of the flow with results compatible to LES. Thus, SST-DES is considered as a suitable turbulence model for the simulation of flow around bluff bodies and a bridge deck section.

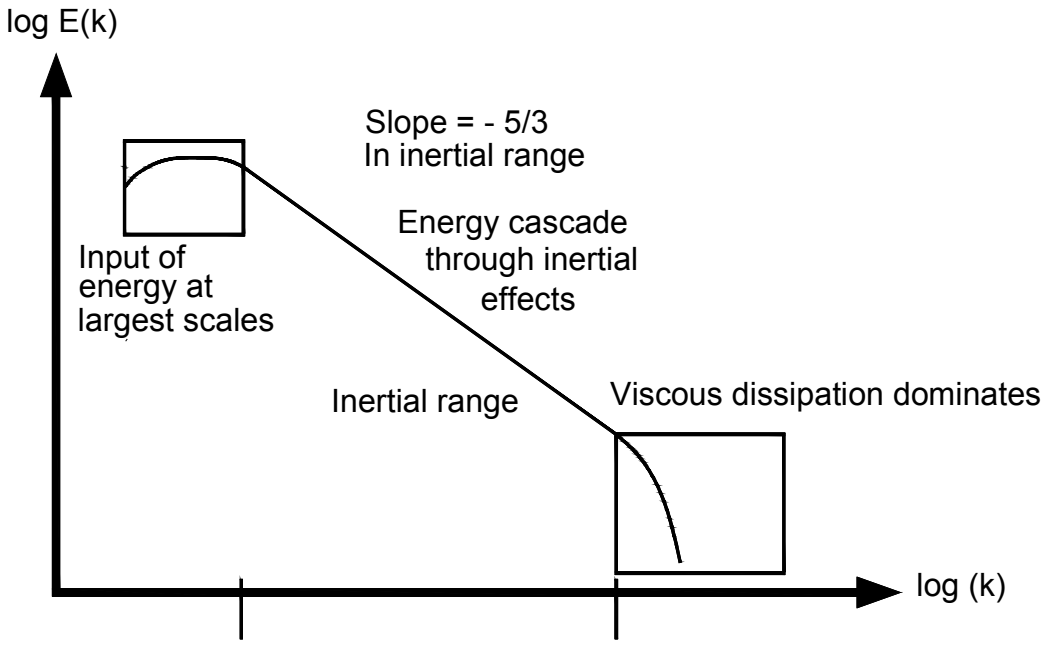

Figure 2.1 Illustration of energy cascade in a flow (energy spectrum against wave number) [5].

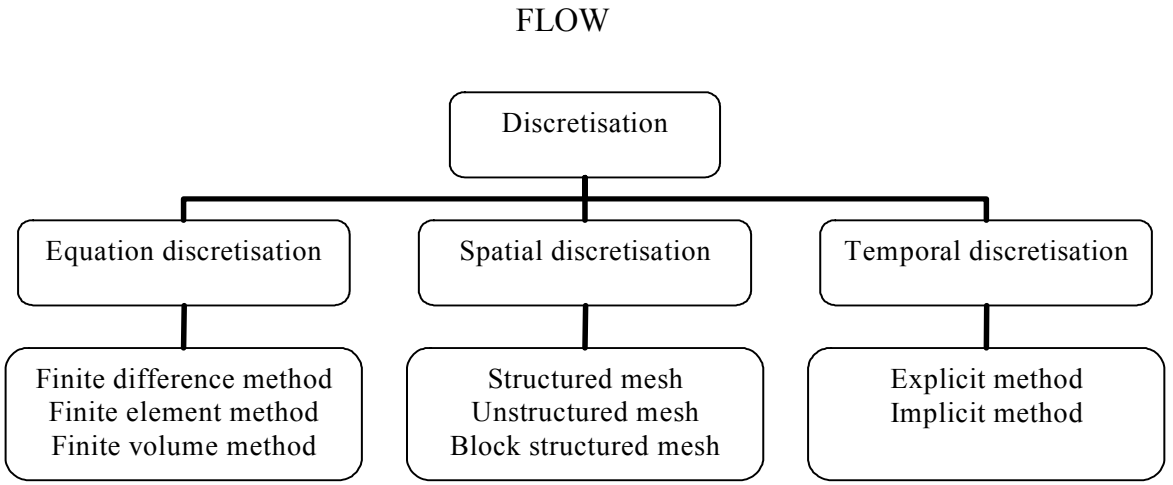

Figure 2.2 Discretisation of flow in CFD.

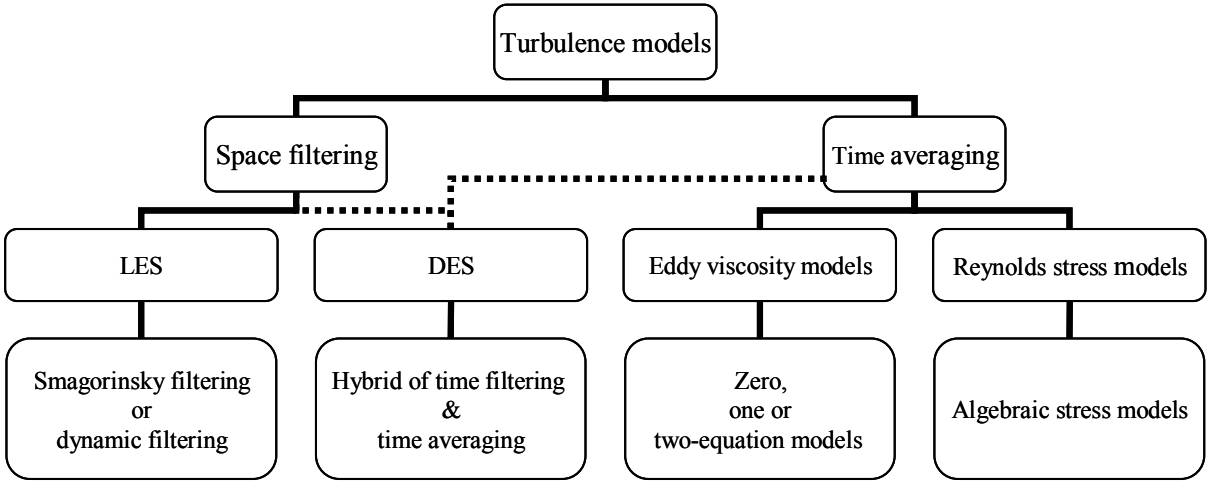

Figure 2.3 Overview of flow treatment, DNS and turbulence models.

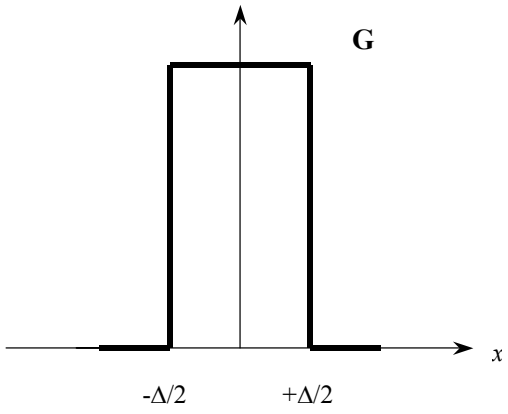

Figure 2.4 Top hat filter in LES.

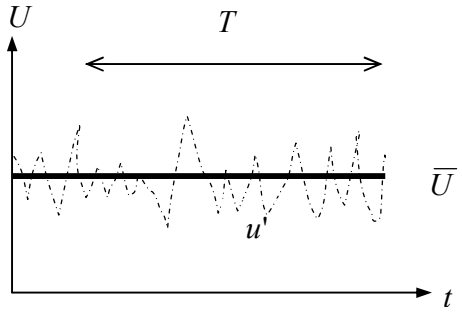

Figure 2.5 Time averaging of turbulence using RANS models.

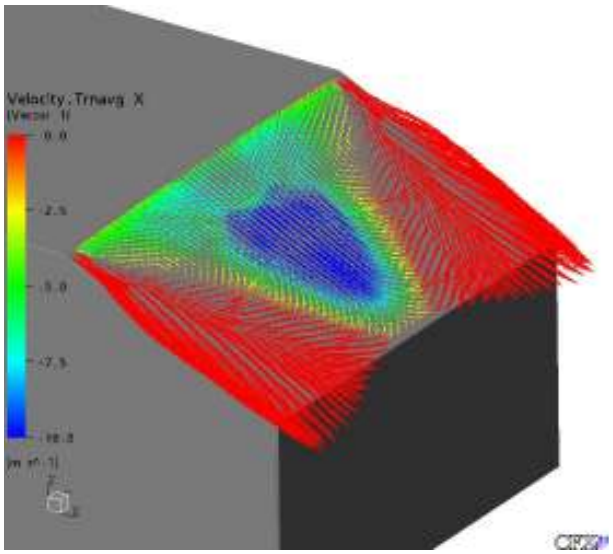

Figure 2.6 Flow structure on the slant of Ahmed Car Body using DES [76].

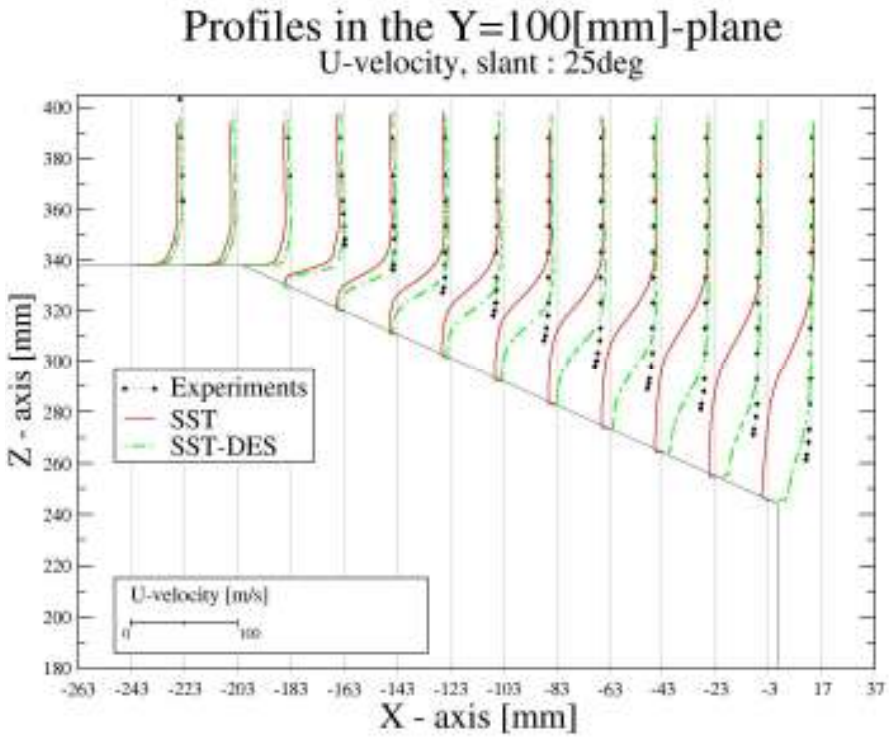

Figure 2.7 Comparison of velocity profiles of Ahmed Car Body for 25° case [76].

3 FLOW AROUND A CIRCULAR CYLINDER

Flow around a circular cylinder has been the subject of both experimental and numerical studies for decades. This flow is very sensitive to the changes of Reynolds number, a dimensionless parameter representing the ratio of inertia force to viscous force in a flow. Work in this chapter aims to validate and identify suitable turbulence models in the application of the flow around a circular cylinder. The validated turbulence model will then be applied to the simulation of the flow around rectangular cylinders and bridge deck sections. Flow around a circular cylinder has been chosen as pilot study for the investigation on the flow around a bridge deck section due to the effect of vortex shedding on such structures. The first stage of the validation process involves the simulation of the flow around a static cylinder using various turbulence models at low Reynolds number ($250 < Re < 10{,}000$) to simulate the basic flow parameters and to capture the vortex shedding phenomenon in the wake region of the flow. Then detailed comparative study of the flow around a circular cylinder with experimental results at Reynolds number of *3,900* is conducted.

To begin with, the basic overview of the flow around a circular cylinder and the flow characteristics such as the Strouhal number, vortex shedding, drag, lift, and pressure coefficients are introduced. Prior to each section of the simulation of the flow around a circular cylinder using different turbulence models, similar work carried out by other researchers and its findings are brought into discussion. Following this, results from the current simulation are compared to experimental works and conclusions on validating the turbulence models are drawn.

Early studies of the flow around a circular cylinder have been done at low Reynolds number. Researchers such as Bloor (1964), Roshko (1954) and Tritton (1959) [14, 102, 133] focused on the flow in the near wake region of the cylinder. Experimental work on the pressure and velocity distribution on circular cylinder flow between Reynolds number of *10* to *80* was carried out by Nishioka and Sato (1974) [89]. Very good agreement with numerical results was observed at this Reynolds number due to the laminar and two-dimensional nature of the flow. By the mid *80s*, CFD started to influence the study of the flow around a circular cylinder following the advances of computer technology. The rapid development of CFD allows a wide range of investigation to be done. Satisfactory results have been obtained between Reynolds number of *100* to *300* from CFD simulation [16, 35].

3.1 CONCEPTUAL OVERVIEW OF FLOW AROUND A CIRCULAR CYLINDER

Flow around a circular cylinder tends to follow the shape of the body provided that the velocity of the flow is very slow, this is known as laminar flow. Flow at the inner part of the boundary layers travels more slowly than the flow near to the free stream. As the speed of the flow increases, separation of flow occurs at some point along the body due to the occurrence of the adverse pressure gradient region (section 3.1.4). Flow separation tends to roll up the flow into swirling eddies, resulting in alternate shedding of vortices in the wake region of the body known as the von Karman vortex street.

3.1.1 Reynolds number

Flow around a circular cylinder varies with the Reynolds number. Small Reynolds number corresponds to slow viscous flow where frictional forces are dominant. When Reynolds number increases, flows are characterised by rapid regions of velocity variation and the occurrence of vortices and turbulence. Mathematically, Reynolds number of the flow around a circular cylinder is represented by,

$$\mathrm{Re} = \frac{uD}{\nu} \qquad \text{Eq. 3.1}$$

where D is the diameter of the cylinder, u is the inlet velocity of the flow, and ν is the kinematic viscosity of the flow.

Experimental study of the flow around a circular cylinder has identified regions where significant patterns of flow occur as the Reynolds number changes, especially when the flow changes from laminar to turbulent state. Generally, the following regimes have been identified from Roshko's (1954) experiment [102]:

Stable range	$40< Re<150$
Transition range	$150< Re<300$
Irregular range	$300< Re<200{,}000$

Similar observations have been made by Zdravkovich (1997) [146]. Flow becomes very irregular with instabilities beyond Reynolds number of *200,000*. Another dominant feature of the flow around a circular cylinder is the three-dimensional nature

of the flow. Bloor (1964) [14] investigated the flow around a circular cylinder between Reynolds number of *200* to *400* when turbulent motion starts to develop in the wake region of the flow. He observed that the transition of flow in the wake region is triggered by large-scale three-dimensional structures. Work from Tritton (1959) [133] suggested that three-dimensional effects started to kick in at Reynolds number of *150* in the flow around a circular cylinder. Bearman (1982) [8] observed oblique shedding and vortex dislocation in the wake region of the flow around a circular cylinder. Similar experiment conducted by Williamson (1997) [142]documented the development of three-dimensional flow structures as depicted in Figure 3.1.

The Reynolds number increases ($50 < Re < 1,200$) down the page in Figure 3.1, primary Karman vortex is first observed at low Reynolds number. Small scale streamwise vortex structures then start to form as Reynolds number increases, followed by the formation of larger three-dimensional scale vortex resulted from vortex dislocations. At higher Reynolds number towards the bottom of the figure, shear layer instabilities of the flow is noticed.

3.1.2 Vortex shedding and Strouhal number

The separation of flow around a circular cylinder causes pairs of eddies to form alternately on the top and bottom part of the cylinder and travel into the wake region resulting in vortex shedding. Vortex shedding is very common in engineering applications. Figure 3.2 shows vortex shedding phenomenon in the wake region of the flow around a circular cylinder. Within certain range of Reynolds number ($250 < \mathrm{Re} < 10,000$), the frequency at which vortices are shed in the flow around a circular cylinder tends to remain almost constant (Figure 3.3).

Strouhal number is a dimensionless parameter which describes the shedding of the vortices in the wake region of a flow. It relates the frequency of vortex shedding to the incident wind speed,

$$St = \frac{f_s D}{u} \qquad \text{Eq. 3.2}$$

where D is the diameter of the cylinder, f_s is the shedding frequency of vortices equal to $1/T$ (Figure 3.2) and u is the incident velocity.

3.1.3 Drag and lift coefficients

Roshko (1994) [102] pointed out that the Strouhal number is related to the drag coefficient of the flow (Figure 3.3). In sub-critical Reynolds number region (*100 <Re <10,000*), increase in the Strouhal number is generally accompanied by a decrease of the drag coefficient. Drag coefficient is calculated as follow:

$$C_d = \frac{F}{\frac{1}{2}\rho u^2 A} \qquad \text{Eq. 3.3}$$

where A is the projected area in the flow direction and F is the sum of the pressure force and the viscous force components on the cylinder surface acting in the along-wind direction. Lift coefficient is calculated similarly but vertical force is considered rather than along-wind force (Figure 3.4).

Figure 3.5 shows a typical plot of the changes of the drag coefficient with the Reynolds number of the flow around a circular cylinder. The 'Region of simulation' shows the range of flow in which the RANS turbulence models are employed for analysis in this chapter. This is in the sub-critical region of flow where the transition to turbulence occurs in the wake region. Higher up the plot at Reynolds number of about *200,000*, the drag decreases dramatically due to the transition to turbulence of the boundary layer near the cylinder wall. Turbulent nature of the boundary layer involves mixing of flow and results in sharper velocity gradient compared to laminar type of flow. Consequently, this delays the separation of flow and pushes the separation point to the rear of the cylinder resulting in a narrower wake, which is accompanied by a drop in the drag coefficient. This is known as the 'drag crisis'. Simulation of the drag crisis phenomenon was not carried out in the current work due to the high computer power required.

Theoretically, the drag force is changing at twice the frequency of the lift force for the flow around a circular cylinder or generally flow involving separation. When a vortex is shed from the top of the cylinder, a suction area is created and the cylinder experiences lift. Half a cycle later, an alternate vortex is created at the bottom part of the cylinder. Throughout the process, the lift force changes alternately in a complete cycle of vortex shedding but the cylinder experiences drag constantly, giving rise to the situation depicted in Figure 3.6, where drag is changing at twice the frequency of the lift. It is important that any turbulence models can simulate all the above-mentioned parameters correctly for the analysis of the flow around bluff bodies.

3.1.4 Pressure coefficient

Apart from the drag and lift coefficient, the pressure coefficient distribution around the surface of the cylinder is important. Near to the surface of the cylinder, flow momentum is quite low due to viscous effects and thus is sensitive to the changes of the pressure gradient. Figure 3.8 shows a typical pressure distribution plot of the flow around a circular cylinder starting from the stagnation point (zero velocity, corresponds to $\theta = 0$ in Figure 3.7. Note that the θ defined in the Figure 3.8 is $180°$ out of phase with the definition of θ in the current work) where pressure coefficient takes a value of one according to Bernoulli's Theorem. The flow speed then starts to increase accompanied by a drop in the pressure coefficient to a negative value (Figure 3.8). In this case, decreasing of pressure in the direction of flow assists the fluid movement and there is no retardation of flow.

The speed of flow then starts to reduce near $\theta = 80°$, accompanied by an increase of pressure in the direction of the flow, which results in the adverse pressure gradient situation. The flow now has to move against the pressure force in addition to the viscous force. This leads to a reduced gradient of the velocity profile and the wall shear stress. Separation of flow occurs when the shear stress cannot overcome the adverse pressure gradient, this usually happens at $80° < \theta < 120°$ for sub-critical flow. After the separation point, pressure remains fairly constant in the wake. Accurate prediction of pressure coefficient distribution around a cylinder means a turbulence model performs well at predicting the flow separation.

3.2 FLOW AROUND A CIRCULAR CYLINDER USING RANS METHOD

This section discusses simulation of the flow around a circular cylinder based on the RANS method. Numerical studies of the flow around a circular cylinder from other researchers are briefly discussed, followed by the current work employing various RANS turbulence models for the computation of the drag coefficient and pressure distribution around the circular cylinder.

Majumdar and Rodi (1985) [69] employed the k-ε RANS model to simulate the flow around a circular cylinder at a sub-critical Reynolds number of $140{,}000$. The model failed to capture the separation point and under predicted the drag coefficient. The recirculation length in the wake region was incorrectly simulated but the shear stress components upstream of the separation point were close to experimental results.

Further work with the k-ε model at the same Reynolds number has been done by Franke *et al.* (1990) [34]. The work concluded that the assumption of an isotropic eddy-viscosity concept of the k-ε model does not represent the flow accurately, it results in the over-production of kinetic energy. Results also suggested that the model neglected the important transport effects of the individual Reynolds stress components.

3.2.1 Flow around a circular cylinder (k-ε, RSM and SST)

In the current work, RANS models such as the k-ε model and the Reynolds stress model (RSM) have been first chosen to test the suitability and the applicability of the models on the flow around a circular cylinder between Reynolds number of *1,000* and *10,000* (Figure 3.5), followed by the SST two-equation RANS model. These low Reynolds numbers in the sub-critical region of flow have been chosen mainly due to the restriction of computer power available (single PC with *1.7 GHz* processor and *1Gigabytes* physical memory). Also, experimental data such as the pressure distribution and drag coefficient are widely available within these Reynolds numbers for comparative study. The RANS models used here employ a finite volume method (FVM) with an unstructured tetrahedral mesh.

- Computational domain

  The domain and the boundary conditions for the simulation of the flow at Reynolds number are depicted in Figure 3.9. The cylinder is simulated with a diameter (D) of *0.1m* and a depth of *2D* to incorporate the spanwise effects, this has been chosen based on a similar case study for initial comparison. Effect of the spanwise effect on the flow will be further discussed in the next chapter, considering a depth of greater than *2D*. Distances of *10D* and *30D* to the side wall and to the downstream boundaries are allowed respectively to prevent blockage ratio and end effects on the flow.

- Boundary conditions

  Longitudinal uniform velocities of *0.135m/s*, *0.338m/s* and *1.35m/s* are introduced at the inlet correspond to the Reynolds number of *1,000*, *2,500* and *10,000* respectively. The outlet boundary is defined with an average static reference pressure of *0Pa*. The rest of the boundaries (side and bottom wall) are free slip walls, in which velocity near the wall is not retarded by frictional effects. The cylinder wall has a normal no slip boundary condition where velocity increases from zero at the wall surface to the free stream velocity away from the surface.

- Meshing

  An unstructured tetrahedral mesh (Section 2.1.3.2) is employed in this simulation (Figure 3.10a). The unstructured nature of the mesh provides flexibility on simulating a curvilinear body such as a circular cylinder. Near to the cylinder wall, a very fine mesh is required to resolve the flow parameters in the boundary layer. In CFX, this is achieved with an inflation layer (Figure 3.10b) for computational efficiency. An inflated mesh extrudes the surface elements into three-dimensional prisms which are finely resolved normal to the wall to capture the changes of the velocity gradient but coarse parallel to it to save computer power. The mesh becomes increasingly coarse in the radial direction to maintain computational efficiency. This can be achieved by setting the desired expansion factor for the coarsening of the mesh away from the wall.

- Discretisation

  Equation discretisation (Section 2.1.3.1) of the RANS models is achieved by using the upwind differencing scheme. Advection schemes with various levels of accuracy (first order, 0.5 blending factor and second order) have been tested and compared for the simulations on the flow around a circular cylinder.

- Computer power

  Accuracy of CFD solution depends very much on the availability of computer power. Current simulation using the RANS models is based on a single Pentium *IV* (*1.7GHz* processor) desktop PC with *1GB* of physical RAM. To provide a basic idea on the computing time for the simulation, current RANS models require about *2* to *3* days simulation time for a mesh size of *0.7* to *1* million elements of ($1{,}000 < \mathrm{Re} < 10{,}000$).

3.2.1.1 Modelling near wall flow

In the Reynolds number within sub-critical flow region, flow near the cylinder surface is laminar and thus viscosity plays an important role. This is known as the boundary layer region of the flow. Within the boundary layer, the flow has zero velocity at the surface of the wall and starts to increase radially following a 'log law' profile until free stream velocity is achieved. Theoretically, a very fine mesh is needed to resolve the flow within the boundary layer. Refined mesh can be built but this suggests that high computer power is needed to solve the flow, and the computational time required will

be impractical for normal engineering applications. So refined mesh near to the wall has to be avoided.

In CFD solver, the near wall situation is usually treated by introducing empirical formulas to represent the 'log law' region of the flow. This aims to avoid generating a very refined mesh in that region. The k-ε model employs the wall function method to model flow near to the wall. In the wall function method, the viscosity sub-layer is represented mathematically by formulas to account for the effect of shear stress. The refinement of the mesh in the boundary region is determined by the dimensionless parameter y^+. Physically, y^+ represents the normal distance of the grid points from the cylinder wall. In the k-ε model, the y^+ value needs to be greater than *11.63* to maintain mesh consistency and to represent the boundary layer correctly.

Although the wall function method gives reasonably accurate solutions near boundary layers, attention is needed in regions with flow separation because the wall function method does not account for viscous effect [74]. Consequently, the Low-Reynolds number method is used to fully resolve the viscosity affected sub-layer. The SST model employs this method in the modelling of flow near to the wall. Basically, the SST model represents the flow near to the wall by resolving the flow parameters without any mathematical representation of the flow profiles as in the wall function approach. Thus, Low-Reynolds number requires finer mesh and a smaller y^+ value, depending on the Reynolds number of the flow.

3.2.2 Result and discussion (k-ε model and RSM)

Table 3.1 and Table 3.2 show the changes of the drag coefficient predicted by the k-ε and the RSM models with simulations of different meshes and order of accuracy. Results for Reynolds Number of *1,000*, *2,500* and *10,000* are shown. The number of elements employed in the simulations are *170,000*, *300,000* and *600,000* respectively. In terms of the number of nodes, these are equivalent to *45,000*, *79,000* and *158,000* respectively. The number of nodes is roughly equal to one quarter of the total number of elements in the simulation for the RANS cases in this Chapter. Table 3.1 shows the values of the drag coefficient (C_d) from the prediction of the k-ε model, notice the percentage changes of the drag coefficient when the mesh is refined. Figure 3.11 plots the changes of drag coefficient against Reynolds number with the refinement of mesh, compared to the experimental data from Zdravkovich (1997) [146]. It is obvious that the k-ε model over predicted the drag coefficient by about twice the experimental value

at lower Reynolds number. For the case of *600,000* elements simulation, the changes of drag coefficient reduced to less than *3%*, indicated that mesh independence is more or less achieved. However, difference between the drag coefficients of the k-ε model and experimental results is still obvious.

Consequently, a more accurate second order advection scheme RSM model is used for the simulations (Table 3.2). Different pattern of changes is observed with respect to the drag coefficient. The drag coefficients predicted from the RSM show discrepancies (Figure 3.12) compared to the experimental data [146] especially at higher Reynolds number. This is attributed to the fact that the RSM employs different wall function method compared to the k-ε model but same mesh has been used for the two models. This results an inaccurate prediction of the drag coefficient near to the cylinder surface. Different mesh should be considered for the RSM simulation on the flow around a circular cylinder.

Table 3.1 Drag coefficient of the flow around a circular cylinder using the k-ε turbulence model.

Reynolds Number	**C_d (Exp.)**	**C_d (*k-e*)**	**Number of elements**	**% Change (simulated results)**	**Advection scheme**
1,000	1.03	2.05	170,000		First order
1,000	1.03	1.85	300,000	-10%	First order
1,000	1.03	1.83	600,000	-2%	First order
2,500	0.90	1.54	170,000		First order
2,500	0.90	1.27	300,000	-17%	First order
2,500	0.90	1.24	600,000	-2%	First order
10,000	1.10	1.42	170,000		First order
10,000	1.10	1.07	300,000	-25%	First order
10,000	1.10	1.03	600,000	-4%	First order

Table 3.2 Drag coefficient of the flow around a circular cylinder using the Reynolds Stress Model (RSM).

Reynolds Number	C_d (Exp.)	C_d (RSM)	Number of elements	% Change (simulated results)	Advection scheme
1,000	1.03	0.95	170,000		Second order
1,000	1.03	0.75	300,000	-21%	Second order
1,000	1.03	0.62	600,000	-17%	Second order
2,500	0.90	0.75	170,000		Second order
2,500	0.90	0.52	300,000	-31%	Second order
2,500	0.90	0.34	600,000	-35%	Second order
10,000	1.10	0.95	170,000		Second order
10,000	1.10	0.75	300,000	-21%	Second order
10,000	1.10	0.25	600,000	-67%	Second order

3.2.3 Result and discussion (SST)

Both the k-ε model and the Reynolds Stress Model (RSM) fail to accurately predict the drag coefficients of the flow around a circular cylinder between sub-critical Reynolds number of *1,000* to *10,000*. In the study of RANS turbulence model on the application of flow around bluff bodies, Menter *et al.* (2001) [77] pointed out that the SST turbulence model performs better than the k-ε model in predicting flow separation and flow changes near to the wall where adverse pressure gradient occurs. Thus, SST model is employed to reanalyze the simulations of the flow around a circular cylinder at Reynolds number of *1,000*, *2,500* and *10,000*.

Figure 3.13 shows the y^+ values for the simulation of the flow around a circular cylinder at Reynolds number of *1,000*, *2,500* and *10,000* using the SST model. An average of less than *3* has been used for the y^+ value. The SST model is then employed to simulate the flow with increasing mesh refinement and a second order advection scheme. The mesh refinement has been done using the mesh adaptation function in CFX, where meshes around regions with rapid flow are automatically refined. Table 3.3 shows the prediction of drag coefficient using the SST model. Compare to the prediction of the k-ε model and the RSM, SST model shows significantly less

percentage changes of drag coefficient when the mesh is refined. This suggested that appropriate mesh is employed around the cylinder surface and the Low-Reynolds number wall modelling method performs better than the wall function method and mesh independence has been achieved.

Figure 3.14 depicts the predicted drag coefficient from SST and experimental data. It is observed that the predicted drag coefficients agreed better with the experimental data [146] compared to previous RANS prediction, implying that the SST model gives better prediction of flow where separation occurs. This observation agreed with findings from other researchers [77, 137]. In terms of the discrepancies of the drag coefficient compared to the experimental data, Rumsey and Biedron (2001) [104] reported a similar situation. The discrepancy is caused by different base suction predicted near the leeward side of the cylinder. This can be seen from Figures 3.15 and 3.16, where a less negative pressure has been predicted, results in lower suction and thus lower drag around this area.

Table 3.3 Drag coefficient of the flow around a circular cylinder using the Shear Stress Transport (SST) model.

Reynolds number	**C_d (Exp.)**	**C_d (SST)**	**Number of elements**	**% Change (simulated results)**	**Advection scheme**
1,000	1.03	0.88	448,000		Second order
1,000	1.03	0.87	572,000	-1%	Second order
1,000	1.03	0.88	719,000	1%	Second order
2,500	0.90	0.82	430,000		Second order
2,500	0.90	0.82	547,000	0%	Second order
2,500	0.90	0.82	671,000	0%	Second order
10,000	1.10	0.86	579,000		Second order
10,000	1.10	0.85	646,000	-1%	Second order
10,000	1.10	0.86	716,000	1%	Second order

Figures 3.15 and 3.16 show the distribution of the pressure coefficient around the cylinder at Reynolds number of *1,000* and *10,000* predicted by the SST turbulence

model compared to the experimental data [146]. The plot is similar to Figure 3.8, but only half of the cylinder surface ($0° < \theta < 180°$) is shown as the flow is symmetrical (Figure 3.17) - no vortex shedding phenomenon has been predicted. First and second order advection schemes have been tested on the simulation. For analysis purposes, the flow is separated into the winward side ($0° < \theta < 60°$), the separation region ($60° < \theta < 120°$) and the leeward side ($120° < \theta < 180°$).

In the windward region ($0° < \theta < 60°$), the predicted pressure coefficients from the SST model (Figure 3.15 and Figure 3.16) for both Reynolds number of *1,000* and *10,000* cases agree generally well with the experimental result [146] apart from the stagnation point ($\theta = 0°$). Theoretically, the pressure coefficient at this point is supposed to be 1 since the flow comes to a rest with zero velocity (Bernoulli's Theorem). The SST model predicted pressure coefficient of slightly greater than 1. The distance between the inlet boundary and the cylinder is thought to be the cause of the discrepancy, as suggested by ANSYS-CFX after some discussion. The cylinder is too near to the inlet boundary resulting in the built up of the flow at the stagnation point of the windward side. No sensitivity test of the domain size has been carried out since the simulation was built to reproduce the experiment's dimension. Increasing the size of the computational domain (distance from inlet and side walls to the cylinder) might reduce the discrepancy. Another contribution to the discrepancy observed is the way finite volume method (FVM) employed in the current SST model computes the flow parameters. The parameters are computes based on the averaged values around the control volumes (section 2.1.3.1) in a flow domain. In this case, the velocity component at the stagnation point is computed as the averaged value of the velocity at that point (zero velocity) and the control volumes around it (in which the vertices contain non-stationary flow values), resulting in the non-zero components as observed in Figure 3.15 and Figure 3.16.

Within the separation region ($60° < \theta < 120°$), the second order advection scheme gave better prediction of the pressure distribution with the experimental data compared to the first order scheme for both Reynolds numbers (Figure 3.15 and Figure 3.16). This is because the higher order terms in the second order advection scheme decay faster compared to the first order scheme and thus minimizes the errors in the solutions. This results in better agreement of the pressure prediction compared to the experimental measurement.

At the leeward side ($120° < \theta < 180°$), both the first and second order advection schemes from the SST fail to accurately predict the pressure distribution after separation

of flow occurred (Figure 3.15 and Figure 3.16), with increasing pressure coefficients observed rather than a more constant behaviour as reported from experiment. This implies that the SST model is incapable of representing the unsteady vortical structures after the flow separates. Greater discrepancy with experimental result [146] is observed for the flow at a higher Reynolds number of *10,000*.

Figure 3.17 depicts the vector plot of the streamwise velocity component for the simulation at Reynolds number of *2,500*. No alternate shedding of vortices is observed since the SST model averages out the unsteadiness of the turbulence, resulting in a pair of symmetric recirculation bubbles in the near wake region of the flow. A similar phenomenon has been observed for the case of flow at Reynolds number of *1,000* and *10,000*, with different lengths of recirculation bubbles.

3.2.4 Conclusion (SST)

Among the RANS models (k-ε, RSM and SST) tested on the flow around a circular cylinder at sub-critical flow, the SST model demonstrated the ability to predict the mean values of the pressure coefficient similar to experimental data, with delay of separation point observed from the second order advection scheme. The effect of grid resolution was tested and the SST model predicted drag coefficient close to experimental result at lower Reynolds number but under-prediction of the coefficient at higher Reynolds number of *10,000* is observed. Two recirculation bubbles were captured in the near wake but no detail of periodic unsteadiness of wake region has been observed. In the light of this, large eddy simulation (LES) is employed in the following section for the capturing of the vortex shedding and unsteady turbulence in the wake region of the cylinder.

3.3 LARGE EDDY SIMULATION OF FLOW AROUND A CIRCULAR CYLINDER

LES is an approach that computes the more dynamic eddies and models the smaller isotropic scale motion. This model is known to maintain and predict the vortex structure very well. In this chapter, flow around a circular cylinder at Reynolds numbers of *250* and *3,900* have been chosen for the LES.

3.3.1 LES of flow around a circular cylinder at Reynolds number of *250*

Laminar vortex shedding known as the von Karman vortex street (Figure 3.18) has been observed in the wake region of the flow around a circular cylinder at low Reynolds number between *40* to *250* [146]. Within these regions of flow, the Strouhal number of the flow has a value of around *0.21*. For Reynolds number that is greater than *250*, the laminar periodic wake becomes unstable and the eddies start to become turbulent. Further increase of Reynolds number turns the wake region into turbulent flow.

3.3.1.1 Experimental work and simulation of vortex shedding

Experimental works [89, 102] have been done on the study of the vortex shedding between the Reynolds number of *40* and *250*. Flow visualization study has also been carried out to observe the behaviour of the vortices [128]. Philips (1956) [99] conducted similar experiments and concluded that between Reynolds numbers of *40* to *80*, the laminar vortex shedding is truly two-dimensional. Beyond this Reynolds number, the existence of three-dimensionality of flow in the wake region has been reported. Gerrard (1978) [39] pointed out that end effects have a significant influence on the two and three-dimensional nature of the flow. At Reynolds number of *120*, Honji and Ishii (1976) [48] observed the existence of spanwise structures in the wake region of the flow. In a flow visualization study using dye, Hama (1962) [42] reported the occurrence of irregular three-dimensional wake flow at similar Reynolds number. This is further confirmed by Bloor (1964) [14] on the observation of three-dimensional flow related to random low frequency irregularities detected on a hot wire experiment between Reynolds number of *200* to *400*. LES is a three-dimensional turbulence model, thus flow around a circular cylinder at Reynolds number of *250* has been simulated using LES to capture the vortex shedding in the wake region of the flow. Some discussions on the work are published in [62].

Numerical simulations [72, 88] on the vortex shedding phenomenon have successfully captured the von Karman vortex street with Strouhal numbers close to experimental findings. Kalro and Tezduyar (1997) [56] employed a three-dimensional finite element formulation on the flow around a circular cylinder at low Reynolds number when vortex shedding occurs. He emphasized the influence of the three-dimensional effect on the calculation of drag coefficient and Strouhal number, which in his computation agreed very well with experimental result compared to the two-dimensional analysis.

3.3.1.2 LES of flow around a circular cylinder

This section describes the LES model used in the investigation of the vortex shedding phenomenon for the flow around a circular cylinder at Reynolds number of *250*, as well as the flow at Reynolds number of *3,900*.

- Computational domain and boundary condition

  The domain geometry and the boundary conditions for the LES at Reynolds number of *250* is the same as the case for the SST simulation (Section 3.3.1). The cylinder has a diameter of *0.1m* but is simulated with unsteady inlet velocity of *0.034m/s* by specifying the turbulence intensity at the inlet of *3%*.

- Meshing

  Tetrahedral unstructured mesh is employed in the current LES of flow around a circular cylinder. The y^+ (Section 3.2.1.1) value around the surface of the cylinder ranges between *1* and *3*.

- Discretisation

  In the LES of flow around a circular cylinder, the Navier–Stokes equations are discretises using a second order central difference scheme. The time discretisation in the current LES is carried out by using a second order backward Euler scheme.

- Computer power

  The LES of flow at Reynolds number of *250* is done on the Pentium *IV* PC. Compared to the SST model, LES needs longer time and requires a more refined mesh to resolve the unsteady scales. Generally, LES takes *4-6* days of simulation time (*1.2 million* to *1.5 million* elements) compared to *2-3* days for a SST simulation (*0.8 million* to *1 million* elements). The residual of the simulation has been set to the fourth order of the actual values for convergence consideration.

3.3.2 Results and discussions (LES at *Re 250*)

Apart from calculating the drag and pressure coefficients of the flow around a circular cylinder, the current LES at Reynolds number of *250* evaluates the Strouhal number of the flow (Eq. 3.2) based on the frequency of the oscillating lift coefficient, which

corresponds to the vortices shed alternately from top and bottom of the cylinder (Figure 3.19). The Strouhal number computed is *0.20*, agreeing well with the experimental value of *0.21* [146]. For the drag coefficient, experimental work gave a value of *1.20* [146] at this Reynolds number and LES predicted a drag coefficient of *1.24* from the time average computation.

Figure 3.19 shows the formation of vortex street (plotted as the vector of the streamwise velocity component) predicted in the wake region of the flow around a circular cylinder using LES at Reynolds number of *250*. Compared to Figure 3.17 of the SST computation, the current plot demonstrates the ability of the LES model to predict the unsteady motion in the wake region of the flow.

The pressure coefficient distribution around the cylinder at Reynolds number of *250* is plotted on Figure 3.20. Result from the SST model has been included for comparison between a RANS model and LES. At the windward side ($0° < \theta < 60°$), both models predict a close trend of pressure distribution on either side of the experimental data. Within the separation region ($60° < \theta < 120°$), LES shows more negative pressure while SST gives closer agreement to experiment result. Both models predict slightly different separation point compared to experimental data. At the leeward side of the flow ($120° < \theta < 180°$), SST shows a discrepancy in predicting the pressure distribution but LES gives very close prediction with experimental data, showing the capability of LES in capturing the complex vortical type of flow, which is crucial in the simulation of flow around bluff bodies. Pressure coefficient of flow at Reynolds number of *1,000* is depicted in Figure 3.21 to show the consistency of the LES at the trailing edge region. From both Figure 3.20 and Figure 3.21, it is noticed that the SST model performs better near the separation region and LES shows good agreement in region where vortices are shed. This suggests that a hybrid RANS/LES model such as the DES model could be beneficial in the applications of the flow around bluff bodies.

3.3.3 LES of flow around a circular cylinder at Reynolds number of *3,900*

Following the application of the LES on the flow around a circular cylinder at Reynolds number of *250*, flow at higher Reynolds number of *3,900* is simulated. This flow is characterised by laminar separation region in which transition to turbulence happens in the shear layer, producing large-scale vortices and complex flow in the near wake

region. Counter rotating streamwise vortices which are highly three-dimensional have been observed in the wake region of flow at this Reynolds number [11].

The choice of the Reynolds number of simulation depends largely on the experimental data available. For the flow around a circular cylinder at Reynolds number of *3,900*, two sets of experimental data provide details of the time average velocity profiles and Reynolds stress distributions in the wake region of the flow. Lourenco and Shih (1993) [64] used the particle image velocimetry (PIV) technique to measure the velocity profiles within three diameters downstream of the cylinder while Ong and Wallace (1996) [96] documented the distribution further downstream. These data provide useful information for comparative study with numerical solutions.

Breuer (1998) [17] investigated the influence of numerical aspects on the LES of flow around a circular cylinder at Reynolds number of *3,900*. He concluded that LES with a second order or higher central difference advection scheme yields the best solution and upwind discretisation scheme is not recommended in LES, as it introduces extra dissipation. Hansen and Long (2002) [43] used LES with the finite volume method (FVM) on an unstructured mesh at the same Reynolds number but has over-predicted the drag coefficient and the base pressure. Both works [17, 43] reported shorter recirculation length of flow compared to experimental result.

Beuadan (1994) [11] simulated the flow past a circular cylinder (*Re 3,900*) using a high order upwind-biased finite difference method (FDM). He pointed out that the dynamic SGS model give better prediction of the Reynolds stresses in the vortex formation region than a fixed coefficient Smagorinsky SGS model. Tremblay (2001) [132] concluded otherwise. He investigated the influences of the SGS model (fixed coefficient Smagorinky and dynamic Germano [38]) and grid resolution on the flow around a circular cylinder at Reynolds number of *3,900* and concluded that the grid resolution has greater effects on the solution of the flow than the SGS model. This could be due to the reason that very different mesh resolution has been used in the simulations.

Three-dimensional simulation is crucial in the flow at Reynolds number of *3,900* past a circular cylinder. Two-dimensional simulation over estimated the drag coefficient by *5-10%* [2] due to the simulation of perfect spanwise correlation of the flow. Two-dimensional calculation also omitted the effects of spanwise wake turbulence. This agreed with the finding of Kalro and Tezduyar (1997) [56], emphasizing the importance of three dimensional calculation in sub-critical region of

flow to accurately resolve the flow parameters such as the drag coefficient and the Strouhal number. Also, the base pressure is more negative in two-dimensional simulation and this affects the wake region prediction of the flow.

In unsteady flow simulation such as LES, certain numbers of vortex shedding cycles need to be simulated in order to accurately predict the near wake structure of the mean flow velocities and Reynolds stress profiles. Franke and Frank (2002) [33] pointed out that simulation of the LES on the flow around a circular cylinder at Reynolds number of *3,900* that is less than *42* averaging cycles might not yield a statistically converged solution of the flow. Comparisons show that time average symmetry flow is achieved for simulations with more than *42* averaging cycles.

Apart from the LES, direct numerical simulation (DNS) of the flow past a circular cylinder has been carried out by Tremblay (2001) [131] at a Reynolds number of *3,900*. The DNS result has been included for comparison with the LES prediction in the current work, which proves very useful in clarifying the discrepancies between experimental data and results from the LES.

Simulation of the LES on the flow around a circular cylinder at Reynolds number of *3,900* in the current work employs similar domain geometry as the previous (*Re 250*) simulation (Figure 3.9). The same boundary conditions have been implemented apart from an inlet velocity of *0.6m/s*.

A structured hexahedral mesh is used in the current simulation rather than the unstructured tetrahedral mesh as discussed before. Biswas and Strawn [12] documented the applications of tetrahedral mesh and hexahedral mesh on CFD problems, and concluded that a tetrahedral mesh is more suitable on flow over complex bodies due to its flexibility. However, in terms of mesh refinement, a hexahedral mesh can be repeatedly subdivided without causing deterioration of the mesh quality. Also, a hexahedral mesh demonstrated more efficient utilization of computer resources for similar level of accuracy of solution compared to a tetrahedral mesh due to the arrangement of the control volumes in the streamwise direction. This reduces the complexity of the simulation when computing the flow parameters around the elements. Frohlich *et al.* (1998) [37] performed LES on the flow around a circular cylinder at Reynolds number of *3,900* with structured and unstructured mesh. Comparisons of the results revealed insufficient representation of separated shear layer and wake region from a tetrahedral mesh due to distortion of the mesh but a hexahedral mesh preserved

the mesh quality better. Current LES employs a block structured hexahedral mesh (Figure 3.22), which provides more flexibility in simulating flow around bluff bodies.

3.3.4 DES of flow around a circular cylinder at Reynolds number of *3,900*

LES gives details on the unsteady motion of flow compared to RANS models. But the price is the increase in computational requirements. DES employs the RANS model at the boundary layer of the flow to save computational power and switches to the LES model in the detached flow region to capture the unsteady scales of the separated shear layer. Also, the SST RANS model predicts separation of flow close to experimental findings. Various works [45, 118] have been carried out using the DES at high Reynolds number (up to *Re 800,000*), with satisfactory result obtained. For the current simulation on the flow around a circular cylinder at Reynolds number of *3,900*, results from the DES are included for comparison purposes and to test the applicability of the model for simulation on the flow around a square cylinder and rectangular cylinders in the next two chapters.

Travin *et al.* (2000) [129] simulated the flow around a circular cylinder at a Reynolds number of *50,000* using a Spalart-Allmaras (S-A) DES model. The model employs a Spalart-Allmaras (S-A) one-equation model [115] for the RANS part, good results have been observed provided that the mesh resolution is fine enough. Current simulation of the DES employs the SST model in the RANS region (around the cylinder surface) rather than the one-equation model. Strelets (2001) [122] used both the S-A DES and the SST-DES models [130] to simulate the flow around a circular cylinder. The SST model normally employs an upwind advection scheme but the SST-DES model used by Strelets switches between a fifth order upwind and a fourth order central scheme depending on the region in the flow. This hybrid upwind/central scheme SST model predicted shorter recirculation bubbles and smaller vortices at the flow separation region. However, the drag coefficient predicted by the hybrid SST model is closer to experimental findings compared to a pure upwind scheme. Current work on the flow around a circular cylinder employs a SST-DES model, which is similar to the SST-DES model of Strelets but with some modification to reduce the grid induced separation problems [115]. Also, a blending of second order upwind scheme and a second order central difference scheme is used rather than the fifth order upwind as in the SST-DES model used by Strelets.

3.3.5 Result and discussion (LES and DES at Re *3,900*)

Simulation of the flow around a circular cylinder at Reynolds number of *3,900* is done on a parallel machine consisting of *24* Pentium *IV* CPU each with *2.5GHz* processor and *1GB* RAM. This is necessary for the capturing of the unsteady flow details in the wake region of the flow and to observe the time history of the flow parameters such as the drag and the lift coefficients - simulation on a single PC is too impractical and time consuming.

A mesh sensitivity analysis has been conducted for the LES of flow around a circular cylinder at Reynolds number of *3,900*. Two mesh types, LES I with *0.24 million* elements and LES II with *0.55 million* elements have been compared. Unlike the RANS cases (section 3.2.2), both LES has similar amount of nodes and elements in the same simulation. Similar case applied to DES. To resolve the flow profiles near the cylinder wall surface, average y^+ values for LES and DES of *3* and *4* have been used respectively. Figure 3.23 defines the centerline and three vertical profile locations in the wake region where flow is analyzed for comparison with the experimental data. Figure 3.24 shows the mean streamwise velocity component at the centerline of the flow (*10D* downstream) as predicted by LES and DES. All velocities are non-dimensionalised by the inlet velocity u_{in}. Both LES show good agreement with experimental data but LES I slightly under-predicts the recirculation length of the flow compared to LES II. Experimental data has been included to provide a general idea of the flow profiles.

Figure 3.25 and Figure 3.26 depict the vertical profiles of the mean streamwise and spanwise velocity respectively in the wake region of the cylinder at *x/D=1*, *x/D=3* and *x/D=5*. At *x/D=1*, the streamwise velocity of LES I shows a lower negative velocity than the LES II prediction, which corresponds to a shorter recirculation length where a higher velocity component is found near the end of recirculation region. Further from the recirculation region, very good agreement is observed at *x/D=3* and *x/D=5* for the streamwise components. For the spanwise velocity component at *x/D=1*, the peaks are correctly identified but different magnitudes are observed. The peaks correspond to the edge of the recirculation bubbles. At *x/D=3* and *x/D=5,* larger discrepancies have been observed between LES I and LES II. Also, the results are not symmetrical. This could be attributed to the simulation time being too short to predict a mean value. The flow has been simulated for roughly *40* averaging cycles before the mean velocity profiles are calculated. For the later validation study on the flow around a circular cylinder in

which comparison of Reynolds stress components are involved, all the mean values of flow profiles have been calculated after simulation of more than *150* averaging cycles.

Another significant observation from Figure 3.26 is the occurrence of the three-dimensional flow structure in the wake region of the cylinder. Top plot (*x/D=1*) of the figure shows the existence of spanwise variation of the flow due to the streamwise vortices in the near wake region. LES captures the situation well while DES shows less significant three-dimensional flow structures.

3.3.5.1 Meshing in DES

In the DES case, both DES I and DES II simulations have a similar number of elements. Meshing in the DES focuses more on local refinement of mesh rather than global refinement as in the LES. An ideal LES means the turbulence resolution length scale used needs to be fine enough to resolve all the motion in the flow [100], which suggests that a very refined mesh is required. On the other hand, the local refinement controls the contribution of the RANS model and the LES in the flow domain to get an optimal DES. Figure 3.27 and Figure 3.28 show the effect of grid refinement on DES I and DES II. The LES contribution is less in DES II (where mesh near the inlet boundary has been coarsen) to achieve computational efficiency.

The mean streamwise velocity components from DES I and DES II show discrepancies around the recovery region (between end of flow recirculation point and *x/D=4.00*) where the mesh in DES II has been refined, leading to closer agreement of DES II with LES result (Figure 3.24). Under-prediction of the recirculation length has been observed in both DES I and DES II in comparison to the LES computation. From Figure 3.27, it is observed that the recirculation region falls in the 'grey area' of DES, where transition between the RANS model and the LES model is ongoing. This 'grey area' is of great concern in DES modelling, it is crucial that LES should immediately produce the required unsteady motion and three-dimensional effects during the transition.

The mesh in the vicinity of the cylinder has been refined in DES II while mesh near the boundary walls has been coarsen to achieve computational efficiency. Also, this prevents the activation of LES in these regions, which depends on the mesh size. Figure 3.29 and Figure 3.30 show the mean streamwise velocity components in the near wake region of the flow for DES I and DES II. At *x/D=1*, DES II predicted shorter recirculation bubbles compared to DES I (Figure 3.29 and Figure 3.30, red line

represents *x/D=1*). This observation suggests that proper mesh refinement in DES is necessary since it produces significant effect on the simulated results.

3.3.5.2 Comparison of experimental data against LES and DES results

Figure 3.31 shows the first *40 seconds* of the time history of the lift and drag coefficients predicted by LES for the flow around a circular cylinder. The Strouhal number of the flow is calculated based on the oscillating frequency of the lift coefficient. The time domain data of the lift coefficient is converted into frequency domain by using the Fast Fourier Transform (FFT). The power spectrum of the lift and the drag coefficients are shown in Figure 3.32, the frequency of the lift coefficient (f_s) is then substituted into Eq. 3.2 to get the Strouhal number. Good agreement with the experimental result is observed from LES. Notice that the frequency of the drag oscillation is roughly twice the frequency of the lift coefficient, corresponding to the observation of theoretical findings (Section 3.1). The average drag coefficient from the LES is *0.99* and experiment data gives a value of *0.98±0.05* [91]. The predicted flow parameters are summarized in Table 3.4 together with the results from the DES. *Lr* in the table represents the recirculation length of the flow in the wake region of the cylinder. The angle of separation of the flow from LES is *88.2°*, close to the experimental value of *85±2°* [114].

Table 3.4 Computed flow parameters (LES & DES) in comparison with experimental results.

	Strouhal number	C_d	*Lr/D*	θ_s
Exp. [Norberg C, 1987]	0.215±0.005	0.98±0.005	1.33±0.2	—
Exp. [Son J *et al.*, 1969]	—	—	—	85±2
LES	0.210	0.99	1.14	88
DES	0.250	0.88	1.04	91

Similarly, the time history of the drag and lift coefficients of the first *40 seconds* from the DES is shown on Figure 3.33. As mentioned, DES employs the SST model in

the vicinity of the cylinder. From Figure 3.33, it was observed that DES predicted lower drag coefficient (in region where SST is active) compared to the experimental data. This is in accord with the observation in Section 3.3.3 on the under prediction of drag coefficient when SST is used alone. The SST model in the current DES employs a second order upwind advection scheme for space discretisation. Strelets (2001) [122] used a fifth order upwind scheme SST (DES) model on the flow around a circular cylinder at higher Reynolds number and still a lower drag coefficient has been observed. When he switched to a hybrid upwind/central advection scheme for the same simulation, great improvement is shown on the prediction of the drag coefficient. Another factor that influences the prediction of the drag coefficient in SST is the refinement of the mesh near the wall of the cylinder. Very refined mesh is needed to accurately capture the viscous drag since the flow is resolved directly without any wall function method employed. Consequently, the under-prediction of the drag coefficient resulted in a higher Strouhal number from the DES compared to the experimental value (Table 3.4). This agreed with the experimental finding of Roshko (1954) [103] (Figure 3.3).

Figure 3.35 depicts the mean centerline velocity of flow from LES and DES compared to experimental results [64, 96] and DNS [131]. In the recirculation region, LES displays close agreement with experimental result and DNS. In the recovery region (*x/D=2* to *x/D=4)*, a similar trend of flow has been predicted by LES compared to DNS but not the experimental data. However, the experimental result is questionable at *x/D=3* where a sudden change of the curve is observed. DES computed the shortest recirculation length among the results, leading to the discrepancy in the recovery region. Consequently, the centerline velocity does not recover to the value of the experimental and DNS result further down the wake region.

The mean streamwise velocity components from the LES and DES at *x/D=1*, *x/D=3* and *x/D=5* with the experiment and DNS results are shown in Figure 3.36. In the recirculation region, both LES and DES predict a narrower wake compared to the measured data and DNS, with the narrowest from DES. This can be deduced from the peaks of the mean spanwise velocity component plot in Figure 3.37 as well. This is a consequence of a later separation angle (*91 °*) (Table 3.4) of DES prediction. For *x/D>1*, less agreement between velocity components of DES have been observed and fluctuation of the result is obvious, indicating that longer simulation time is necessary. However, the distribution of the profiles from experiment shows a rather strange behaviour, where the spanwise velocity component at the centerline is not zero. At

x/D=1, DES shows less intense recirculation (Figure 3.37) near the centerline region compared to LES, experimental and DNS computation, owing to the presence of shorter recirculation bubbles. Further down the flow at *x/D=3* and *x/D=5*, the spanwise velocity components exhibit fluctuations due to the coarsening of the mesh, with the DES computation having a coarser mesh and thus greater discrepancy at *x/D=5*. The spanwise mesh resolution also contributes to the asymmetry of the curves. Fluctuations are observed in the experimental results to some extent as well.

Figures 3.38 to 3.40 show the streamwise Reynolds stress ($u'u'/U_{in}^2$), the spanwise Reynolds stress ($v'v'/U_{in}^2$) and the Reynolds shear stress ($u'v'/U_{in}^2$) components from the simulation and experiment at *x/D=1*, *x/D=3* and *x/D=5* respectively. All the Reynolds stress components are normalized by the square of the inlet velocity, U_{in}^2. For the streamwise Reynolds stress component, prediction from both the LES and DES show lower peaks compared to both the experimental result and the DNS. The work of Beaudan (1994) [11] on the LES of flow around a circular cylinder reported a similar situation from a fixed Smagorinsky SGS model compared to the dynamic SGS model. In the Smagorinsky SGS model (Section 2.2.1.2), filtering introduces a wave number cut-off where small eddies are modelled using an eddy viscosity model. The eddy viscosity model predicted different viscosity intensity compared to the dynamic model, causing the discrepancy observed in the Reynolds stress components. Hansen and Long (2002) [43] observed similar low streamwise Reynolds stress components when applying LES with the fixed Smagorinky SGS model on the flow around a circular cylinder at the same Reynolds number. In the light of this, an alternative attempt was made by transforming the Navier-Stokes equation into a time-dependent base flow and a time-dependent disturbance to form the Nonlinear Disturbance Equations (NLDE) [82] for solving the flow. Stress components closer to experimental results are observed [43] by using the NLDE method on the flow around a circular cylinder rather than the conventional decomposition of flow into steady and unsteady components. Despite the lower intensity of the stress components computed, the location of the peaks of the stress components were correctly identified by the LES and DES.

For the spanwise Reynolds stress component (Figure 3.39), agreement between simulated and measured experimental results as well as DNS computation are fairly good at *x/D=1,* suggesting that the three-dimensionality effect correspond to the spanwise component has been well simulated by the LES and DES. Further down the wake region, the simulation indicated reduced effect of three-dimensionality due to the coarsening of the mesh. This can be observed in Figure 3.41 of the instantaneous

pressure changes in the wake region of the flow for LES case. The vortical structures can be visualized at the near wake with spanwise changes but the effect reduces further downstream. Better agreement of the spanwise Reynolds stress with experimental results is observed from the LES and DES rather than DNS beyond the recirculation region. Notice the discrepancy of the DNS result [131] with the measured experiment and simulated data. Similar situation has been observed in the DNS of flow around a circular cylinder conducted by Ma *et al.* (1999) [67].

The Reynolds shear stress (Figure 3.40) from the LES and DES are generally lower than the experimental and DNS computation as a consequence of the under prediction of both the streamwise and spanwise Reynolds stress components. Other researchers [17, 30] reported that a dynamic subgrid scale model shows better prediction of the stress components compared to the fixed Smagorinsky model employed in the current simulation. Despite this discrepancy, the peak locations and the size of the wake were well predicted from both of the simulation except for the case of DES at *x/D=5,* which shows almost zero value of vertical shear stress profiles.

3.3.5.3 Computational time

It is claimed that the advantage of the DES over LES is the shorter computational time required for simulation. Meshing is different in LES and DES. Refinement of mesh in LES needs to be done evenly throughout the computational domain while DES requires a more local mesh refinement. In other words, meshing in DES is more flexible and users have more control on the number of elements used in the simulation to be computationally efficient. Usually, regions where RANS model is active can be simulated with a much coarser mesh.

Figure 3.42 shows the CPU time (in minutes) for the LES and DES cases with different mesh size, corresponding to the meshes used in the mesh independence test at the beginning of this chapter. The CPU time here refers to the time in minutes required for the computer to calculate one time step on a single CPU. To provide an idea of the CPU time compared to normal wall clock time, the *5.8* CPU time of LES took *4* days of computational time running on *12* CPU with a total time step of *12,000* (in order to get sufficient vortex shedding cycles). Non-dimensional form of the computational time is written as,

$$\Delta t^* = \frac{\Delta t U}{D} \qquad \text{Eq. 3.4}$$

where Δt is the timestep, U is the streamwise velocity and D is the diameter of the cylinder. The non-dimensional time for the current simulation has a value of *0.04* based on Eq. 3.4.

From Figure 3.42, it is noticed that similar amount of time is required for the LES and DES for a *0.2 million* mesh. This mesh is considered a coarse mesh in LES but a medium or fine mesh in the DES. For a satisfactory mesh in the LES (*0.55 million*), simulation time is about *1.4* times longer than the DES case (Figure 3.42), which only takes about *2.9* days.

Although it is not at order of magnitude faster in this case (*Re 3,900*), the situation is expected to be different at higher Reynolds number. It is reported that the number of elements in a mesh LES required near the viscous sublayer is proportional to $Re^{1.8}$ [13], but not in the case with DES where a RANS model helps to save computational power. So a much longer computational time is expected for LES at higher Reynolds number and the application of DES will be an advantage.

3.4 CONCLUSION

From the current work on the simulation of the flow around a circular cylinder using the RANS, LES and DES models, it is concluded that the k-ε and RSM models fail to correctly predict the drag coefficient of the flow at sub-critical Reynolds numbers. Changing the mesh resolution shows inconsistent results. The more advanced two-equation SST model performed better than the k-ε and the RSM models. Drag coefficient closer to the experiment data has been predicted by using the SST model. The pressure distribution around the cylinder surface from the SST simulation agreed well with measured data near the leading edge and flow separation region but no unsteadiness of flow has been observed in the wake region. The flow separation point predicted is slightly behind the measured data.

In the LES and DES computations, the unsteady scales of the flow and the vortex structure have been well predicted. LES correctly computed the recirculation length, separation point, drag coefficient and the Strouhal number of the flow while DES gave slightly different values from the measured experimental data. For the analysis of the velocity profiles distribution in the wake region of the flow, both LES and DES captured good streamwise and spanwise velocity profiles. The Reynolds stresses components were generally under predicted from both cases due to the deficiency of the fixed Smagorinsky SGS model on the assumption of the eddy viscosity distribution.

DES proves to be computationally more efficient than LES and requires fewer elements for simulations at similar Reynolds number.

From the comparison study on the LES and DES of flow around a circular cylinder, several points have been identified for further improvement on the current work. It is worth examining the effect of the dynamic SGS model over the fixed Smagorinsky model on the flow around a circular cylinder especially on the impact of the prediction of Reynolds stress components. Also, the spanwise mesh resolution and the extent of the cylinder in the spanwise direction (two times the diameter of the cylinder in this case) on the flow profiles ought to be further investigated. In the next two chapters, the simulation of flow around a square and rectangular cylinders have been modelled with larger spanwise length (based on the experimental setting of the test in the wind tunnel). Finally, more work needs to be done on the improvement of the performance of DES on the 'grey area' where transition of the RANS model and the LES occurs.

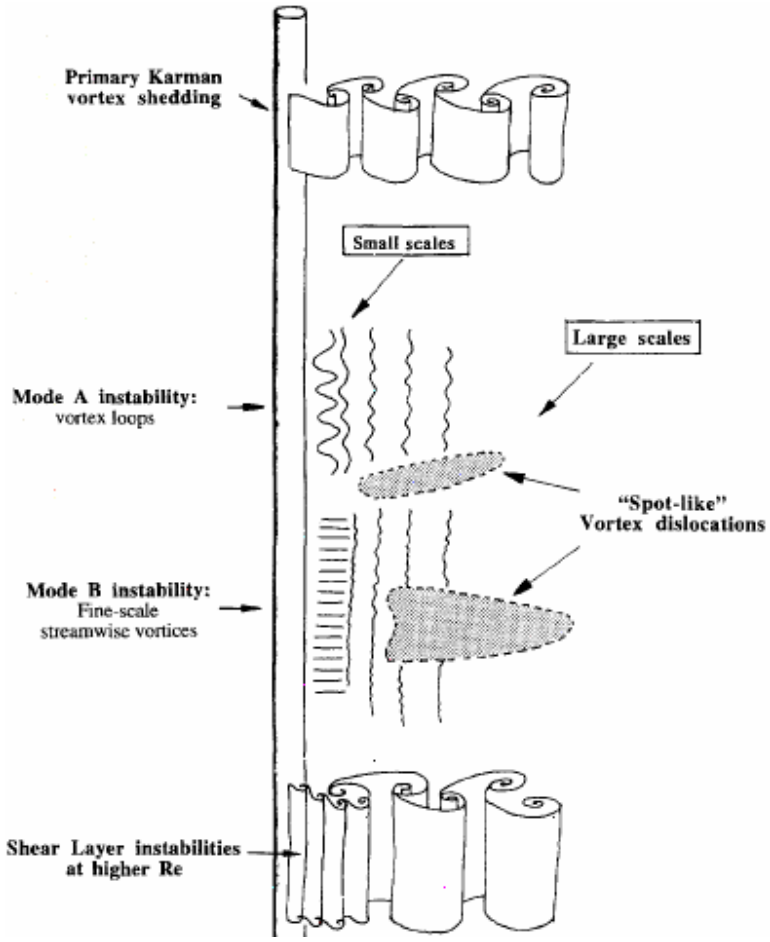

Figure 3.1 Development of three-dimensional flow in the wake region [142].

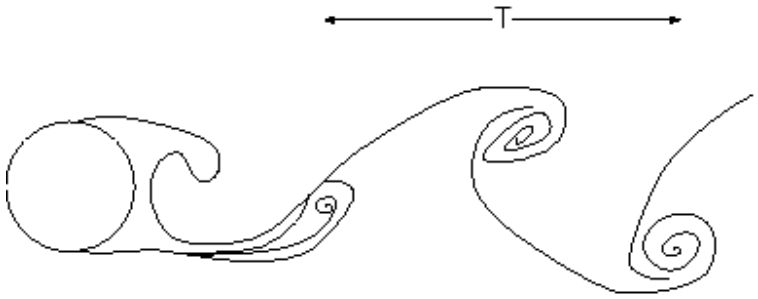

Figure 3.2 Vortex shedding in the wake region of the flow around a circular cylinder [1].

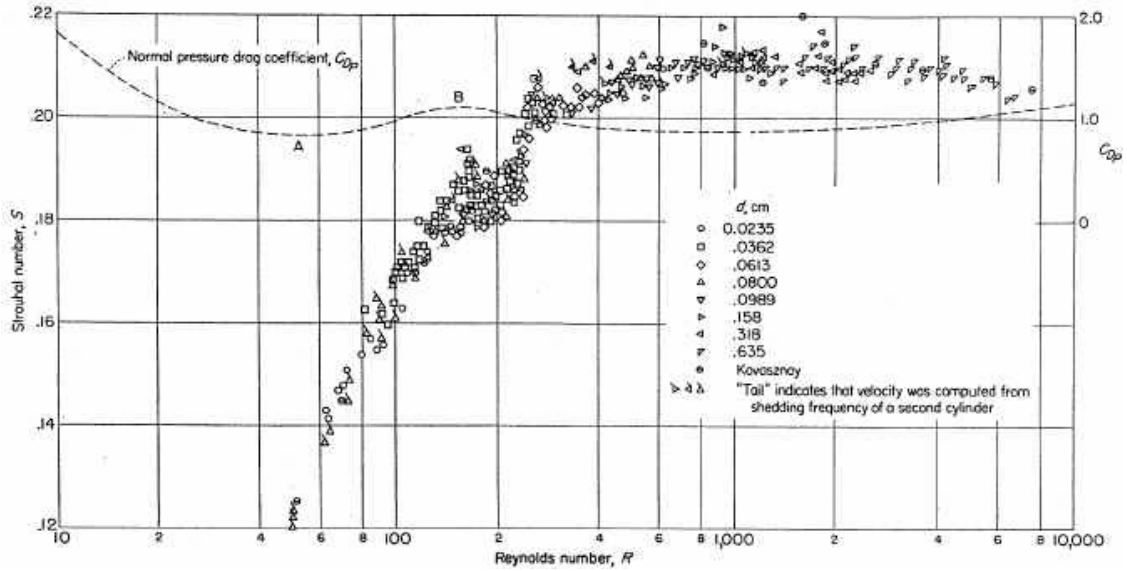

Figure 3.3 Changes of Strouhal number and drag coefficient with Reynolds number in the subcritical flow region [102].

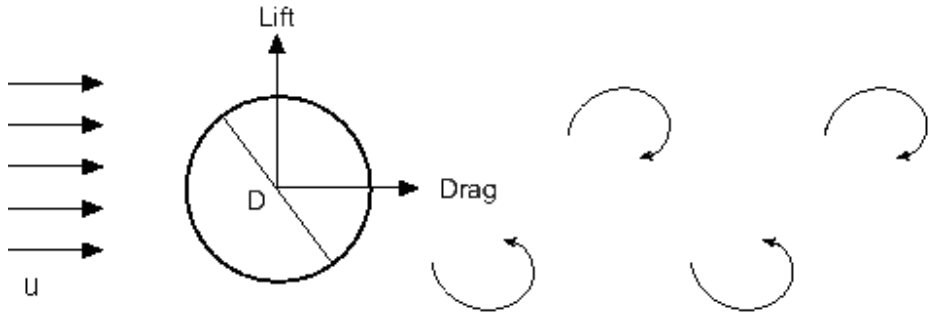

Figure 3.4 Schematic diagram of forces acting around a circular cylinder.

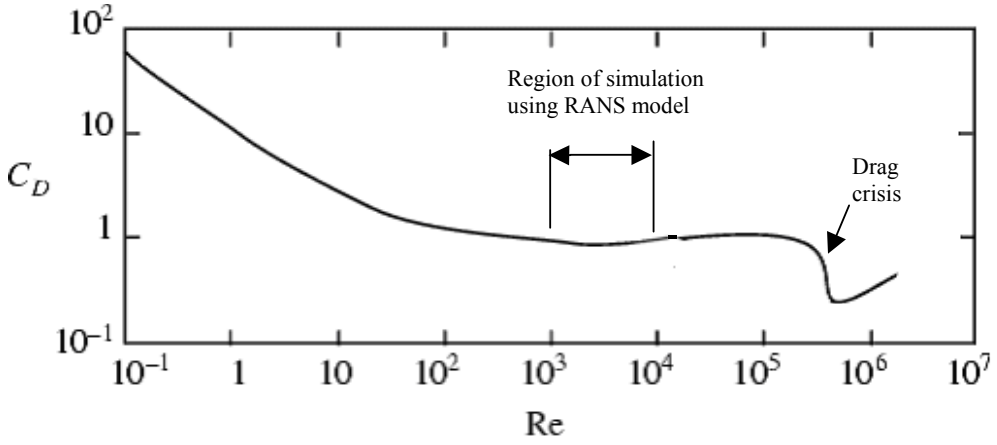

Figure 3.5 Drag coefficient of the flow around a circular cylinder [109].

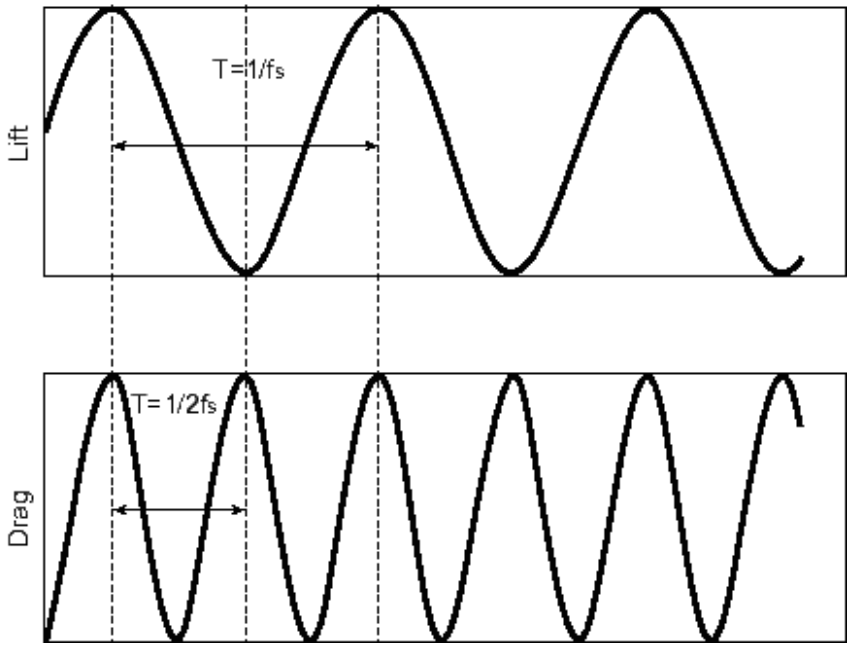

Figure 3.6 Lift and drag force of the flow around a circular cylinder.

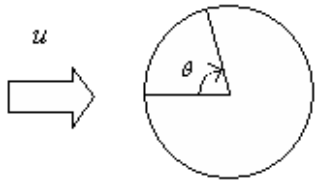

Figure 3.7 Definition of θ of the flow around a circular cylinder, u is the longitudinal velocity component.

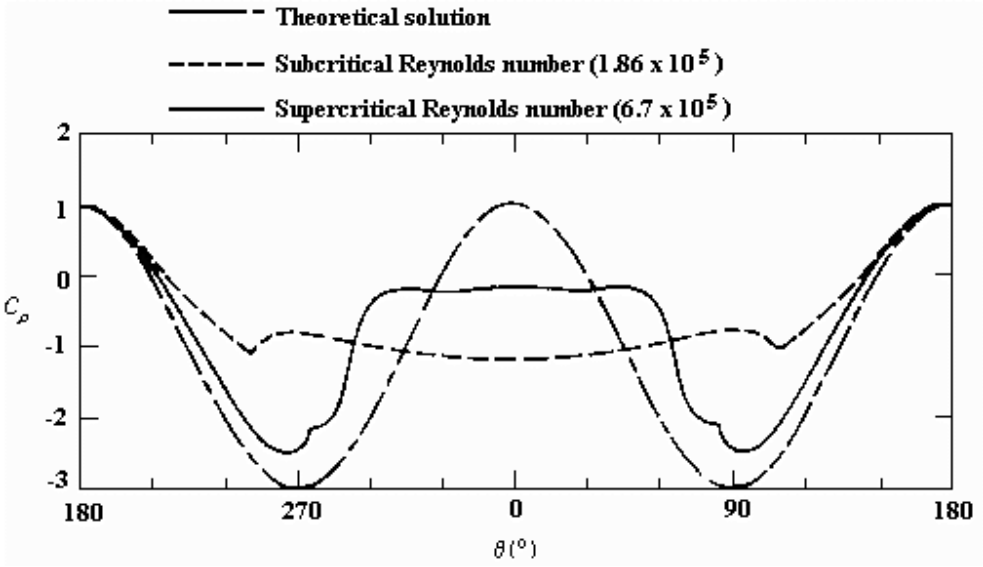

Figure 3.8 Measured pressure coefficient distributions on cylinder surface compared to theoretical result assuming ideal flow [24].

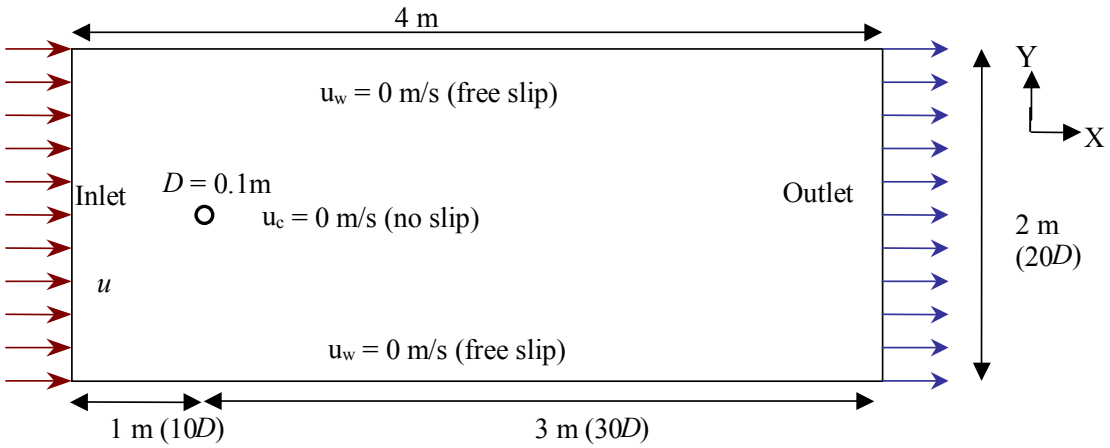

Figure 3.9 Computational geometry and boundary conditions (not to scale).

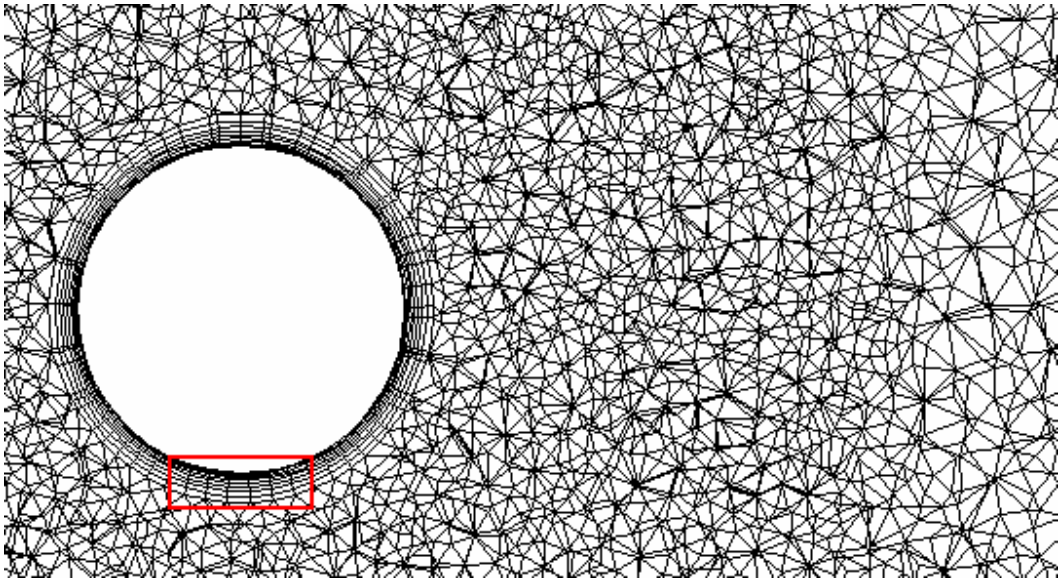

Figure 3.10a An unstructured tetrahedral mesh around a circular cylinder.

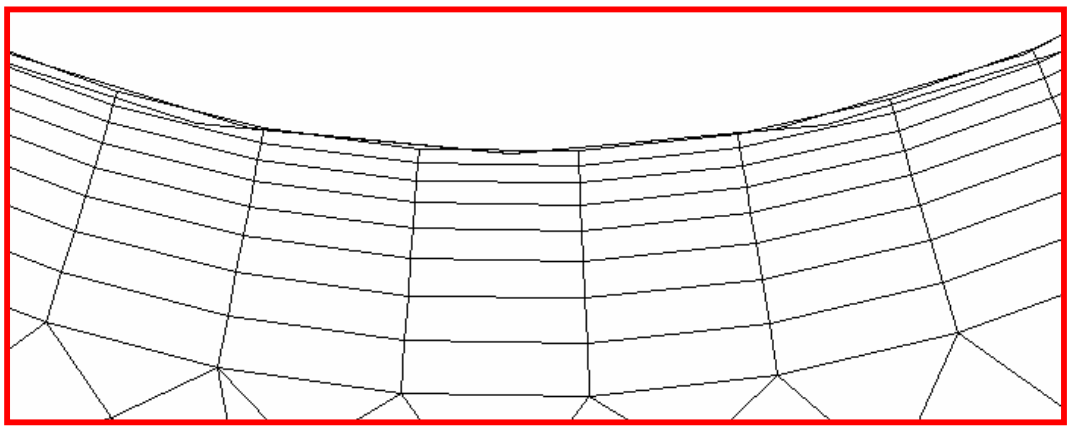

Figure 3.10b Inflation of mesh around the cylinder surface.

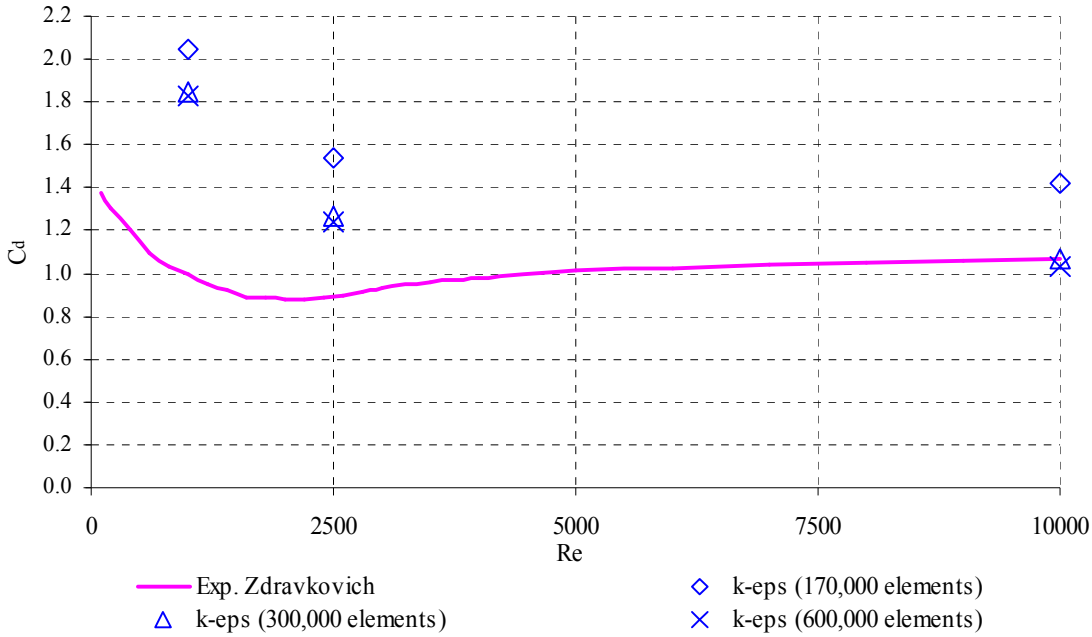

Figure 3.11 Drag coefficient (k-ε model) of the flow around a circular cylinder compared to experimental result [146].

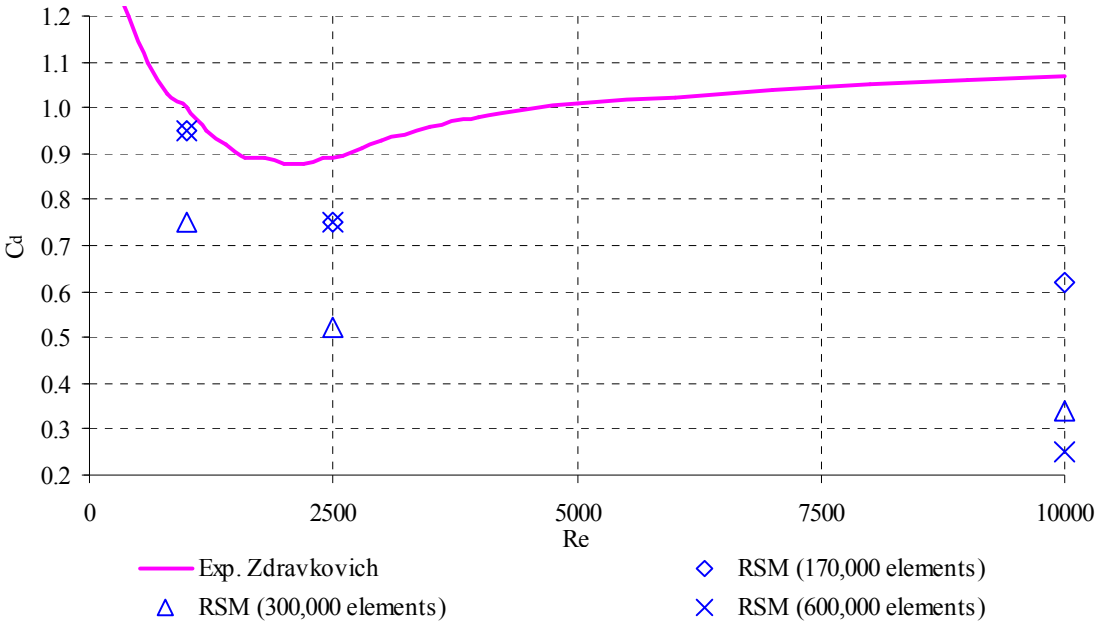

Figure 3.12 Drag coefficient (Reynolds Stress Model, RSM) of the flow around a circular cylinder compared to experimental data [146].

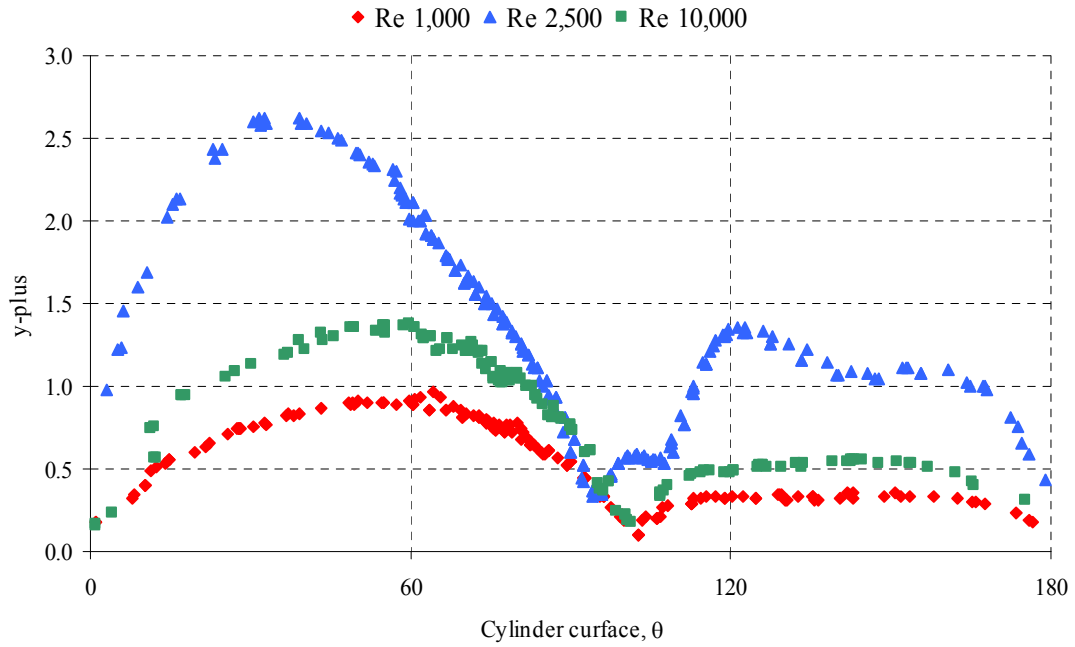

Figure 3.13 y^+ values for Reynolds number of *1,000*, *2,500* and *10,000* of the flow around a circular cylinder using the Shear Stress Transport (SST) turbulence model.

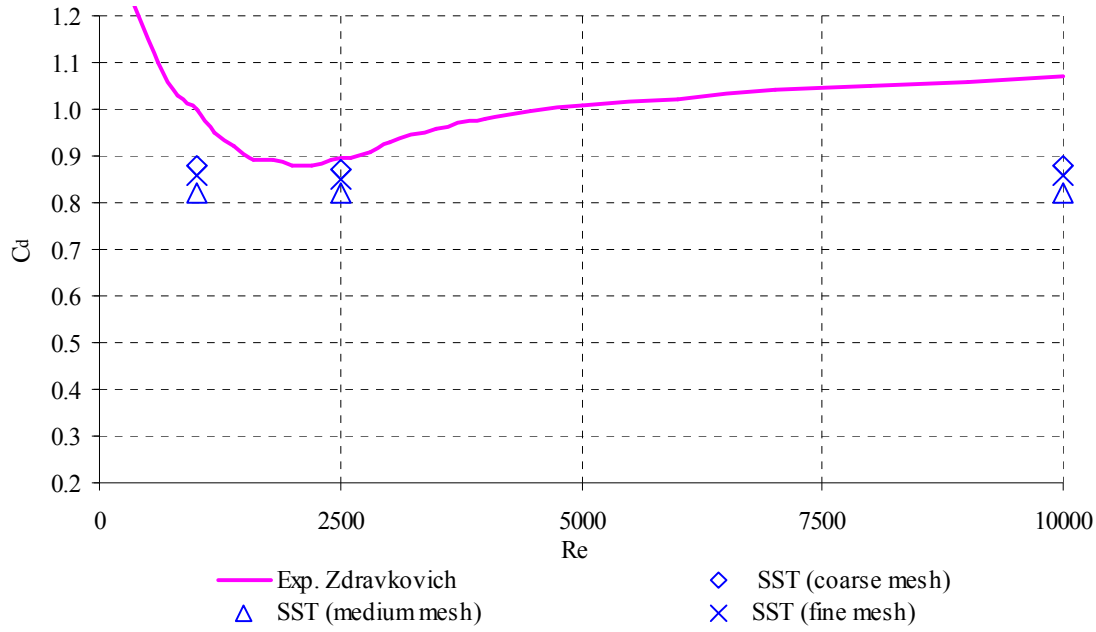

Figure 3.14 Drag coefficient (SST model) of the flow around a circular cylinder compared to experimental data [146].

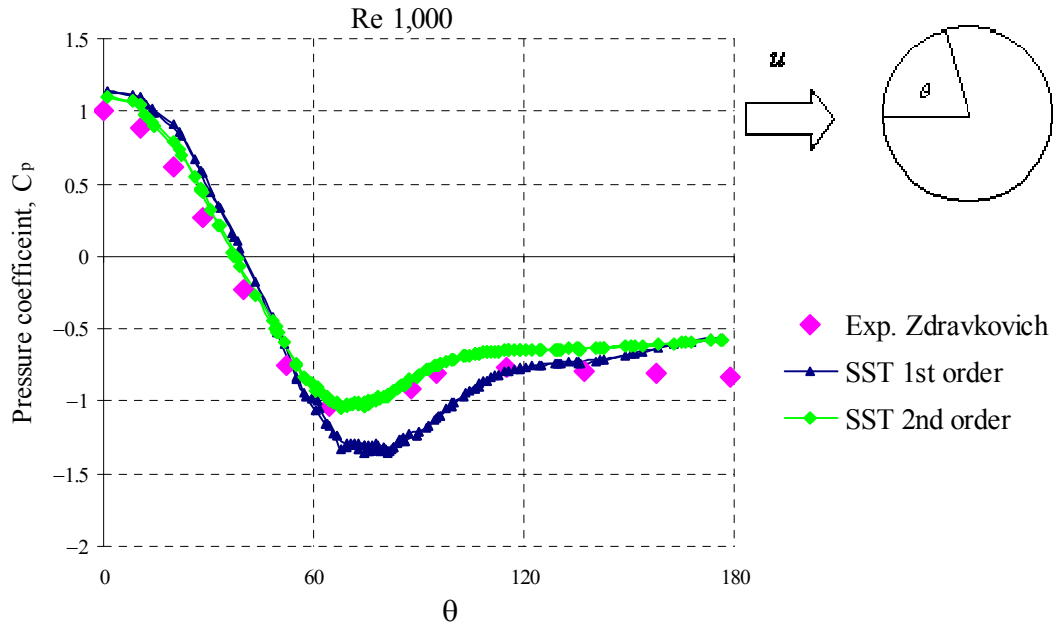

Figure 3.15 Pressure coefficient distribution (SST model) around circular cylinder at Reynolds number of *1,000*.

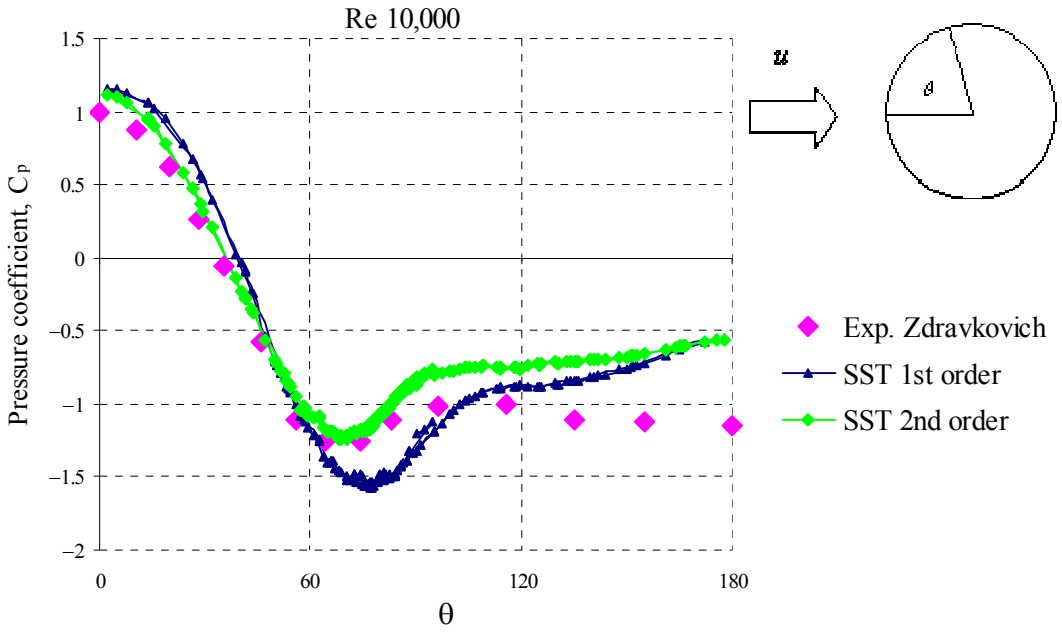

Figure 3.16 Pressure coefficient distribution (SST model) around a circular cylinder at Reynolds number of *10,000*.

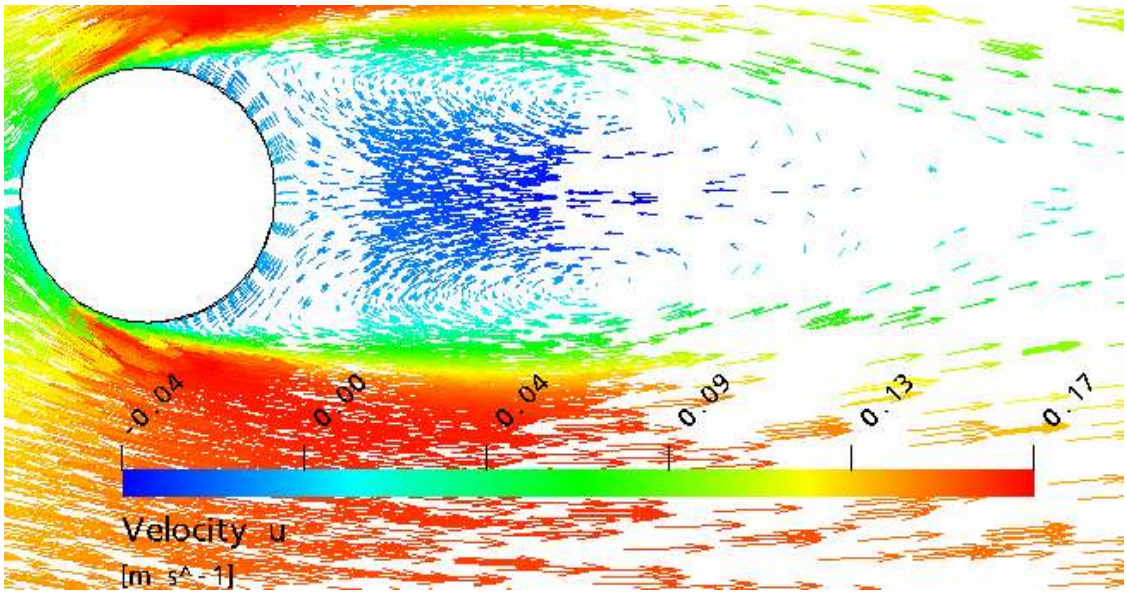

Figure 3.17 Vector plot coloured by the streamwise velocity component at Reynolds number of *2,500* (SST).

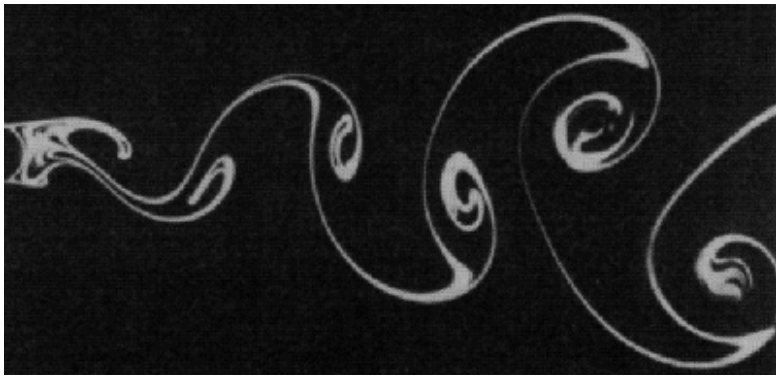

Figure 3.18 Von Karman vortex street in the wake of a circular cylinder [29].

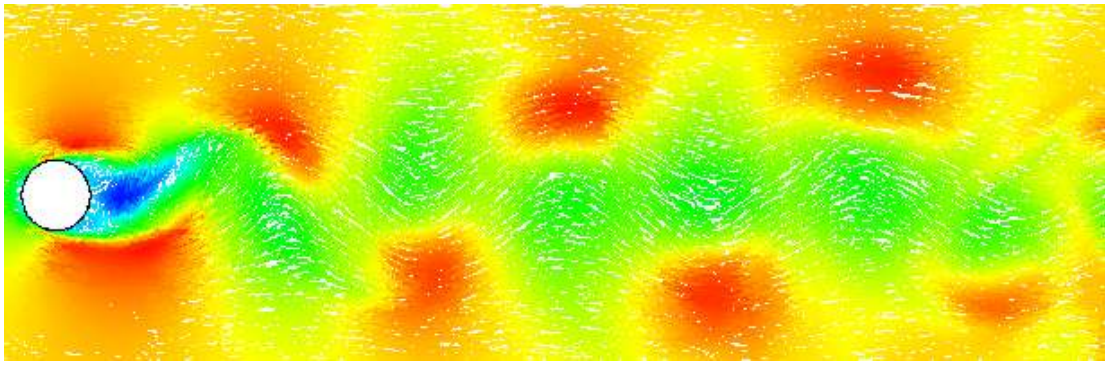

Figure 3.19 Vector plot coloured by the streamwise velocity component showing vortex shedding at Reynolds number of *250* (LES).

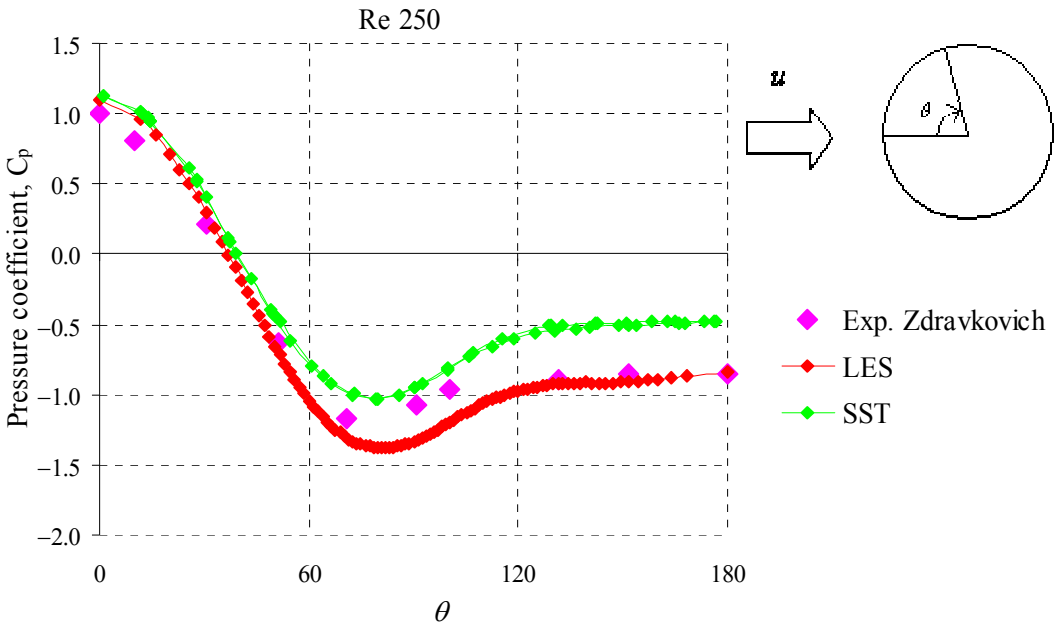

Figure 3.20 Pressure coefficient distribution (LES & SST) around a circular cylinder at Reynolds number of *250*.

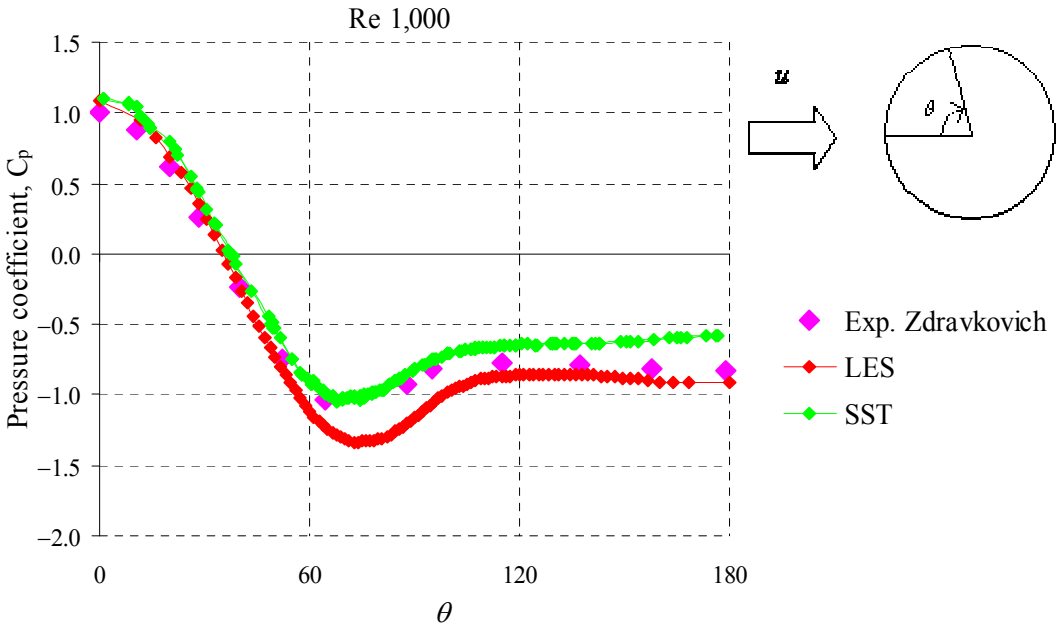

Figure 3.21 Pressure coefficient distribution (LES & SST) around a circular cylinder at Reynolds number of *1,000*.

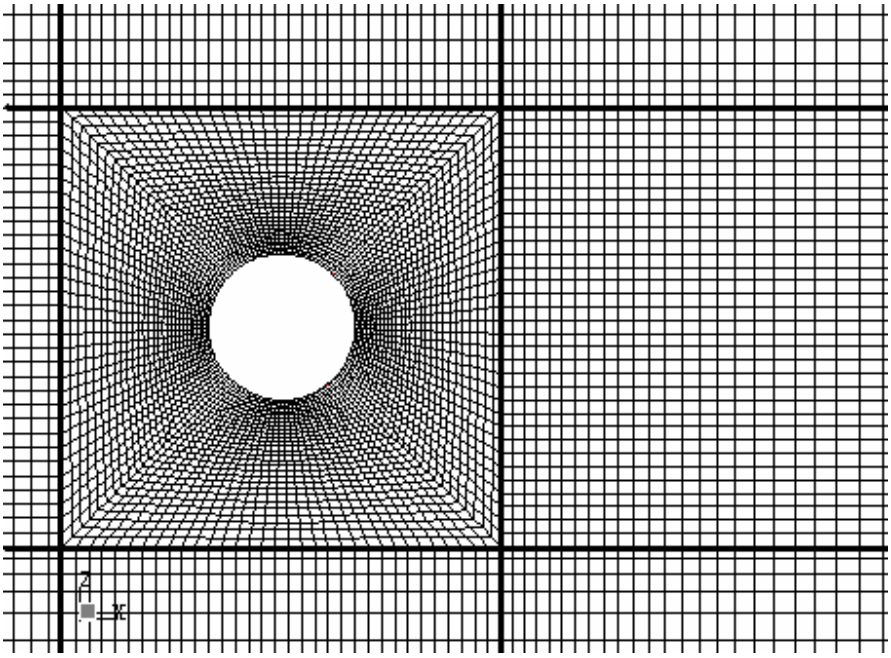

Figure 3.22 A Block structured hexahedral mesh at Reynolds number of *3,900*.

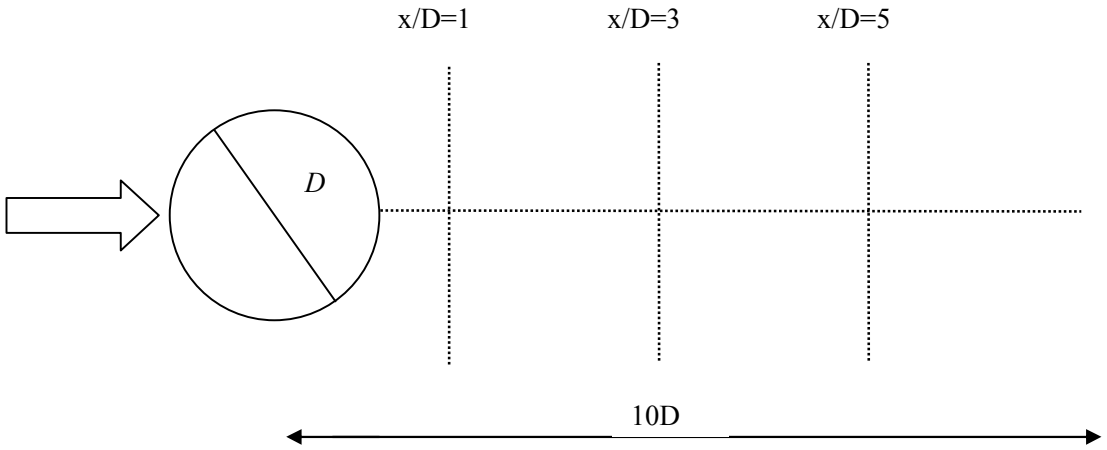

Figure 3.23 Definition of centerline and vertical profiles of flow in the wake region of the cylinder (not to scale).

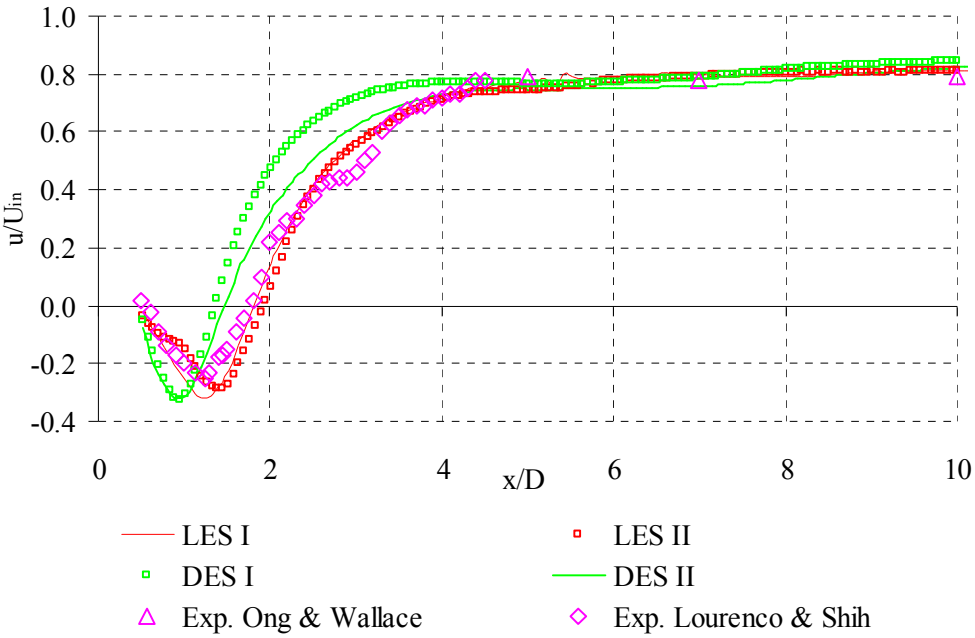

Figure 3.24 Mean streamwise velocity components at centerline of cylinder (*Re 3,900*).

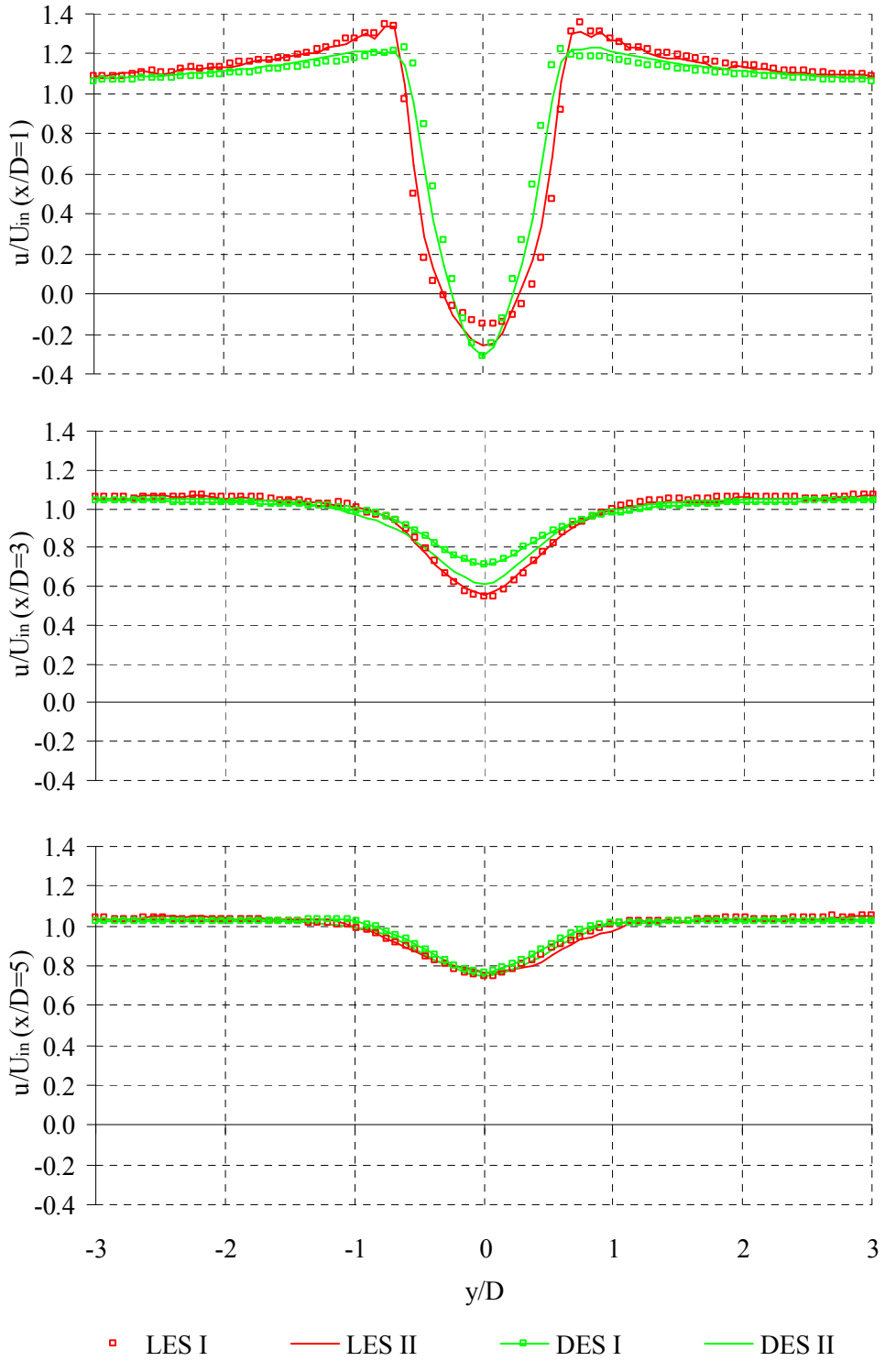

Figure 3.25 Mean streamwise velocity components (LES & DES) in the wake of the flow around a circular cylinder (Re *3,900*).

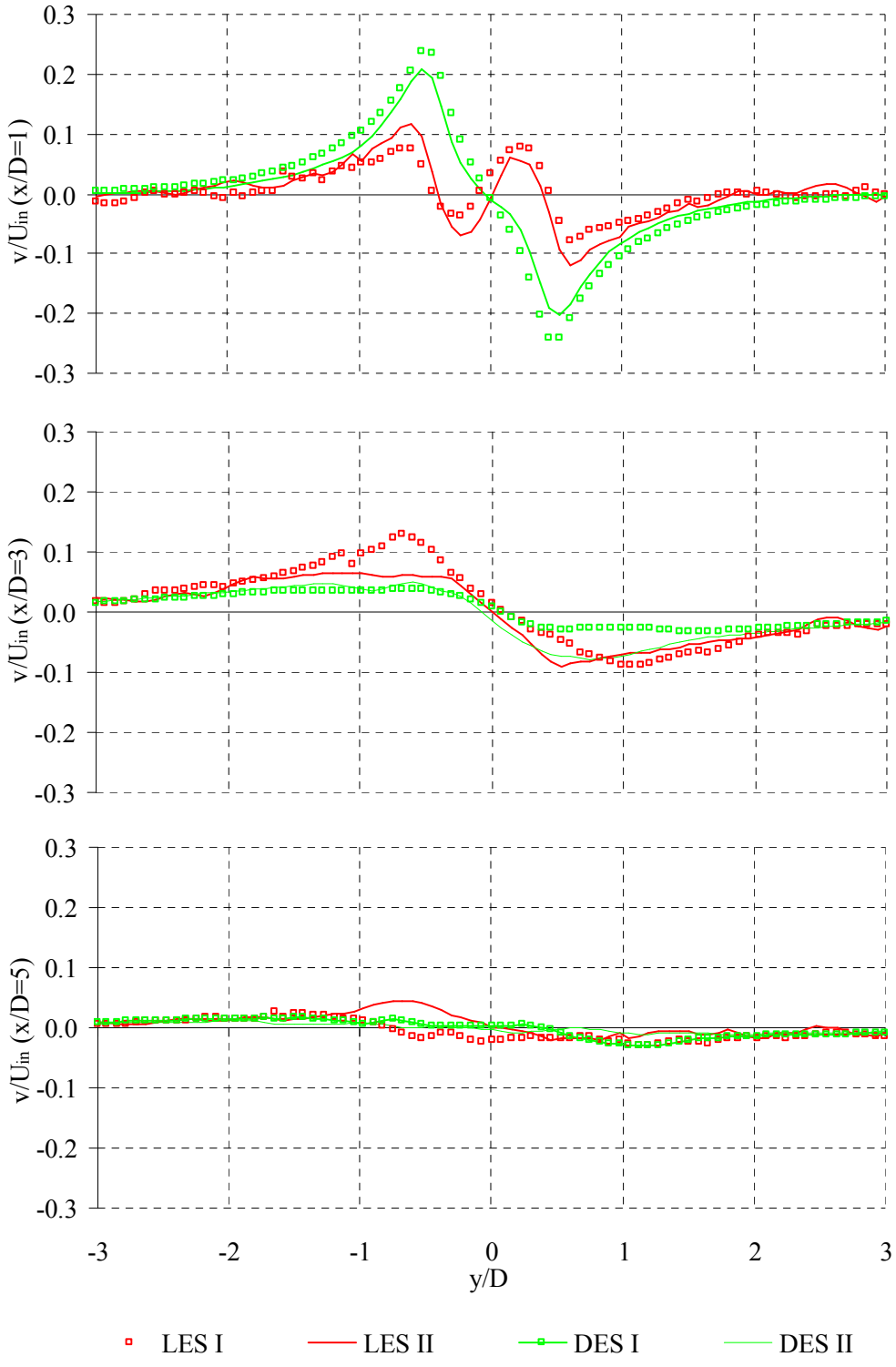

Figure 3.26 Mean spanwise velocity components (LES & DES) in the wake region of the flow around a circular cylinder (*Re 3,900*).

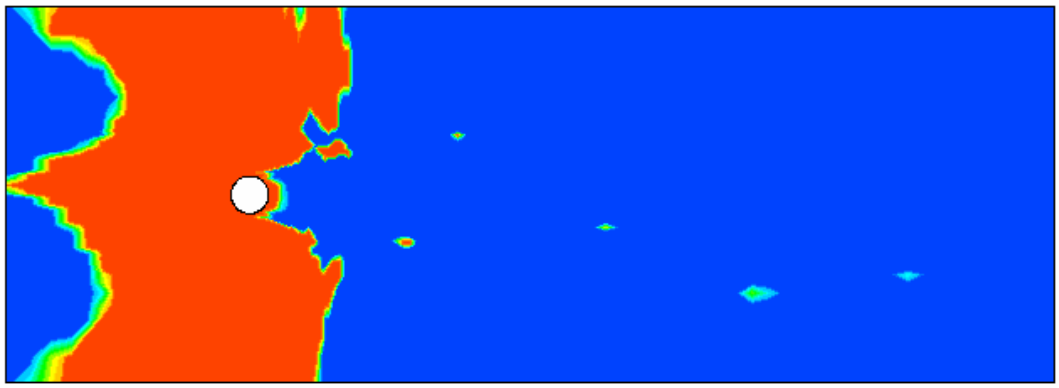

Figure 3.27 Region for RANS (Red) and LES model (Blue) in DES I.

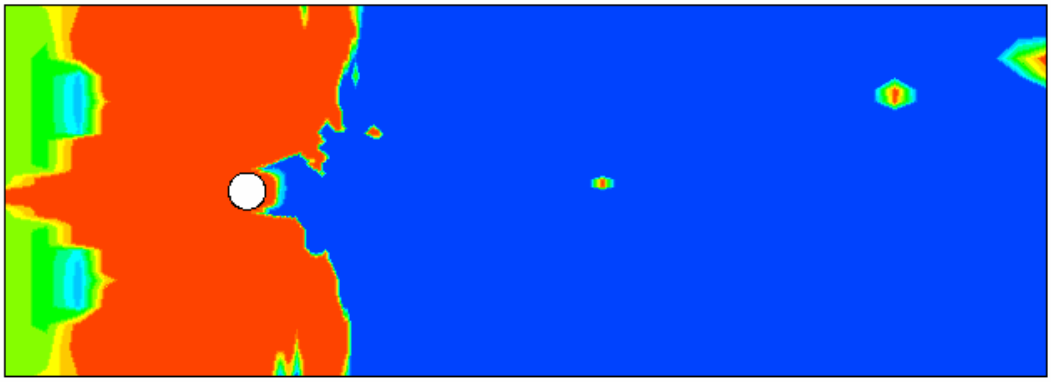

Figure 3.28 Region for RANS (Red) and LES model (Blue) in DES II (green shows transition between RANS and LES models).

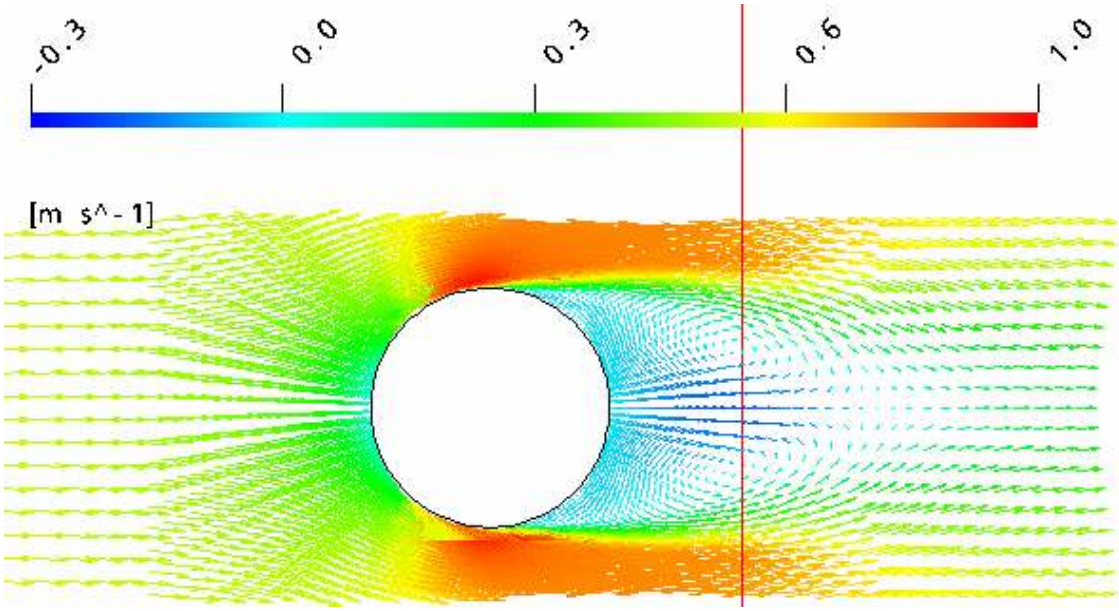

Figure 3.29 Recirculation bubbles of mean streamwise velocity component at Reynolds number of *3,900* (DES I).

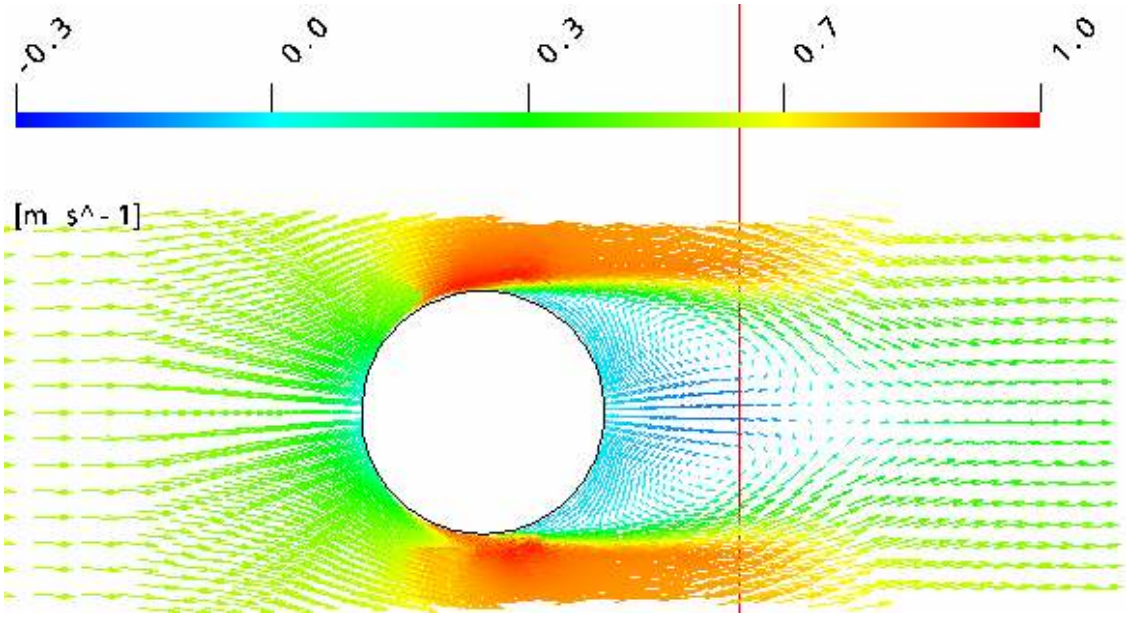

Figure 3.30 Recirculation bubbles of mean streamwise velocity component at Reynolds number of *3,900* (DES II).

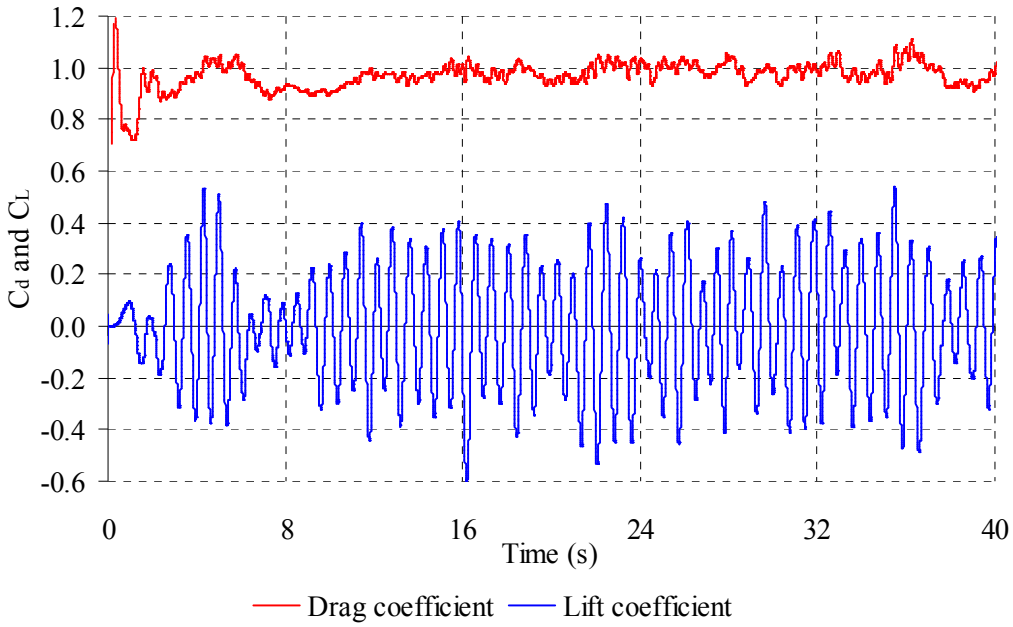

Figure 3.31 Time history of lift and drag coefficients of the flow around a circular cylinder at Re *3,900* (LES).

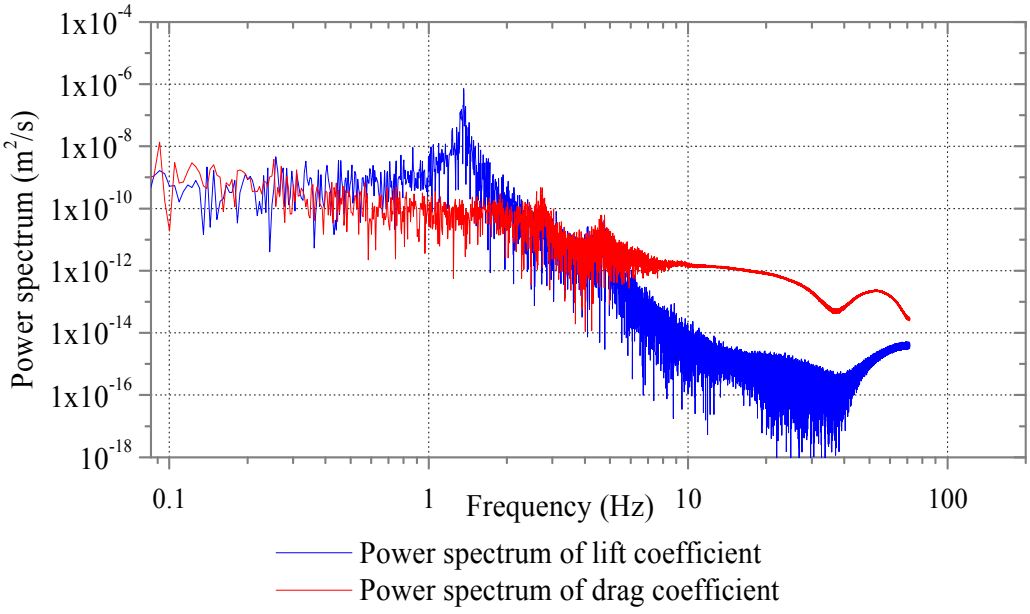

Figure 3.32 Power spectrum of lift and drag coefficients of the flow around a circular cylinder at Reynolds number of *3,900* (LES).

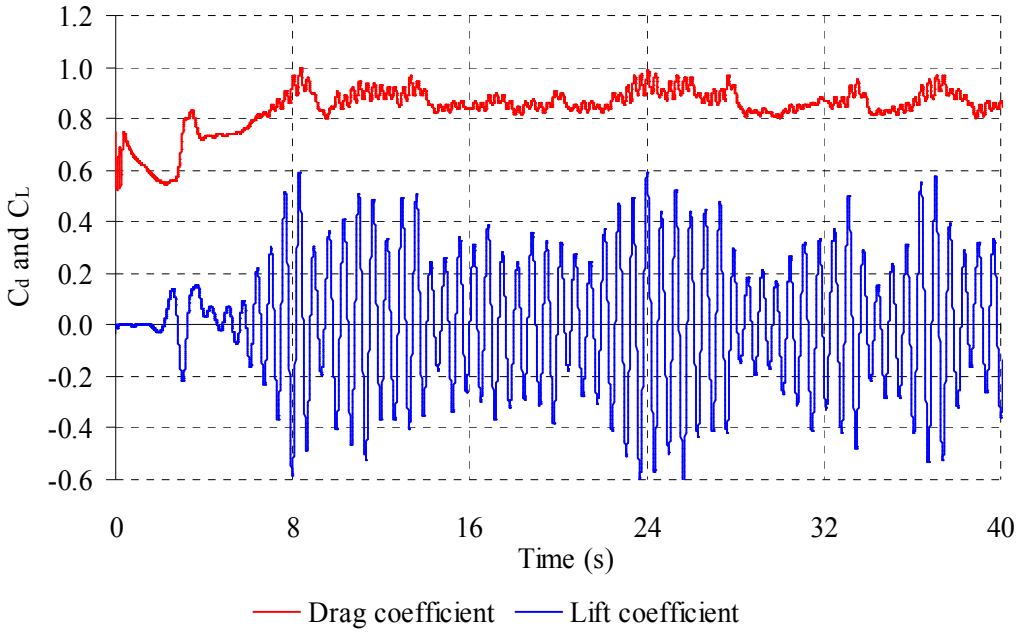

Figure 3.33 Time history of lift and drag coefficients of the flow around a circular cylinder at Reynods number of *3,900* (DES).

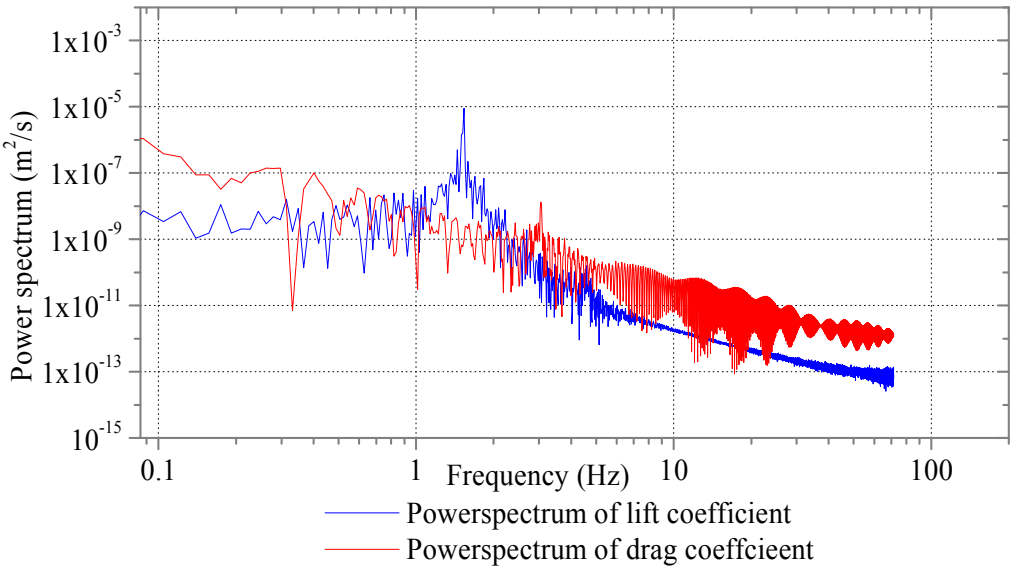

Figure 3.34 Power spectrum of lift and drag coefficients of the flow around a circular cylinder at Reynolds number of *3,900* (DES).

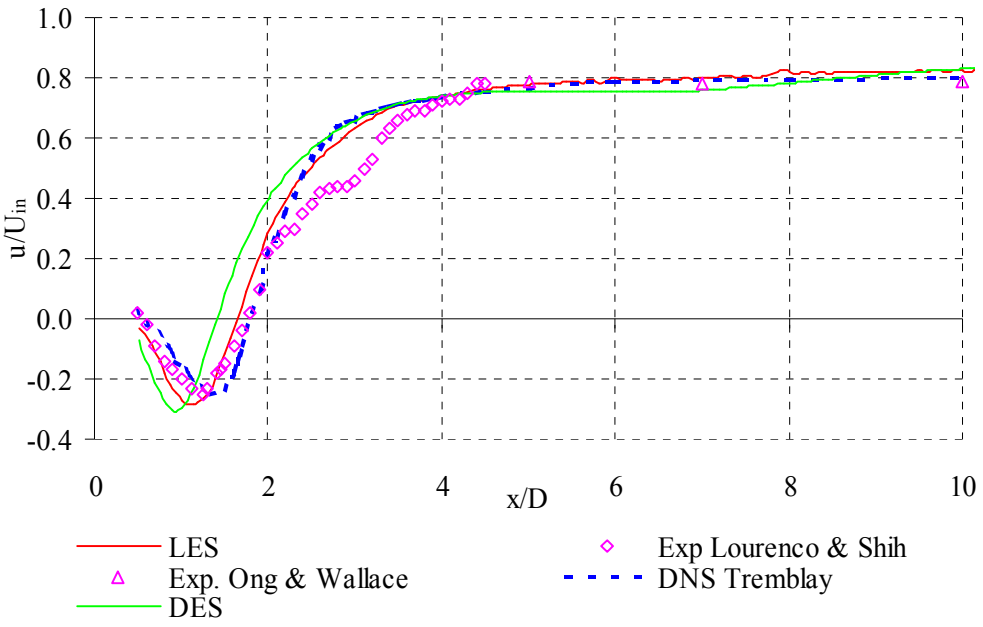

Figure 3.35 Mean centerline velocity components (LES & DES) of the flow around a circular cylinder at Re *3,900* in comparison to experimental and DNS results.

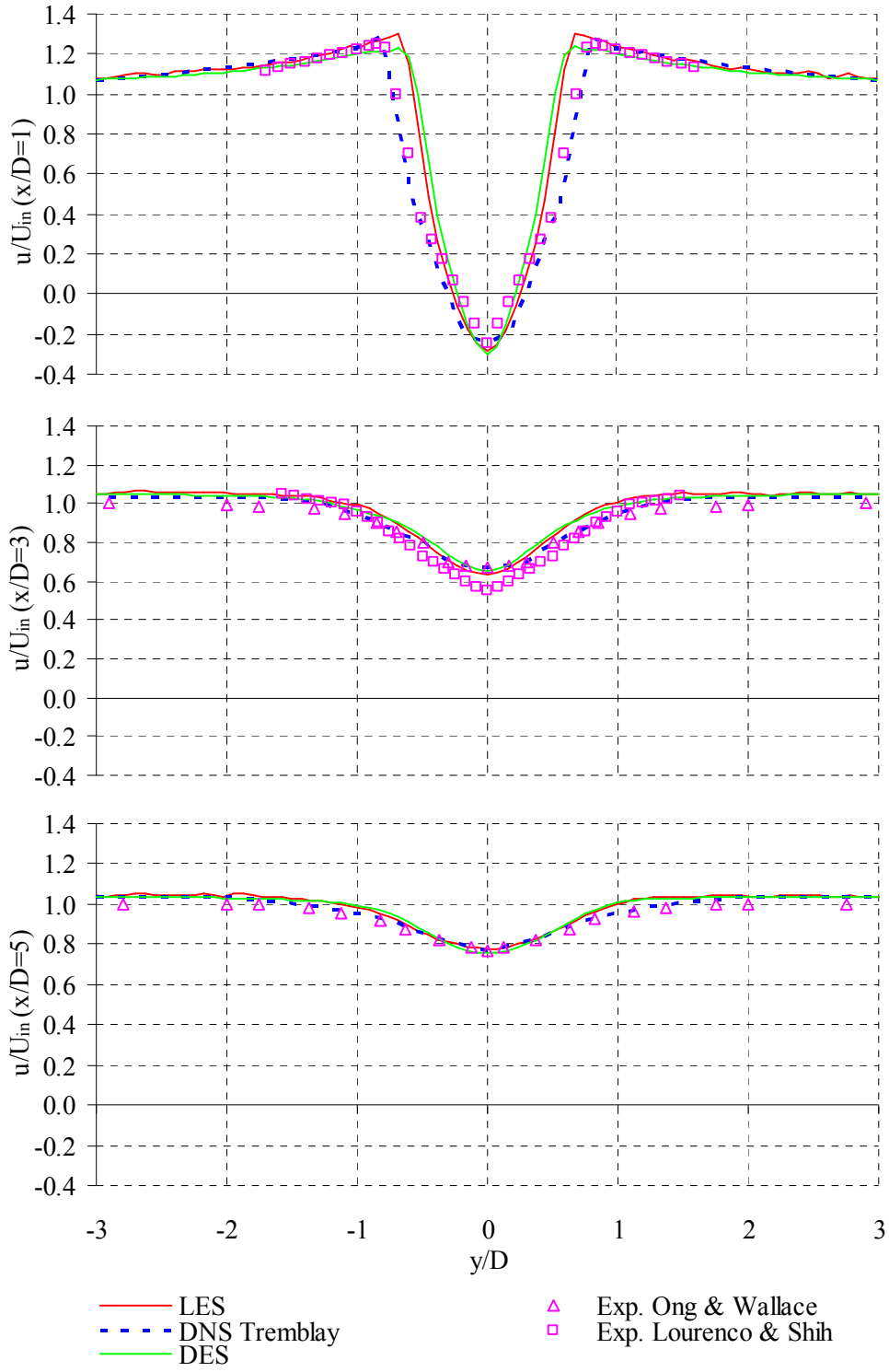

Figure 3.36 Mean steamwise velocity component (LES & DES) of the flow around a circular cylinder at Re *3,900* in comparison to experimental and DNS results.

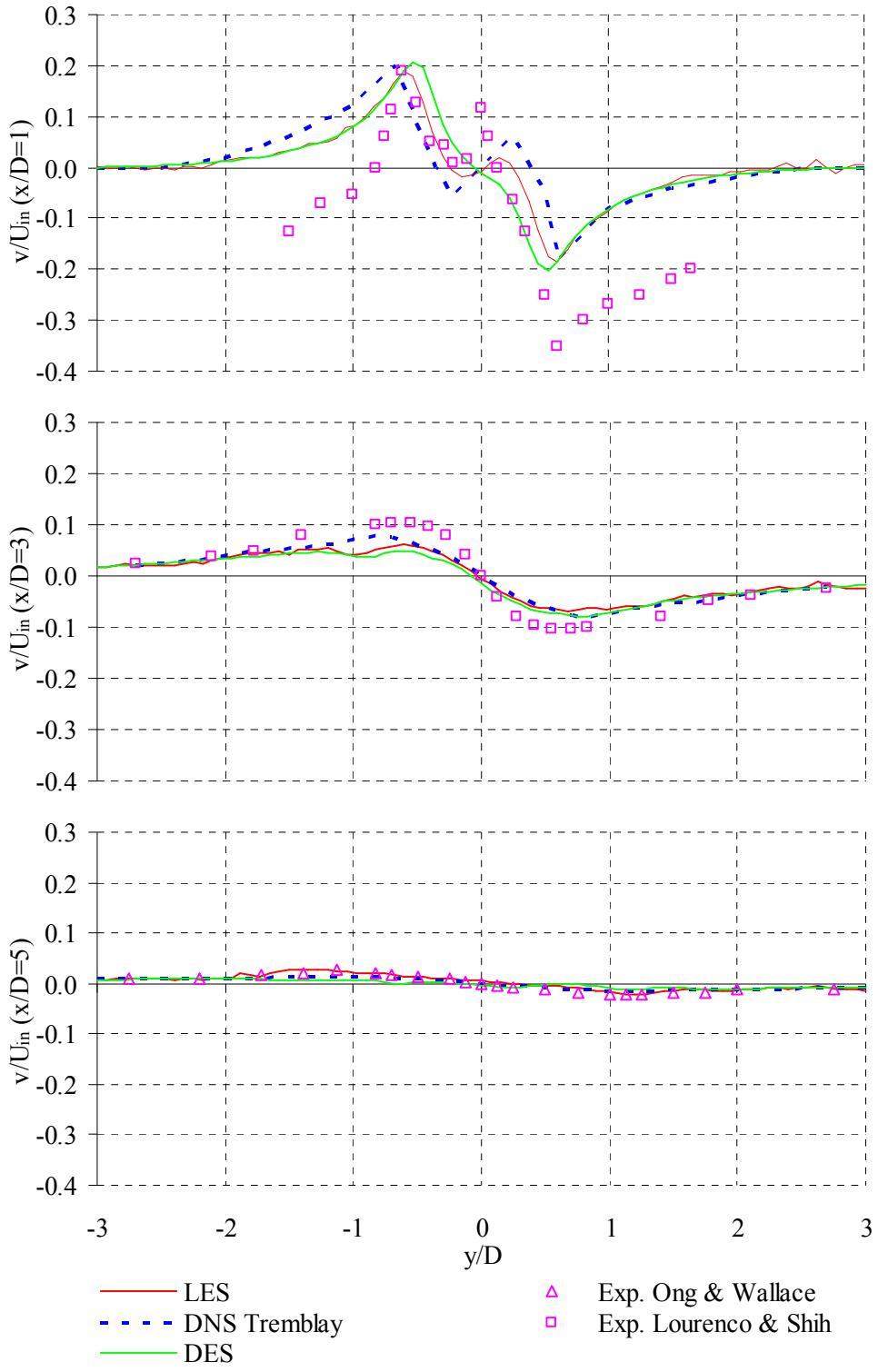

Figure 3.37 Mean spanwise velocity (LES & DES) of the flow around a circular cylinder at Re *3,900* in comparison to experimental and DNS results.

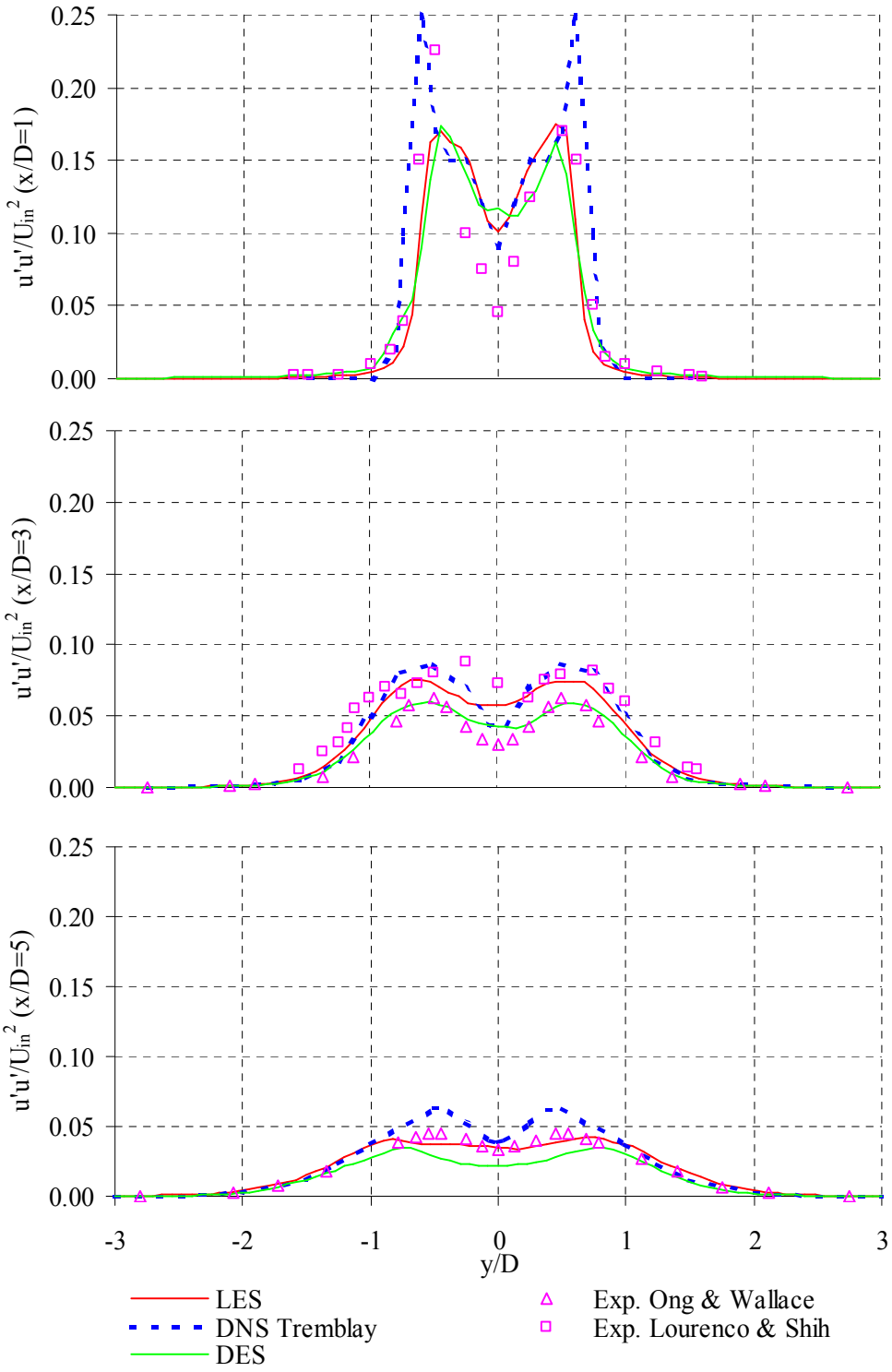

Figure 3.38 Mean streamwise Reynolds stress (LES & DES) of the flow around a circular cylinder at Re *3,900* in comparison to experimental and DNS results.

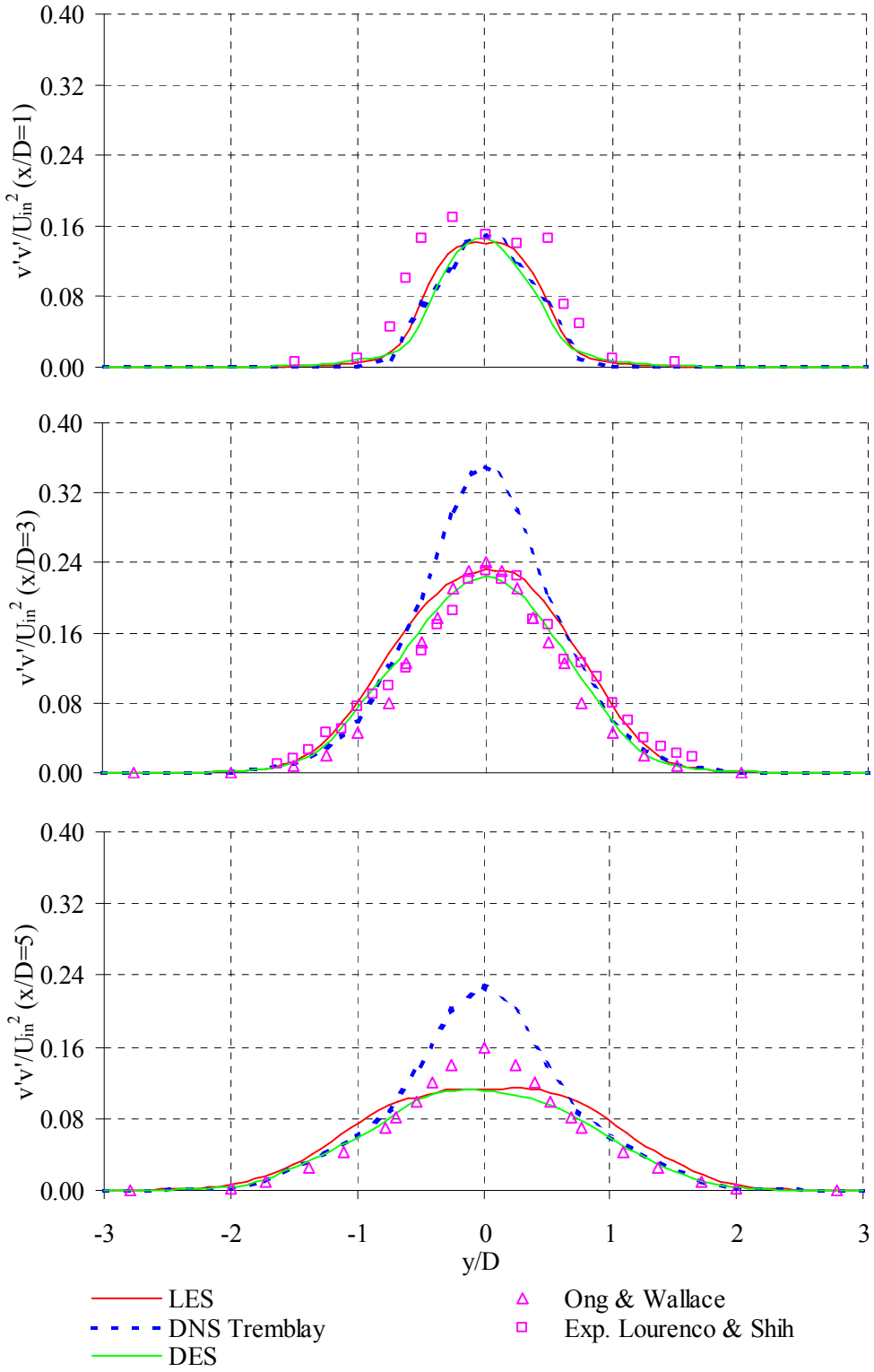

Figure 3.39 Mean spanwise Reynolds stress (LES & DES) of the flow around a circular cylinder at Re *3,900* in comparison to experimental and DNS results.

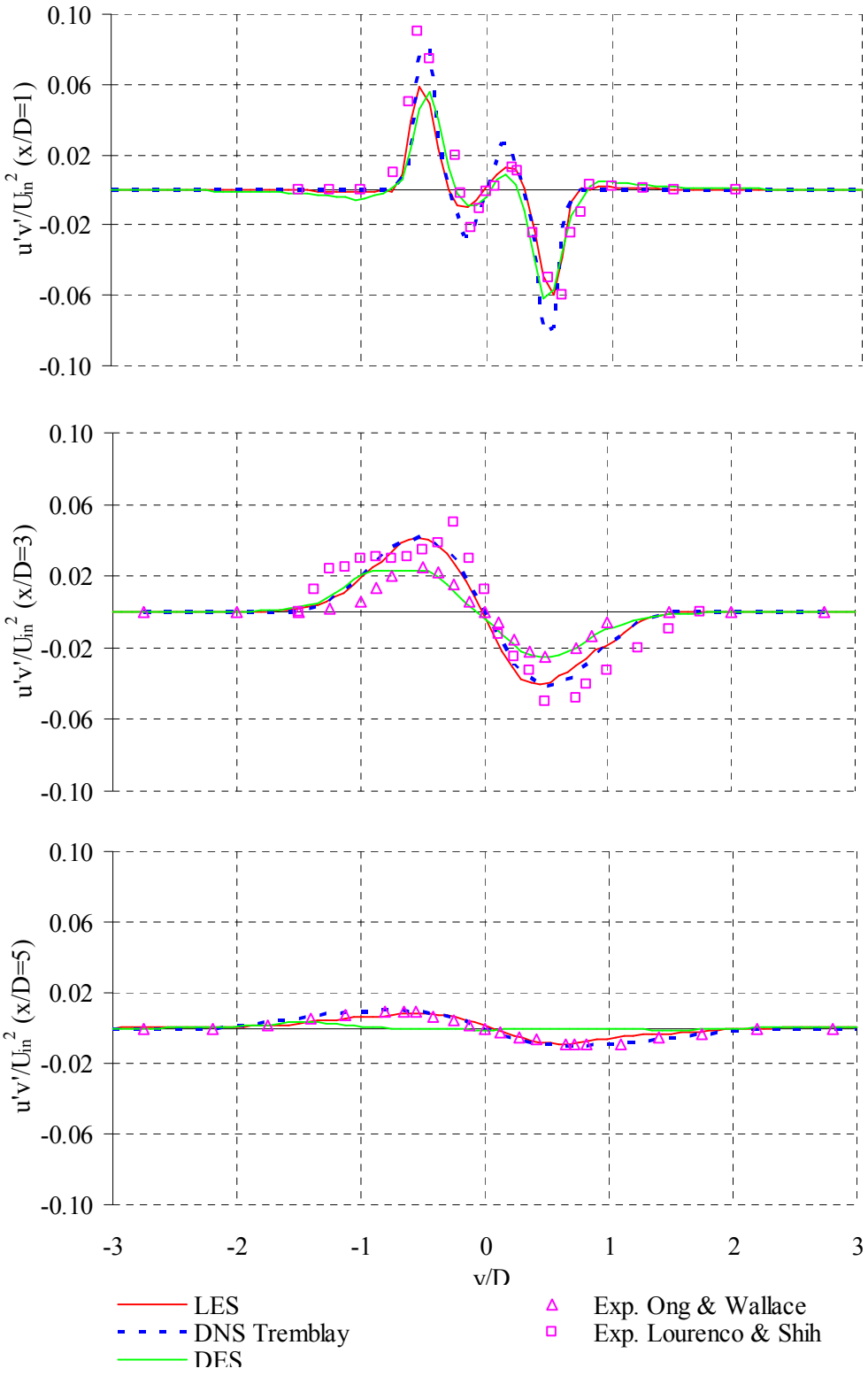

Figure 3.40 Mean Reynolds shear stress (LES & DES) of the flow around a circular cylinder at Re *3,900* in comparison to experimental and DNS results.

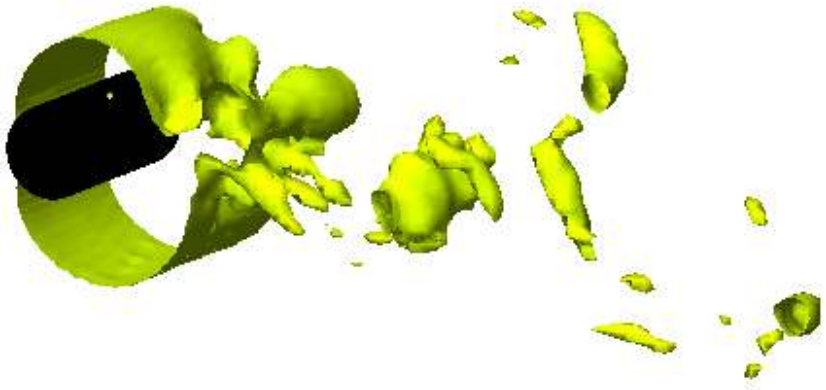

Figure 3.41 Instantaneous pressure changes in the wake region of the flow (LES).

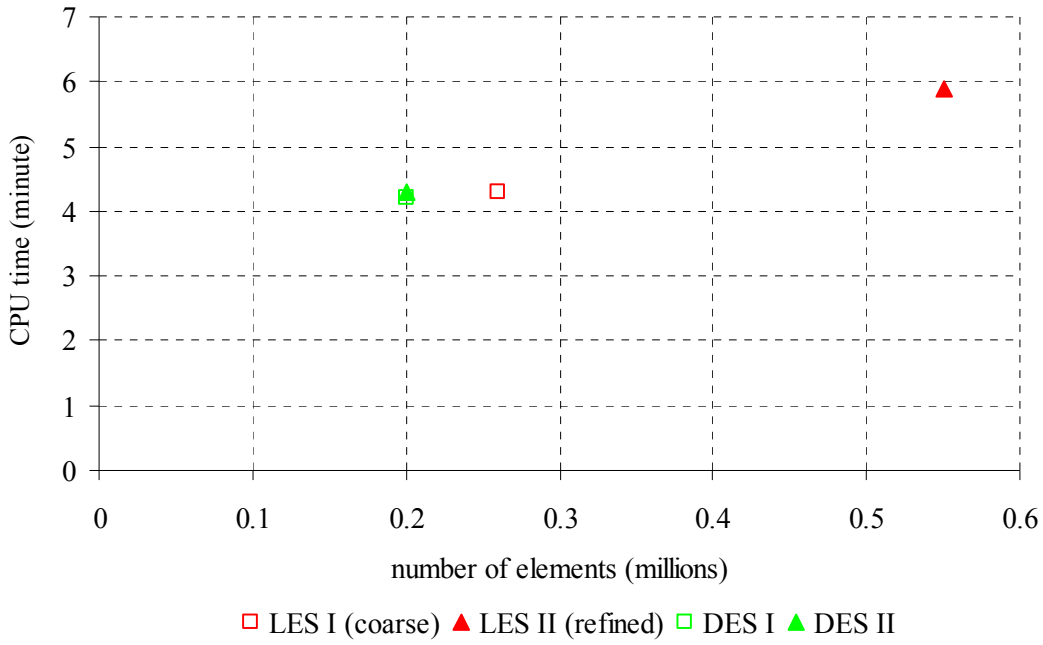

Figure 3.42 Measured CPU time for LES and DES cases for the flow around a circular cylinder (*Re 3,900*).

4 FLOW AROUND A SQUARE CYLINDER

In the previous chapter, the simulation of flow around a circular cylinder has been discussed and investigated. This chapter investigates the performance of LES and DES in simulating the velocity, Reynolds stresses and pressure field of the flow around a square cylinder. Validation of the turbulence models in predicting these flow parameters is performed by comparative study with experimental data. Comparison includes the Strouhal number, drag coefficient and the vortex shedding phenomenon of the flow. Various set up of the simulations and mesh sensitivity test have been conducted for the verification of the computations. The Reynolds numbers for the simulation range between *Re 500* to *Re 22,000*.

4.1 REVIEW OF FLOW AROUND A SQUARE CYLINDER

This section briefs the reader on the experimental and numerical studies of the flow around a square cylinder conducted by other researchers. This is to provide the reader with a general idea on the characteristics of the flow around a square cylinder. The numerical studies describe various discretisation methods and turbulence models employed in other researchers' work, which serve as a reference for the current work on the simulation of the flow around a square cylinder.

4.1.1 Experimental studies of flow around a square cylinder

Flow around a square cylinder is similar in many ways to the flow around a circular cylinder. However the wake region of the flow around a square cylinder is wider, resulting in a slightly lower Strouhal number. Roshko (1954) [103] pointed out that the shedding frequency is related to the width of wake, showing a roughly inversely proportional behaviour. Wider wake corresponds to lower Strouhal number. A similar regular vortex street is observed in the wake region of the flow around a square cylinder at low Reynolds number as for the flow around a circular cylinder. As Reynolds number increases, flow becomes more turbulent and exhibits three-dimensional nature in the wake region of the flow.

Durao *et al.* (1988) [28] conducted a detailed experimental investigation of the near wake flow around a square cylinder using laser doppler velocimetry at a Reynolds

number of *14,000,* when intense velocity fluctuation has been observed in the recirculation region of the flow. His work focused on the study of the velocity fluctuation components (Reynolds stresses components) apart from the global vortex shedding phenomenon. Time mean values of the flow quantities have been documented up to *6H* downstream of the cylinder.

Similar work has been done by Lyn *et al.* (1995) [66] at higher Reynolds number of *22,000*. Both reported high Reynolds stress components at region of peak vorticity and fully turbulent flow in the near wake region. Although the Reynolds number simulated by these two researchers are different, the flow characteristics show similar behaviour, since flow separation on a square cylinder is fixed at the corner and thus less influence of Reynolds number is observed compared to the flow around a circular cylinder. These two sets of results provide good data for the validation tests of the numerical solutions from turbulence models.

4.1.2 Numerical studies of flow around a square cylinder

Sohankar *et al.* (1996-1999) [111-113] employed LES on the simulation of a series of flows around a square cylinder ranging from Reynolds number of a few hundreds to *22,000*. For low Reynolds number simulations between Reynolds number of *200* and *500*, limited experimental results are available so results from the two-dimensional and three-dimensional simulations of Sohankar have been used for the comparison study with the simulation in this chapter. Simulated results of Sohankar concluded that the Strouhal number was close to other experimental findings of slightly higher Reynolds number but the flow profiles differ significantly between the two-dimensional and the three-dimensional flow. A longer recirculation length has been predicted by the two-dimensional simulation. Closer agreement of the mean drag and pressure coefficients with experimental result has been observed from the three-dimensional calculation. This corresponds to the findings of Okajima (1983) [95] who pointed out that flow at these Reynolds numbers shows strong three-dimensional characteristics. He also pointed out that increasing the spanwise length (the depth of the cylinder) has a rather small influence on the mean flow parameters at low Reynolds number.

As an alternative to the conventional finite volume (FVM), finite difference (FDM) and finite element method (FEM) for solving the Navier-Stokes equations, Breuer *et al.* (2000) [18] employed the Lattice Boltzmann method to solve the flow around a square cylinder between Reynolds number of *60* and *300*. The Lattice-

Boltzmann method simulates the movement and interaction of the fluid particle density distribution by solving a discrete Boltzmann-type equation. The flow parameters and profiles simulated from this entirely different numerical technique were then compared to results from a finite volume method (FVM) simulation at the same Reynolds number. Good agreement has been observed between the results. The Lattice-Boltzmann method demands much less computational power and memory compared to the finite volume method (FVM) but restriction is made to low Reynolds number since it is a two-dimensional computation. Further investigation is necessary for the extension to three-dimensional simulation at higher Reynolds number.

Another method employed on the simulation of flow around bluff bodies apart from the conventional methods is the discrete vortex method (DVM). DVM simulates the vorticity field rather than the velocity field as in the conventional techniques. The vorticity field is discretised into a series of vortex particle which carry a certain amount of circulation and these are then tracked in the flow field [63]. Vezza and Taylor (1999) [136] applied the DVM on the flow around a square cylinder and concluded that the Strouhal number computed generally matched other experimental results. The drag coefficient predicted is slightly higher with greater pressure suction in the leeward surface of the cylinder [136]. This has been explained by the two-dimensional nature of the simulation, which agrees with the finding of Sohankar *et al.* (1996) [111] in computing the flow around a square cylinder at lower Reynolds number using two-dimensional simulation. On the other hand, less computer power is needed for the simulation using DVM compared to LES or DES.

Murakami *et al.* (1990) [84] investigated the performance of the k-ε RANS model on a square section compared to the prediction from LES. He pointed out that the k-ε model, which is essentially two-dimensional failed to represent a more realistic flow compared to the three-dimensional LES solution. Similarly, Lubcke *et al.* (2001) [65] tested both the RANS method and LES technique in computing the flow around a square section, he concluded that the RANS method failed to capture the dynamics of the flow especially in the near wake region of the cylinder. This is due to the fact that all scales of turbulence are modelled in the RANS model while LES numerically resolves the major scale of the turbulence. In the light of this, an advanced RANS method known as the explicit algebraic stress model (EASM) has been employed by Lubcke *et al.* (2001) for the flow around a square cylinder at Reynolds number of *22,000*. EASM modified the transport equation of the Reynolds stress tensor based on the assumption of a non-linear stress-strain relationship of the flow [65]. Comparison of

the solution from RANS, EASM and LES suggested that the EASM enhanced the prediction of unsteady flow condition and illustrated many features of LES. Furthermore, the EASM requires much less computer power compared to LES.

At higher Reynolds number of *22,000*, Sohankar *et al.* (1999) [110] investigated the effect of different subgrid scale models on the flow profiles around a square cylinder using LES. The Smagorinsky model, the standard dynamic model and a dynamic one-equation model have been tested. The dynamic one equation model differs in that it does not require any free constants, unlike the Smagorinsky model. Furthermore, no arbitrary averaging of the dynamic coefficient is involved as in the standard dynamic model to maintain numerical stability. Sohankar reported that the Smagorinsky model failed to account for the backscattering of flow and failed to predict the reduction of length scales near to the wall due to the application of a fixed constant, whereas the standard dynamic model predicted different Reynolds stress components due to the over prediction of the eddy viscosity. Also, higher pressure has been computed in the wake region of the flow, resulting in a lower drag force. On the other hand, the dynamic one equation model predicted flow profiles and distribution closest to the experimental results among the three models. Furthermore, the dynamic one equation model required the least computational power among the three.

Nakayama and Vengadesan (2002) [87] conducted tests on the influence of various orders of discretisation schemes on the flow around a square cylinder using LES based on the finite difference method (FDM). The results suggested that LES with third and fifth order upwind biased schemes performed better than the second order and the fourth order central differencing schemes in predicting flow profiles around the wake region of the flow. This observation is similar to the findings of Beaudan (1994) [11] in the application of the LES on the flow around a circular cylinder. However, the latter demands more computer power than the central differencing scheme due to higher order accuracy of the solution.

4.2 RESULTS AND DISCUSSION (LES AND DES)

This section of the chapter discusses the solutions from LES and DES on the flow around a square cylinder. The results from LES and DES are compared to experimental work from other researchers. Agreement and discrepancies between the measured and simulated results are pointed out and discussed.

4.2.1 Simulation set up

The simulation in this section employed the LES and the DES models used in the previous chapter. Only flow at zero angle of incidence has been conducted in the current study due to time limitation for the project. The author is aware of the significant effect of the non-zero incident flow. Positive incident flow generates negative cross wind force as a consequence of the pressure distribution around the cylinder, which results in aeroelastic instability if the enveloped structure is free to move. This is very important in the study of the flow around a bridge deck section. Further investigation on the flow with angles of incidence should be carried out in the parallel projects within the same research group.

Domain size:

- The computational domains used on the simulation for the flow around the square cylinder in this chapter have been built to the size of the experimental works that the simulations are compared to. The wake region of the flow ranges from *18H* to *25H* (where H is the height of the cylinder) to ensure that there is enough space for vortex shedding to develop. The section has a depth of *7H* in order to maintain the three-dimensional nature of the flow. The previous chapter concluded that the spanwise extent of the cylinder needs further investigation. This has been increased compared to the study of the flow around a circular cylinder which used only two times the diameter of the cylinder as the spanwise length.

Discretisation:

- The LES uses a second order central differencing scheme for space discretisation and a second order backward Euler scheme for the time discretisation. Similar case applies to the LES part in the DES model. For the SST model in the DES, a second order upwind differencing scheme is used for the space discretisation.

Meshing:

- As mentioned in the previous chapter, meshing is different in the LES and the DES. Figures 4.1 and 4.2 show mesh of the LES and the DES of flow around a square cylinder. It can be seen that LES requires more globally refined mesh compared to DES in order to properly resolve the eddies in the

flow. On the other hand, only mesh around the wake region in the DES is refined to capture the vortex structures. The rest of the regions where SST are active have a coarser mesh, which helps to save computational power.

Time step and convergence:

- The time step used in the simulation is *0.00015,* where *50* time steps are necessary to generate one vortex cycle in the flow. This is equivalent to *0.08* in term of the non-dimensional timestep as defined in Eq. 3.4. The residuals of convergence of the solution are maintained at 10^{-4} to keep the errors at an acceptable level.

4.2.2 LES and DES of flow past a square cylinder

To begin with, LES of flow around a square cylinder has been done at low Reynolds number ($Re< 600$) to capture the von Karman vortex street in the wake region of the flow (Figure 4.3). This is similar to the observation on the application of LES on the flow around a circular cylinder in the previous chapter. The mesh used for the simulation is very similar to the mesh for the flow around a circular cylinder. Basic flow parameters such as the drag coefficient and the Strouhal number (Table 4.3) were computed and compared to simulation from other researchers since limited experimental measurement is available at this Reynolds number. Subsequently, flow at higher Reynolds number has been simulated for the square section. This includes Reynolds number of *3,000, 14,000* and *22,000* with both the LES and the DES turbulence models. Various meshes have been built for mesh sensitivity analysis for the models at Reynolds number of *14,000*. Simulations for other Reynolds numbers have been conducted with mesh similar to the refined mesh of the flow at a Reynolds number of *14,000*.

4.2.2.1 Mesh sensitivity analysis

Figure 4.4 depicts the position of the centerline and vertical profiles at which the comparison study of the flow profiles has been made for the simulation of the flow around a square cylinder. In Figure 4.5, the predictions of mean streamwise velocity components with different meshes from both LES and DES at the centerline are shown. LES I and LES II have *0.60 million* and *0.72 million* elements respectively. For the DES cases, the number of elements used are *0.12 million*, *0.27 million* and *0.42 million* for the DES I, DES II and DES III respectively. Figure 4.6 shows the vertical profiles

of the mean streamwise velocity components predicted by LES and DES at *x/H=1.5*. From the figures, good agreement has been observed among the results apart from the coarse mesh (*0.12 million*) of DES I in the prediction of the mean streamwise velocity components. The mesh independence test ensures consistency of results is achieved using different mesh sizes. Only two LES cases were simulated as higher computer power is needed for this model compared to DES.

Apart from the flow profiles, the Strouhal number (Table 4.1) and the drag coefficient (Table 4.2) of the flow around a square cylinder with different meshes have been compared to experimental data. Generally, the simulated Strouhal number and drag coefficient for the various meshes compared well with experimental measurement. The low percentage changes of the parameters (less than *4%* for Strouhal number and less than *6%* for drag coefficient) suggests that mesh sensitivity test has been achieved for the simulations.

Table 4.1 Measured and simulated Strouhal number of a square cylinder for mesh independence test.

Exp. Data (Strouhal no.)	**LES (Strouhal no.)**	**DES (Strouhal no.)**
Durao *et al.* '88 *0.133*	LES I *0.132*	DES I *0.136*
Lyn *et al.* '95 *0.130*	LES II *0.130*	DES II *0.132*
	-	DES III *0.138*

Table 4.2 Measured and simulated drag coefficient of a square cylinder for mesh independence test.

Exp. Data (C_d)	**LES (C_d)**	**DES (C_d)**
Bearman *et al.* '82 *2.10*	LES I *2.07*	DES I *2.15*
Norberg '93 *2.11*	LES II *2.20*	DES II *2.16*
	-	DES III *2.25*

4.2.2.2 Comparison study with experimental results

In the comparison study of the flow around a square cylinder at various Reynolds numbers (*Re 500* to *Re 22,000*), global flow parameters such as the Strouhal number, the drag coefficient and the pressure coefficient distribution around a square cylinder were computed. Figure 4.7 depicts the power spectrum of the oscillating frequency of the lift coefficient of the square cylinder. This frequency can be used to calculate the Strouhal number of the flow based on Eq. 3.2. It is noticed that the Strouhal number is more or less constant with respect to the changes of the Reynolds number. This agrees with the experimental observation of Okajima (1982) [95], who reported a Strouhal number of *0.131* within Reynolds number of *100* to *12,000* for the flow around a square cylinder. At higher Reynolds number of *22,000*, Lyn's *et al.* experiment (1995) [66] reported a Strouhal number of *0.130*.

Table 4.3 shows the Strouhal number corresponding to the peak of the spectrum in Figure 4.7 for quantitative comparison with experimental results. Generally, the computed results agreed well with the experimental data. For the flow at low Reynolds number of around *500*, limited experimental data is available so the simulated result from Sohankar *et al.* (1999) [113] has been compared. Table 4.4 compares the simulated drag coefficients from LES and DES of the flow around a square cylinder with other researchers' findings at various Reynolds numbers. LES predicted closer agreement of drag force compared to DES.

Table 4.3 Comparison of simulated and measured Strouhal number of a square cylinder at various Reynolds numbers.

Reynolds number	**Other work (Strouhal no.)**	**LES (Strouhal no.)**	**DES (Strouhal no.)**
22,000	*0.130* Exp. Lyn *et al.* '95	*0.132*	-
14,000	*0.133* Exp. Durao *et al.* '88	*0.130*	*0.138*
3,000	*0.132* Exp. Okajima '82	*0.136*	-
500	*0.130* Exp. Okajima '82	*0.130*	-

Table 4.4 Comparison of simulated and measured drag coefficient of a square cylinder at various Reynolds numbers.

Reynolds number	**Other work (C_d)**	**LES (C_d)**	**DES (C_d)**
22,000	*2.10* Exp. Bearman *et al.* '82	*2.07*	-
14,000	*2.11* Exp. Norberg '93	*2.20*	*2.25*
3,000	*2.10* Exp. Igarashi '87	*1.97*	-
500	*1.87* LES Sohankar *et al.* '99	*1.71*	-

4.2.2.3 Velocity profiles at centerline

For the validation of LES and DES, results of the experiment from Durao *et al.* (1988) [28] have been used for the comparison study. The work documented both the streamwise and spanwise mean flow components and the mean velocity fluctuation components in the wake region of the cylinder.

Figure 4.8 shows the mean streamwise velocity components (u/U_{in}) at the centreline for the flow around the cylinder from LES and DES compared to the experimental data. Good agreement has been observed in the recirculation region up to $x/H = 3$, with DES predicting a slightly shorter recirculation length. Further into the wake region, the simulated results level off at different velocities with the DES prediction closer to the experimental data. Sohankar *et al.* (2000) [110] experienced a similar situation in his simulation at Reynolds number of *22,000*. He pointed out that this is due to the different mesh resolution employed in the wake region of the flow.

4.2.2.4 Reynolds stress profiles at centerline

In Figures 4.9 to 4.10, the simulated and measured streamwise and spanwise Reynolds stress components ($u'u'/U_{in}^2$ and $v'v'/U_{in}^2$) have been plotted at the centerline of the square cylinder at Reynolds number of *14,000*. Both simulations give good agreement in the near wake region but the simulated streamwise Reynolds stresses ($u'u'/U_{in}^2$) between $x/H=3$ to $x/H=5$ are higher compared to experimental results. This suggests that higher turbulence fluctuation has been computed from LES and DES compared to the experimental data. Similar observation has been noticed in the flow around a circular cylinder in Chapter Three.

4.2.2.5 Velocity profiles in the wake region

Apart from the comparison of the velocity components at the centerline, the vertical profiles in the wake region of the flow at $x/H=1.50$, $x/H=1.83$ and $x/H=4.50$ have been studied. Figures 4.11 to 4.15 show the comparisons of the streamwise and spanwise velocity as well as the Reynolds stress components from LES and DES with experimental results at the various vertical profiles locations (Figure 4.4). Only half of the profiles ($y/H=0$ to $y/H=3$) have been shown in the current case compared to the profiles in the previous chapter on the flow around a circular cylinder ($y/D=-3$ to $y/D=3$) due to the limited availability of the experimental data. To ensure a statistically

converged solution, the other half of the profiles (*y/H=-3* to *y/H=0*) have been plotted and symmetrical profiles have been noticed for all the velocity components (Figures 4.16 to 4.18). From the observation, the simulations showed converged solutions judging from the symmetrical distribution of the velocity and Reynolds stress profiles.

The streamwise velocity (u/U_{in}) profiles from both LES and DES (Figure 4.11) generally agreed well with the experimental data within *y/H=1.0*. At *x/H=1.50* (near to the end of recirculation bubbles), DES gives a lower negative velocity compared to a higher velocity component of LES, which suggests a slightly shorter recirculation length of DES computation. This agrees with the plot of the velocity components from LES and DES as depicted in Figures 4.19 and 4.20. Experimental result measured a longer recirculation length hence shows lower velocity value at *y/H=0*. Further downstream at *x/H=1.83* (immediately after recirculation region), discrepancies of the streamwise velocity components have been observed between LES and DES as well as measured data due to different recirculation lengths predicted. Further away from the centerline, computed results show generally smaller values of streamwise velocity components compared to experimental measurement. This is caused by the prediction of narrower wake which resulted in an earlier recovery of freestream velocity.

The size and shape of the wake region affect the spanwise velocity (v/U_{in}) profiles in the flow. The peaks of the spanwise velocity component profiles usually correspond to the edge of the shear layer between the wake and the freestream flow. At *x/H=1.50* and *x/H=1.83* (around the recirculation region), both LES and DES predicted a narrower wake compared to experimental measurement (Figure 4.12). Away from the centerline (*y/H> 1.50*), good agreement has been observed. Further downstream at *x/H=4.50* (outside recirculation region), a less intense peak is observed from LES and DES compared to experimental measurement.

4.2.2.6 Reynolds stress profiles in the wake region

Figure 4.13 shows the vertical profiles of the streamwise Reynolds stress components ($u'u'/U_{in}^2$). Good agreement with the experimental data has been observed for the profiles at the appointed x/H locations. This suggested that LES and DES manage to capture the turbulence intensity well in the wake region of the flow apart from slight discrepancies near the centerline (*y/H<0.5*) at *x/H=1.83* and *x/H=4.50*. The Smagorinsky model in LES models the small scale eddies based on the eddy viscosity model. The discrepancy observed is attributed to different viscosity intensities

predicted by the Smagorinsky model. Beudan (1994) [11] reported a similar situation in the application of LES with Smagorinsky model in the flow around a circular cylinder. He pointed out that LES with the dynamic SGS model showed improvement in the prediction of the streamwise Reynolds stress component.

Figure 4.14 depicts the spanwise Reynolds stress components ($v'v'/U_{in}^2$) at the same x/H locations as the streamwise components. Experimental data of Durao *et al.* [28] show that the spanwise Reynolds stress components attained a maximum value around the rear stagnation point of the flow which is slightly behind the recirculation bubbles. This corresponds to the plot at *x/H=1.83* in Figure 4.14. LES manages to predict a close value of the spanwise stress component but DES gave a smaller value compared to experimental measurement. Figure 4.15 shows the vertical profiles of the Reynolds shear stress components. Generally, good agreement of the shear stresses ($u'v'/U_{in}^2$) has been observed between the experimental measurement and the prediction of LES and DES.

4.2.2.7 Pressure distribution around a square cylinder

Apart from the velocity profiles, pressure distribution is important in the study of flow around bluff bodies. Pressure changes accordingly with the vortices motion in the vicinity of the bodies. Flow separates alternately around symmetrical bodies with sharp corners such as the leading edge of a square section to form vortices around the cylinder. This usually introduces periodic forces on the body due to the pressure changes. This situation is particularly significant in flow involving fluid and structure interaction such as the flow around a tall building or suspension bridge. Although pressure induced force does not effect the simulation on a fixed square cylinder very much, the capability of the turbulence models (LES and DES) to accurately predict the pressure coefficient on the fixed cylinder simulation is important in the application of the flow around longer afterbody sections and around a moving bridge deck section, which will be investigated in the next two chapters.

Figure 4.21 compares the computed and measured pressure coefficients (C_p) around the square cylinder at a Reynolds number of *14,000*. Experiments data of Bearman and Obasaju (1982) [9] and Norberg (1993) [92] have been used for the comparison study since Durao's experiment did not include pressure measurement. From Figure 4.21, good agreement of the simulated and experimental measurement is observed for the pressure distribution around the square cylinder except at the

stagnation point. This point is located at the midpoint of the windward face (*0-1*) where velocity is at rest with maximum pressure (by Bernoulli's Theorem). Both LES and DES predict values greater than unity at this point. The causes of the discrepancy are explained in section 3.2.3. Similar situation has been observed in the application of LES on the flow around a circular cylinder. Greater discrepancy is observed for the case of the flow around a square cylinder compared to that of a circular cylinder. This is because higher Reynolds number is simulated in the current case and thus increasing the build up of the flow at the stagnation point of the cylinder. It is also noticed that the pressure shows symmetrical distribution, which suggests that satisfactory computational time has been simulated to achieved a converged solution.

4.2.3 Comparison of LES and DES

Apart from the comparison study between the numerical solutions and the experimental data for the flow around a square cylinder, the performance of LES and DES are compared. From the prediction of the velocity distribution from LES and DES at the centerline of a square cylinder, both simulation gave higher values of streamwise velocity component (Figure 4.8) and the spanwise Reynolds stress components (Figure 4.10) in the wake region of the flow ($x/H > 3.00$). Difference in the size and length of the recirculation region predicted has resulted in the discrepancy observed. This agreed with the findings of Sohankar *et al.* [110] when simulating the flow around a square cylinder. Also, a similar situation has been observed in the application of LES and DES on the flow around a circular cylinder in the previous chapter.

The size and shape of the wake around bluff bodies influences the velocity distribution around the bodies. DES has predicted a slightly shorter and narrower wake compared to LES (Figure 4.20). This caused the discrepancies of the vertical profiles between LES and DES predictions near the wake region at $x/H=1.50$ and $x/H=1.83$. Figure 4.22 shows the instantaneous distribution of the region where RANS and LES models are active in DES. Clearly, the figure depicts that at $x/H=1.50$ and $x/H=1.83$ (white lines) transition between the two models (RANS and LES) occurs, known as the 'grey area'. During the transition, it is essential for LES to create the necessary turbulence and unsteadiness immediately to properly represent the complex flow in the wake region. The usage of RANS or LES near the 'grey area' is determined by the blending factors (Section 2.2.3) of the DES model.

One of the benefits of DES compared to LES is that shorter simulation time is needed for similar simulation. The issue of computational time for LES and DES will be discussed in the next chapter for an overall comparison with the simulation of the flow around rectangular sections.

4.3 CONCLUSION

Investigation of the flow around a square cylinder began with the comparisons of the velocity distribution of the flow with experimental data. Details on the mean streamwise and spanwise velocity components as well as the mean Reynolds stress components have been compared with experimental data at various locations in the wake region of the flow. Both the simulated results from LES and DES show generally good agreement with the experimental findings.

Apart from the velocity profiles, the pressure distribution around the square section has been compared with experimental data too. LES and DES managed to predict the pressure distribution well except at the stagnation point in the leeward face of the cylinder. Observation on the comparison between LES and DES shows that LES generally predicted slightly closer numerical solutions to experiment data than DES.

At Reynolds number of *14,000* and *22,000*, the spanwise length for the simulation of the flow around a square cylinder has been increased to *7H* (compared to *2D* for the flow around a circular cylinder at Re *3,900*) to capture the three dimensional effect of the flow. Also the simulation time for the flow around a square cylinder is longer compared to the simulation of the flow around a circular cylinder to ensure a statistically converged solution, especially for the mean stress components prediction further downstream of the flow.

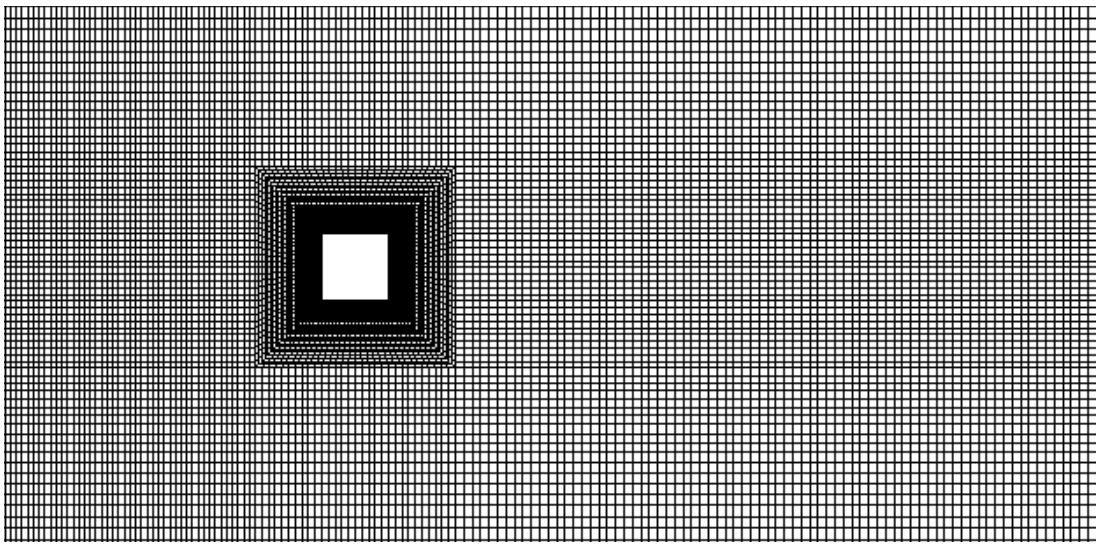

Figure 4.1 Mesh in LES at Reynolds number of *14,000*.

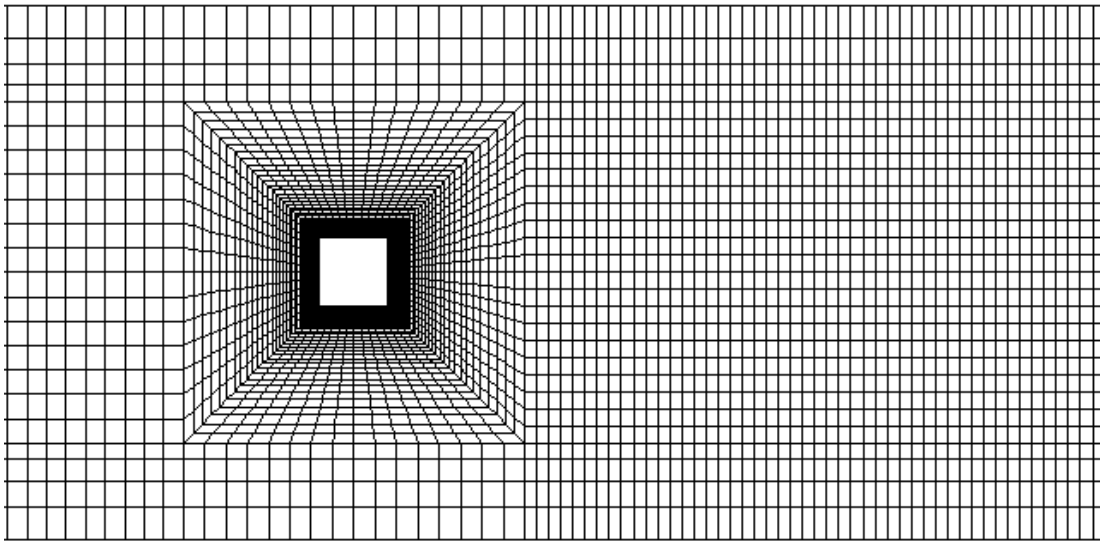

Figure 4.2 Mesh in DES at Reynolds number of *14,000*.

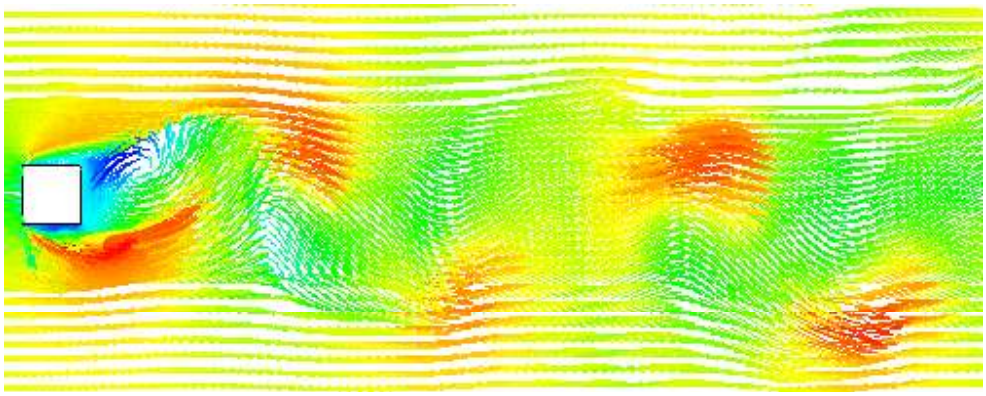

Figure 4.3 Vector plot of streamwise velocity component showing vortex street in the wake region of a square cylinder at Reynolds number of *500* (LES).

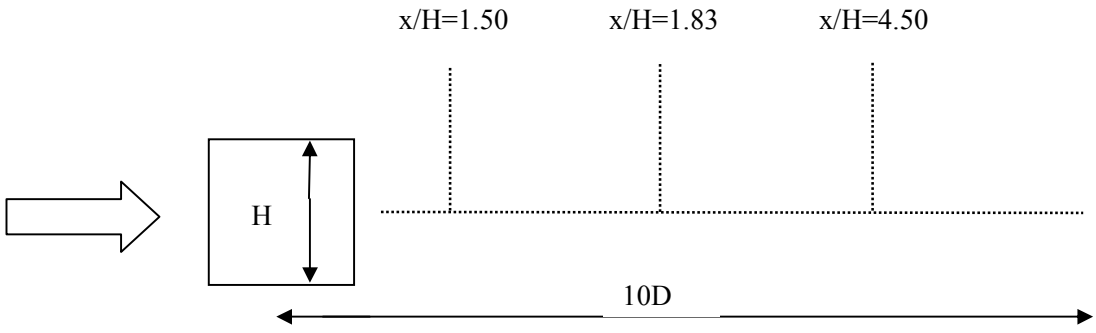

Figure 4.4 Definition of centerline and vertical profiles of flow in the wake region of the square cylinder (not to scale).

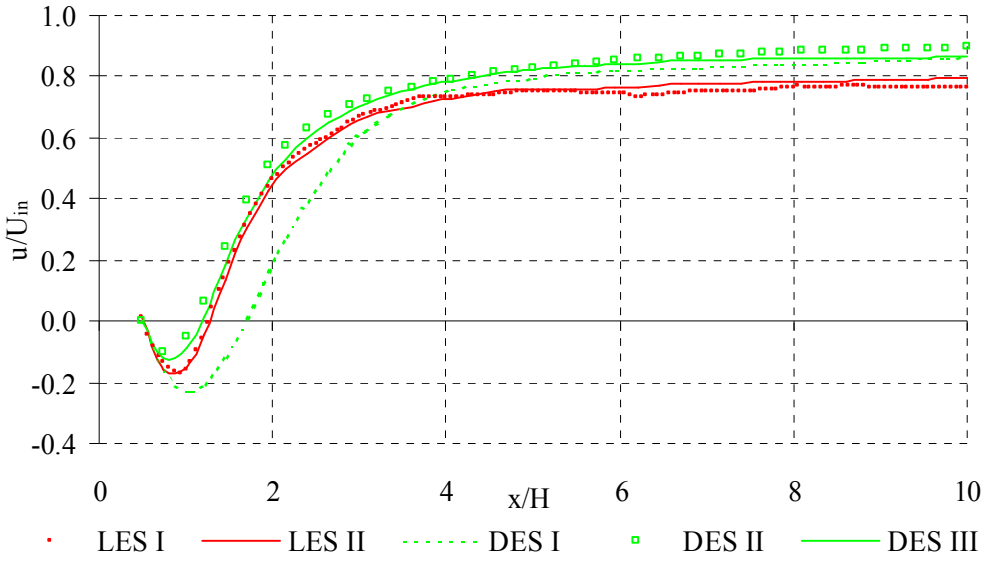

Figure 4.5 Mean streamwise velocity components at centerline (for different meshes).

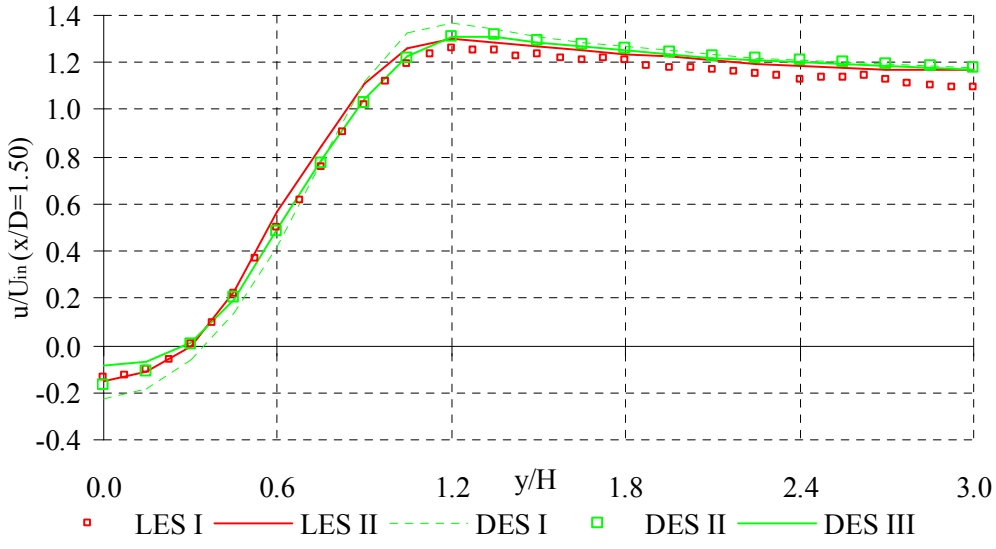

Figure 4.6 Vertical profiles of mean streamwise velocity components at *x/D=1.5* (for different meshes).

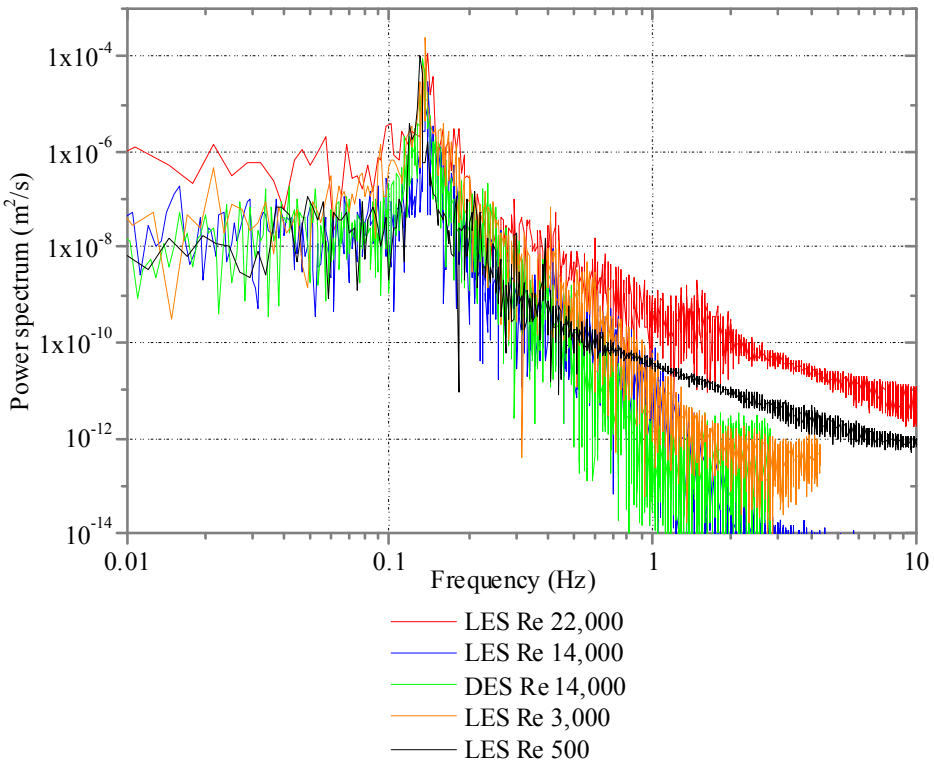

Figure 4.7 Power spectrum of Strouhal number calculated based on the oscillating frequency of lift coefficient.

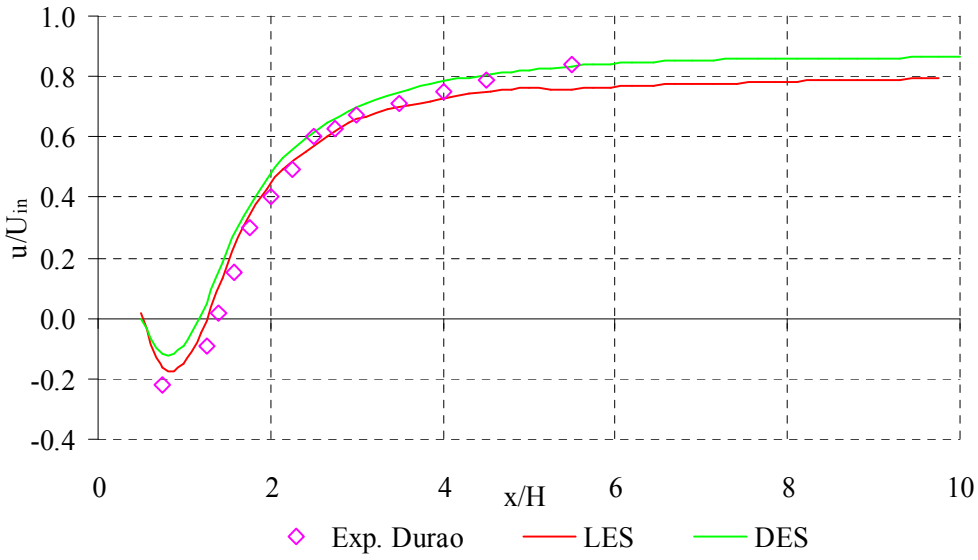

Figure 4.8 Simulated and measured mean streamwise velocity components at centerline of square cylinder (*Re 14,000*).

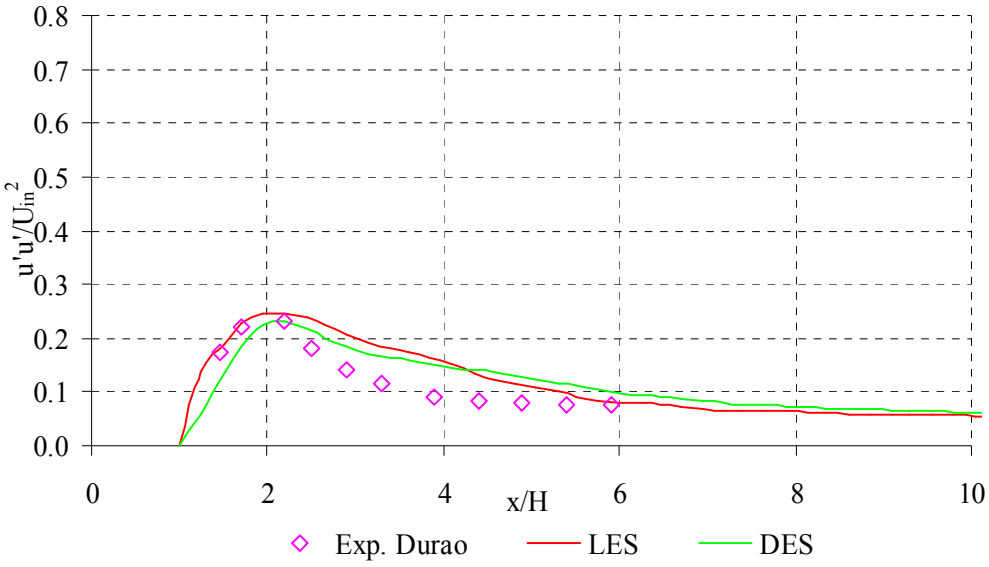

Figure 4.9 Simulated and measured mean streamwise Reynolds stress components at centerline of square cylinder (*Re 14,000*).

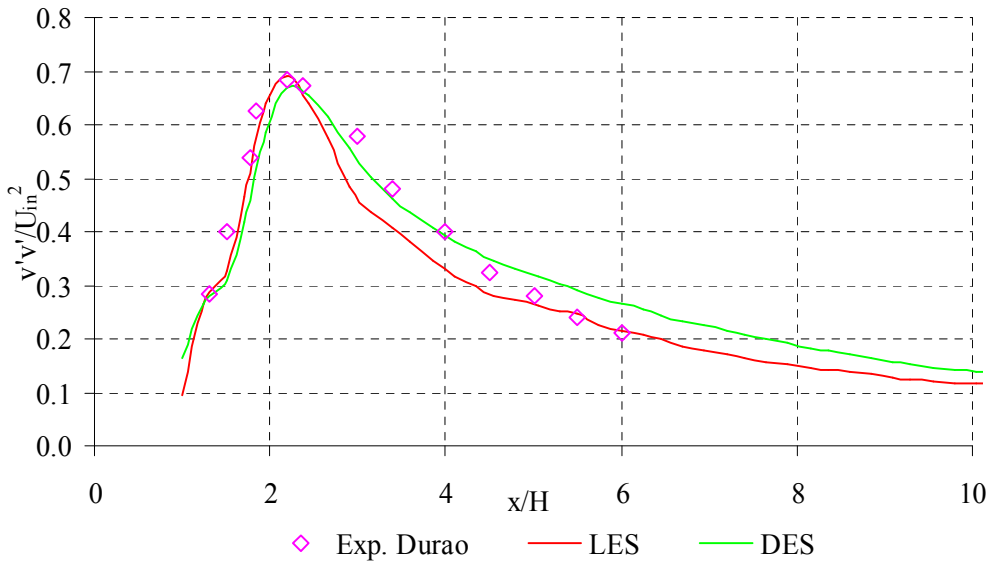

Figure 4.10 Simulated and measured mean spanwise Reynolds stress components at centerline of square cylinder (*Re 14,000*).

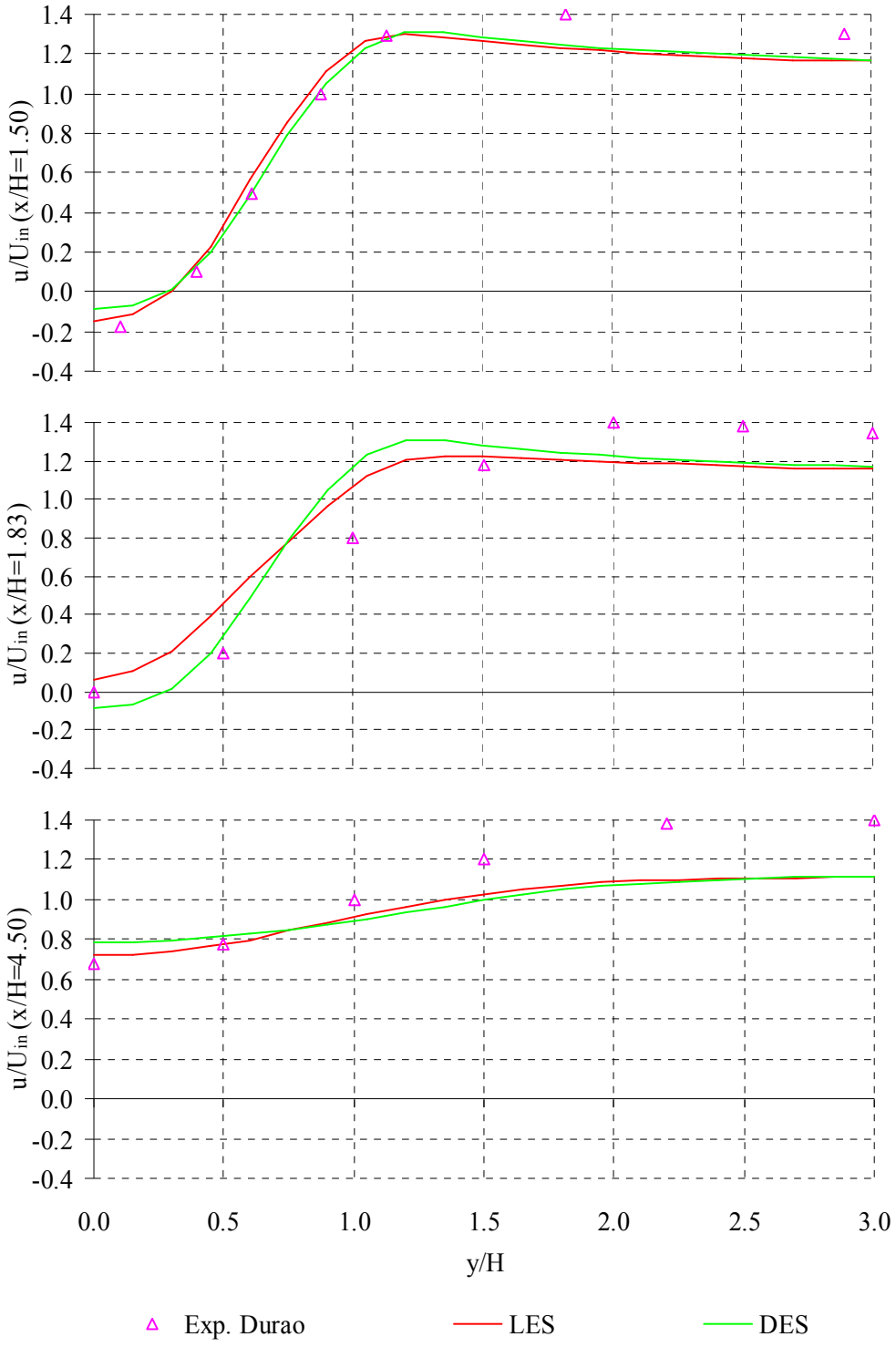

Figure 4.11 Simulated and measured mean streamwise velocity components at various vertical profiles in the wake region of the cylinder (*Re 14,000*).

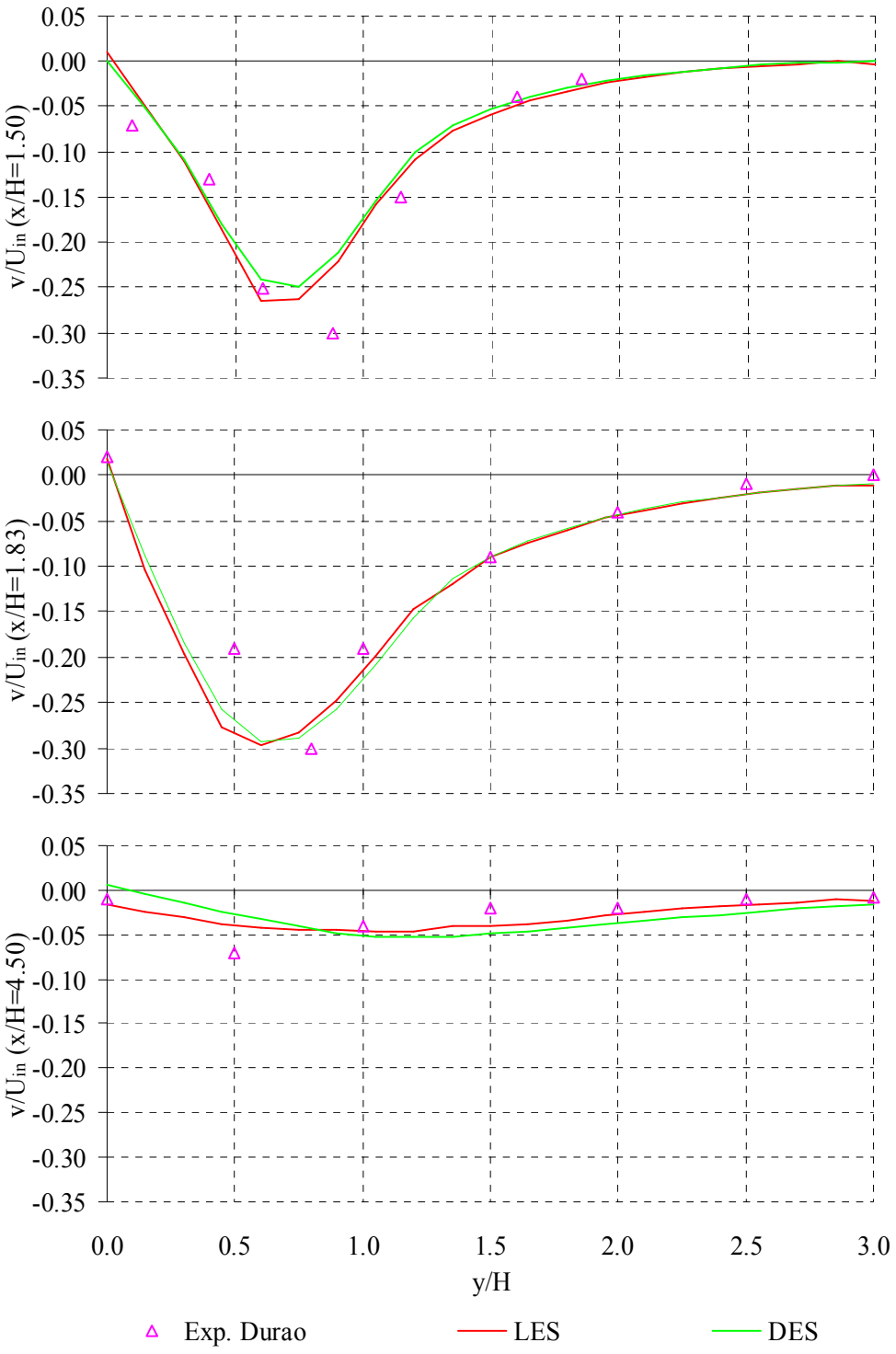

Figure 4.12 Simulated and measured mean spanwise velocity components at various vertical profiles in the wake region of the cylinder (*Re 14,000*).

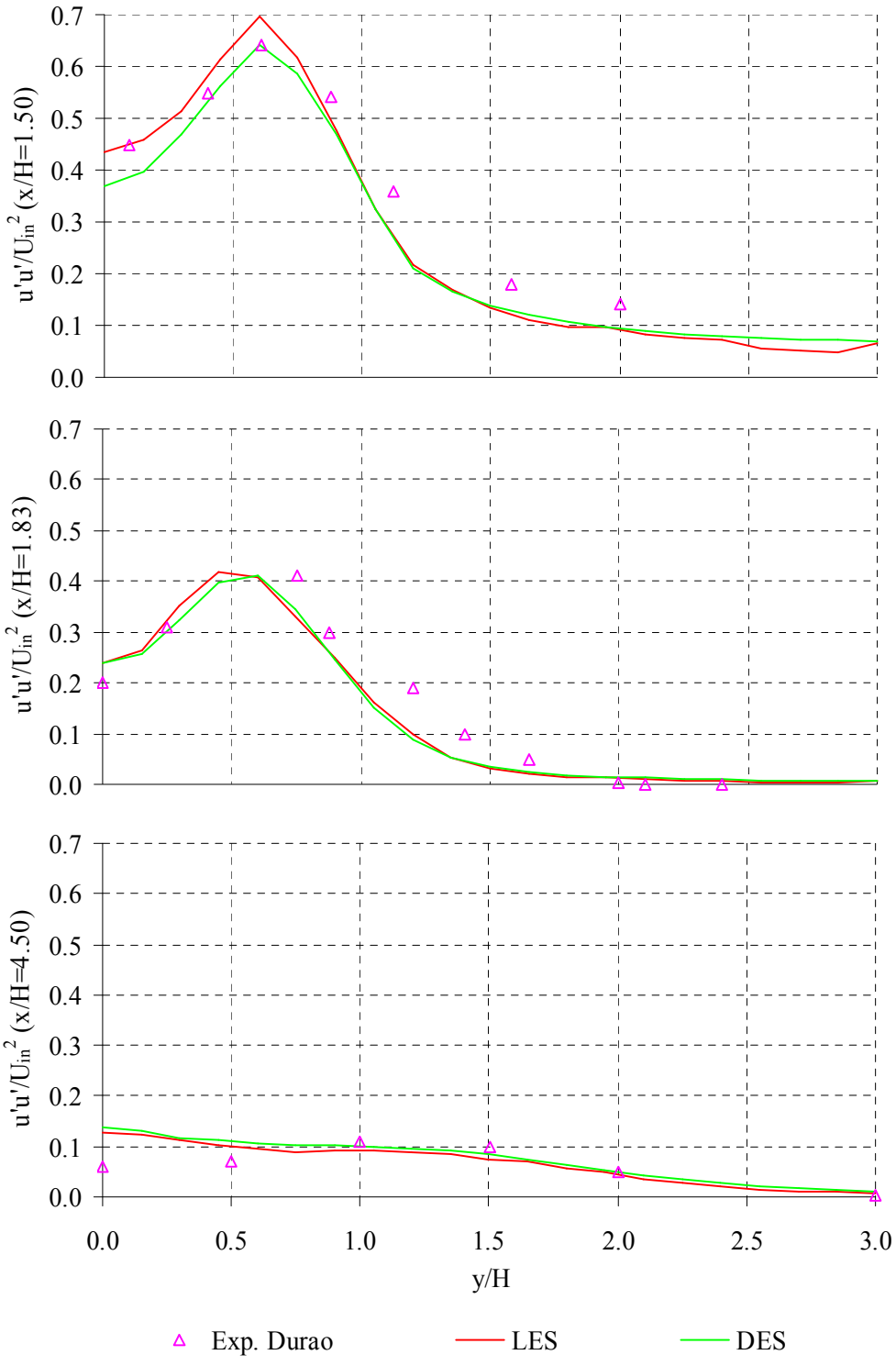

Figure 4.13 Simulated and measured mean streamwise Reynolds stress components at various vertical profiles in the wake region of the cylinder (*Re 14,000*).

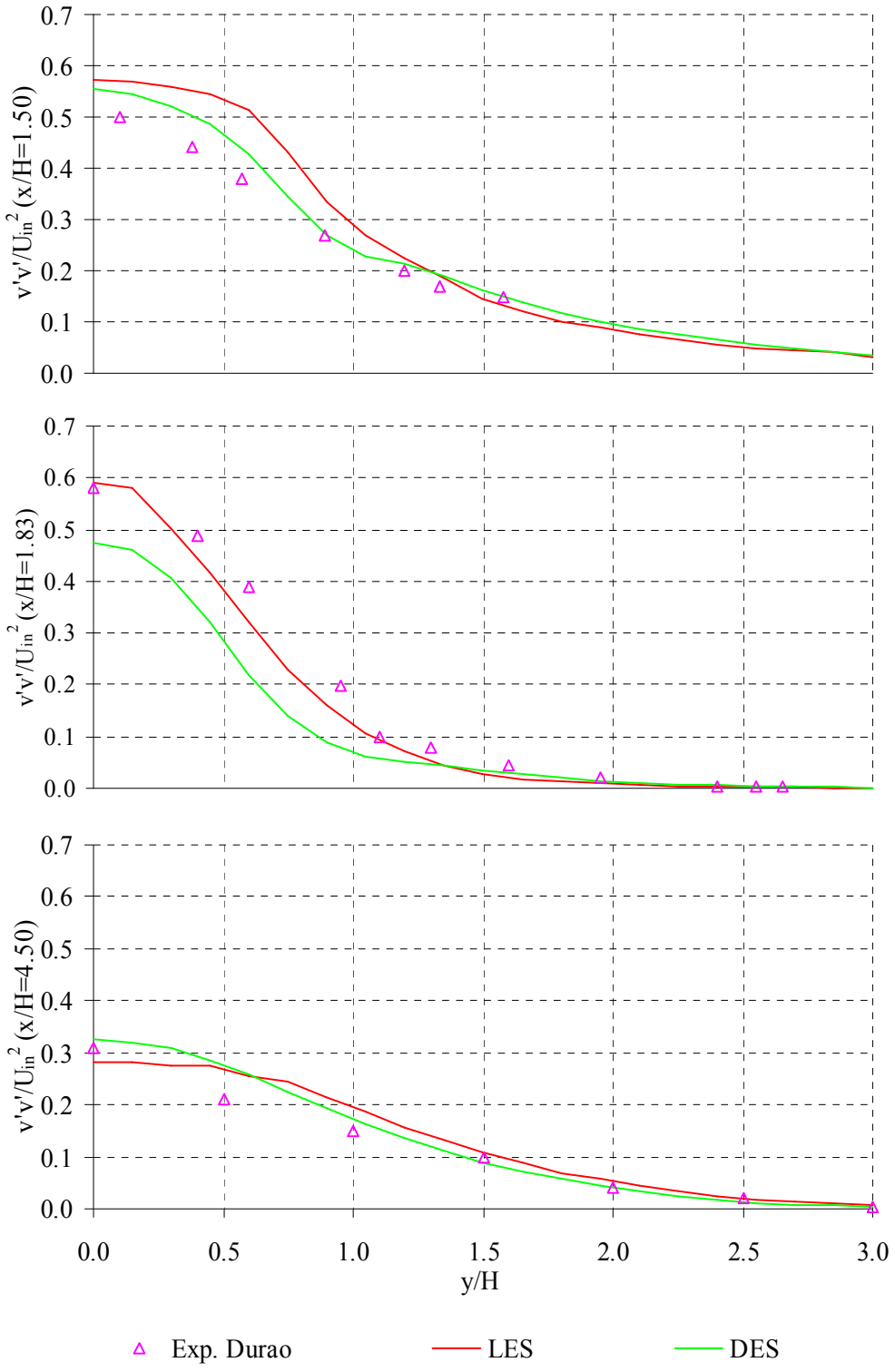

Figure 4.14 Simulated and measured mean spanwise Reynolds stress components at various vertical profiles in the wake region of the cylinder (*Re 14,000*).

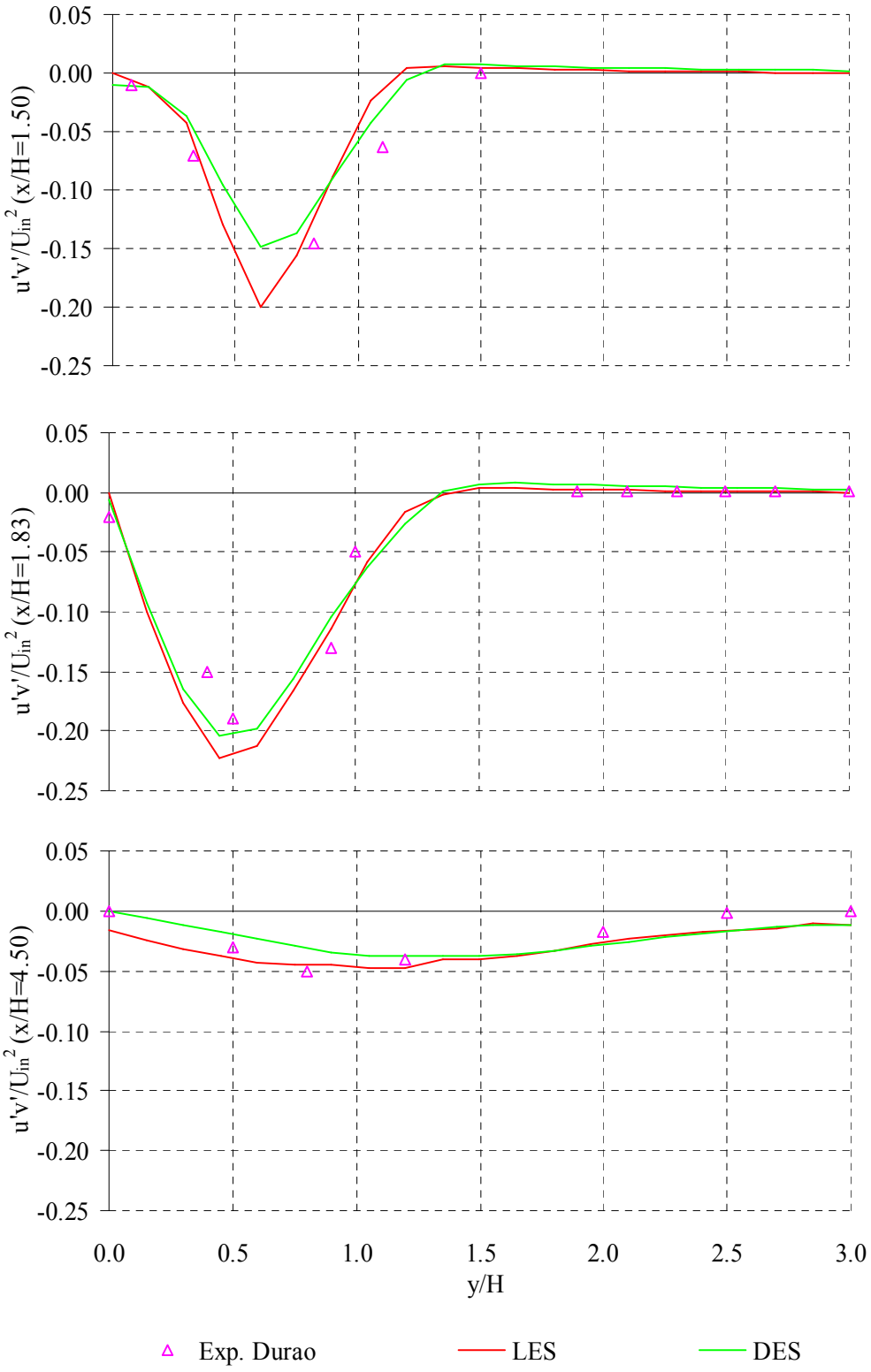

Figure 4.15 Simulated and measured mean Reynolds shear stress components at various vertical profiles in the wake region of the cylinder (*Re 14,000*).

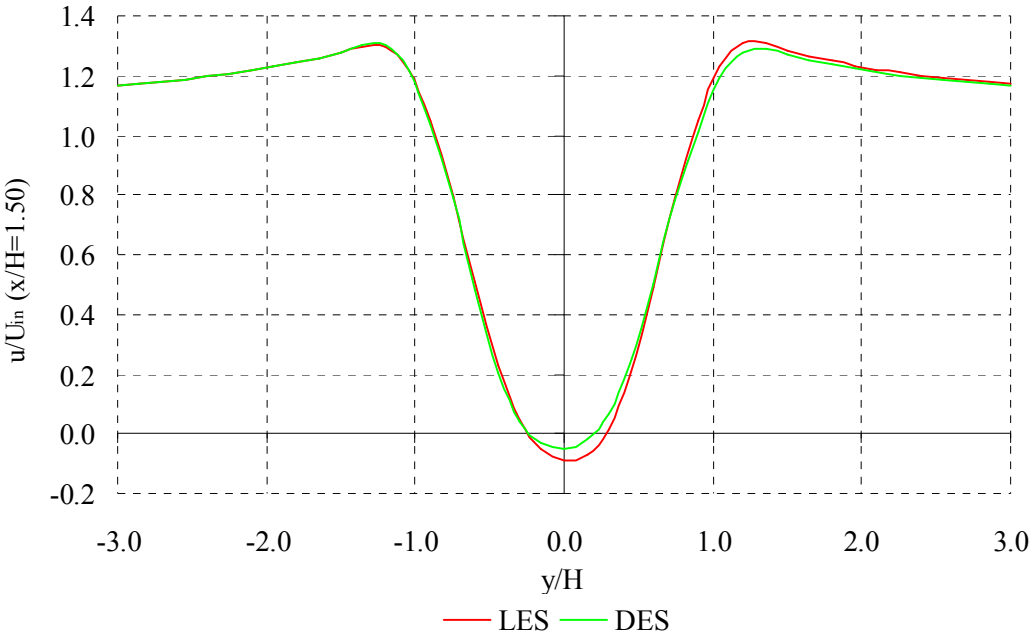

Figure 4.16 Simulated streamwise velocity component from *y/H=-3* to *y/H=3*.

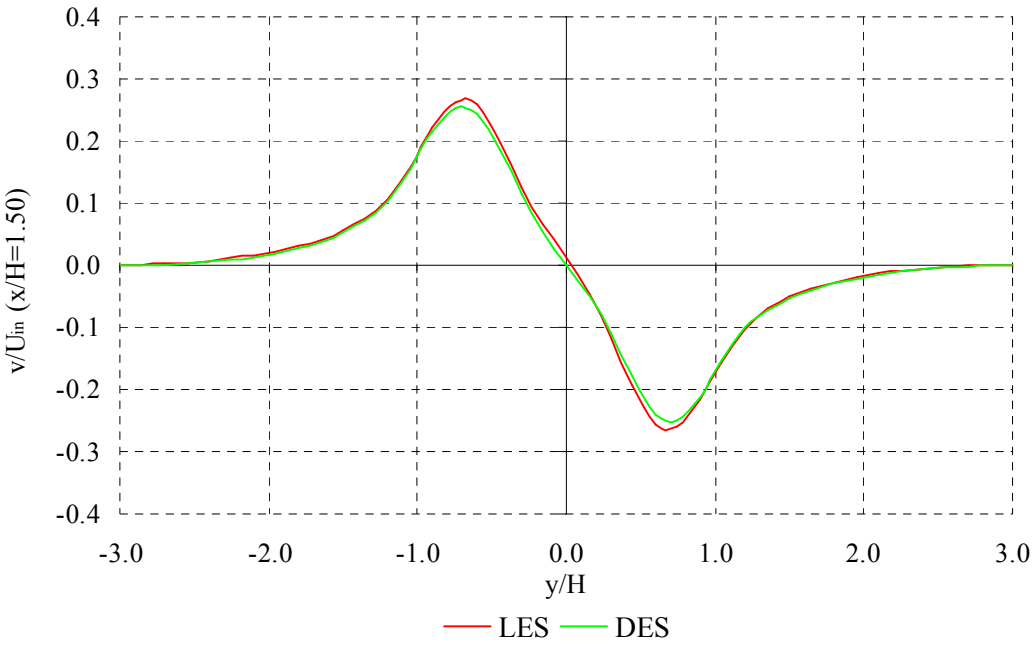

Figure 4.17 Simulated spanwise velocity component from *y/H=-3* to *y/H=3*.

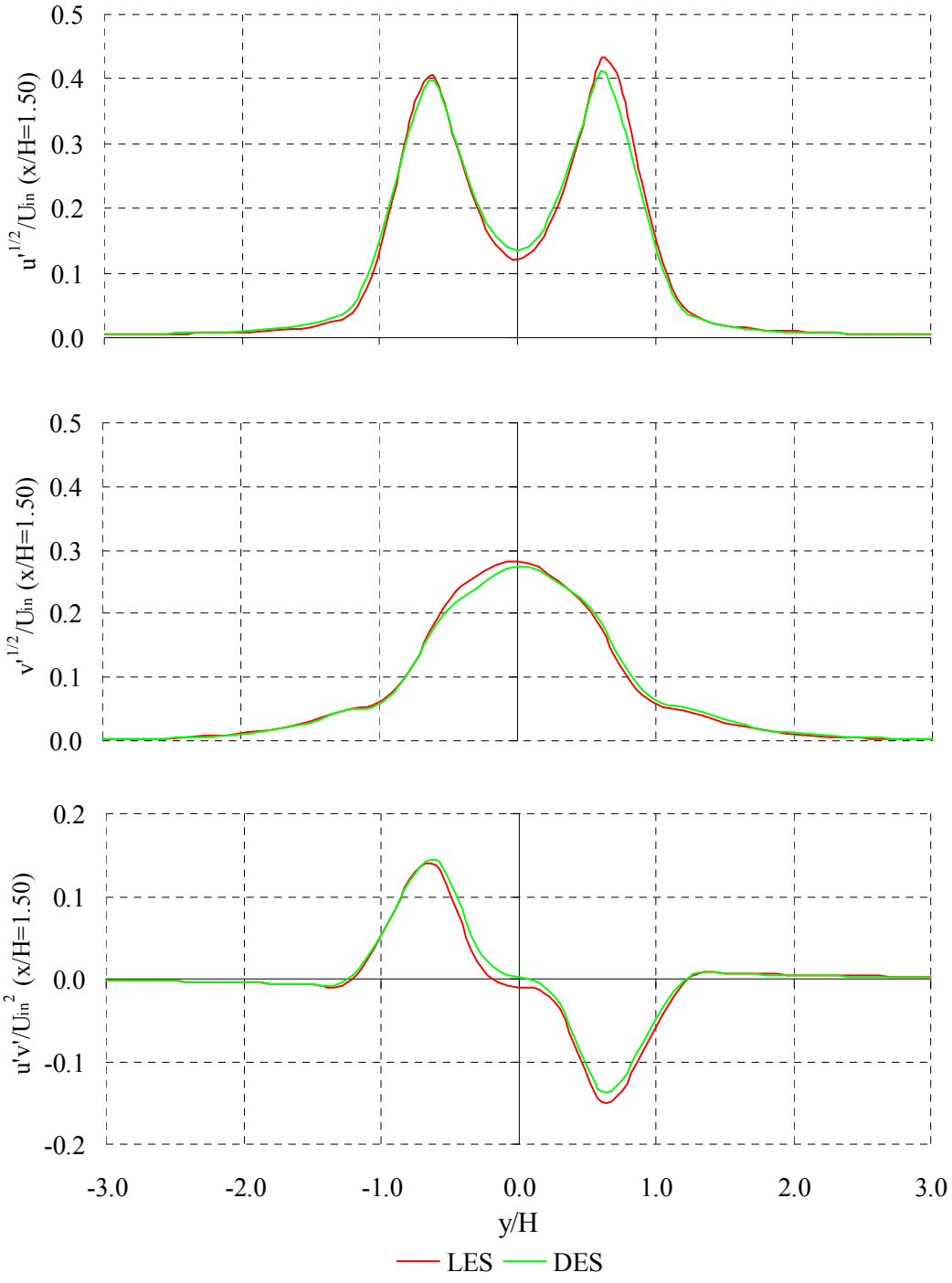

Figure 4.18 Simulated streamwise, spanwise and shear stress components from *y/H=-3* to *y/H=3*.

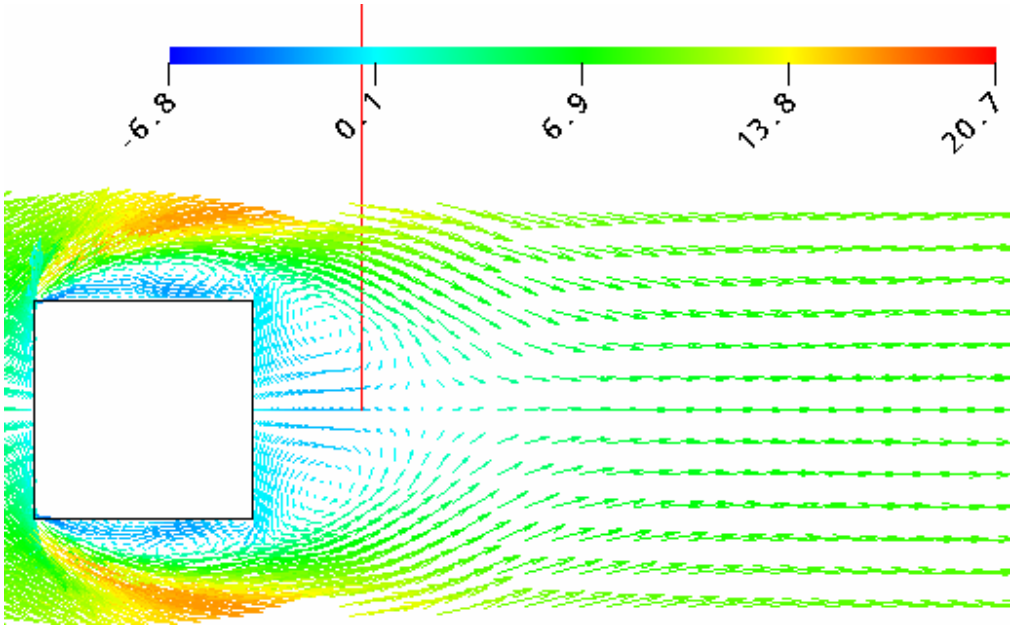

Figure 4.19 Mean streamwise velocity components at Reynolds number of *14,000* computed by LES.

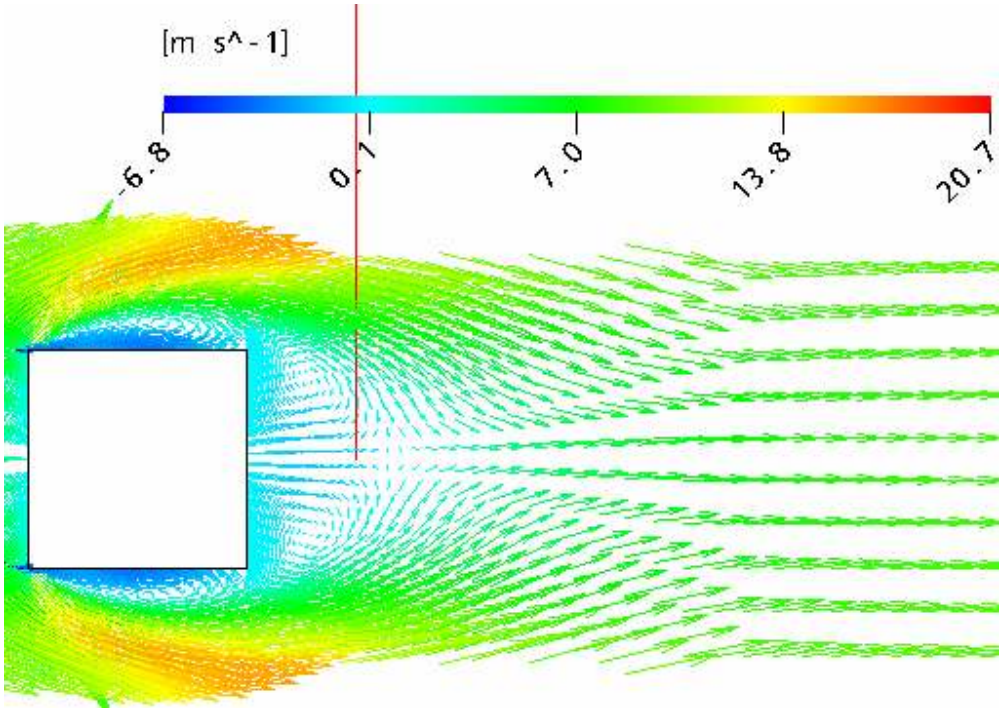

Figure 4.20 Mean streamwise velocity components at Reynolds number of *14,000* computed by DES.

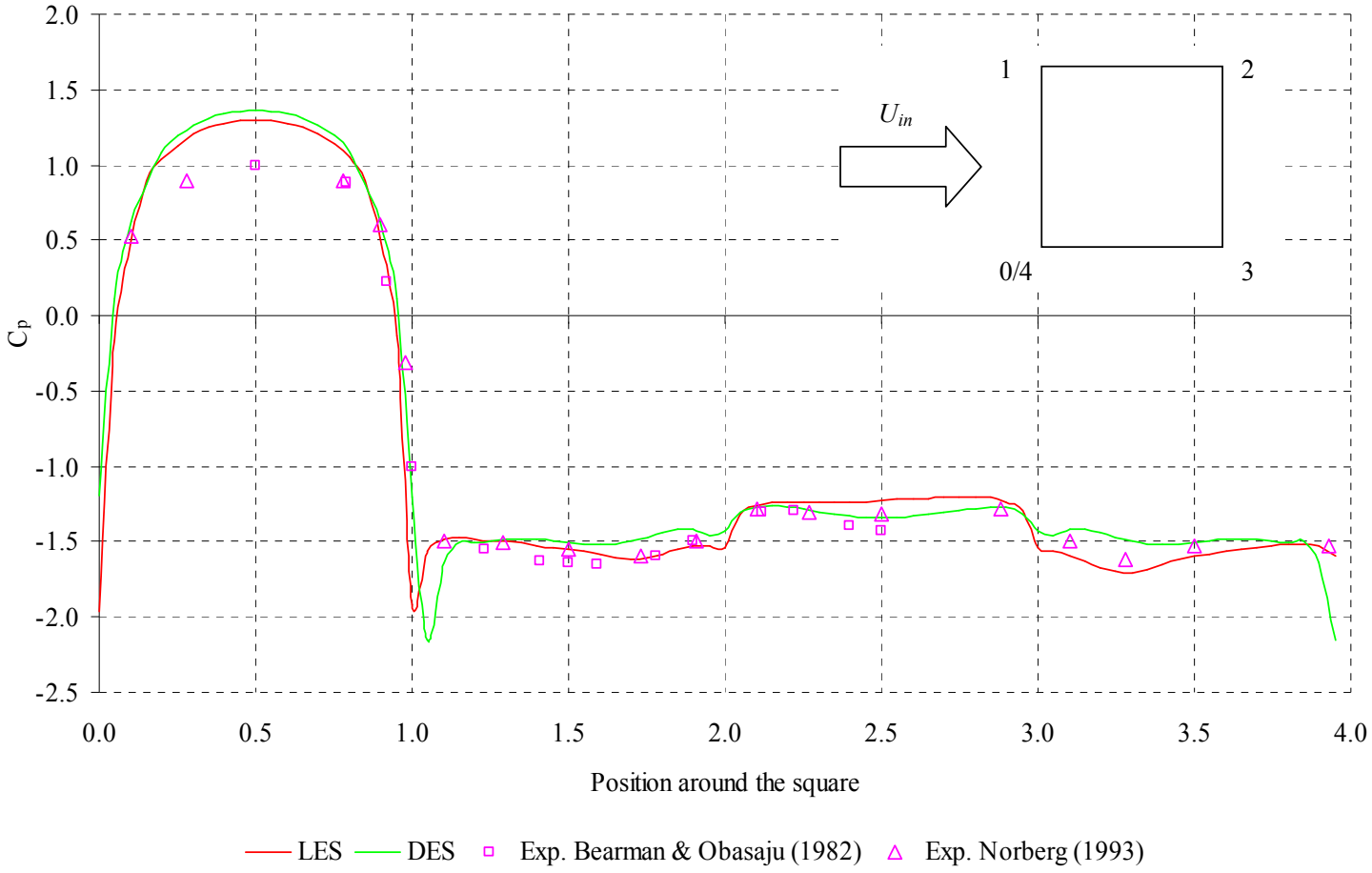

Figure 4.21 Comparisons of pressure coefficient around a square cylinder.

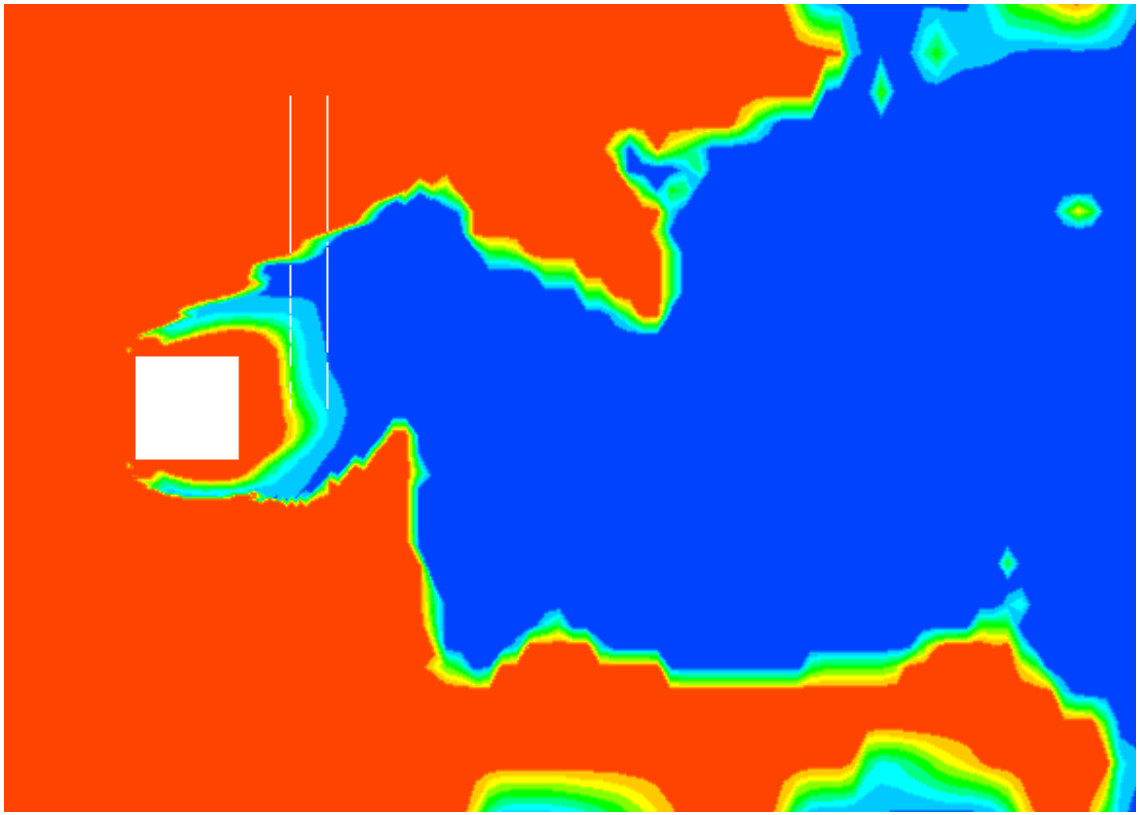

Figure 4.22 Instantaneous flow Region for RANS (red) and LES (blue) model in DES (Re *14,000*).

5 FLOW AROUND RECTANGULAR CYLINDERS

From the study of the flow around rectangular cylinders, one learns about the flow characteristics around similar shape bodies such as the deck section of long span bridges. Majority of the bridge deck sections resemble more complex rectangular shape. Flow separates from the leading edge corner and forms vortices that travel along the surface of the deck, which are eventually shed from the trailing edge resulting in the vortex shedding phenomenon. A vortex core tends to have a local minimum pressure, so the formation and progression of vortices introduce forces on the deck surface. The same phenomenon is observed on the flow around rectangular section with similar ratio. Also, the Strouhal number and drag coefficient of the flow change accordingly.

The aim of the work in this chapter is to simulate the flow behaviour around the rectangular cylinders using LES and DES through comparative study with experimental findings. This ensures that the turbulence models used are capable of predicting the flow behaviour around a bridge deck section, which will be discussed in the next chapter. Similarities between the flow around rectangular cylinders and the bridge deck section provide basic knowledge on the investigation of the flow characteristics around the deck section. The simulation of flow around a bridge deck section would involve huge computer power and thus a step by step parametric investigation is necessary to ensure that proper simulation techniques are employed.

5.1 PHYSICS OF FLOW AROUND RECTANGULAR CYLINDERS

This section provides the reader with basic knowledge on the flow characteristics around rectangular sections. Studies show that the flow around these sections is significantly affected by the afterbody length of the cylinder, which is expressed as the ratio of the breadth to the height (*B/H*) of the cylinder (Figure 5.1). Researchers [23, 85, 95] have pointed out that pressure distribution around the cylinder surface provides basic knowledge of the force exerted by the fluid on a body, the pressure distribution varying according to the *B/H* ratios of the section.

In the experimental study of the flow around rectangular sections with various aspect ratios, Komatsu and Kobayashi (1980) [59] concluded that the flow around the section tends to follow a similar pattern. Figure 5.2 shows the distribution of pressure and vortex formation around an oscillating rectangular section. In the top left corner sketch, *S1* represents flow separation from the leading edge of the cylinder, the shed

vortex reattaches on the cylinder surface and travels to the trailing edge (*T1 to T4*) forming a complete cycle of shedding when it leaves the trailing edge of the cylinder. At the bottom surface, new separation begins (*S'1*) half a cycle later (when *T2* travels along the top surface) and similar vortex progression is observed (*T'1 to T'4*). As the vortex moves along, the vortex core is accompanied by a reduction in pressure at the adjacent surface of the cylinder. Consequently, the separated vortex *S1* and travelling vortex *T4* produce an overall positive lift which synchronizes the cylinder to its maximum displacement position. Similarly, *S'1* and *T'4* vortices produce the same effect, with the cylinder returned to its original position when *T'1* and *T3* develop (Bottom left sketch). The cycle then repeats itself as *S1* starts to form again from the top leading edge with maximum displacement.

In an experimental study of the vortex convection and formation around rectangular sections, Matsumoto (1999) [71] concluded that the average velocity for the vortex to travel from the leading edge of the cylinder to trailing edge is approximately *60%* of the approach inlet velocity.

The following section reviews previous experimental work done on the flow around rectangular sections with various *B/H* ratios. Findings and conclusions of the experimental works regarding the flow characteristics and the influencing factors on the flow are summarized. The results are then used for the comparisons study with LES and DES results.

5.1.1 Experimental studies on the flow around rectangular cylinders

In the previous chapter, it was shown that separation of flow at the leading edge corner of a square cylinder does not show reattachment on the side surface due to the short afterbody length. For greater B/H ratio cylinders such as *B/H=3*, the breadth of the body is long enough to allow reattachment of the separated flow, which significantly affects the flow characteristics such as the shedding of vortices from the trailing edge of the sections. This vortex shedding phenomenon can be described using the Strouhal number, which relates the shedding frequency of the vortices to the streamwise velocity of the flow. The experimental work of Okajima (1983) [94] showed that flow changes from separated to reattachment type of flow within *B/H=2.5* to *B/H=2.8*. Reattachment of flow along the side surface causes the wake to expand considerably less than the flow without reattachment (flow around a square cylinder). Consequently, the shedding

frequency increases, resulting in a sudden jump of Strouhal number between critical aspect ratio of *B/H=2.5* and *B/H=2.8* (Figure 5.3).

Other researchers predicted slightly different values of aspect ratio when reattachment of flow happened but is generally within *B/H=2* to *B/H=3*. This varies accordingly with the input flow parameters. Noda and Nakayama (2003) [90] conducted experiments on the flow around a cylinder section of *B/H=2.5* and discovered that flow with higher free stream turbulence intensity triggers reattachment of flow but flow with lower turbulence intensity does not reattach at the same aspect ratio of *B/H=2.5*.

Apart from the above mentioned situation that changes the vortex shedding frequency, another parameter that affects the Strouhal number is the Reynolds number. The effect is only significant when the Reynolds number is low. Within Reynolds number of a few hundreds, flow around rectangular sections of *B/H=1* to *B/H=3* shows changes of the Strouhal number as the Reynolds number increases. For instance, at Reynolds number of less than *400*, the Strouhal number of a *B/H=2* rectangular section increases with the Reynolds number. Beyond Reynolds number of *500*, a sudden drop in the Strouhal number happens and two shedding frequencies have been observed for the flow due to the changes of flow pattern around the section and the width of the wake [85, 97]. This observation agreed well with the investigation of Okajima (1982) [95] who studied the relationship of the Strouhal number and the Reynolds number for rectangular sections between *B/H=1* and *B/H=4*. At higher Reynolds number, all the experimental works report nearly constant Strouhal number as the Reynolds number increases.

Figure 5.3 shows a typical plot of the changes of Strouhal number with the B/H ratios for rectangular cylinders of *B/H=1* to *B/H=5*. Visually, two significant trends have been observed as the B/H ratio increases, depicted by the red lines in the figure. Sudden change of the Strouhal number between *B/H=2* and *B/H=3* is observed due to the reattachment of flow. As mentioned, reattachment of flow changes the vortex shedding frequency. Scattered Strouhal numbers have been observed between *B/H=2* and *B/H=3*, this is due to the fact that the length of the recirculation bubbles of the flow is about the size of the side surface of the rectangular section around this aspect ratio. This results in the sensitivity of reattachment of flow between *B/H=2* and *B/H=3* cylinder sections, where reattached type of flow (in which vortices are shed faster) gives higher Strouhal number while separated type of flow is associated with lower shedding frequency.

Figure 5.4 shows the experimental findings of the changes of the drag coefficient with the aspect ratios between *B/H=1* to *B/H =4*. The drag coefficient increases steadily from *B/H=0*. Bearman (1965) [10] pointed out that drag force is related to the base suction in the near wake region of the flow where vortex formation occurs. Lower base suction results in lower drag. Bearman also concluded that the further downstream the vortices form from the trailing edge of the cylinder, the lower the drag. This observation generally agreed with works from other researchers [78, 92].

From *B/H=0* to *B/H=0.5*, the drag force is increasing (Figure 5.4). Mills *et al.* (2002) [78] pointed out that the position of the vortex formation in the wake region of a cylinder between these B/H ratios is essentially unchanged, thus increasing the aspect ratio moves the vortex formation region closer to the cylinder, creating higher base suction and thus drag force. From Figure 5.4, peak drag coefficient has been observed at aspect ratio of about *B/H=0.6*. According to the smoke wire flow visualization experiment of Norberg (1987) [92], extremely powerful vortices with strong curvatures have been observed at the near wake separating shear layers at this aspect ratio. Norberg referred this as the 'golden section' ratio in the flow around rectangular section, when the flow exhibits maximum base suction in the wake region. Further increase of the aspect ratio from *B/H=0.6* changes the shear layer curvatures and thus the interaction of vortices at the trailing edge. Consequently, high base suction is no longer maintained and a steady decrease in drag is observed from *B/H=1* to *B/H=2*. At *B/H=1*, the separated flow covers the whole side surface of the cylinder forming a more intense vortex compared to a *B/H=2* cylinder, resulting in greater base suction and thus higher drag.

As the afterbody length increases to the ratio where reattachment of flow is possible (*B/H=2* to *B/H=3*), pressure distribution along the side surface of the cylinder changes. A region of higher pressure occurs after flow reattachment, known as the pressure recovery region [92]. This region pushes the vortices further downstream and results in a lower suction area with smaller drag force. This explains the steady decrease of drag coefficient as the aspect ratio increases. Yu and Kareem (1996) [143] investigated the pressure distribution on the side surface of rectangular cylinders between aspect ratio of *B/H=1* to *B/H=4*. They concluded that the pressure in the recovery region increases proportionally with the aspect ratios, associated with lower suction in the wake region of the cylinder. No obvious pressure change has been observed for cylinder between aspect ratio *B/H=1* to *B/H=2,* indicating no reattachment of flow on the side surface. The observation of Yu and Kareem agreed with the

findings of Norberg (1987) [92] on the flow around cylinders with the same aspect ratios.

The flow around rectangular sections with aspect ratio smaller than *5* has been discussed above. For cylinders with longer aspect ratio (*B/H>4*) the reattachment of the flow allows vortices to travel further along the cylinder side surface to the trailing edge, this in turn affects the shedding characteristics of the flow in the wake region. Nakamura *et al.* (1991) [86] studied the vortex shedding characteristics of rectangular cylinders with longer afterbody length up to *B/H=16*. The experiment was conducted within Reynolds number of *1,000* to *3,000.* Three regimes have been identified based on the flow behaviours on the side surface of the cylinders.

At *B/H<3.2*, most of the flow separates from the leading edge without reattachment on the side surface and forms a regular vortex street in the wake region of the cylinder. A fraction of the flow reattached occasionally because measurement reported that the wavelength of the vortex shedding at *B/H=3* is about the breadth (*B*) of the cylinder. Between *B/H=3.2* to *B/H=7.6*, a regular vortex street is still observed in the wake region but the separated shear layer reattaches periodically to the side surface of the cylinder. From *B/H=7.6* to *B/H=16,* reattachment of flow always happens but the separation bubbles grow and divide randomly, causing irregular shedding of vortices in the wake region.

Traditionally, the Strouhal number is calculated based on the height (*H*) of the cylinder (Figure 5.1). Nakamura *et al.* (1991) [86] pointed out that there exists a relationship between the Strouhal number based on the breadth (*B*) of the cylinders and the B/H ratios. To prevent confusion, the Strouhal number calculated based on the breadth of the cylinder is denoted by St_B in the rest of the chapter. Nakamura concluded that from *B/H=3* to *B/H=5*, St_B showed a near constant value of *0.6*. Further increase of B/H ratios triggered a stepwise increase in the St_B values approximately equal to *0.6n* where *n* is the number of vortices along the side surface of the cylinder at any instant. The stepwise increase of St_B is depicted in Figure 5.5, with measurement from other researchers for comparison purposes.

Nakamura *et al.* (1991) [86] reported that the stepwise increase of St_B is related to the impinging shear instability phenomenon. The impinging shear layer instability is a situation where the separated shear layer around bluff bodies becomes unstable in the presence of sharp corners. In the flow around rectangular sections between *B/H=3* to *B/H=8*, the separated shear layer interacts directly with the vortices shed from the

trailing edge of the cylinder. When the flow separates from the leading edge of a rectangular section, the travelling vortices along the cylinder side surface generate a pressure pulse that travels upstream to develop a feedback loop. The pressure pulse controls the separating shear layer at the leading edge such that a particular shedding phase between the vortices of the leading edge and the trailing edge is created [127]. This suggests that the trailing edge vortices could be shed in phase with the leading edge separation or completely out of phase, this is determined by the B/H ratios of the cylinders. St_B remains constant if the time taken for the vortices to travel to the trailing edge within certain B/H ratios is almost identical. Increase of *n* produces higher vortex shedding frequencies and results in the stepwise increase of St_B as the B/H ratio increases.

Figure 5.6 shows the flow around a *B/H=8* rectangular cylinder with *n=2*. The number of vortices on the side surface of the cylinder affects the way vortex is shed in the wake region of the flow. Generally, the following observation has been noted between the aspect ratio and the number of vortices on the side surface of the cylinder [78],

3<B/H<5	*n=1*
6<B/H<8	*n=2*
9<B/H<11	*n=3*
12<B/H<16	*n=4*

The measurements of Nakamura generally agreed with other experimental work [78, 121] but discrepancies have been observed especially at the B/H ratio before the next stepwise changes of St_B occurred (Figure 5.5), such as at *B/H=5* and *B/H=8*. Measurement at these aspect ratios revealed existence of two peak shedding frequencies. Physically, this is due to the changing of the vortex shedding frequencies characterized by the transition of shedding mode associated with *n*. For instance, the two frequencies observed at *B/H=8* are associated with the *n=2* and *n=3* shedding modes, resulting in the two Strouhal numbers of the flow.

As reported by Mills *et al.* (2002) [78], the stepwise increase of St_B was observed only for rectangular sections with Reynolds number smaller than *2,000*. Beyond this Reynolds number, the initially laminar type separated shear layer becomes turbulent

with increasing three-dimensional effects. Consequently, flow becomes more random and the periodic vortex street convection becomes weaker. These result in the changes of the pressure pulse feedback mechanism and thus the changes of St_B. The stepwise increase of St_B might still happen at higher Reynolds number but the pattern might not be that obvious.

5.1.2 Numerical studies on the flow around rectangular cylinders

The numerical studies of the flow around rectangular cylinders have gained popularity in the last decades due to the rapid advance in computer technology. Comparatively, these elongated bodies demand higher computer power compared to a square cylinder in order to properly resolve the near wall flow parameters and shear layer flow along the surface of the cylinders. The key features in the simulation of the flow around rectangular cylinders is the ability of the turbulence models to capture the changes of the flow characteristics with respect to the increasing B/H ratio and the prediction of the reattachment of flow along the side surface of the cylinders. The following paragraphs discuss numerical studies of the flow around rectangular sections with various aspect ratios. The discussion starts with flow with low Reynolds number, followed by higher Reynolds number flows as the B/H ratio increases.

Shimada and Ishihara (1999) [106] employed a modified k-ε model to capture the unsteady vortex structure in the wake region of the cylinder sections with different aspect ratios. In this model, the production of the turbulent kinetic energy is expressed in term of a vorticity tensor and a velocity strain tensor [57]. This aims to improve the prediction of the vortex shedding in the wake region of the flow which the standard k-ε model failed to simulate. Results from the modified k-ε model gave good agreement of the changes of Strouhal number with B/H ratios compared to experimental findings. The drag coefficients have been well predicted as well. Consequently, the modified model was applied to investigate the aeroelastic response of an elastically supported *B/H=2* cylinder. As concluded, the motion induced vortex oscillation and the coupling of galloping and vortex induced vibration were successfully simulated from the modified k-ε model, provided that proper spanwise momentum diffusion is incorporated [107].

Yu and Kareem (1998) [144] applied LES with the Smagorinsky sub-grid model to the flow around rectangular sections between *B/H=1* to *B/H=4* to observe the changes of separated type of flow to reattached flow as the aspect ratio increases. From the

changes of the pressure profiles along the side surface of the cylinders, reattachment of flow has been reported between *B/H=2* and *B/H=3*, in agreement with the experimental observations discussed earlier. Compared to the earlier two-dimensional LES of Yu and Kareem [143] on the flow around rectangular sections, the results showed discrepancies especially in the prediction of the Strouhal number. The two-dimensional simulation also failed to capture the lift and drag coefficient compared to experimental findings.

As discussed in the previous section, the characteristics of formation and convection of the vortices along the side surface for longer afterbody sections results in the stepwise changes of St_B. Numerically, Ohya *et al.* (1992) [93] simulated the flow around rectangular sections with aspect ratio of *B/H=3* to *B/H=9* at Reynolds number of *1,000*. A finite difference method (FDM) with third order upwind scheme was employed to solve the two-dimensional Navier-Stokes equations for the flow. The simulations successfully captured the stepwise changes of St_B as observed in the experiment [86]. The number of vortices, *n*, observed along the side surface of the cylinders agreed with the measured results, corresponding to *n=1, 2* and *3* for the changes at the aspect ratios of *B/H=3, 6* and *9* respectively. Two shedding frequencies have been observed for the *B/H=8* cylinder, in which a similar situation was noted in the experiment. Physically, the two dominant shedding frequencies correspond to the *n=2* to *n=3* shedding modes respectively. However, slightly lower St_B have been predicted for both modes compared to experimental measurement.

Further numerical simulation of the stepwise increase of St_B at *0.6n* has been conducted by Tan *et al.* (1998) [127]. The finite element method (FEM) has been used on cylinder sections with aspect ratios between *B/H=3* to *B/H =16* at low Reynolds number. For cylinders with *B/H=3, 6* and *9*, corresponding to aspect ratios of cylinders at the beginning of each stepwise change of St_B, regular single frequency shedding was observed. This is attributed to the merging of the trailing edge vortices from the top and bottom surface of the cylinder causing a larger base suction area in the wake region for a stronger locking of the vortices. At other B/H ratios, the merging of the vortices is slightly out of phase, resulting in weaker shedding of vortices. Consequently, the regular vortices are disturbed and mixture of shedding modes with *n=2* and *n=3* occurs. This explained the observation of the two shedding frequencies of a *B/H=8* cylinder.

5.2 RESULT AND DISCUSSION (LES AND DES)

In this section, the performances of LES and DES on the flow around rectangular sections are discussed. Advantages and weaknesses of each turbulence model are identified and the suitability of the models for the applications of the flow around bridge deck sections is assessed. The next section (section 5.3) contains similar discussion but the flow is computed at higher Reynolds number (*Re 42,800* and *Re 100,000*) compared to the simulations presented here. In section 5.4, analysis is done on the formation and convection of the vortices on the cylinder surface to study the aerodynamic forces exerted on the cylinder due to the pressure changes. This is important in the context of the simulation of flow around a bridge deck section at a later stage of the work in this thesis.

The meshes around the cylinder sections simulated in this chapter are similar to the one employed for the simulation of the flow around a square cylinder (fine mesh in the mesh sensitivity analysis) to make sure that flow near to the wall is properly resolved. The LES and DES approaches employed for the flow around rectangular sections use the same discretisation methods as in the flow around square cylinder (section 4.2.1), in which a second order central differencing scheme is employed for the LES whereas the SST model uses a second order upwind differencing scheme for space discretisation. Both turbulence models employ a second order backward Euler scheme for time discretisation.

5.2.1 Flow around a cylinder with aspect ratio of *B/H=2*

Investigation on the flow around a cylinder with aspect ratio of *B/H=2* focuses on the changes of the flow characteristics especially on the vortical structures around the section, which affects the Strouhal number of the flow. To begin with, changes of the Strouhal number with increasing Reynolds number have been investigated. The vortical structures around the cylinders will be the main discussion rather than the velocity distribution in the wake region of the flow as in the case of the flow around a square cylinder.

Flow around a square cylinder shows almost constant Strouhal number with changes of Reynolds number within $100 < Re < 12{,}000$ [94]. On the other hand, a *B/H=2* rectangular section shows a change of shedding frequency as Reynolds number increases. The change is attributed to the size of the separated vortex that is similar to the afterbody length of a *B/H=2* section. Okajima (1982) [95] observed that the

Strouhal number of a *B/H=2* section increases from *0.1* to *0.18* as the Reynolds number increases from *40* to *500*. Low speed flow promotes reattachment as it is more laminar and has higher flow resistance compared to flow at higher speed. Vortices are thus shed more frequently after reattachment compared to the separated type of flow, resulting in the increase of the Strouhal number. Beyond Reynolds number of *500*, more constant Strouhal number is observed. This is attributed to the changes of the characteristics of vortex formation around the cylinder, where transition from reattachment type to separated type of flow happens as Reynolds number increases. From Figure 5.7, LES has shown the capability of capturing the Strouhal number changes with the increase in Reynolds number. The dramatic decrease of the Strouhal number was predicted well by LES but slightly lower Strouhal number has been observed at higher Reynolds number (*Re> 3,000*). The DES prediction at higher Reynolds number has been included, in which lower Strouhal number was computed as well. A similar phenomenon has been observed in the experiment by Nakaguchi *et al.* (1968) [85]. Table 5.1 depicts the measured and simulated Strouhal number around a *B/H=2* cylinder quantitatively.

In terms of the drag force around a *B/H=2* section, LES and DES generally computed drag coefficients close to experimental results [23, 50, 58]. Table 5.2 shows the comparison of the simulated and measured drag coefficient of the flow around a *B/H=2* section at various Reynolds numbers. A lower drag coefficient has been predicted by LES at Reynolds number of *500*. At this Reynolds number the vortex formation is quite different from those at the higher Reynolds number range due to lower flow speed. This changes the vortex structures in the wake region of the flow and results in different base pressure, which in turn affects the drag force. LES did not capture this change well and thus a discrepancy in the drag coefficient has been observed. The above-mentioned discrepancy could be attributed to the nature of LES in computing turbulence type of flow. Employing a laminar simulation might improve the prediction of the drag coefficient of the flow. Changes of Strouhal number with Reynolds number for cylinders with higher aspect ratios is not that significant since the flow always reattaches on the side surface of the cylinders, maintaining a more stable vortex shedding frequency in the wake region of the sections.

Table 5.1 Comparison of simulated and measured Strouhal number of a *B/H=2* rectangle at various Reynolds numbers.

Reynolds number	**Exp. Okajima '82 (Strouhal no.)**	**LES (Strouhal no.)**	**DES (Strouhal no.)**
14,000	*0.09*	-	*0.07*
3,000	*0.08*	*0.08*	*0.08*
900	*0.07*	*0.06*	-
500	*0.16*	*0.16*	-

Table 5.2 Comparison of simulated and measured drag coefficient of a *B/H=2* rectangle at various Reynolds numbers.

Reynolds number	**Other work (C_d)**	**LES (C_d)**	**DES (C_d)**
14,000	*1.60* Exp. Norberg '93	-	*1.55*
3,000	*1.62* Exp. Igarashi '87	*1.60*	*1.55*
900	*1.52* Exp. Courchesne *et al.* '79	*1.54*	-
500	*1.48* Exp. Knisely '90	*1.33*	-

5.2.2 Flow around cylinders with aspect ratio of *B/H=3* to *B/H=8*

In the discussion on the flow characteristics around rectangular sections of aspect ratio from *3* to *16* (Section 5.1), it was experimentally and numerically shown that the Strouhal number St_B, based on the breadth of the section, of the flow around rectangular sections increases in a stepwise manner as the aspect ratio becomes larger. This phenomenon is directly related to the formation and progression of vortices along the side surface of the cylinders. The travelling vortices generate a pressure pulse that locks the shedding of the leading edge and trailing edge vortices [127]. This changes the way vortices are shed and thus affects the Strouhal number of the flow.

5.2.2.1 Vortex formation around a cylinder with aspect ratio of *B/H=3*

To investigate the above-mentioned situation, the formation and progression of vortices along the side surface of a *B/H=3* cylinder was studied. According to the investigation of Tan *et al.* (1998) [127] on the flow around rectangular sections, the repeated regular flow pattern of velocities at the leading and trailing edges of a cylinder indicates locking of the leading and trailing edges vortices. This phenomenon has been observed from the time history of the mean streamwise velocities plot for the current *B/H=3* section simulation (Figure 5.8). This agreed with the findings of both the experimental [86] and numerical works [127] on the impinging shear layer stability phenomenon on rectangular sections (Section 5.1.2).

Investigation of the flow around a *B/H=3* cylinder revealed some features of the vortical formation and progression around and in the wake region of the flow. Figure 5.9 illustrates the different vortical structures around the cylinder which will be referred to in the following discussion. In the numerical study of Tan *et al.* (1998) [127] on the flow around rectangular sections, it was pointed out that when vortices resulting from the leading edge separation merged with the trailing edge vortices in the wake region, a higher base suction region was created. On the other hand, if the vortices are shed out of phase then it suppresses the trailing edge vortices. This situation indirectly affects the aerodynamic force induced on the cylinder.

Figures 5.10a, 5.10b and 5.10c show the instantaneous plot of the streamwise velocity component around a *B/H=3* cylinder for one complete shedding cycle (*6* diagrams altogether). The shedding of the vortices is related to the force induced by the pressure on the cylinder surface. A shedding vortex is usually accompanied with a negative pressure area at the adjacent surface, inducing force on the cylinder. Figure

5.11 depicts the time history of the surface pressure force acting on the top and bottom surface of the *B/H=3* cylinder. The six markings on the top and bottom surface of the cylinder correspond to each instantaneous diagram of the streamwise velocity component shown on Figures 5.10a, 5.10b and 5.10c.

At *4.9742 seconds* (Figure 5.10a), two vortices at the bottom surface of the cylinder creates a suction area which pulls it downward. Together with the anticlockwise vortex in the wake region with the vortex centre nearer to the bottom surface, these vortices generate a total downward force on the cylinder. This corresponds to the pressure force acting on the bottom surface of the cylinder as shown in Figure 5.11.

In the second and first diagram (*4.9757 seconds* and *4.9772 seconds*) of Figure 5.10a and 5.10b respectively, the vortex in the wake region starts to shed away from the cylinder with the one of the bottom surface vortex approaching the trailing edge. Consequently, the pressure force on the bottom surface of the cylinder reduces (Figure 5.11). At the same time, the vortex near to the trailing edge of the top surface in the previous time step (*4.9742 seconds*) begins to shed into the wake region and a new vortex is created at the leading edge resulting from flow separation. These vortices progress along the top surface (*4.9772 seconds* and *4.9787 seconds*) to create a positive lift (upward force). This is indicated in Figure 5.11 where the pressure force progressively increases on the top surface of the cylinder.

The time step (*4.9787 seconds*) is at half a shedding cycle later than the first diagram (*4.9742 seconds*) but a similar situation is observed. Maximum lift force is now observed at the top surface of the cylinder rather than the bottom surface. Again, this is caused by the combination of a rotating vortex in the wake region with the vortices at the top surface to create the total positive lift on the cylinder. The last two diagrams (*4.9802 seconds* and *4.9817 seconds*) in Figure 5.10c correspond to the vortex in the wake region being shed away and the vortex at the top surface approaching the trailing edge. A new vortex is now being shed from the leading edge at the bottom surface and results in the increase of the pressure force. The cycle then repeats with a total negative lift (downward force) attained at the bottom surface as in the first diagram of Figure 5.10a.

For cylinders with different aspect ratios, the interactions of vortices are different. For instance, cylinders with longer afterbody length allow more vortices to progress along the side surface which changes the way vortices are shed in the trailing edge.

Instead of shedding individually, the vortices shed from the top and bottom of the trailing edges might combine to induce vibration to the cylinder. This is further discussed in section 5.2.2.3 on the study of the flow around *B/H=5* to *B/H=8* cylinder sections.

5.2.2.2 Flow field around a cylinder with aspect ratio of *B/H=4*

In the previous discussion on the flow around a *B/H=3* cylinder, the effect of vortices on the cylinder has been investigated. Although the result gave good indication on the vortical structures formation and progression, validation is needed to ensure that the observation is theoretically correct. So, the next discussion compares the simulated velocity and pressure distribution of a *B/H=4* cylinder with respect to the finding of experimental work of Komatsu and Kobayashi (1980) [59]. The purpose is to demonstrate the ability of the DES model to capture the essential features of vortices, velocity and pressure distribution in the vicinity of the cylinder. Figures 5.12a and 5.12b show the instantaneous flow pattern of one complete shedding cycle on a *B/H=4* cylinder. The symbols (*S1*, *T1* to *T4*, *S'1* and *T'1* to *T'4*) represent the same phenomenon as in Figure 5.2 (experimental findings of Komatsu). *S1* and *T1* to *T4* indicate the separating vortices and the travelling vortices on the top surface of the cylinder respectively. Similarly, *S'1* and *T'1* to *T'4* represent the situation at the bottom surface of the cylinder. In the simulated result, the additional symbols (*M1* and *M'1*) indicate the combination of the vortices from top and bottom surface of the flow respectively, which were not included in Komatsu's observation.

Visually, very similar vortex patterns (vector plot in Figures 5.12a and 5.12b) have been predicted by DES compared to the experimental observation (left column in Figure 5.2). For pressure distribution (contour lines in Figures 5.12a and 5.12b), DES predicted similar distribution but with lower magnitude compared to experimental finding (right column in Figure 5.2). This is attributed to the difference between a stationary cylinder (Figures 5.12a and 5.12b) and an oscillating cylinder (Figure 5.2) in which additional forces introduced by the movement of the cylinder influence the pressure distribution. Overall, DES prediction showed good agreement for the vortical formation and pressure distribution around the cylinder with experimental observations. This is crucial for later simulation of the flow around a bridge deck section where more complex vortex interaction is involved due to the open cross section deck shape.

5.2.2.3 Changes of Strouhal number with increasing B/H ratio

For cylinder sections with longer afterbody length of *B/H=5*, 6, *7* and *8*, studies [86, 127] showed that the Strouhal number based on the breadth of the cylinder (St_B) increase in a stepwise manner (section 5.1.1 and 5.1.2) with the increase in the aspect ratio. Following this, simulations have been carried out on the cylinder sections of *B/H=5* to *B/H=8* to investigate the above-mentioned phenomenon. Figure 5.13 depicts the simulated and experimental results for the changes in the Strouhal number St_B with the increase in aspect ratio. From Figure 5.13, current simulated results obtained with LES and DES are well within the experimental findings from other researchers [78, 86, 121].

As discussed in Section 5.1.1 and 5.1.2, the stepwise increase of St_B is caused by the changing of the number of vortices *n* at the side surface of the cylinder. Generally, studies [78, 86, 93, 127] on the changes of St_B with increasing aspect ratio have only been done within Reynolds number of *2,000* to *3,000*. As the Reynolds number increases, the pattern of changes of St_B might be different as flow around the sections is becoming more complex and chaotic. General pattern of the St_B might still occur but the stepwise increase of St_B is expected to be less obvious. From *B/H=3* to *B/H=5*, only one vortex (*n=1*) is observed at the side surface of the cylinder. When the aspect ratio is greater than *B/H=5*, the longer afterbody length allows two vortices to progress on the surface. This *n=2* situation corresponds to St_B of about *1.1* (Figure 5.13). The simulated result managed to capture these changes well. Figure 5.14 shows the vortical structures (*n=2*) of the flow around a *B/H=8* cylinder, demonstrating the capability of LES in capturing the unsteady flow mechanism around the section with respect to published data.

From Figure 5.13, it is obvious that scattered results were noticed between *B/H=5* and *B/H=6* cylinders, when the transition from *n=1* to *n=2* of the vortices on the side surface of the cylinder happened. Two shedding frequencies for both *B/H=5* and *B/H=6* cylinders have been observed from the experiments of Stokes and Welsh (1986) [121]. In the simulated result of LES, a similar situation was noticed for a *B/H=5* cylinder (Figure 5.15). During the transition of *n=1* to *n=2*, the periodic nature of the flow is disturbed, resulting in irregular shedding of vortices and changes of pressure distribution around the cylinder. The loss of the regular shedding nature of the flow can be observed on the plot of the time history of the drag coefficient of a *B/H=5* cylinder. Figure 5.16 compares the time history of the drag coefficients for a *B/H=4* and a *B/H=5*

cylinder. Visually, the coefficient of the *B/H=4* cylinder possesses a rather regular shedding pattern whereas the *B/H=5* has lost its periodic nature. Figure 5.15 plots the power spectrum of the lift coefficients of the *B/H=4* and *B/H=5* cylinder, the Strouhal number of the cylinders can be obtained by substituting the peak frequencies in the figure into Eq. 3.2. Clearly, the *B/H=5* cylinder shows double frequency shedding, corresponding to the irregular nature of the drag coefficient observed in Figure 5.16. For a higher aspect ratio of *B/H=8*, when transition of *n=2* to *n=3* happens, a similar situation has been observed.

Apart from these irregular shedding modes, cylinders with other aspect ratios (*B/H=3, B/H=4, B/H=6,* and *B/H*=7) show a single peak lift spectrum indicating only one dominant shedding frequency. Among these regular shedding cases, *B/H=3* and *B/H=6* cylinders have a higher Strouhal number, which correspond to a faster shedding of vortices in the wake region of the flow (Figure 5.17). For a *B/H*=3 cylinder, the reattachment of flow happens near to the trailing edge corner. Consequently, the trailing edge vortex is shed in phase with the newly generated vortex from the leading edge. Similar shedding pattern happens in a *B/H=6* cylinder but with two vortices (*n=2*) convecting along the side surface of the cylinder at any time during the flow. Other aspect ratio cylinders have trailing edge vortices shed slightly out of phase with the leading edge periodic vortex due to different afterbody length, changing the frequency at which vortices are shed. This agreed with the findings of Tan *et al.* (1998) [127]. From the investigation on the simulated results, it is concluded that St_B of rectangular sections between *B/H=3* and a *B/H=8* increases at a rate of *0.6n*. This observation agrees well with the findings from other researchers [78, 121, 127].

5.2.3 Summary of analysis of flow around rectangular sections

For a *B/H=2* cylinder, studies show more significant changes of Strouhal number with the increase of Reynolds number compared to cylinder sections with other aspect ratios, in which more constant Strouhal number has been noticed. The change is caused by the similar size of the side surface of a *B/H=2* cylinder and the length of the recirculation vortices. Changes in the speed of flow (Reynolds number) affect the way vortices are shed in the wake region and thus the Strouhal number. Both LES and DES have been employed to capture this phenomenon. Good agreement has been observed at lower Reynolds number but slightly lower Strouhal number has been predicted at higher Reynolds number.

For cylinders with aspect ratio of *B/H=3* to *B/H=8*, study has been done on the formation and progression of the vortices around the sections and their aerodynamic effects on the cylinders. For instance, analysis on a *B/H=3* cylinder showed that the pressure force induced on the cylinder is related to the distribution of vortices around the cylinder surface. Further to this analysis, the vortical structures and pressure distribution around a *B/H=4* cylinder has been compared to experimental results and good agreement has been observed. Together with the observation on the simulated results for *B/H=5* to *B/H=8* cylinders, changes of the Strouhal number of the cylinders with the increase of the aspect ratio have been investigated. The turbulence models employed are able to capture the stepwise changes of the Strouhal number (St_B) with the increase in aspect ratio well, which is in accordance with experimental findings.

To summarize the section on the validation of the LES and DES turbulence models on the flow around rectangular sections, two basic flow parameters, the Strouhal number and the drag coefficient of the cylinders from *B/H*=1 to *B/H=8* have been compared to various experimental data [23, 50, 58, 86, 92, 94, 95, 121, 126]. Figure 5.17 shows the simulated and measured Strouhal number of the cylinders with increasing aspect ratio.

Three significant trends (denoted by the blue dotted lines) have been noted as the aspect ratio increases (Figure 5.17). There is an obvious change known as the discontinuity of the Strouhal number between the dotted lines. The first discontinuity occurs between a *B/H=2* and a *B/H=3* cylinder. This arises due to the changes from separated type of flow to reattachment type of flow on the side surface of the cylinder, thereby affecting the rate at which vortices are shed and thus the Strouhal number. The second discontinuity happens between cylinder with aspect ratio *B/H=5* and *B/H=6*, the changes are attributed to the increase of the number of vortices convecting along the surface of the cylinder. Similarly, the additional vortex changes the Strouhal number by affecting the way in which vortices are shed from the trailing edge. As seen from Figure 5.17, the changes of Strouhal number with aspect ratio have been well predicted by LES and DES.

Figure 5.18 shows the changes of the drag coefficient around the rectangular sections with the increase in the aspect ratio of the cylinder. Research work [92, 127] concluded that drag coefficient is directly related to the base suction pressure in the wake region of the cylinder. Greater suction corresponds to higher drag force on the cylinder. As the afterbody length increases, the effect of the base suction decreases (section 5.1.1). Also, frictional effect contributes to the increase of the drag force as

aspect ratio increases. This explains the steady decrease of the drag coefficient in Figure 5.18. Generally, good agreement has been observed from the simulated results. The slight discrepancies observed are due to the different Reynolds number used in the simulated and the measured data. Different discretisation schemes employed in LES and DES also contribute to the discrepancy in the results (*B/H=8*). For *B/H=5* to *B/H=8* cylinder sections, fewer experimental data are available so some numerical results have been included for comparison.

Moment plays an important role in the aerodynamics of rectangular cylinders. Pitching moment (moment acting with respect to the spanwise axis of the flow) comes into play as a result of different pressure distribution on the top and bottom surface of the cylinder. The pressure distribution introduces lift force which effectively places a torque or moment on the cylinder. This effect is significant at higher aspect ratio such as *B/H=8*.

If the structure is not restraint, existence of the pitching moment could change the angle of attack of the incoming wind and the flow structure around the cylinder. This might lead to the aeroealastic instabilities mentioned in Chapter One. Thus, further investigation on the angle of attack of the flow around rectangular cylinders should be carried in the parallel projects within the same research group. If the structure is long and slender, such as long span bridges, torsional moment will be induced. This is the moment subjected to the twisting of the structure enveloped in the flow due to wind load which could result in the torsional divergence instability. The author is aware of the sensitivity of the flow around bluff bodies and bridge deck sections to the angle of attack but current project only investigated flow with zero angle of attack. Various angles of attack of flow should be further investigated in the future work.

5.2.4 Comparison between LES and DES

All the simulation work previously presented in this chapter on the flow around rectangular cylinders involves validation of the LES and the DES through the comparison of the computed results with experimental data. Both simulations gave good predictions. In order to investigate the suitability of the models on the application of the flow around a bridge deck section, the computed results from both the LES and DES are compared and discussed here. The comparison first investigates the capability of the models to predict flow distribution, particularly the vortical structures around the cylinders. Apart from comparing the simulating capability of LES and DES, the

computational time needed for the models has been recorded. DES should need less computational time than LES due to the usage of a RANS model around the near wall region of the cylinders. This appears to be the advantage of DES when simulating flow at high Reynolds number.

For cylinders with higher aspect ratios, comparison between LES and DES focuses on the vortex structures along the side surface of the cylinders. As discussed in the previous section, interaction of the vortices around the cylinders significantly affects the aerodynamic forces induced on the sections. From the plot of the time history of the lift and drag coefficients of LES and DES at the same Reynolds number (Figure 5.19), we observed that LES actually predicted a more random fluctuation of lift and drag while DES gave very regular changing pattern of forces around a *B/H=4* rectangular cylinder. This is because DES employs SST model near the wall of the cylinder while LES computes the flow directly above the filter length scale. SST is a RANS model which computes the average flow and averages the unsteadiness to give a regular pattern of forces as observed in Figure 5.19. Physically, the randomness of the flow predicted from LES is clearly visible on the plot of the velocity streamline and pressure compared to DES prediction (Figure 5.20 and 5.21). Relatively more complex and more intense vortex interaction is predicted by LES compared to DES.

This suggests that LES gives a more 'realistic' prediction of forces acting on the cylinder when complex flow with vortex interaction is involved. This is important in the application of the flow around a bridge deck section where vortical structures play a major role in generating the vortex induced forces. When comparing the result of LES and DES of the flow around a *B/D=8* rectangular cylinder, a similar pattern of irregular and random fluctuation of forces has been observed from LES. LES even successfully predicted the two peak power spectrum indicating two different shedding frequencies of the vortices, which agreed with the observation of other experimental work. DES only computed a single frequency shedding mode. As a conclusion, LES gives more accurate representation of complex flow situation compared to DES. Yet one has to consider the computational cost and simulation time needed for LES at higher Reynolds number. The issue of computational time for LES and DES is discussed next.

5.2.4.1 Computational time for LES and DES

The simulation of the flow around rectangular cylinders discussed in this chapter has been done on a parallel computing system consisting of clusters of PC units running on

Linux. DES has been known for its computational efficiency compared to LES [115]. In the following, the computational time for both models is compared. Comparison starts with low Reynolds number (*Re 3,000*) simulation on rectangular sections with increasing aspect ratio. This is followed by higher Reynolds number (*Re 14,000*) case of the flow around a square section with different meshes (coarse and fine meshes).

Figure 5.22 shows the CPU time (in minutes) needed for the simulations around a *B/H=2*, a *B/H=4* and a *B/H=8* cylinder at Reynolds number of *3,000*. The CPU time here refers to the time in minutes required for one CPU to compute a time step in a simulation. To provide the reader with an idea on the average running time for the simulations discussed, two cases are chosen as representation for the LES and the DES. From Figure 5.22, LES on a *B/H=8* cylinder at Reynolds number of *3,000* needed *9.5* CPU time for a *12,000* time steps simulation (flow around the simulated Reynolds number mentioned in this chapter usually need *12,000* to*15,000* time steps to get a statistically converged solution). This is equivalent to *80* days of simulation time. If *12* processors unit on the parallel computer are used to simulate the case, it will take *6.6* days of computational time. Whereas for DES, the time taken for the same Reynolds number simulation is *6.4* CPU time which is equivalent to *4.4* days of simulation time. The cost per node per iteration for LES and DES are 6.13×10^{-5} and 6.30×10^{-5} respectively. This suggests that additional computational cost of LES is mainly induced by higher number nodes required for the simulation. DES is about *34%* (for the two cases mentioned above) cheaper because the use of a hybrid turbulence approach allows for a lower nodes number.

In terms of the non-dimensional timestep as defined in Eq. 3.4, simulations of the flow around rectangular cylinders in this chapter ranges between $0.04 < \Delta t^* < 1.2$. Physically, this equals to the timestep of *0.00007 and 0.003* respectively. The timestep is calculated such that roughly *30-50* steps are required to compute one vortex cycle in the flow.

The number of elements used for each simulation in Figure 5.22 is shown on Figure 5.23. From the figures, it can be seen that increasing the number of elements causes a nearly proportional increase in the CPU time needed for a simulation at same Reynolds number of *3,000*. This has been observed for both LES and DES. This is further demonstrated by comparing the simulation time for a square cylinder (Chapter Four) with different meshes at Reynolds number of *14,000* (Figure 5.24). From Figures 5.22 and 5.24, it can be seen that increasing of the aspect ratios has no influence on the computational time required for the simulations. The number of elements used in the

simulation is the major deciding factor for the computational time needed. Figure 5.25 shows the number of elements used for each simulation of the flow around a square cylinder in Figure 5.24.

Comparison between Figures 5.22 and 5.24 indicates that the time required for LES increases dramatically compared to DES as the Reynolds number increases. DES is nearly two times faster than LES at Reynolds number of *14,000*. Comparatively, DES is a more suitable model for the simulation of the flow around a bridge deck of the wind tunnel scale (*1:40*) compared to LES due to it computational efficiency. This is because the Reynolds number involved in the wind tunnel test is several times higher than cases on the rectangular sections discussed in this chapter so far. Next section contains study on the flow around rectangular sections at higher Reynolds number close to the range of the flow around a bridge deck section. The effect of computational time at these Reynolds numbers will also be discussed.

5.3 DES AT HIGHER REYNOLDS NUMBER

From the study of the flow around bluff bodies in the previous two chapters, it is concluded that DES is a more suitable model for the simulation of flow around a bridge deck section compared to LES, thus DES is used to simulate flow at much higher Reynolds number close to the Reynolds number of the flow around a bridge section in the wind tunnel test. This is within the range of *Re 30,000* to *Re 80,000*. Two cases have been simulated on the high Reynolds numbers range, a *B/H=4* cylinder and a *B/H=8* cylinder. The Reynolds numbers simulated are at *42,800* and *100,000* respectively. A *B/H=8* cylinder is chosen as the aspect ratio is similar to the bridge deck section of the wind tunnel test.

5.3.1 Strouhal number and drag coefficient

For the case of a *B/H=4* cylinder, the result has been compared to other experimental findings and numerical solutions at similar Reynolds number. Tables 5.3 and 5.4 show the comparison of the simulated and experimental results of the Strouhal number and the drag coefficient of the flow respectively at a Reynolds number of *42,800*. Although some discrepancies have been observed among the experimental and simulated results from other researchers, the simulated result from DES are close to the solutions of the work compared.

To investigate the ability of DES in predicting the vortex distribution at high Reynolds number, the recirculation length and the reattachment point (Tables 5.5 and 5.6) of the simulation on the *B/H=4* cylinder has been compared to experimental data from Mizota and Okajima (1981) [79] at the same Reynolds number. Numerical simulations [106, 144] at similar Reynolds numbers has been included for an overview of the value of the compared parameters. Generally, the predicted results are within published data (Tables 5.5 and 5.6). This suggests that DES is capable of predicting the formation and size of the separation bubbles well at high Reynolds number.

Table 5.3 Comparison of simulated and measured Strouhal number of a *B/H=4* cylinder at high Reynolds number.

Reynolds number	**Other work (Strouhal no.)**	**DES (Strouhal no.)**
100,000	*0.16* Num. Yu *et al.* '98	-
60,000	*0.13* Exp. Nakaguchi *et al.* '68	-
42,800	*0.12* Exp. Mizota *et al.* '81	*0.15*
22,000	*0.14* Num. Shimada *et al.* '02	-
10,000	*0.14* Num. Tamura *et al.* '96	-

For a *B/H=8* cylinder, simulation has been done at a Reynolds number of *100,000*. Again, this has a similar objective to the case of the previous *B/H=4* simulation, but at higher Reynolds number with aspect ratio closer to the sectional wind tunnel test of the bridge deck section. Another purpose of the simulation is to investigate the computational time of simulation. This helps to provide an idea on the time required for the simulation of the flow around the bridge deck section, which needs a lot more

elements compared to the rectangular sections discussed in this chapter so far. The closest experimental data available for comparison is the measurement from Okajima (1983) [94] at a Reynolds number of *42,000*. From his work, a Strouhal number of *0.153* has been measured. DES computed a value of *0.150* (Table 5.7). No experimental measurement of drag force is available at this high Reynolds number so comparison has been made with the simulated results. The computed drag coefficient of DES (C_d=*1.18*) shows close agreement to the simulated result of Shimada *et al.* (2002) (C_d=*1.10*) as shown in Table 5.8.

Table 5.4 Comparison of simulated and measured drag coefficient of a *B/H=4* cylinder at high Reynolds number.

Reynolds number	**Other work (C_d)**	**DES (C_d)**
100,000	*1.30* Num. Yu *et al.* '98	-
60,000	*1.21* Exp. Nakaguchi *et al.* '68	-
42,800	*1.15* Exp. Otsuki *et al.* '78	*1.28*
22,000	*1.10* Num. Shimada *et al.* '02	-
10,000	*1.23* Num. Tamura *et al.* '96	-

Table 5.5 Comparison of simulated and measured recirculation length (on top and bottom surface) of a *B/H=4* cylinder at high Reynolds number.

Reynolds number	**Other work (recirculation length)**	**DES (recirculation length)**
42,800	*3.00* Exp. Mizota *et al.* '81	*2.89*
100,000	*2.72* Num. Yu *et al.* '98	-
22,000	*3.10* Num. Shimada *et al.* '02	-

Table 5.6 Comparison of simulated and measured reattachment point of a *B/H=4* cylinder at high Reynolds number.

Reynolds number	**Other work (reattachment point)**	**DES (reattachment point)**
42,800	*1.70* Exp. Mizota *et al.* '81	*1.55*
100,000	*1.53* Num. Yu *et al.* '98	-
22,000	*1.80* Num. Shimada *et al.* '02	-

Table 5.7 Comparison of simulated and measured Strouhal number of a *B/H=8* cylinder at high Reynolds number.

Reynolds number	**Other work (Strouhal no.)**	**DES (Strouhal no.)**
42,000	*0.150* Exp. Okajima '82	*0.153* *(Re 100,000)*

Table 5.8 Comparison of simulated and measured drag coefficient of a *B/H=8* cylinder at high Reynolds number.

Reynolds number	**Other work (C_d)**	**DES (C_d)**
22,000	*1.10* Num. Shimada *et al.* '02	*1.18* *(Re 100,000)*

5.3.2 Computational time

In terms of the computational time for the higher Reynolds number simulations, comparison has been made for cases with Reynolds number of *42,800* and *100,000*. Both simulations have similar numbers of elements but the latter has a coarser mesh in the far wake region, which will not affect the solution by much. The purpose is to investigate the effect of Reynolds number on the computational time.

Figure 5.26 depicts the computational time for the DES cases for the flow at Reynolds number of *42,800* and *100,000*, with the estimated time required if LES is used instead. The estimation has been made based on the comparison of LES and DES cases from the rectangular cylinder simulations at lower Reynolds number. The observation demonstrates the practicality of DES at high Reynolds number compared to LES. For instance, previous discussion mentioned that LES required *6.5* days of computational time for a Reynolds number of *3,000* simulation, however *35* days (notice the increase of the y-axis value compared to that in Figures 5.22 and 5.24) of computational time on *12* processors has been estimated for LES for the Reynolds number of *100,000* case (this estimation has been done based on linear extrapolation of the previous simulations considering the Reynolds number and number of elements employed). This might be slightly impractical for the current project, bearing in mind that even longer time will be needed if LES is applied on the simulation of the flow around a bridge deck section. On the other hand, DES requires *17* days for the same simulation at Reynolds number of *100,000* compared to LES. Thus, DES is suitable for the simulation of the flow around a bridge deck section.

Overall, analysis in this section has demonstrated the capability of DES in capturing flow parameters such as the Strouhal number and the drag coefficient that are

in agreement with other researchers' findings at Reynolds numbers near to the flow around a bridge deck section (model scale).

5.4 PRESSURE AND VORTICES AROUND RECTANGULAR CYLINDERS

As discussed, vortex formation and progression induce forces on the bodies enveloped in the flow. A vortex creates a negative pressure suction area adjacent to the surface where it progresses. Thus the study of pressure distribution is important in the analysis of the aerodynamic forces around a structure. The following section describes the application of a mathematical technique known as principal component analysis (PCA) on the analysis of the pressure distribution around a *B/H=4* and a *B/H=8* rectangular section.

5.4.1 Principal Component Analysis (PCA)

In the study of the pressure fluctuation around bluff bodies using PCA, Holmes (1990) [47] pointed out that the covariance matrix of the pressure fluctuation contains information on the magnitude and distribution of the underlying fundamental modes of the pressure distribution around a body. Studies show that these modes are represented by the eigenvectors of the corresponding covariance matrix of the pressure distribution on the body's surface.

PCA aims to simplify complex data by reducing its dimensionality to extract the major features within the data. This is done by rotating the data such that the maximum variability is projected onto the new axes. Physically, a set of correlated variables are transformed into a set of uncorrelated data on a new coordinate system arranged in decreasing variance.

The new series of data are termed the principal components of the PCA. The first principal component gives the greatest amount of variation among the components, followed by the second principal component with the next largest percentage of total variance. By doing so, the redundancy contained within the data can be reduced without losing much of the information of the original data.

Mathematically, to perform PCA on a data set x, the eigenvalues, λ_i and the eigenvector, e_i [55] of a covariance matrix C_x can be evaluated from the solution of [47]:

$$C_x e_i = \lambda_i e_i \qquad \text{Eq 5.1}$$

The eigenvalues is calculated as the roots of,

$$\left|C_x - \lambda_i I\right| = 0 \qquad \text{Eq. 5.2}$$

where $i \in [1, 2, \ldots, n]$, n is the total number of the input data and I is the identity matrix. The eigenvalues are associated with the variance of each of the components [22]. Each eigenvalue is accompanied by an eigenvector, the nonzero vector e_i that satisfies Eq. 5.1.

The principal components of PCA are made up of columns of the eigenvectors of the covariance matrix C_x. By arranging the eigenvectors in the order of descending eigenvalues ($\lambda_i > \lambda_{i+1} \ldots$), one gets the most significant changes of the variables in the data in the first principal component. Normally, the first few principal components retain more than *90%* of the total variation of the original data, thereby reducing the number of variables in the data making it much easier to analyse. The principal components are mutually orthogonal and independent to each other.

In PCA, the variables x are decomposed in the process of the eigenanalysis. It is possible to regenerate the variable x using the PCA results as follows:

$$x = A^T Y + \mu_x \qquad \text{Eq. 5.3}$$

where A^T is the transpose matrix whose columns are given by the eigenvector of the covariance matrix and Y is the coefficients of the principal components. μ_x is the mean value of the data set x. From Eq 5.3, the original data can be reconstructed from the terms on the right hand side of the equation to see how well the original data can be represented from the first few principal components in the analysis. This will be discussed in the next section.

Baker (2000) [6] adopted a similar technique known as the proper orthogonal decomposition (POD) to study the fluctuating pressure field around a wall, a cube and a building. Full scale experimental data was compared to the analytical result from the POD to identify the physical mechanisms that associate with the eigenvector mode shapes. In the analysis, the pressure fluctuation was expressed as the multiple of spatial and temporal functions which are orthogonal and uncorrelated [7]. Mathematically, the eigenvectors of the pressure coefficient covariance matrix represent the spatial functions which are the corresponding mode shapes of the fluctuating pressure field. The sum of the eigenvalues gives the total variance of the fluctuating pressure and thus represents the total fluctuating energy of the flow. From the study, it was concluded that POD is

capable of representing the pressure field on the surface of a structure through the analysis on a short time series of the flow. This proves helpful in providing insight into the physical mechanism involved in the flow around the structure.

5.4.1.1 PCA on the flow around rectangular sections

In the analysis of the pressure distribution around the rectangular cylinder sections, pressure has been extracted from points around the surface of the cylinder. Since the flow around rectangular cylinders in the current analysis is unsteady and chaotic, it is difficult to determine the dominant trends of the pressure distribution around the cylinder and the aerodynamic force induced. Thus, PCA has been applied to study the pressure distribution around the surface of the cylinder.

The analysis is done based on the procedures outlined in the previous section (section 5.4.1). The major features of the pressure distribution around the surface are identified from the principal components of the analysis. As mentioned, the first principal component corresponds to the eigenvalues with the highest values, which quantifies the largest variation of pressure with respect to the total pressure changes in the flow within the time series considered in the analysis.

The principal components represent the fluctuating nature of the flow. From the plot of the first principal component of the pressure distribution around the cylinder in Figure 5.27, it is noticed that large pressure fluctuation is observed near the trailing edge of the section (top and bottom surfaces). Physically, this indicates the presence of vortical structures at these regions. Similarly, a smaller amplitude pressure distribution is observed near to the leading edge of the cylinder. The near zero pressure at the middle part of the top and bottom surfaces of the cylinder suggests existence of reattachment of flow. All these vortical structures on top and bottom surfaces of the cylinder introduced vertical force on the section. This is discussed in the next section. On the front and rear surfaces, the distribution of the principal component suggests that small vortices are found near to the corners of the cylinder.

Figure 5.28 shows the second principal component of the pressure distribution around the cylinder. Compared to the first principal component, this component has a more even pressure distribution (comparing area on both sides of the x-axis in the graphs) on the top and bottom surfaces of the cylinder. Comparatively, a more intense pressure distribution (judging from the one-sided pressure distribution on the graphs) is

noticed at the front and rear surfaces of the cylinder. This significantly affects the force distribution around the cylinder (see section 5.4.1.2).

From both Figures 5.27 and 5.28, it is noticed that the principal components of the pressure distribution from LES shows larger amplitude (comparing the *y*-axis values on the graphs) compared to the analysis from DES, indicating that stronger vortices have been predicted from LES compared to DES. This agreed with earlier observation in this chapter on the comparison of the performance of LES and DES on the flow around rectangular sections.

Notice that the pressure distribution on the top and bottom surfaces of the cylinder shows different trends in the first principal component compared to the second principal component. A large amplitude pressure distribution appears near the trailing edge (Figure 5.27) of the cylinder in the first principal component. This happens at the middle part of the cylinder in the second principal component distribution (Figure 5.28). Physically, this indicates the movement of the vortex along the cylinder surface. Only two principal components are discussed here, with more components involved, one can extract information on the progression of the vortices along the cylinder. This aids in the understanding of the pressure induced force around bluff bodes and is discussed in section 5.4.1.3.

The first and second principal components of the pressure changes account for more than *85%* of the total changes on the cylinder surface. This is depicted in Figures 5.29 and 5.30, where the eigenvalues of the pressure distribution from LES and DES on the flow around the *B/H=4* cylinders are plotted. This suggests that the analysis of the first and second principal components of the pressure distribution around the cylinder has retained most of the total variance of the pressure field without losing much information.

As mentioned, the original data *x* (which is the pressure distribution in this case) is decomposed in the PCA (Eq. 5.3). To investigate the validity of the application of the PCA on the pressure distribution around the cylinder, the original pressure data before the application of PCA is reconstructed based on Eq. 5.3. The reconstructed data should show close resemblance to the original instantaneous pressure distribution on the cylinder surface. Figure 5.31 shows the reconstructed pressure distribution using the first five principal components of the PCA for both LES and DES. Similar trend has been observed between the original pressure distribution and the reconstructed data.

Following the application of the PCA on the flow around a *B/H=4* cylinder, further investigation has been done on the flow around a *B/H*=8 cylinder. The first and second principal components of the pressure distribution of a *B/H=8* cylinder from LES and DES are depicted on Figure 5.32 and 5.33. Generally, similar vortical structures as the *B/H=4* cylinder have been observed except that more eddies and vortices appear on the top and the bottom surfaces of the *B/H=8* cylinder. Also, LES computed more fluctuating and unsteady pressure distribution with higher magnitude compared to DES, indicating stronger vortices and more complex flow around the cylinder. This observation agreed with earlier findings in section 5.2.4 on the comparison of the flow around rectangular sections using LES and DES.

The eigenvalues plots (Figures 5.34 to 5.35) show that most of the variation (> *82%*) of the pressure distribution of the flow around a *B/H=8* cylinder is contained in the first two principal components of the PCA. However, in the LES the eigenvalues of the first and second principal components of the top and bottom surfaces of the cylinder show very close values. This indicates that these two components are equally dominant with respect to the variation of the total pressure changes. This analysis on the pressure fluctuation and vortex distribution of the flow around a *B/H=8* cylinder provides further insight and understanding on the flow characteristics around a bridge deck section, which has a similar aspect ratio to the cylinder.

5.4.1.2 Pressure force around rectangular sections

In order to investigate the effect of the pressure distribution on the aerodynamic forces around the cylinders, the pressure of the first and second principal components of the *B/H=4* and *B/H=8* cylinders has been integrated to compute the force induced on the cylinder surfaces. Figures 5.36 and 5.37 shows the pressure forces around the *B/H=4* and *B/H=8* cylinders.

Generally, the first principal component of the pressure distribution induces lift force and the second principal component is responsible for the drag force around the cylinder (Figures 5.36 and 5.37). Analysis from the first principal components of the pressure distribution around a *B/H=4* cylinder in the previous section suggests the presence of small vortices near the front and the rear corners of the section. Compared to the larger vortices on the top and bottom surfaces, the force induced by these smaller vortices has less influence, and the overall vertical force induced on the cylinder is dominated by the larger vortices.

From the second principal components of the pressure distribution around a *B/H=4* cylinder in Figure 5.28, it is noticed that both the pressure distribution on the top and bottom surfaces of the cylinder show a more or less balance value (comparing the total area on both side of the *x*-axis of the graphs). On the other hand, the principal components on the front and rear surfaces of the cylinder are distributed only on one side of the graphs. This situation creates pressure force at the front and rear surfaces of the cylinder resulting in the drag force as observed in Figure 5.36. For the force distribution around a *B/H=8* cylinder (Figure 5.37), similar situation has been observed as in the *B/H=4* cylinder.

5.4.1.3 The coefficients of the principal component

In the PCA, changes of the coefficients (*Y* in Eq 5.3) of the principal components with time of the first three principal components from LES and DES of the flow around a *B/H=4* cylinder are plotted in Figures 5.38 and 5.40 respectively. The power spectrum of the coefficients based on FFT analysis are shown in Figures 5.39 and 5.41. Strong dominant frequency has been observed from both of the coefficients, with the first and second principal components showing the same peak frequency. Comparison shows that this frequency is very close to the shedding frequency of the Strouhal number of the cylinder. Thus, the changes of the coefficients can be related to the vortex shedding of the flow. A less significant frequency is observed from the coefficient of the third principal component (Figures 5.39 and 5.41). Physically, this is related to the smaller eddies and scales in the flow accompanying the main vortex mentioned above.

If the distribution of the coefficients from the first and the second principal components are superimposed, one gets an overall representation (since the first two principal components contain more than *85%* of the total variation) of the pressure distribution of the flow. Between the first and the second principal components of the PCA, there is a phase shift involved as time elapses. By examining the overall pressure distribution from the superimposed coefficients of the principal components, information on the vortex progression along the surface of the cylinder can be extracted. This helps in the investigation and understanding of the vortical structures around the cylinder.

From the above analysis, it can be seen that PCA is a useful tool in dealing with complex problem such as the variation of the pressure distribution around the cylinder surface discussed above. The main features of the distribution can be extracted and

represented with reduced dimensionality and complexity. Furthermore, the PCA provides information on the physical mechanisms such as the vortex progression and distribution around the cylinder, as well as the pressure forces induced.

Observation on the applications of PCA on the flow around a *B/H=4* and a *B/H=8* cylinder sections suggests that similar technique is applicable on the flow around the Kessock Bridge deck section. This is crucial since the pressure distribution around the deck section is more complex due to its open cross section shape. Also, the analysis is particularly useful in the study of the response of bridges to wind excitation.

5.4.2 Vortices formation and progression along the cylinders

From the PCA analysis of the pressure distribution discussed above, it is obvious that the pressure affects the forces around the cylinder surfaces. As mentioned, pressure around the cylinder surface varies accordingly with the distribution of vortices. Thus it is important to ensure that the vortex formation and progression on the cylinder surfaces are properly predicted by LES and DES.

Matsumoto (1999) [71] studied the flow around rectangular cylinder sections with various aspect ratios. The work concluded that vortices along the top and bottom surfaces of the cylinder progress at about *60%* of the inlet velocity toward the trailing edge corners. Based on this observation, analysis has been done on the velocity of the vortices' progression predicted by LES and DES on the *B/H=4* cylinder.

In order to compute the speed of the vortices on the surface of the cylinder, the cross correlation of the pressure along the top and bottom surfaces of the rectangular cylinder has been extracted. The cross correlation of the pressure distribution on the surfaces is calculated using the following equation,

$$R_{xy}(m) = E\{x_n y_{n-m}\} \qquad \text{Eq. 5.4}$$

In the equation, x_n and y_n are the variables, which are the sets of pressures extracted from the points along the top and bottom surfaces of the cylinder in this case. n corresponds to the number of points where pressure has been extracted on the surface. $E\{\}$ is the expected value of the terms in the parenthesis. In the calculation, there is a time factor involved in the m term known as the time lag. The time lag provides information on the changes of the pressure from the previous time step onto the current step as time elapses in the flow. Thus, knowledge of the progression of the vortices

along the surface can be extracted from the plot of the time lag against the distance along the cylinder surfaces.

Figures 5.42 to 5.45 show the time lags on top and bottom surface of a *B/H=4* cylinder computed from LES and DES respectively. Physically, a positive *m* in Eq. 5.4 gives a backward shift of the variables involved, as derived in the MATLAB toolbox [70]. Thus the negative lags (Figures 5.42 to 5.45) in the LES and DES predictions indicate movement of the vortices from the leading edge of the cylinder to the trailing edge. Since the graphs of the time lag versus cylinder surface contain information of both time and distance, the speed of the progressing vortices can be obtained from the gradient of the graphs.

Table 5.9 shows the percentage velocities of the vortices progression along the surfaces of the cylinder with respect to the inlet velocities of LES and DES. The values computed are close to the *60%* (with respect to the inlet velocity) observation of Matsumoto experiment [71]. A slight discrepancy has been observed on the values since the cylinders simulated by LES and DES are fixed while Matsumoto worked on moving cylinders. This difference produces no significant effect on the vortex structure around the cylinder but comparison of the aerodynamic induced force between a moving and stationery cylinder should be avoided due to the additional force from the movement of the cylinder. Theoretically, the top and bottom vortex progression computed from the same turbulence model (LES or DES) should be equal. The disagreement observed in the current analysis could be attributed to the fact that the simulated solutions have not yet statistically converged to the desired level, longer simulation time might give closer agreement between the speed of the vortices on the top and bottom surface of the cylinder.

Table 5.9 Percentage velocities (with respect to inlet velocity) of vortices progression on top and bottom surface of a *B/H=4* cylinder.

	LES	**DES**
% of inlet velocity	*57%* Top surface	*64%* Top surface
	55% Bottom surface	*61%* Bottom surface

5.5 CONCLUSION

The study of the flow around rectangular sections provides fundamental understanding of the flow characteristics around the sections and bodies with similar shapes. This also provides insight into the aerodynamic characteristics of the flow around a bridge deck section. Validation of the turbulence models (LES and DES) on the flow around rectangular sections with various aspect ratios has been conducted based on the comparison of fundamental flow characteristics with experimental findings. These include velocity profiles, pressure field and distribution of vortices, as well as the changes of Strouhal number and drag coefficient at different aspect ratios. Generally, good agreement has been observed between the simulated and the experimental data.

Apart from the validation study, comparison has been made between the numerical solutions of the two turbulence models used for the simulations. Observation concluded that DES gives good prediction of the unsteady flow features with reasonable computer power requirement at high Reynolds number. Consequently, DES has been employed to simulate the flow with Reynolds numbers of up to *100,000*. Observations demonstrated the capability of the model in predicting basic flow parameters close to experimental findings at this Reynolds number.

From the work done on the LES and the DES in this chapter, it was concluded that LES is a reliable and an accurate model for unsteady and complex flow simulation. Details of eddies and vortex structures are well captured but a more refine mesh is needed compared to DES. On the other hand, DES shows computer efficiency but good

knowledge on meshing in DES is required to obtain an appropriate solution. The author suggests that application of DES is best accompanied by a LES case as guidelines and reference for the DES solution.

Final section of the chapter discussed the application of the principal component analysis (PCA) on the study of the pressure distribution around the cylinders. The method simplified and identified the dominant pressure distribution on the surface of the cylinder and thus the aerodynamic forces induced. This approach proved fruitful and indicated the possibility of its application on the flow around a bridge deck section in the next chapter where complex flow features with intense vortex interaction is involved. Investigation also focused on the vortices formation and progression along the cylinder surface and analysis concluded that LES and DES have predicted vortical behaviours close to experimental observation.

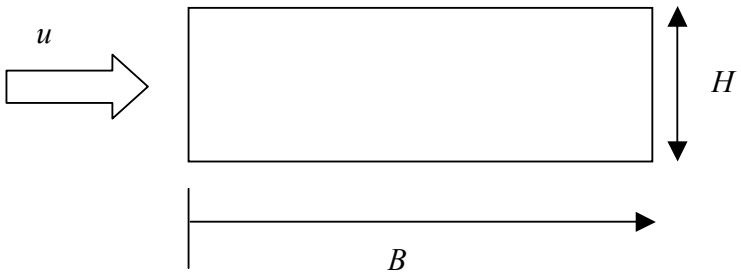

Figure 5.1 The afterbody length of a rectangular cylinder, defined as the ratio of breadth to height (*B/H*) of the cylinder.

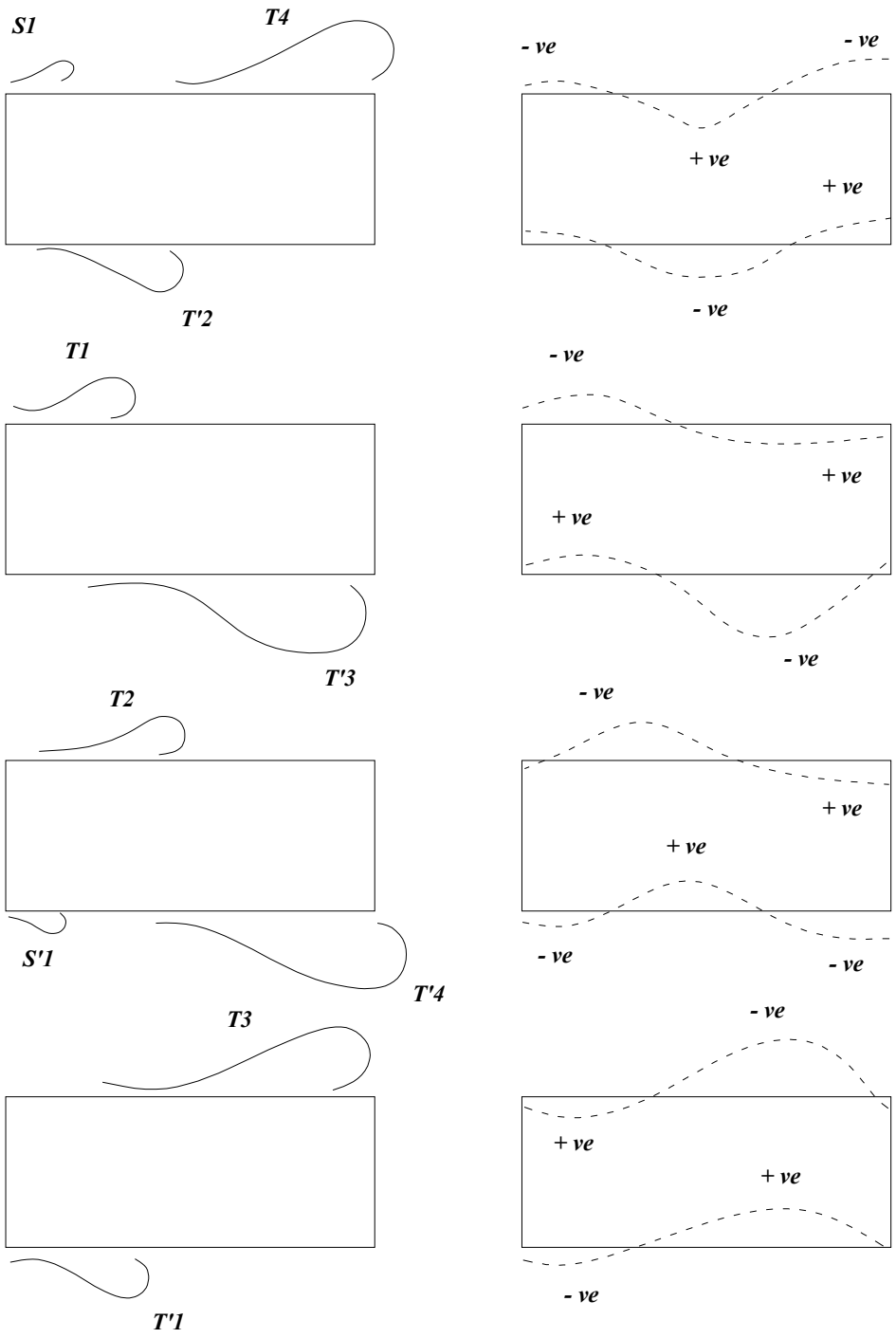

Figure 5.2 Vortices formation and development with pressure distribution around an oscillating cylinder [59].

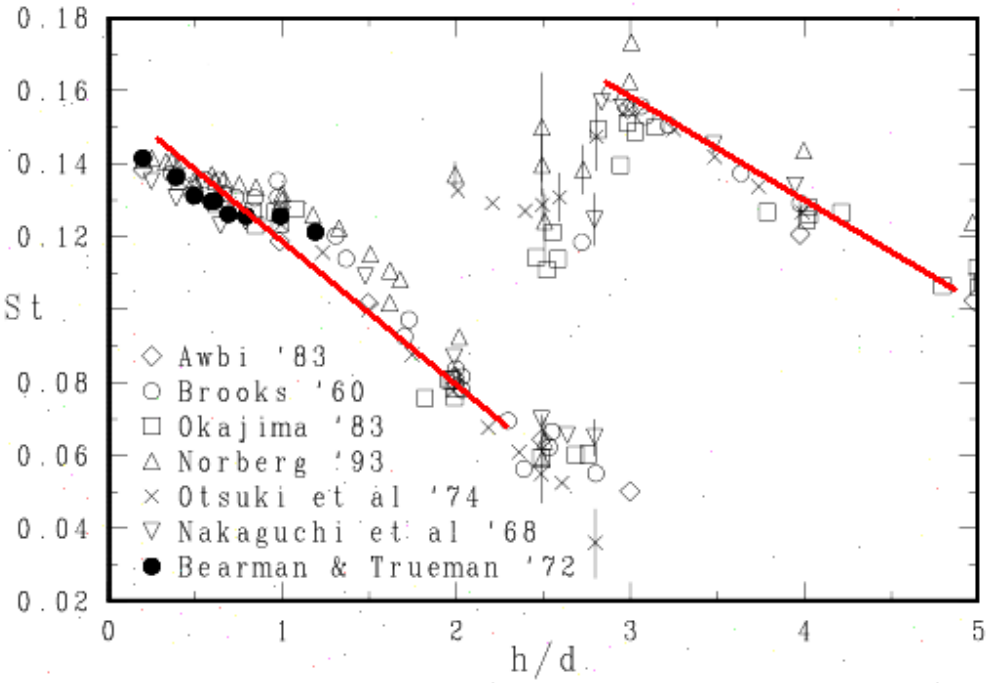

Figure 5.3 Changes of Strouhal number with aspect ratios of the flow around rectangular cylinders from experimental works [112] (h/d = B/H in the context of this chapter), the red lines indicating pattern of changes of Strouhal number.

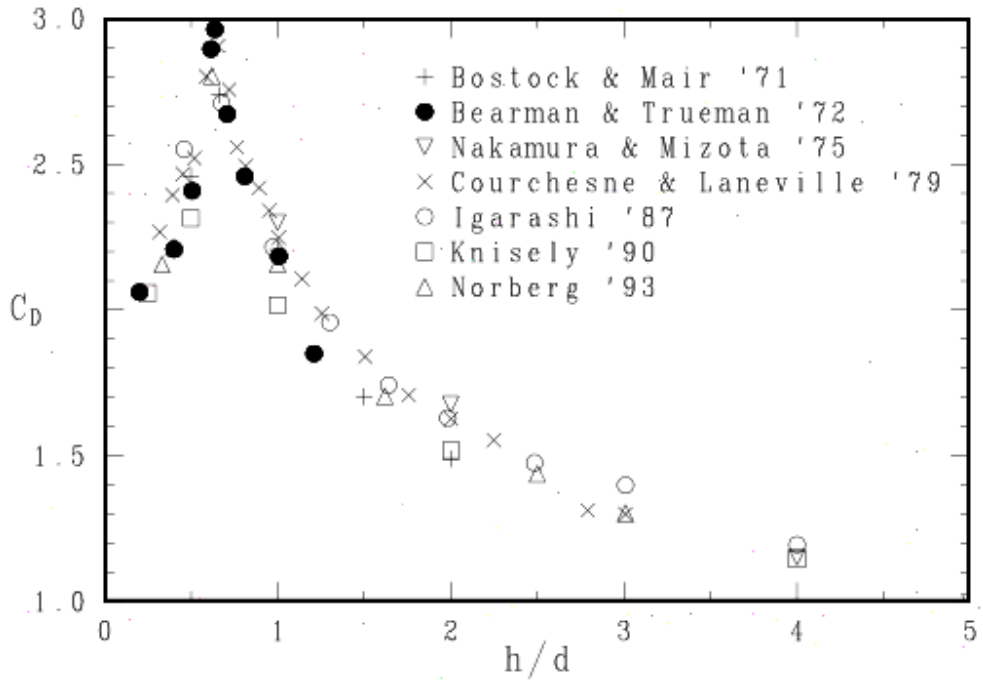

Figure 5.4 Changes of drag coefficient with aspect ratios of the flow around rectangular cylinders from experimental works [112].

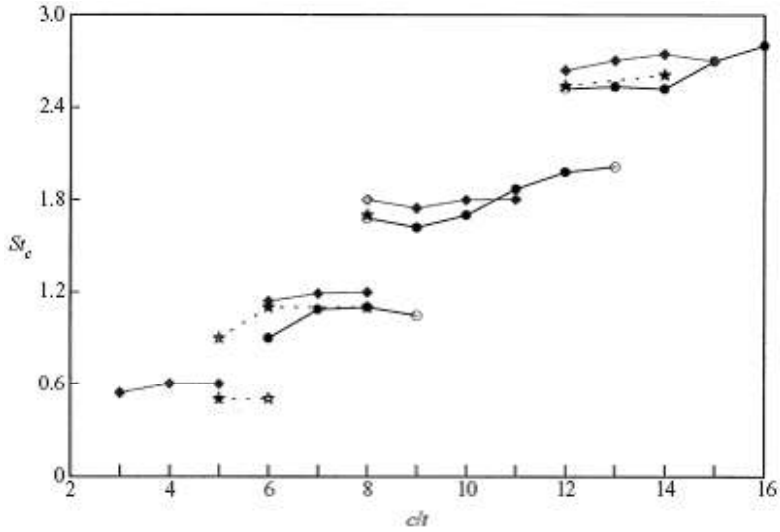

Figure 5.5 Changes of Strouhal number based on breadth of cylinders against B/H ratios [78], ((c/t =B/H in the context of this chapter)♦, Nakamura *et al.* 91' [86], ★, Stokes *et al.* 86' [121], •, Mills *et al.* 02' [78], solid symbols represent primary peaks, open symbols represent secondary peaks).

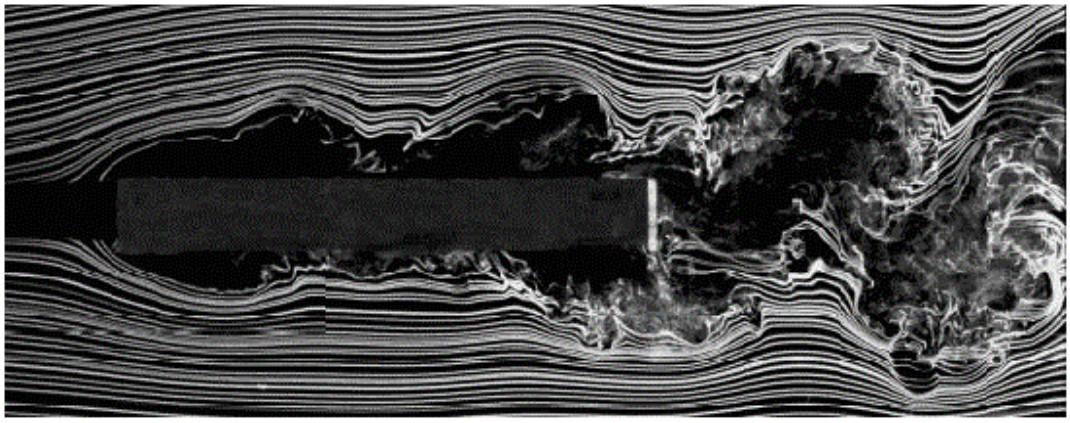

Figure 5.6 Flow visualization of vortices structures on the vicinity of a *B/H=8* rectangular cylinder with *n=2* [78].

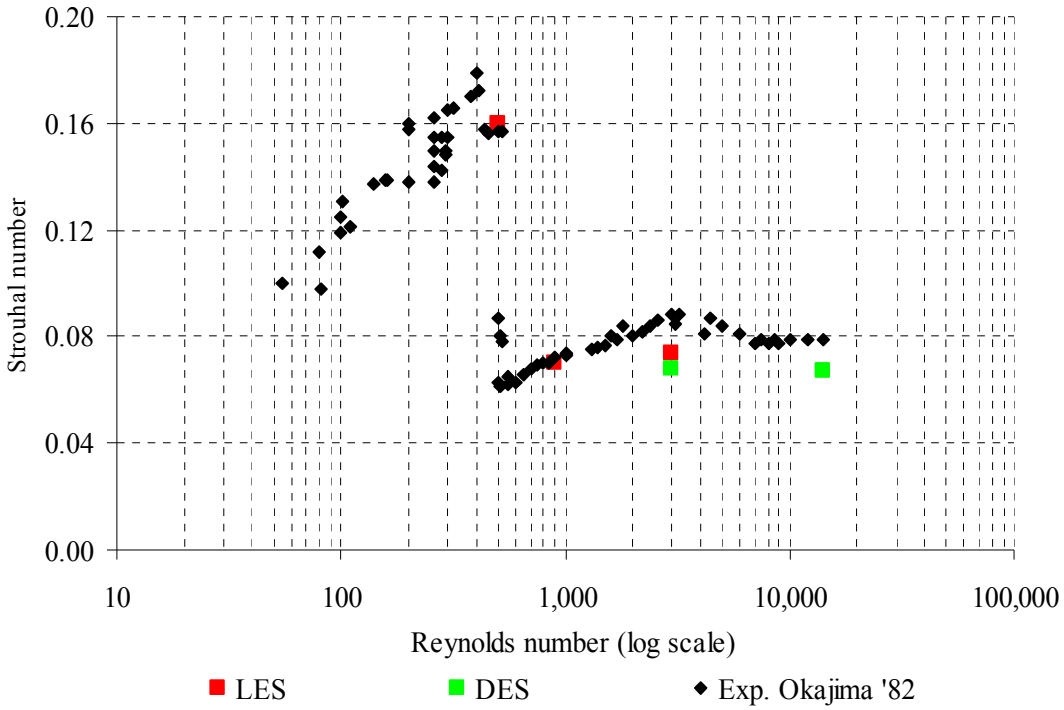

Figure 5.7 Changes of Strouhal number of a *B/H=2* cylinder with increasing Reynolds number.

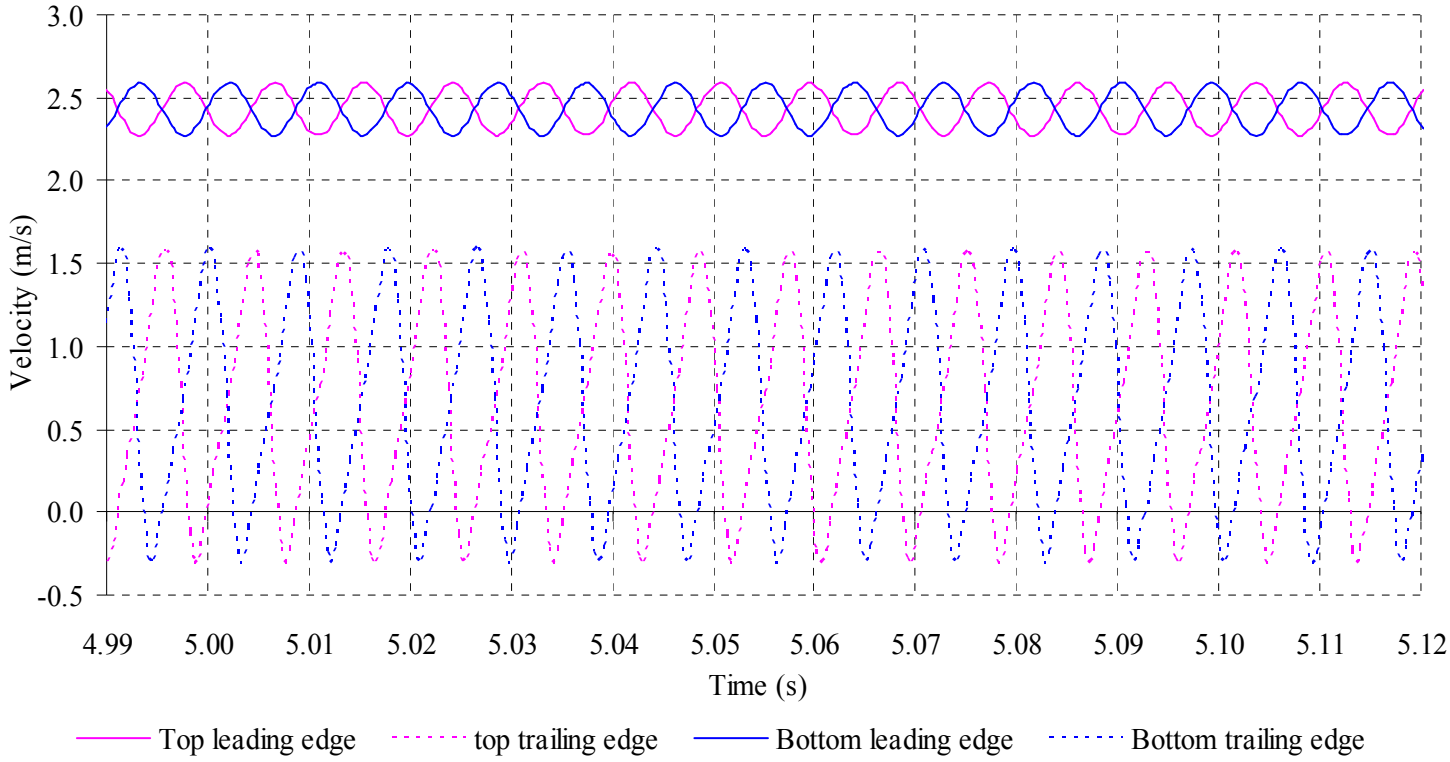

Figure 5.8 Top and bottom mean streamwise velocity of a *B/H=3* cylinder.

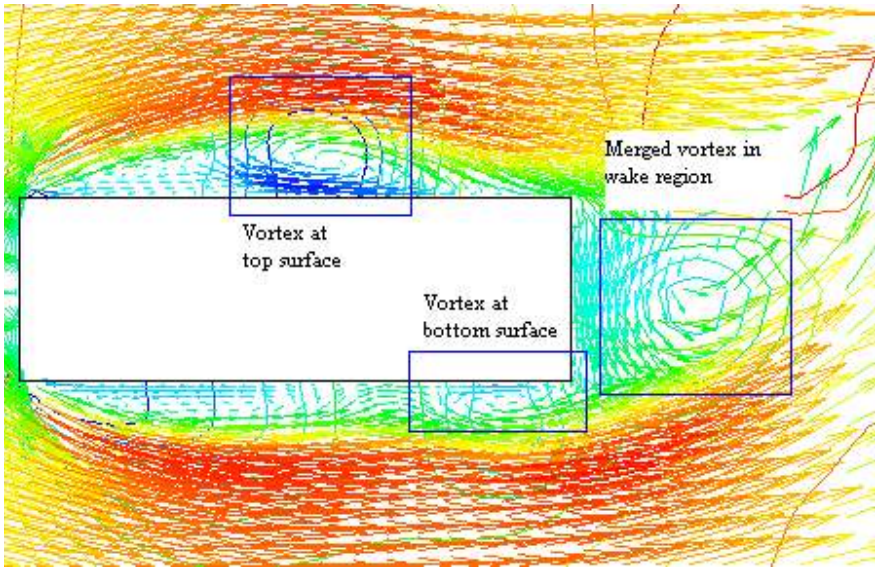

Figure 5.9 Vortices around a of *B/H=3* rectangular cylinder.

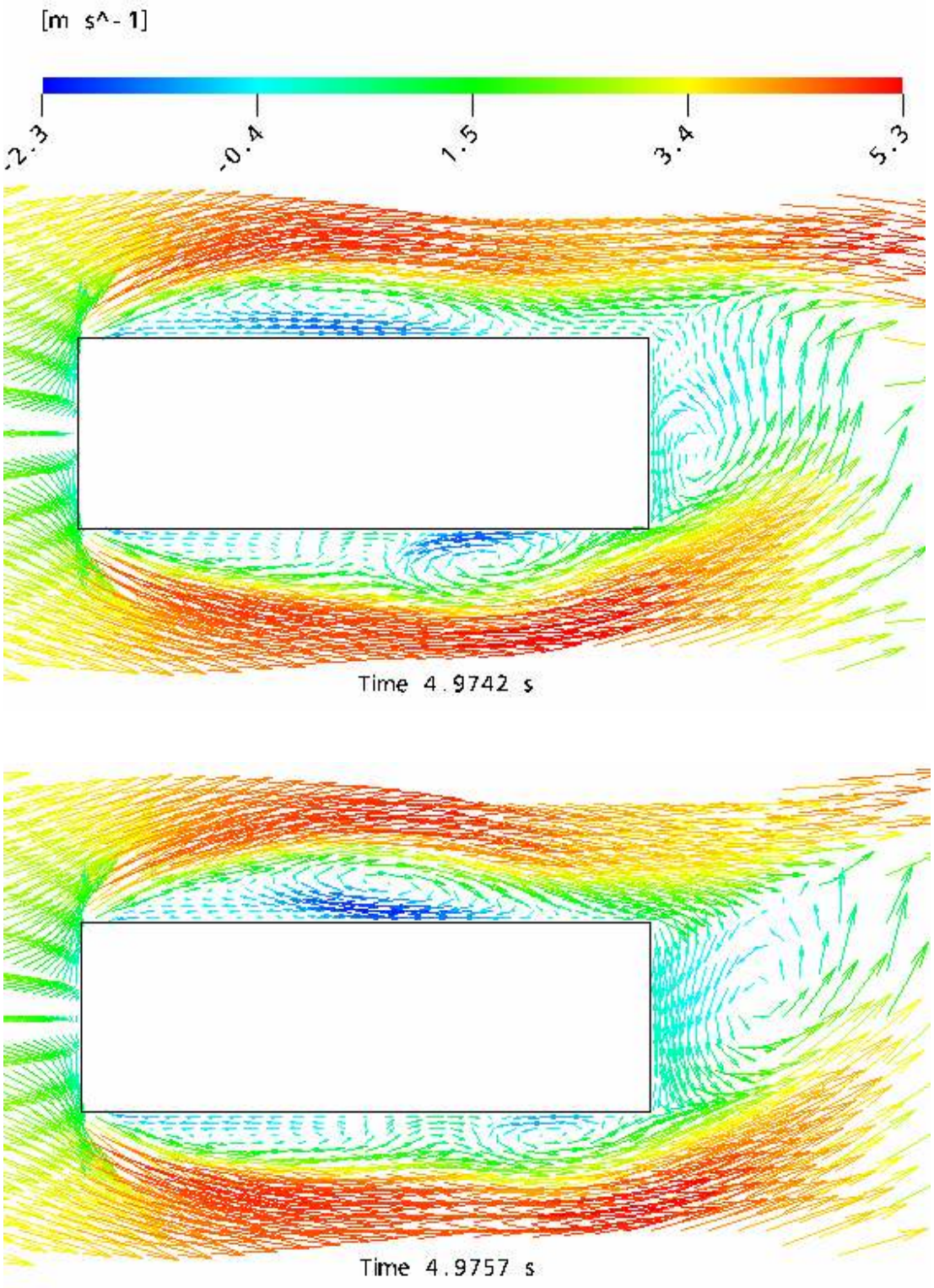

Figure 5.10a Instantaneous streamwise velocity component of the flow around a *B/H=3* cylinder (LES).

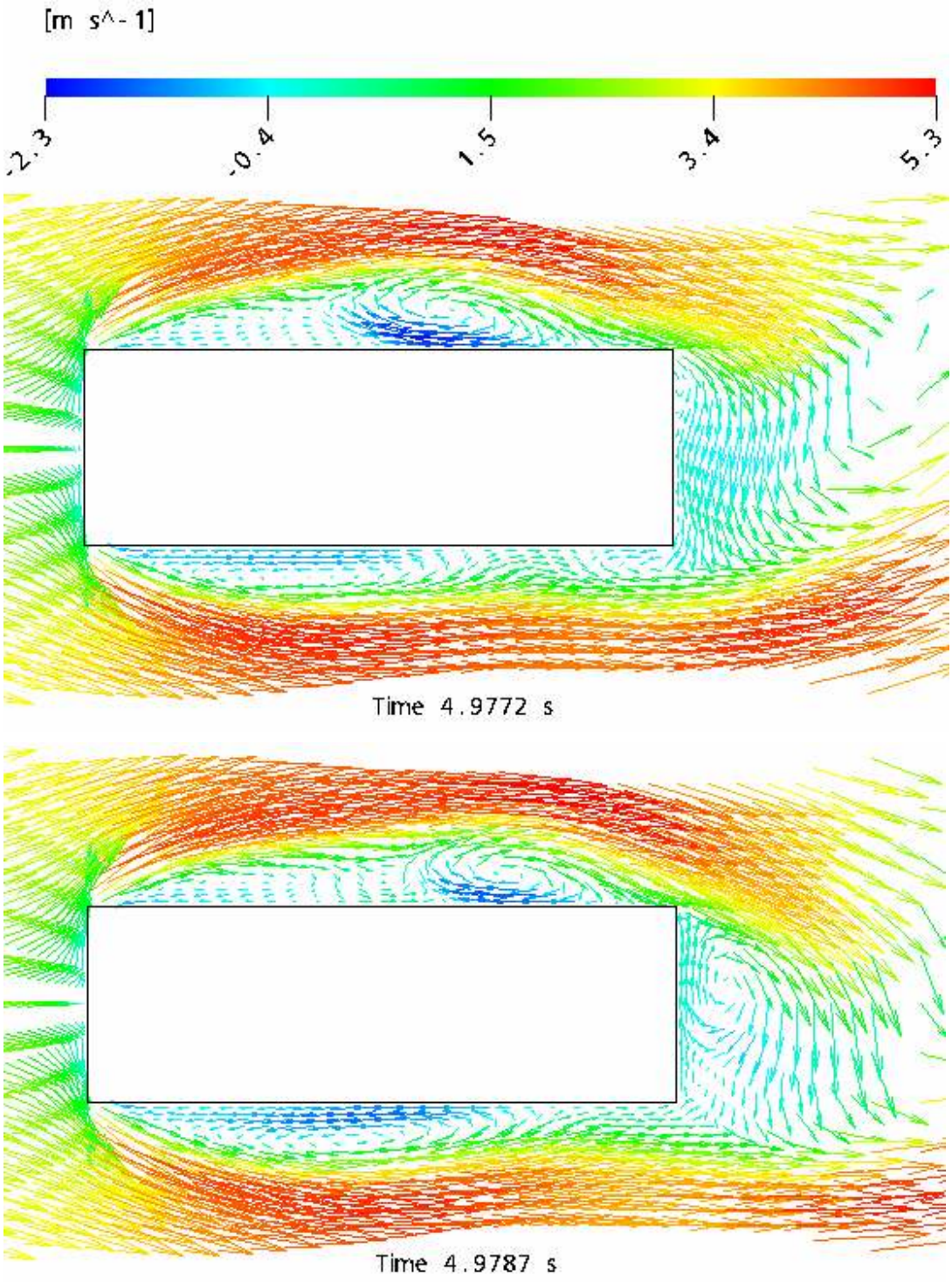

Figure 5.10b Instantaneous streamwise velocity component of the flow around a *B/H=3* cylinder (LES).

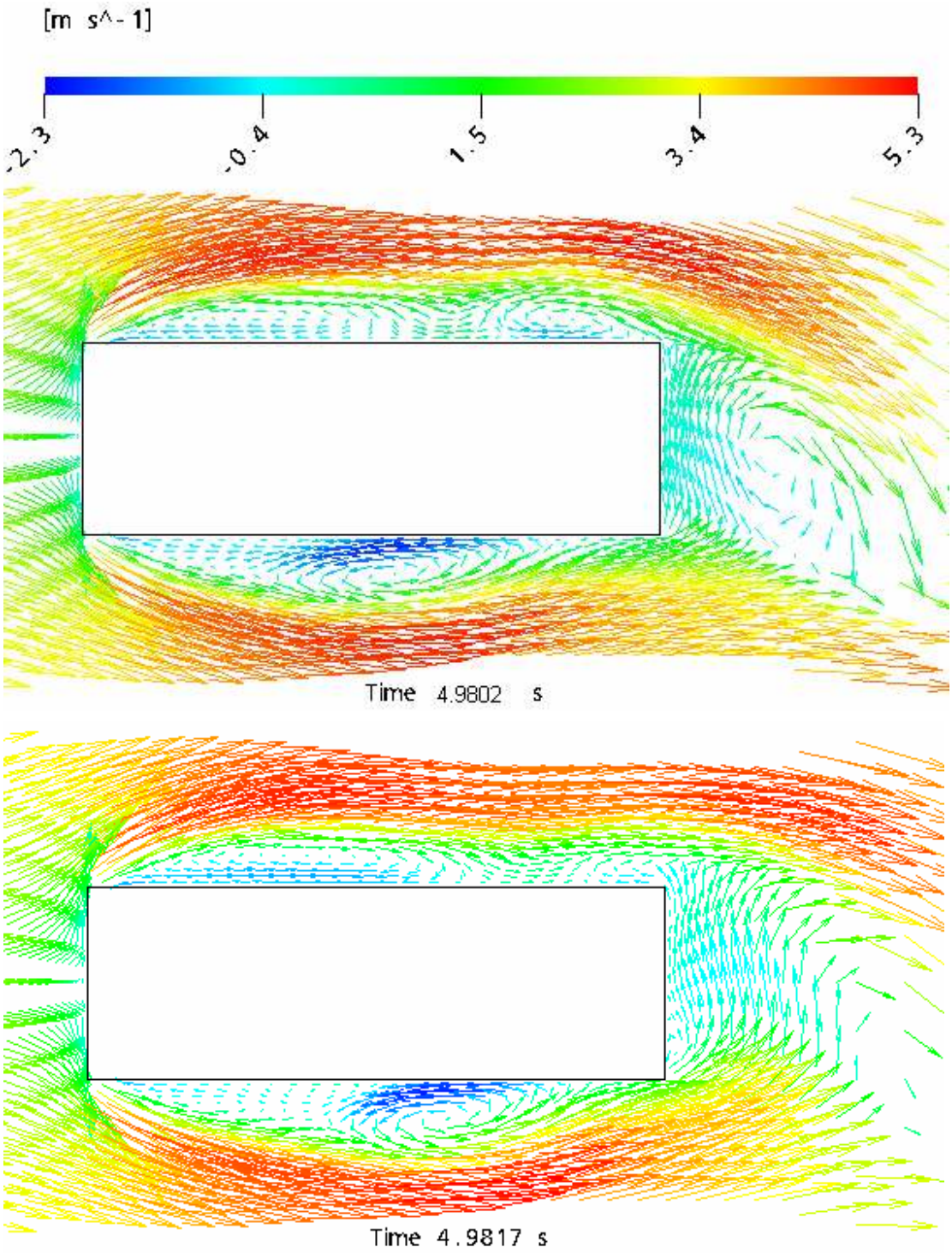

Figure 5.10c Instantaneous streamwise velocity component of the flow around a *B/H=3* cylinder (LES).

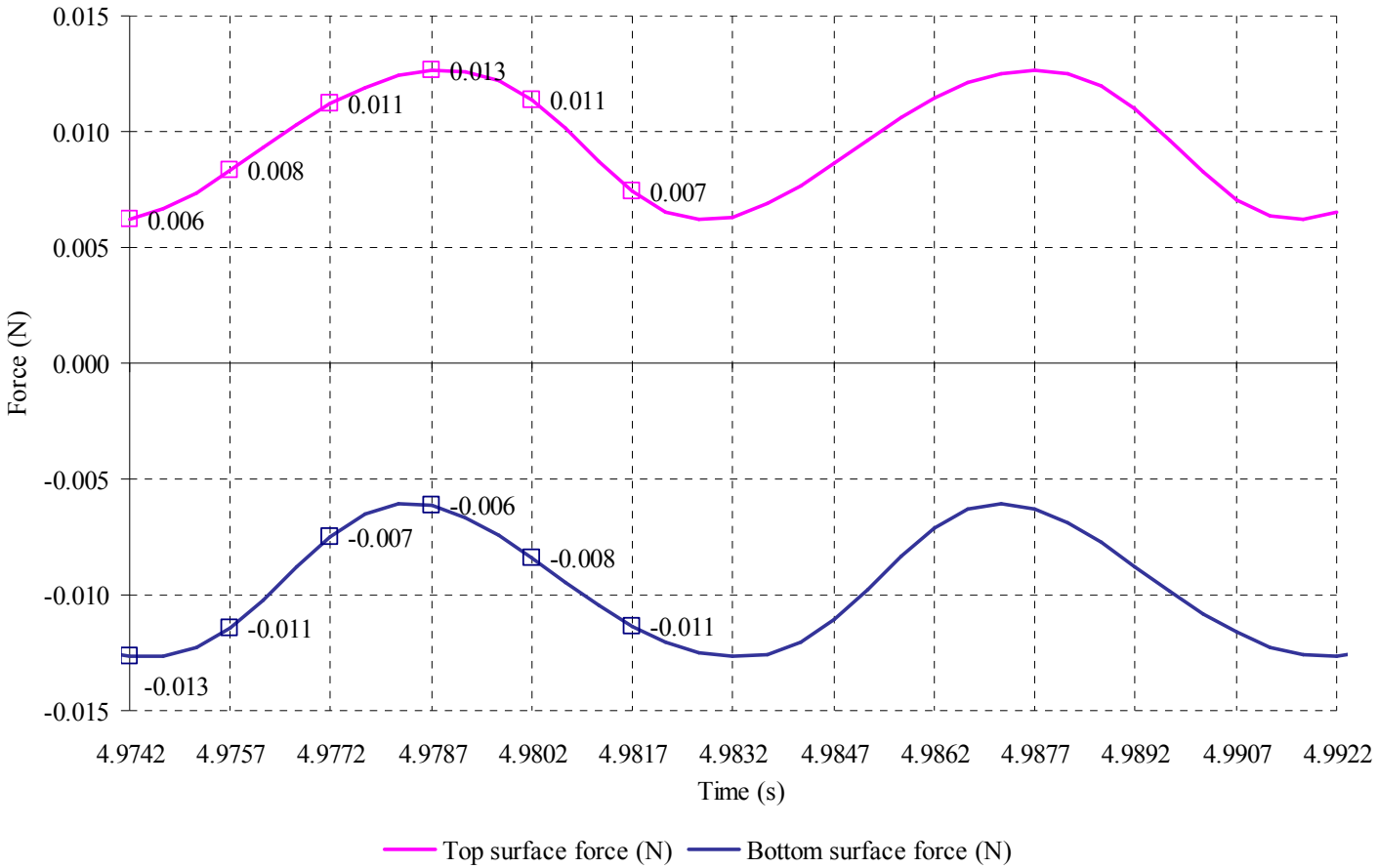

Figure 5.11 Top and bottom surface pressure force acting on a *B/H=3* rectangular cylinder.

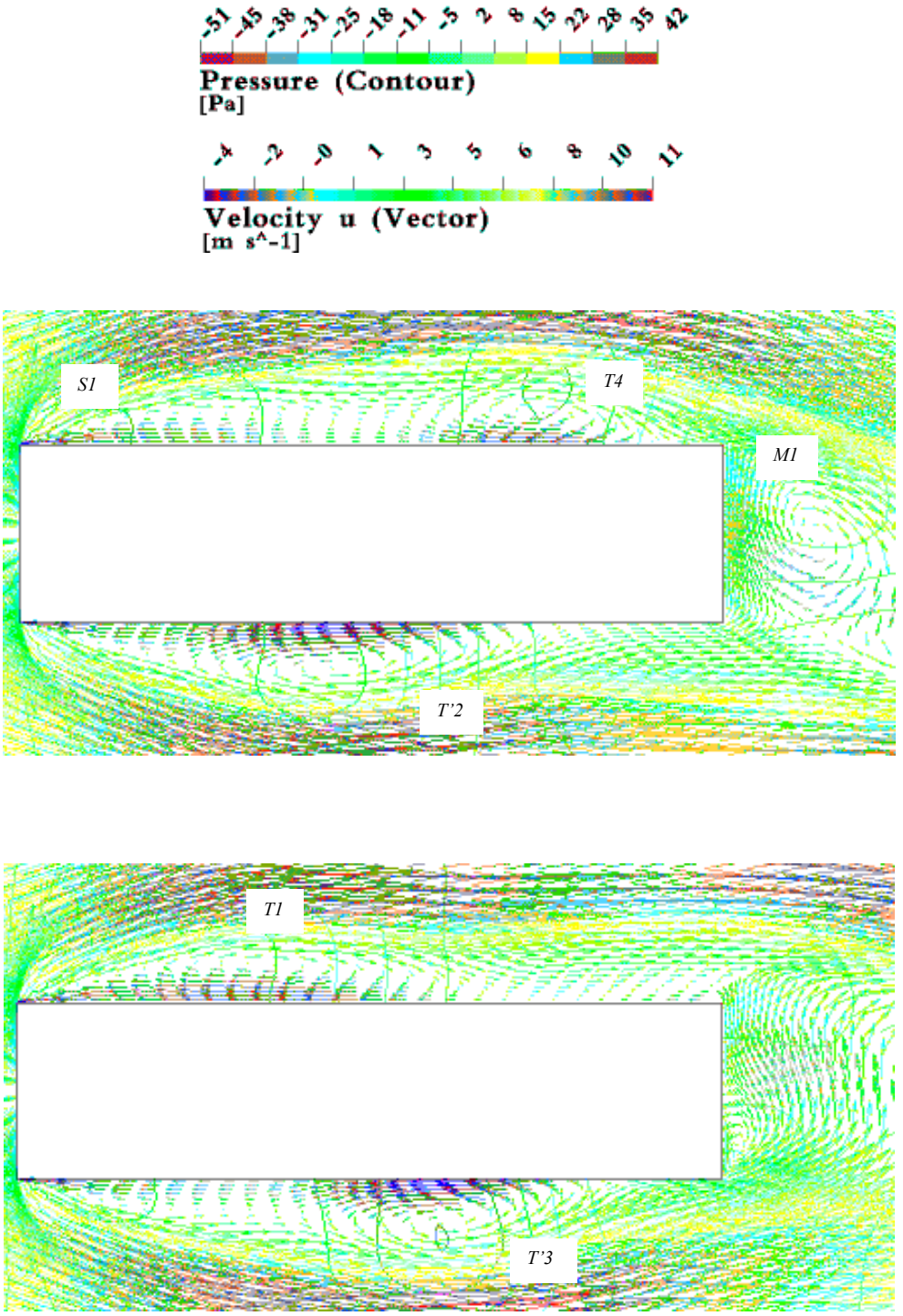

Figure 5.12a Vortex formation and pressure distribution around a *B/H=4* rectangular cylinder at Reynolds number of *3,000* (*DES*)

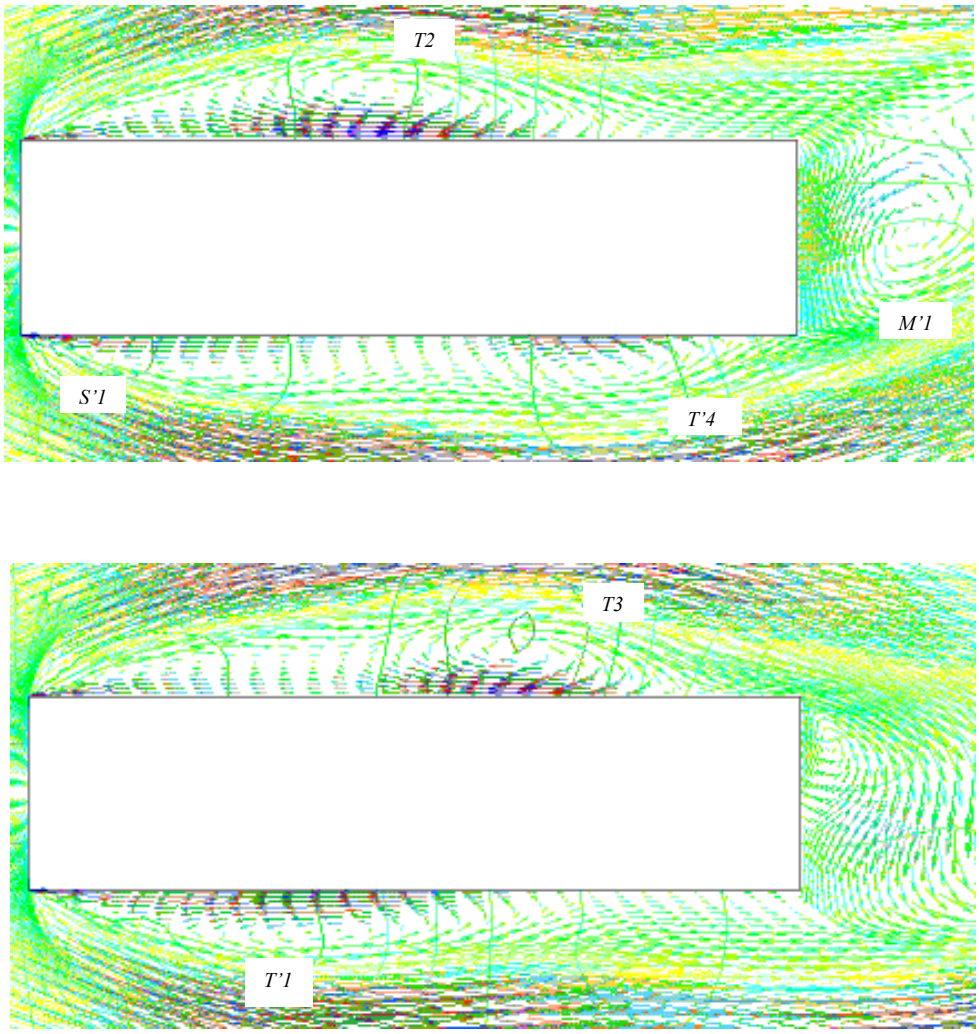

Figure 5.12b Vortex formation and pressure distribution around a *B/H=4* rectangular cylinder at Reynolds number of *3,000* (DES).

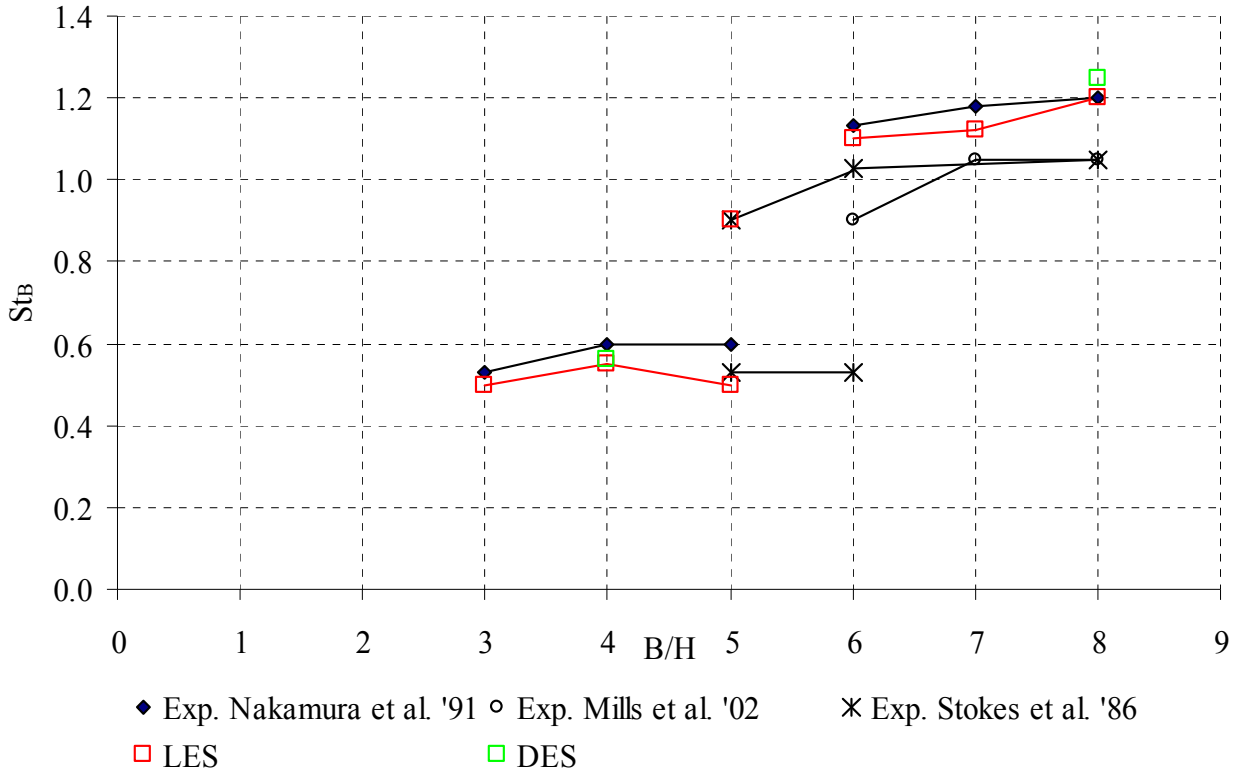

Figure 5.13 Changes of Strouhal number (St_B) of cylinders against increase of aspect ratio.

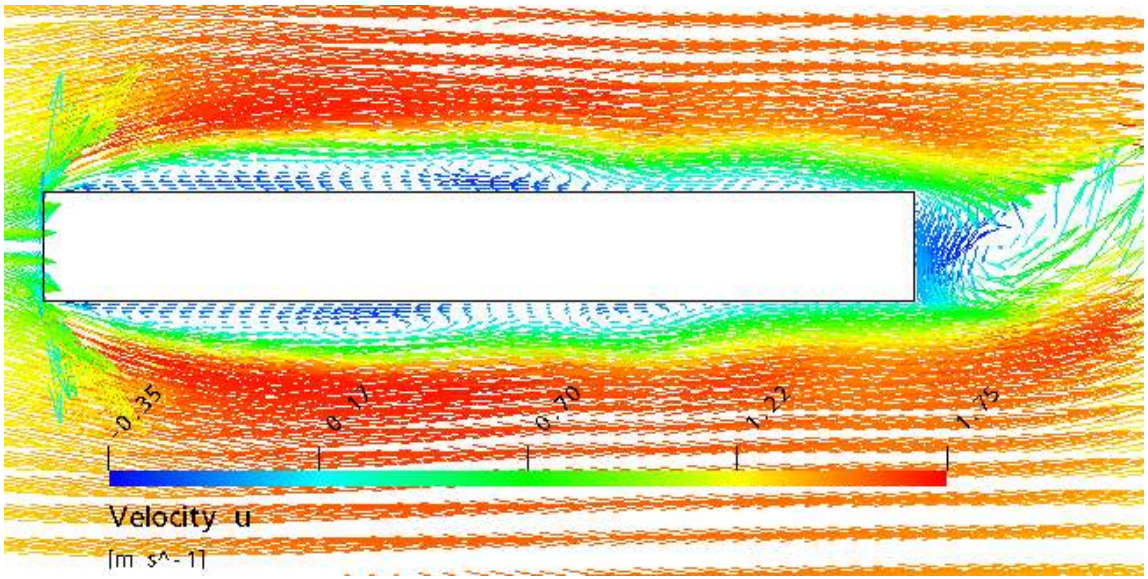

Figure 5.14 Vortices (*n=2*) around a *B/H=8* cylinder (DES).

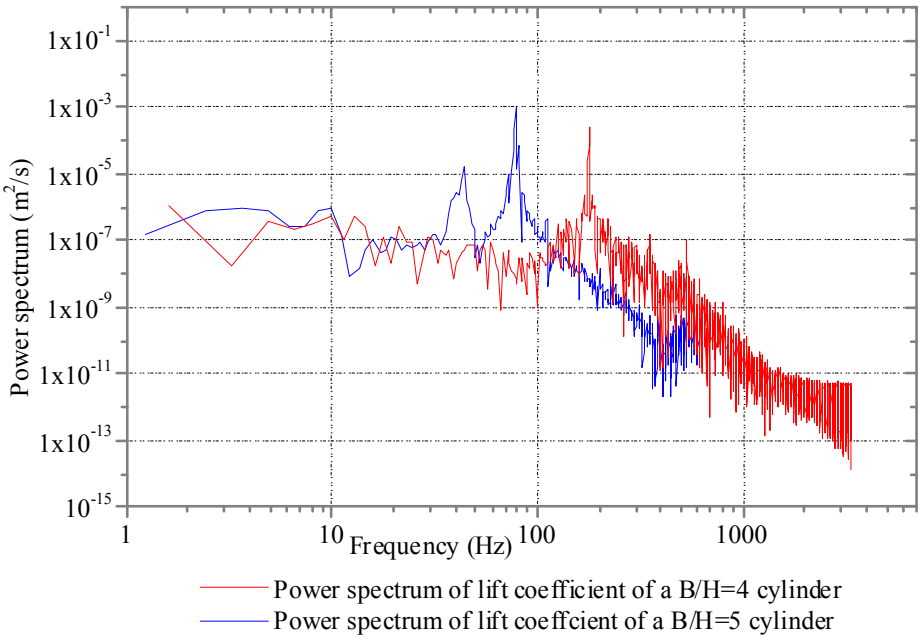

Figure 5.15 Power spectrum of lift coefficient of a *B/H=4* and a *B/H=5* cylinder.

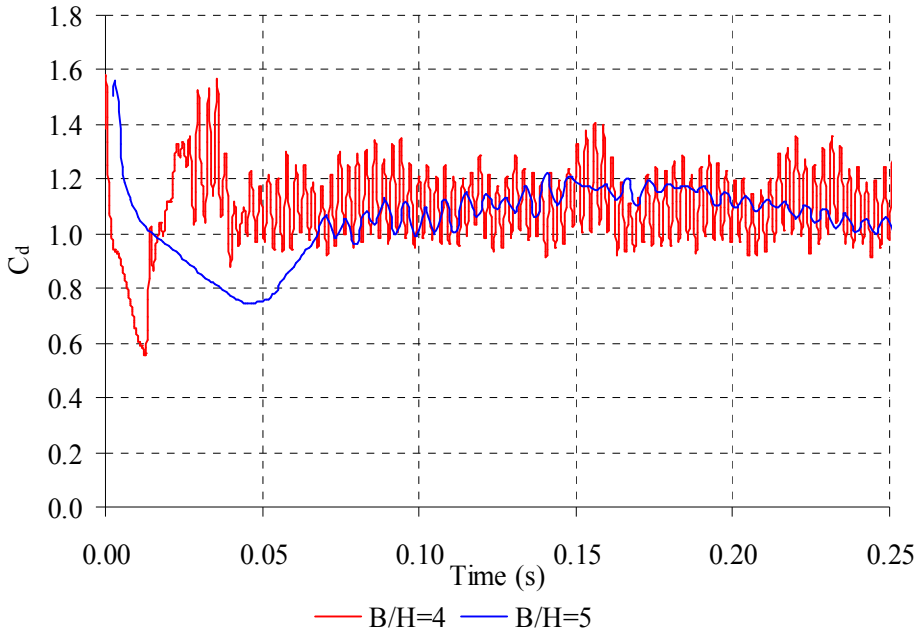

Figure 5.16 Time history of drag coefficients of a *B/H=4* and a *B/H=5* cylinder.

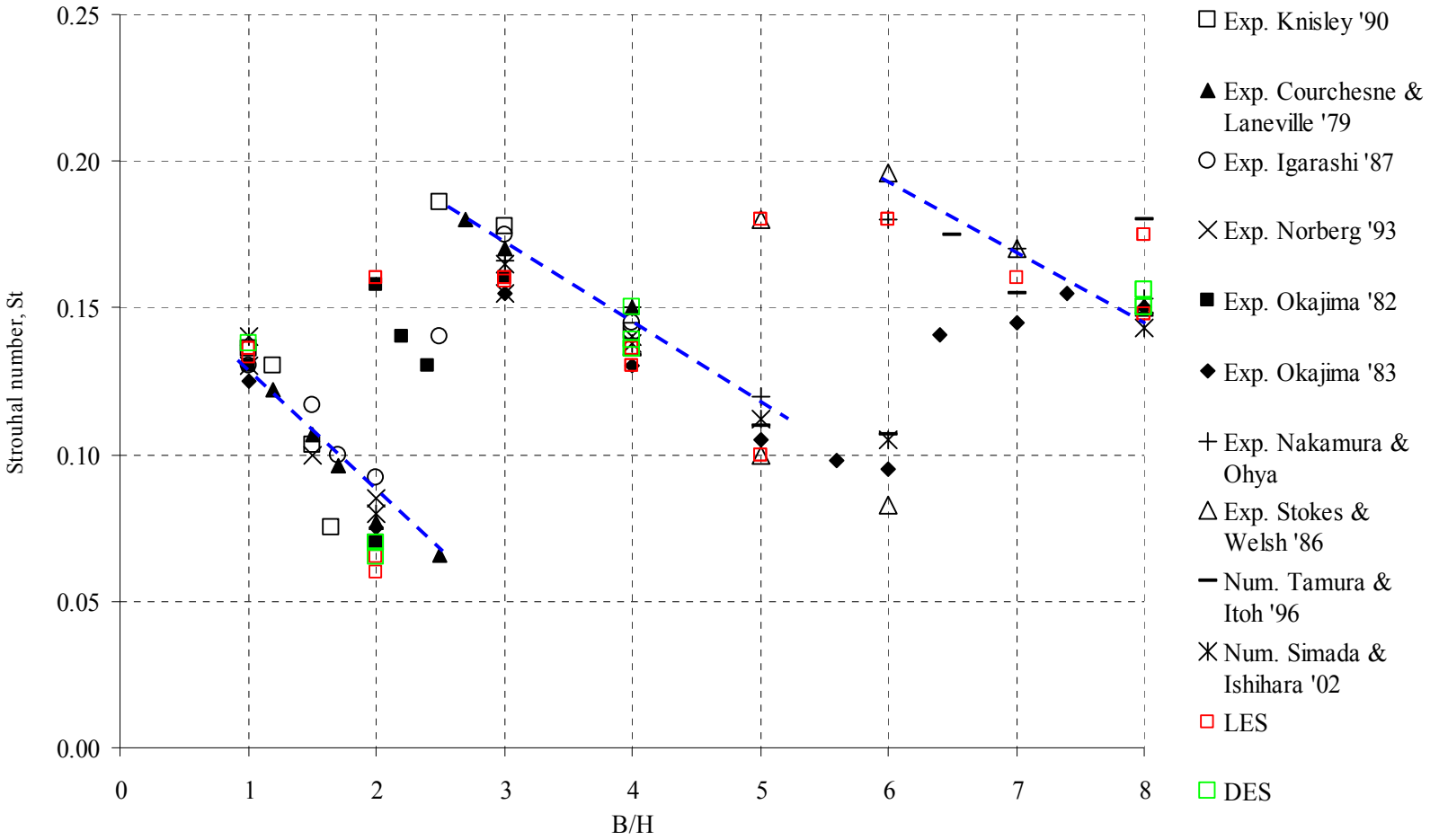

Figure 5.17 Strouhal number of rectangular cylinders with aspect ratio from *B/H=1* to *B/H=8* (blue lines indicating pattern of changes of Strouhal number).

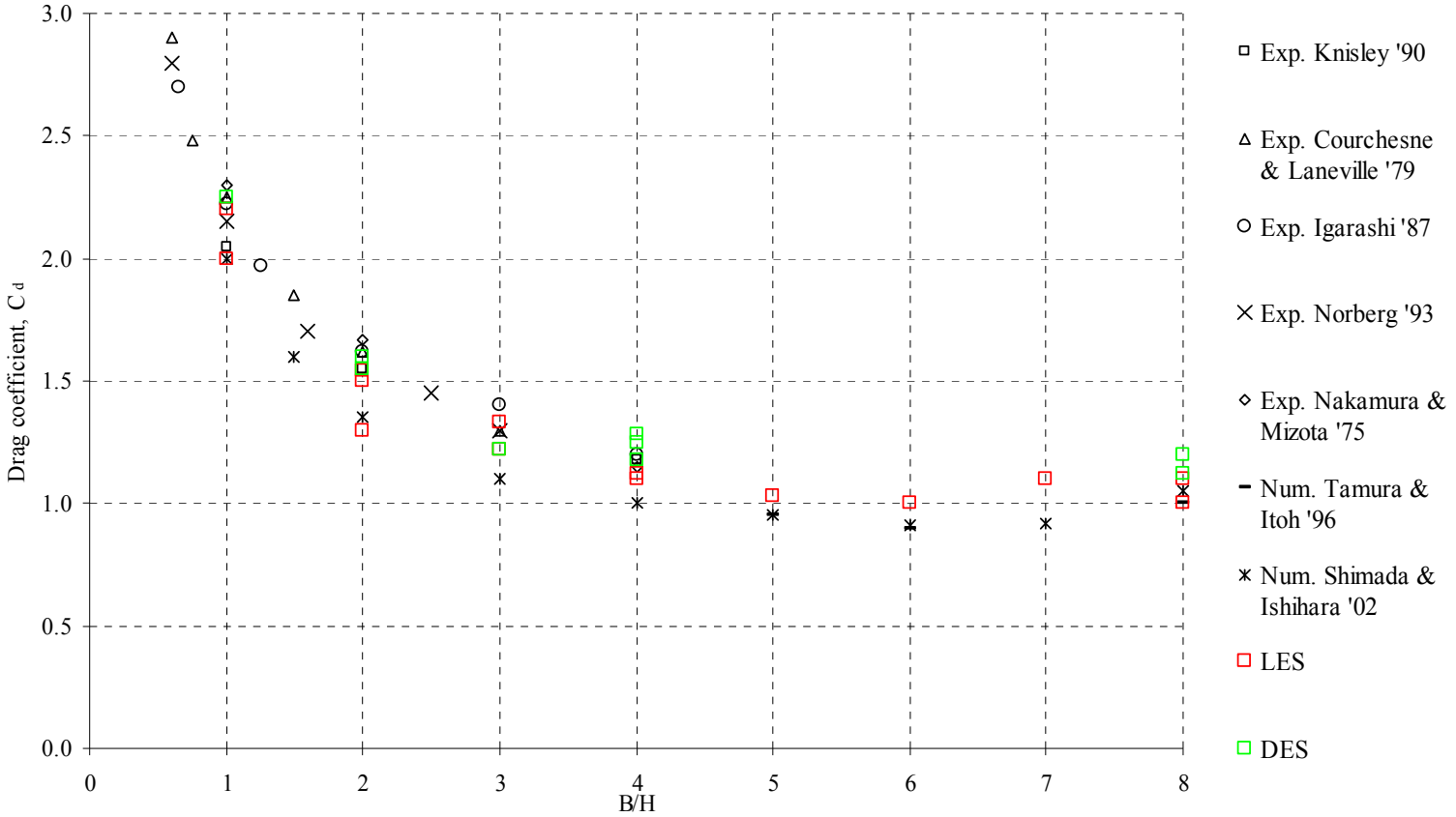

Figure 5.18 Drag coefficient of rectangular cylinders with aspect ratio from *B/H=1* to *B/H=8*.

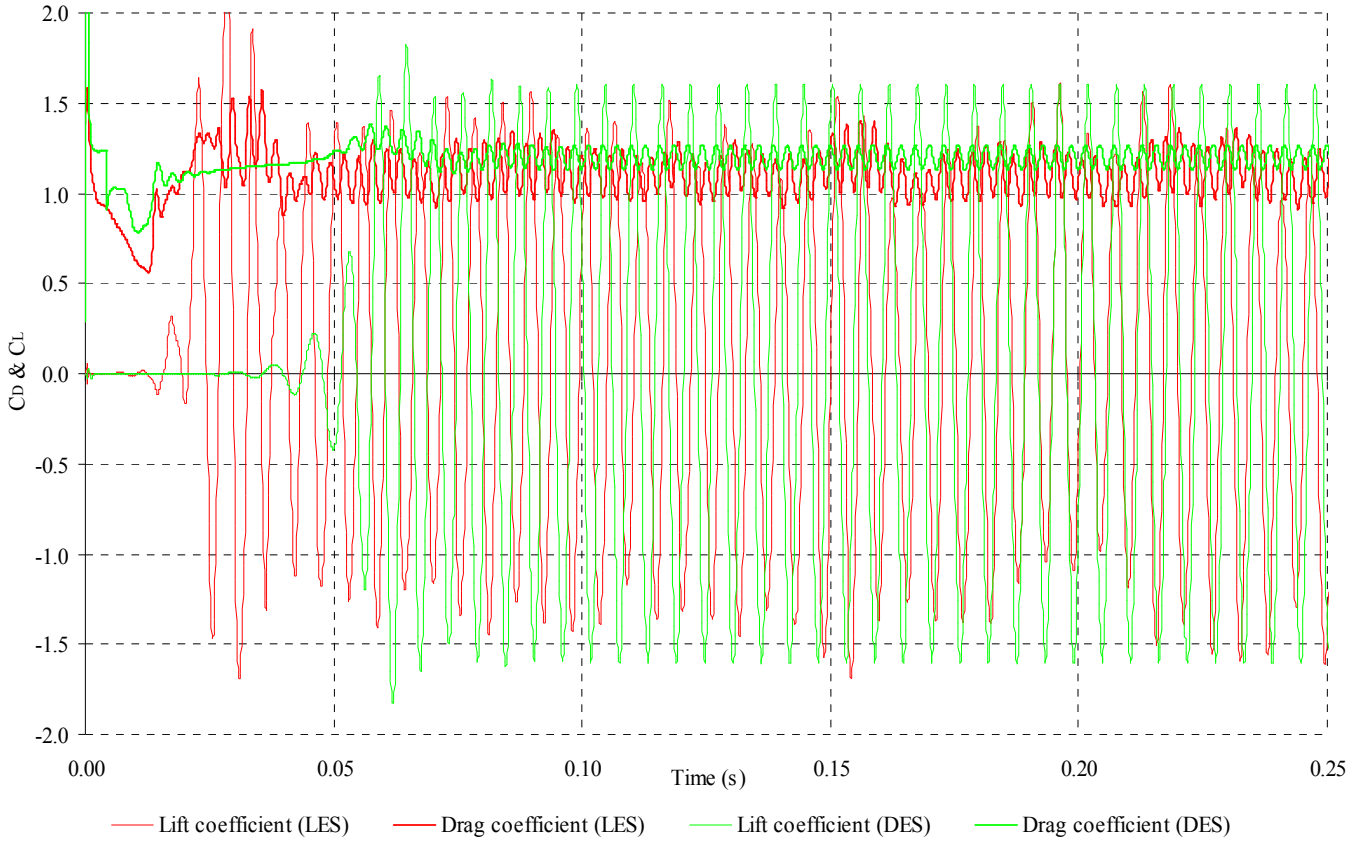

Figure 5.19 Lift and drag coefficients of a *B/H=4* cylinder (LES and DES).

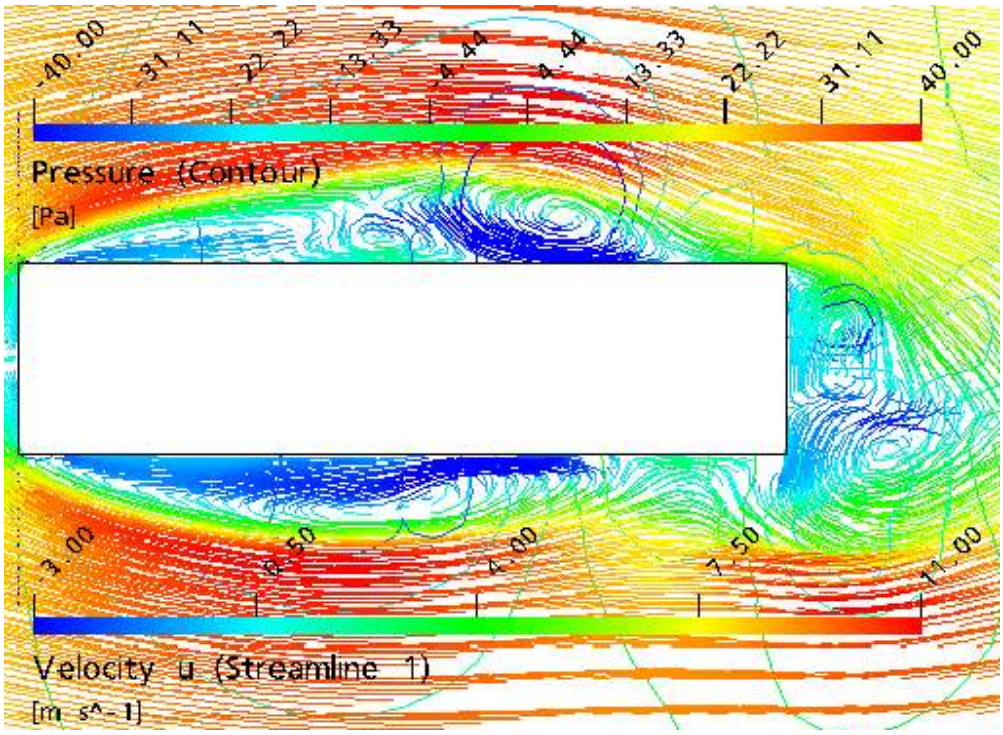

Figure 5.20 Pressure contour and velocity streamlines around a *B/H=4* cylinder (LES).

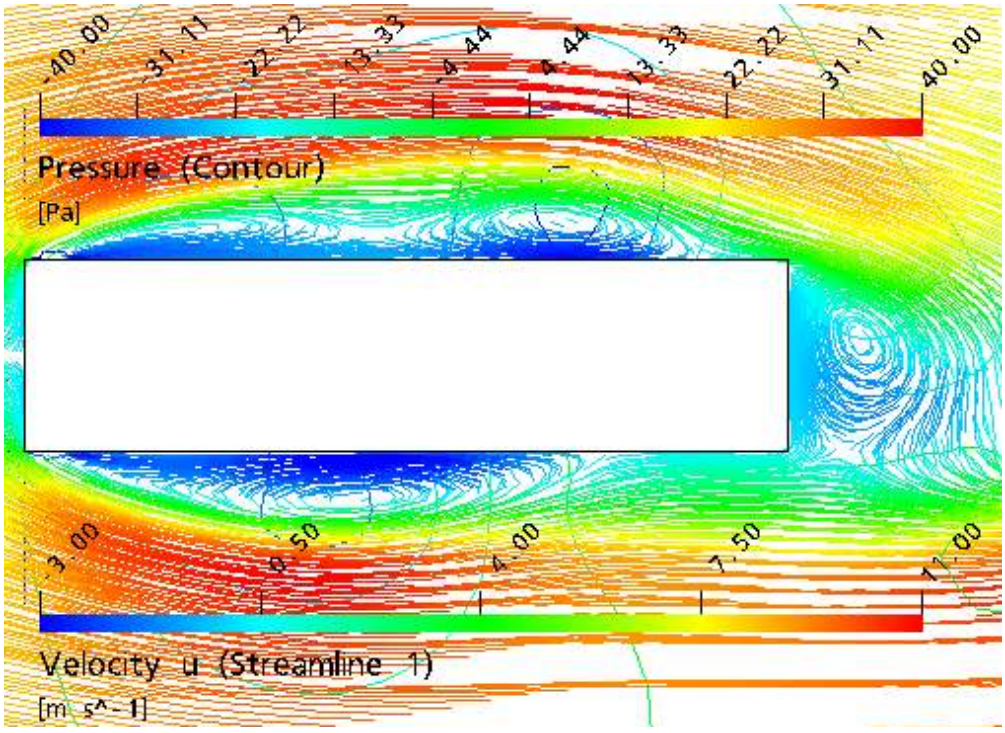

Figure 5.21 Pressure contour and velocity streamlines around a *B/H=4* cylinder (DES).

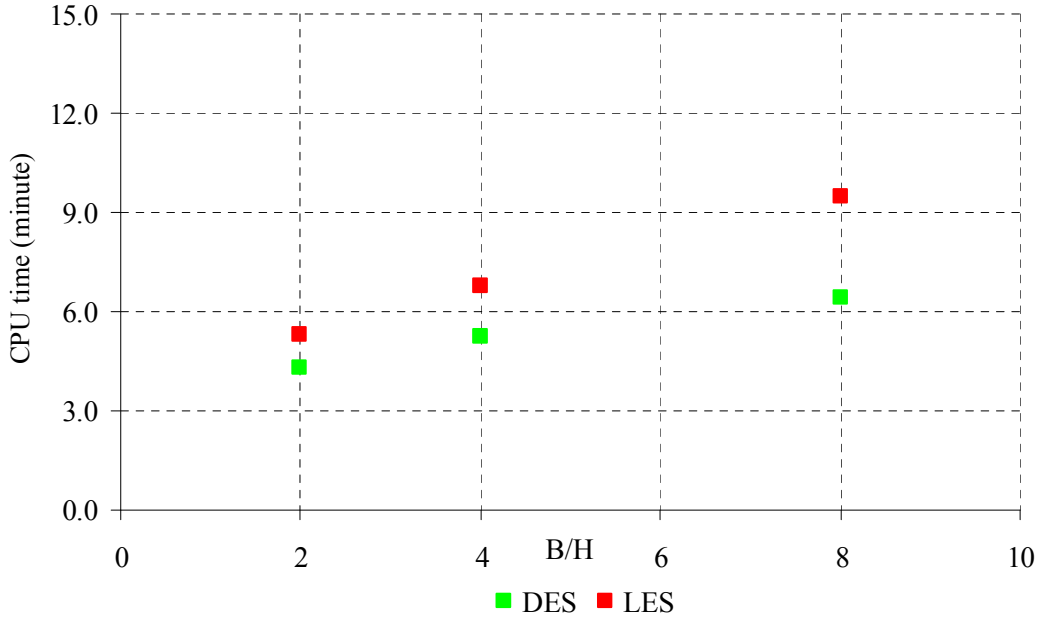

Figure 5.22 Computational time of cylinder sections (*B/H=2*, *B/H=4* and *B/H=8*) at Reynolds number of *3,000*.

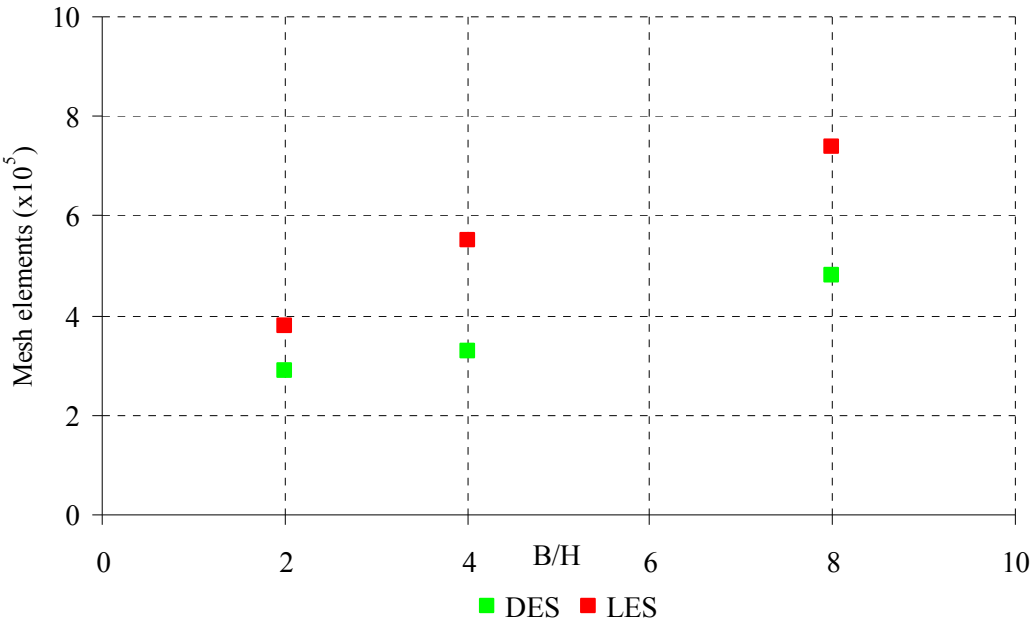

Figure 5.23 Mesh elements of cylinder sections (*B/H=2*, *B/H=4* and *B/H=8*) at Reynolds number of *3,000*.

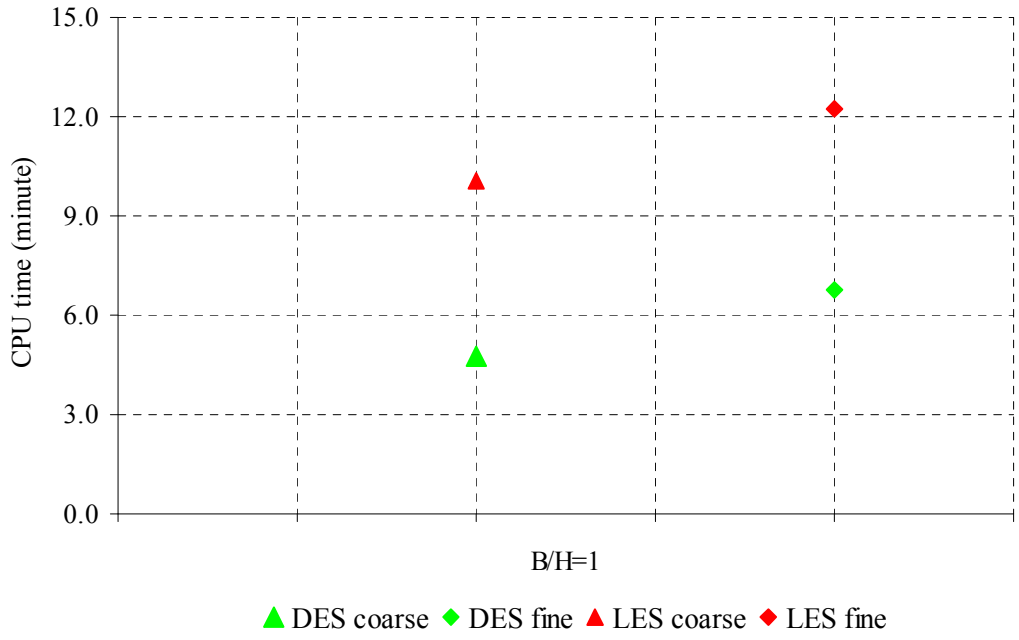

Figure 5.24 Computational time of a square section at Reynolds number of *14,000* (with coarse and fine meshes).

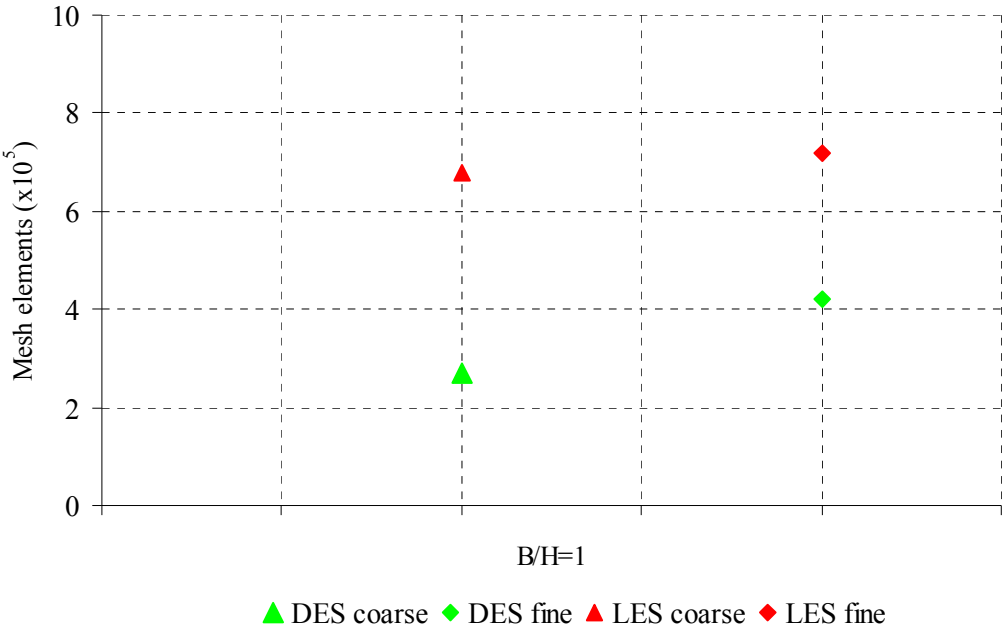

Figure 5.25 Mesh elements of a square section at Reynolds number of *14,000* (with coarse and fine meshes).

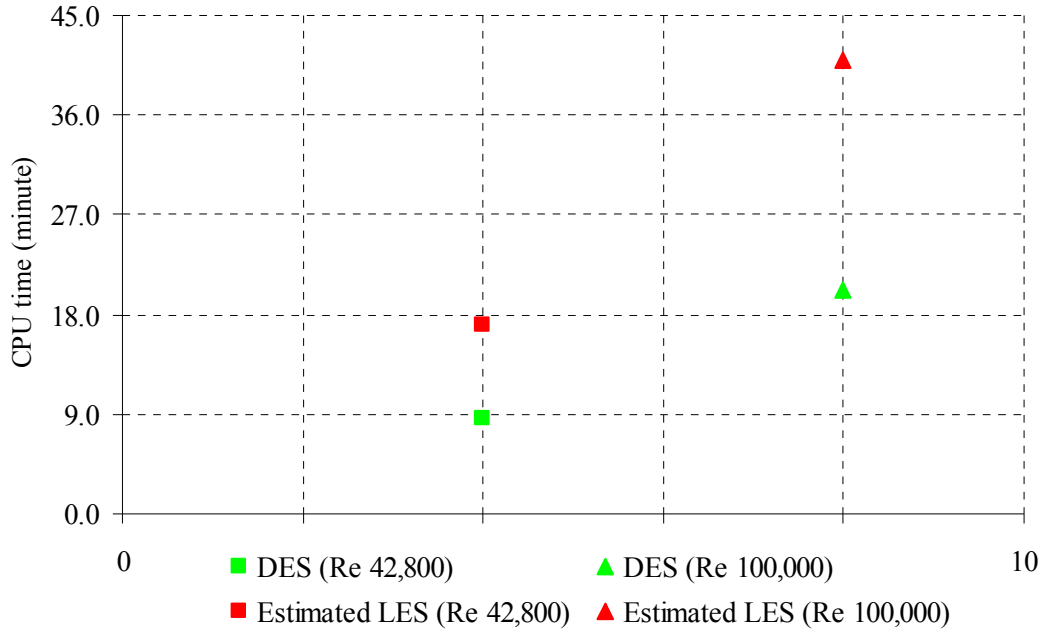

Figure 5.26 Computational time for DES at Reynolds number of *42,800 and 100,000* (with estimation of LES computational time).

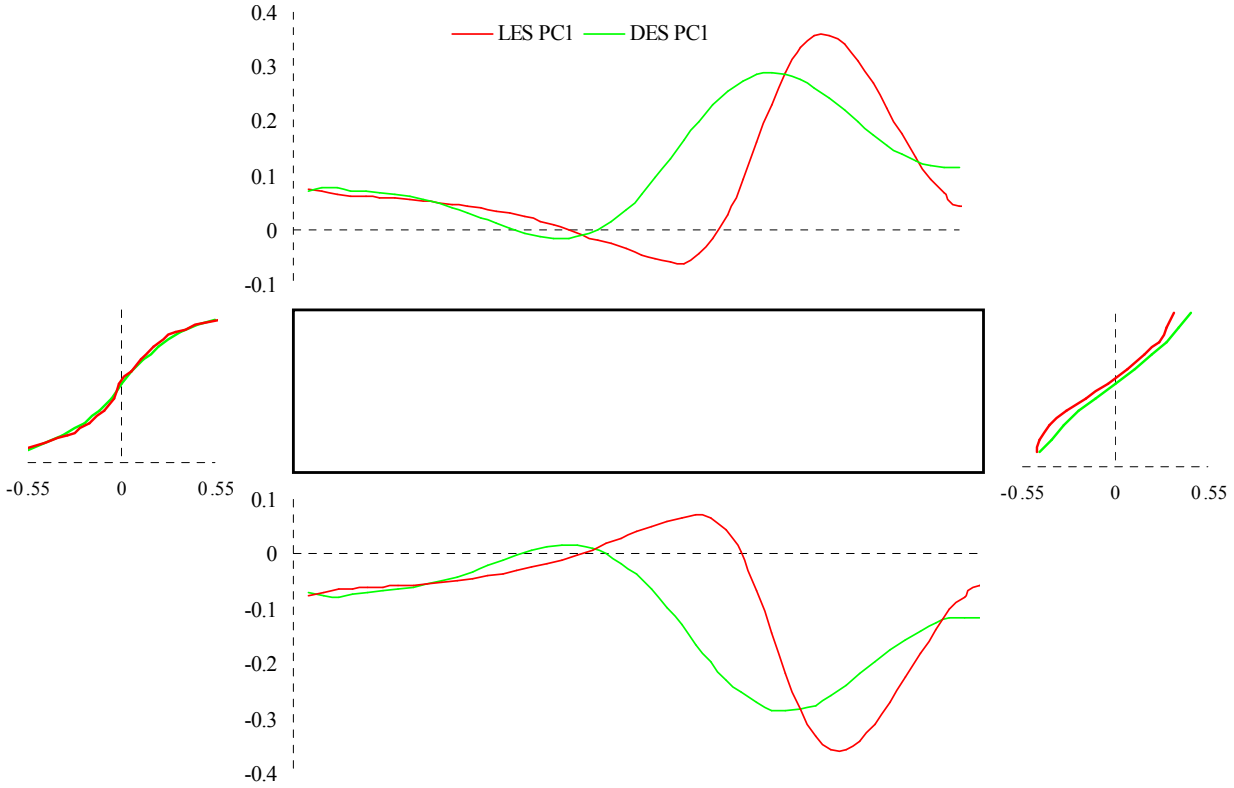

Figure 5.27 First principal component of pressure distribution (N/m^2) of a *B/H=4* cylinder.

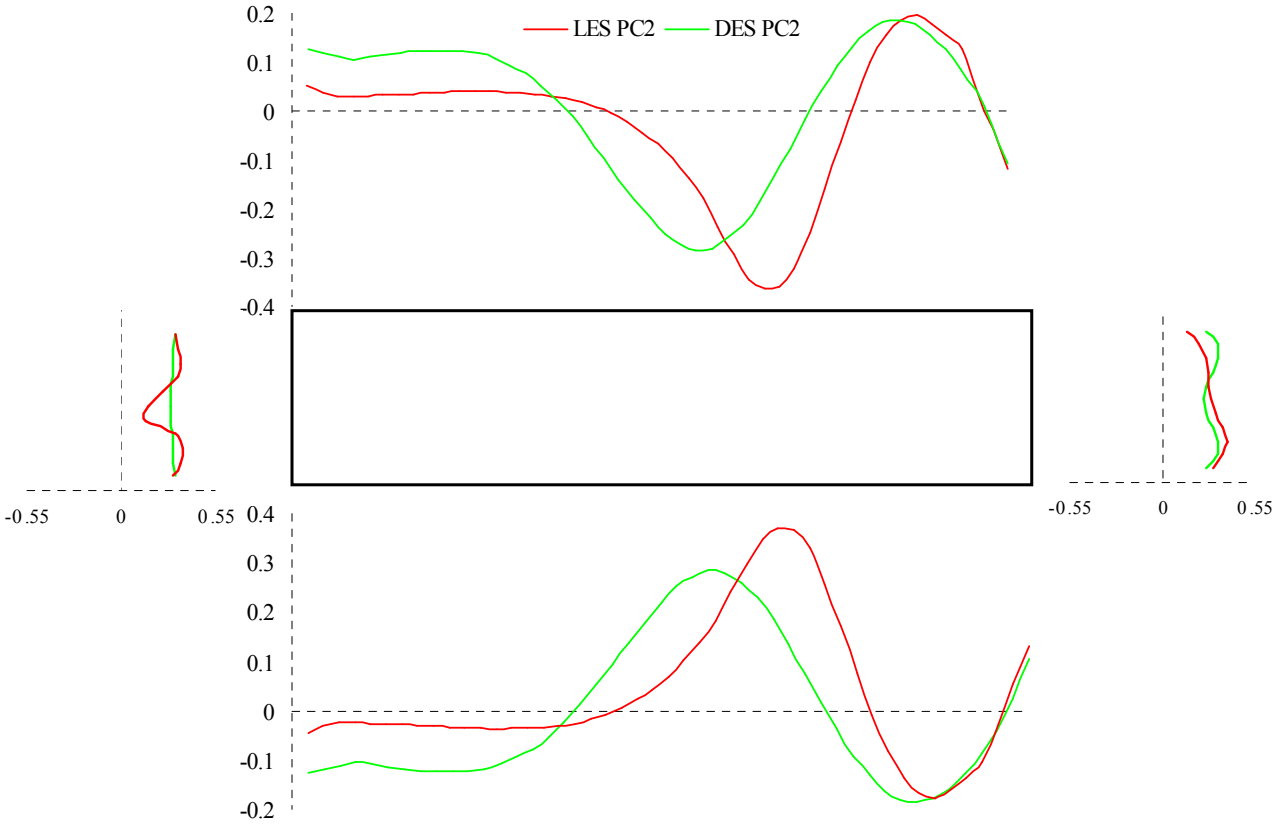

Figure 5.28 Second principal component of pressure distribution (N/m^2) of a *B/H=4* cylinder.

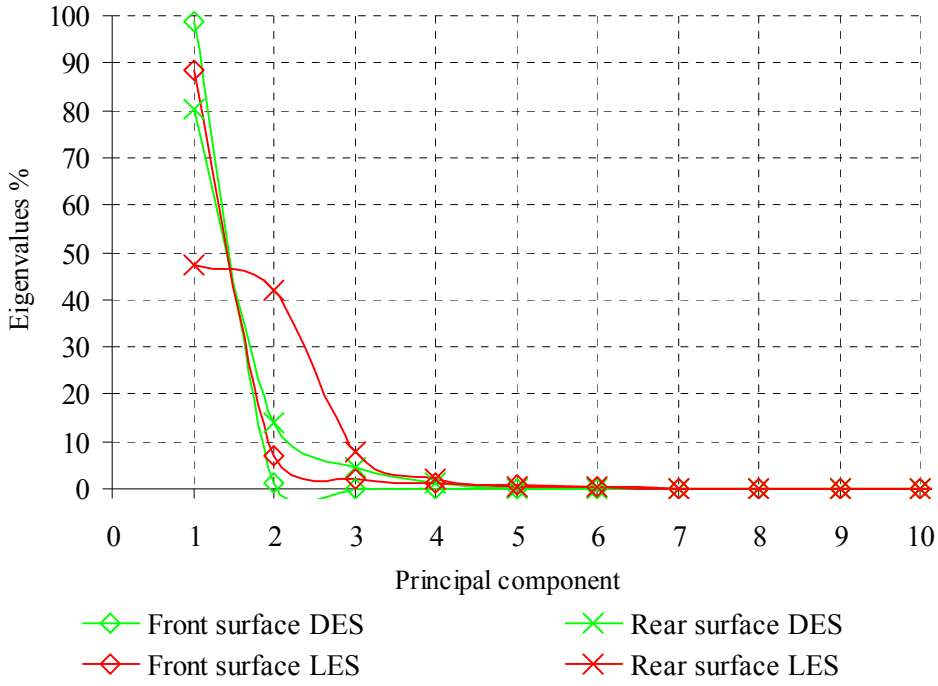

Figure 5.29 Eigenvalues of front and rear surface of a *B/H=4* cylinder.

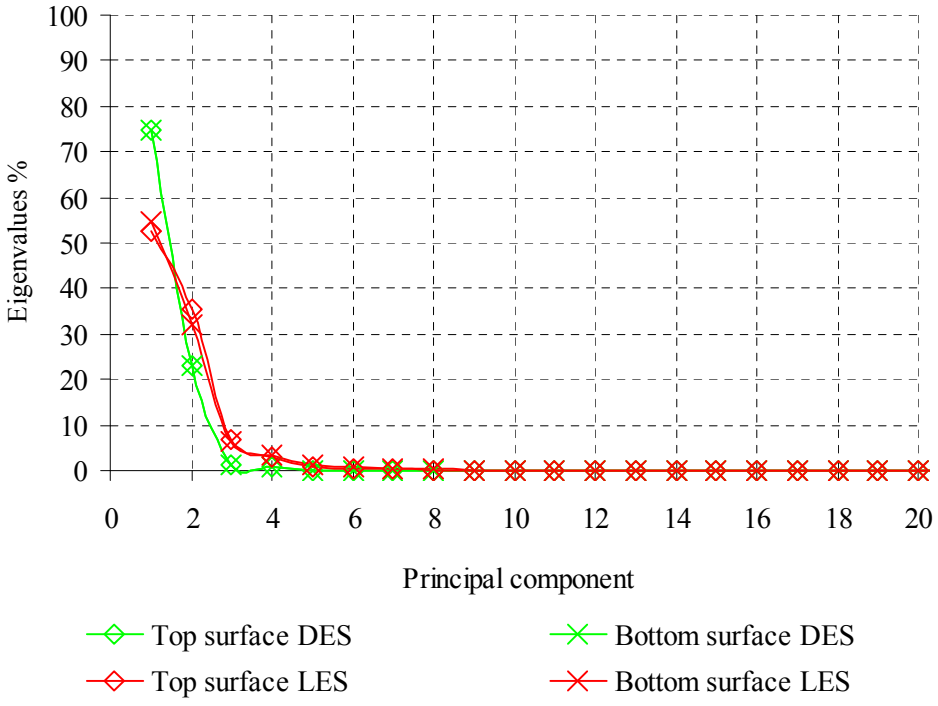

Figure 5.30 Eigenvalues of top and bottom surface of a *B/H=4* cylinder.

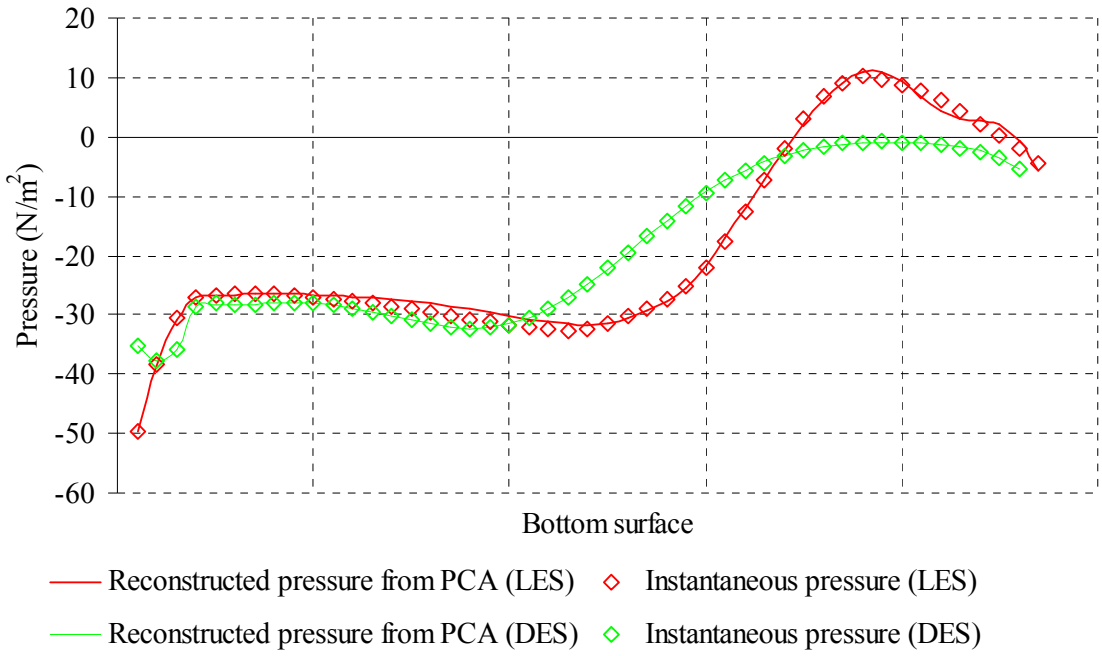

Figure 5.31 Reconstruction (from first five principal components) of the pressure distribution around a *B/H=4* cylinder.

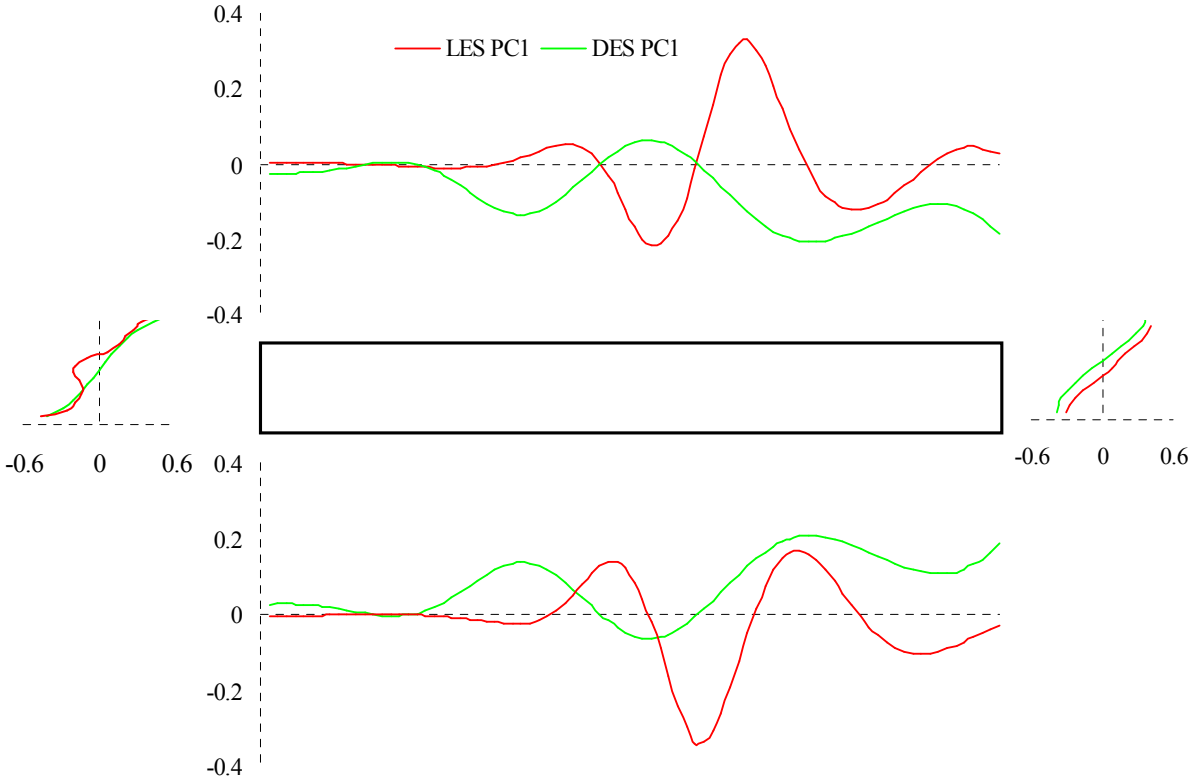

Figure 5.32 First principal component pressure distribution (N/m^2) of a *B/H=8* cylinder.

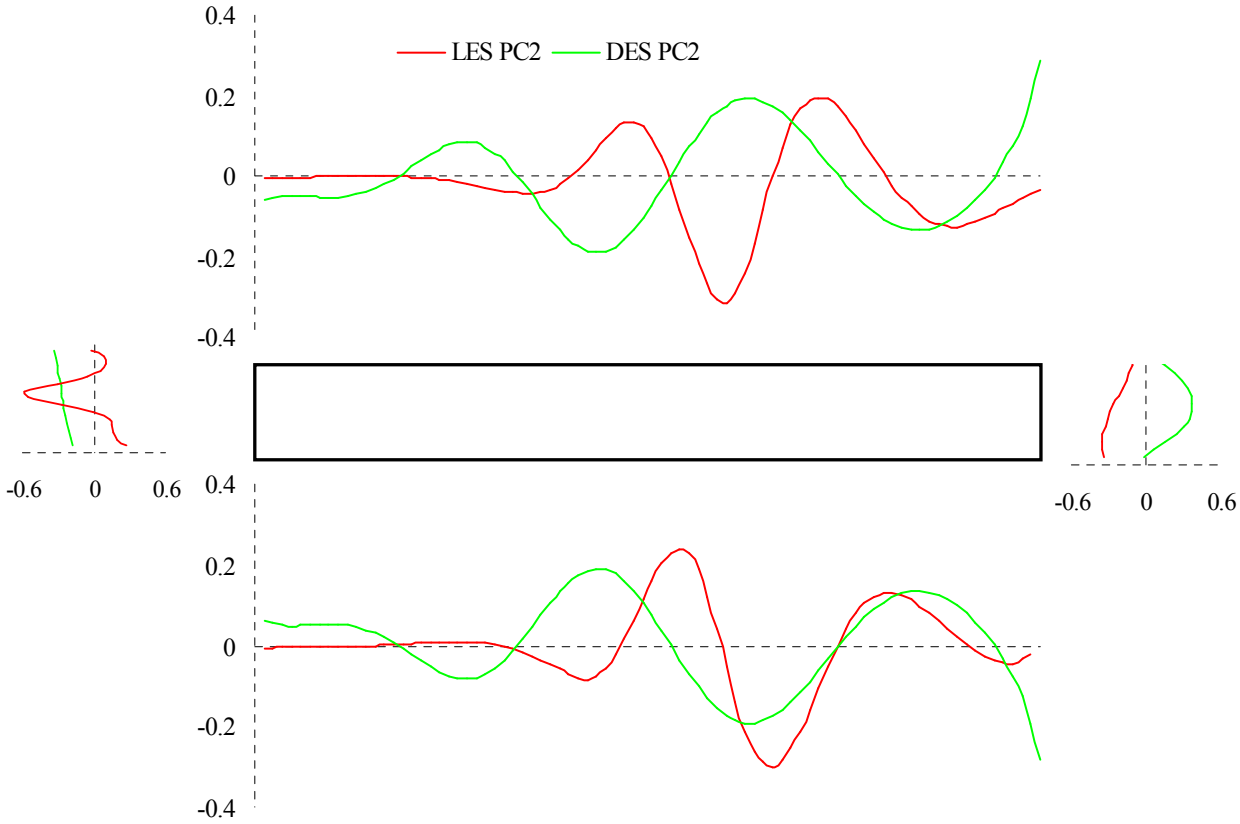

Figure 5.33 Second principal component of pressure distribution (N/m^2) of a *B/H=8* cylinder.

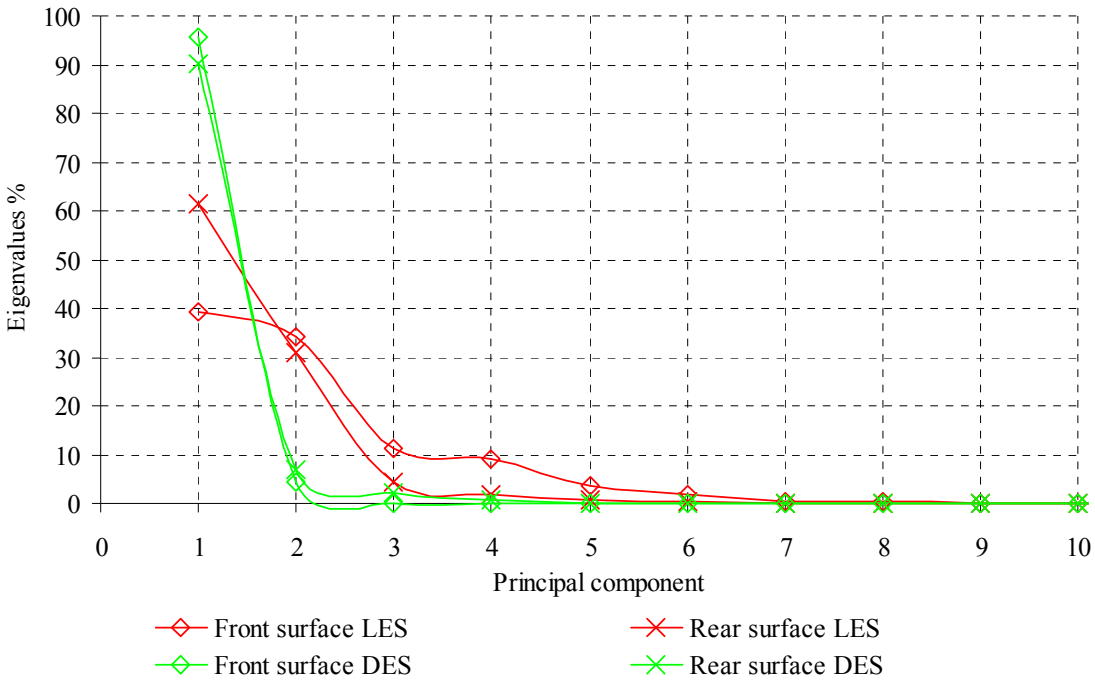

Figure 5.34 Eigenvalues of front and rear surface of a *B/H=8* cylinder.

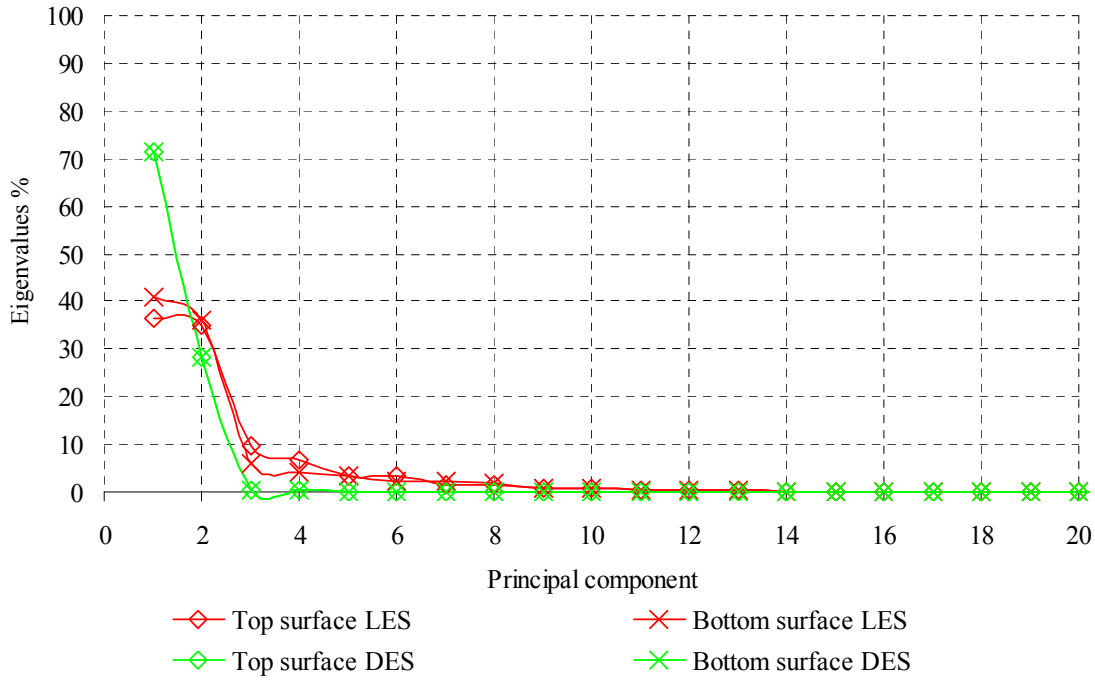

Figure 5.35 Eigenvalues of top and bottom surface of a *B/H=8* cylinder.

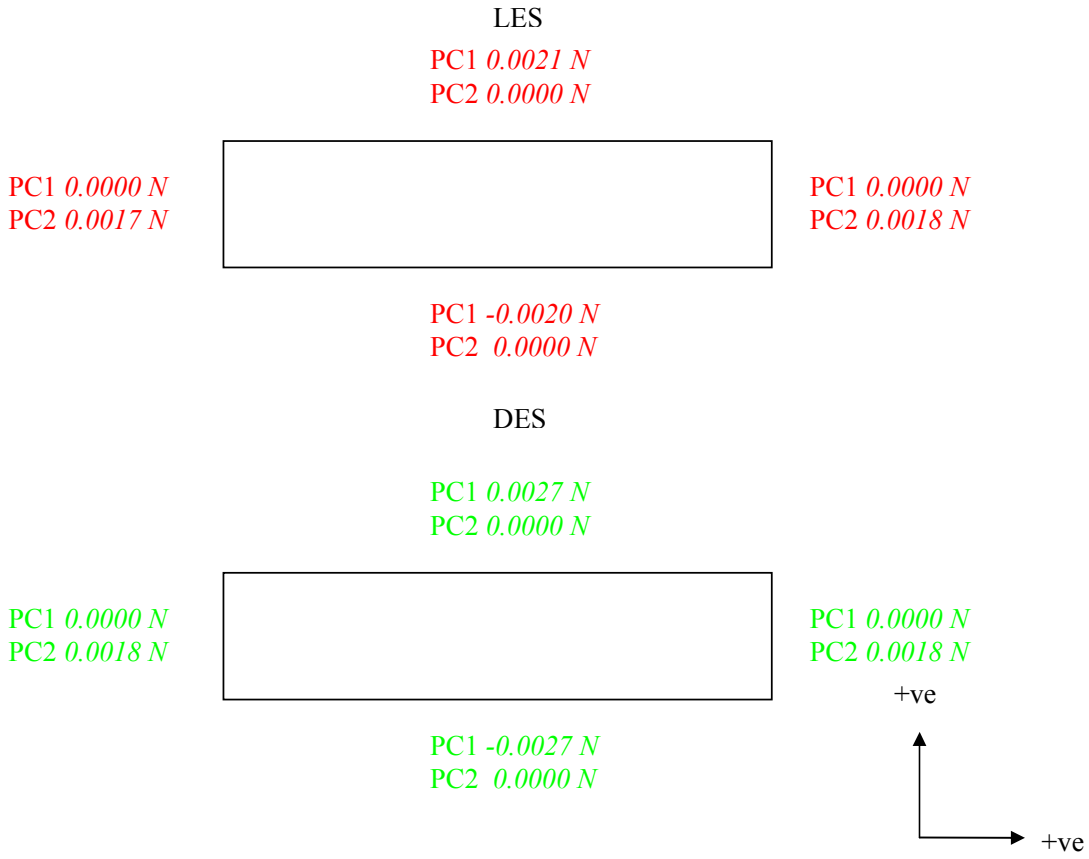

Figure 5.36 Pressure force of the first and second principal components around a *B/H=4* cylinder.

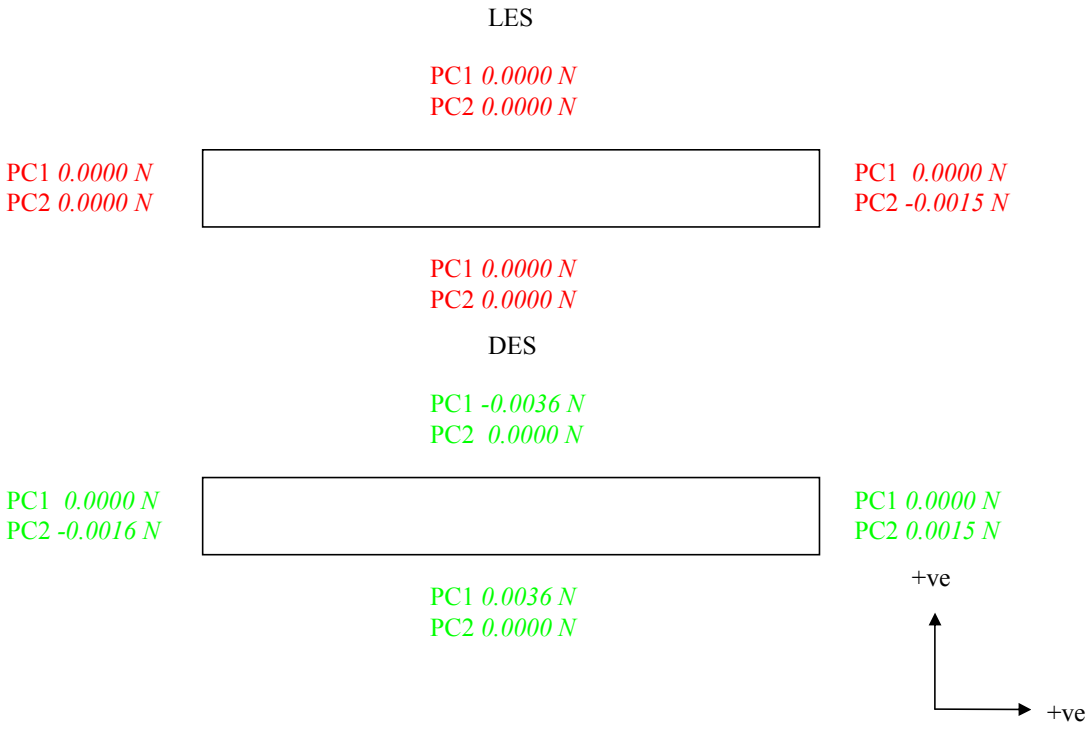

Figure 5.37 Pressure force of the first and second principal components around a *B/H=8* cylinder.

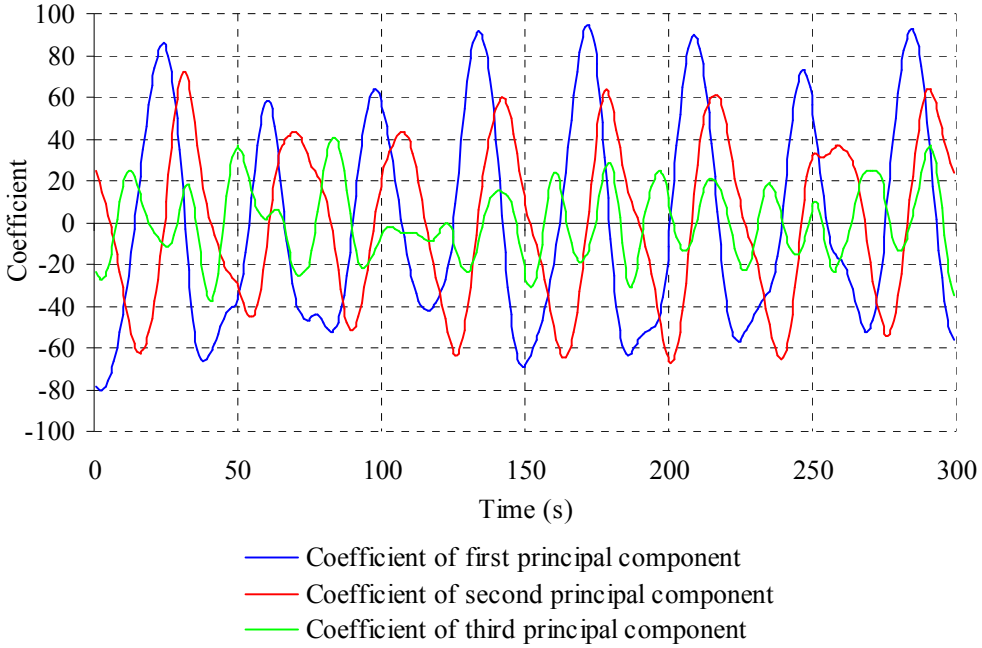

Figure 5.38 Coefficients of the principal components of a *B/H=4* cylinder (LES).

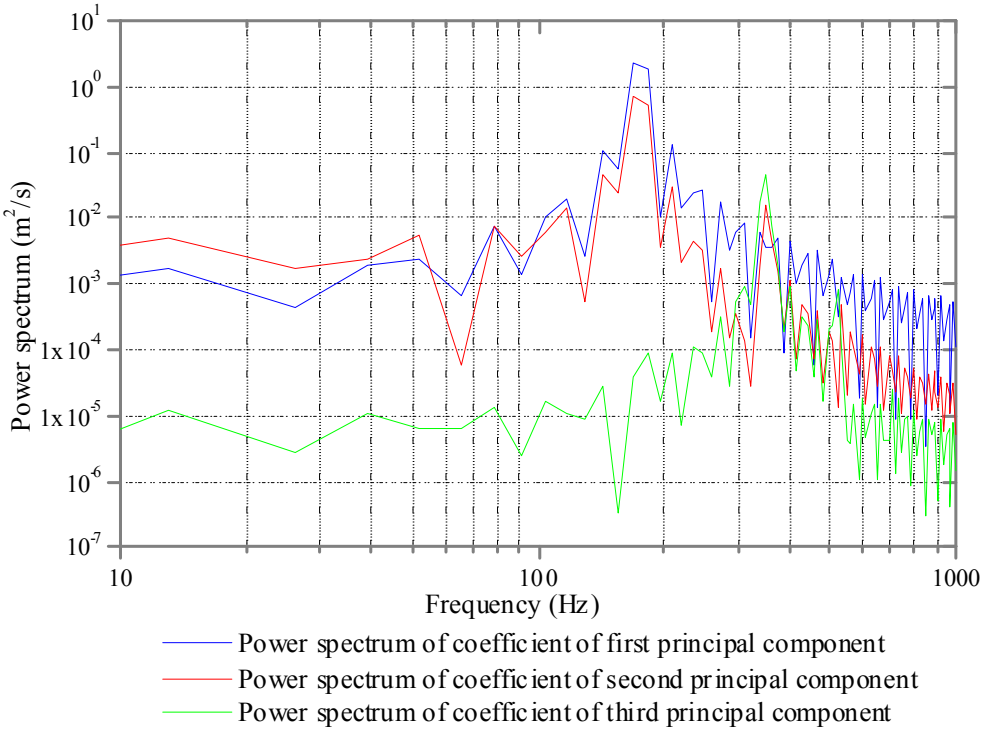

Figure 5.39 Power spectrum of the coefficients of the principal components of a B/H=4 cylinder (LES).

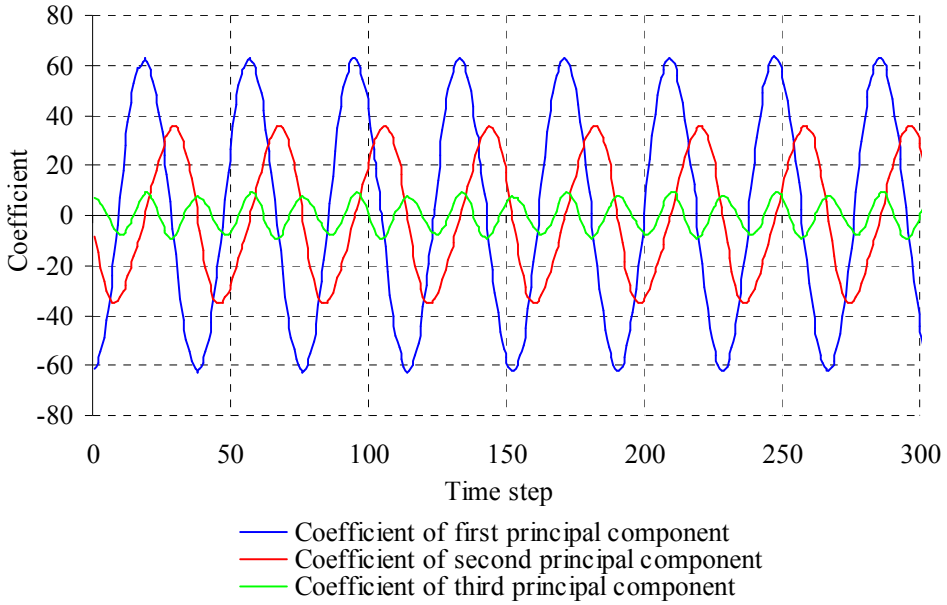

Figure 5.40 Coefficients of the principal components of a *B/H=4* cylinder (DES).

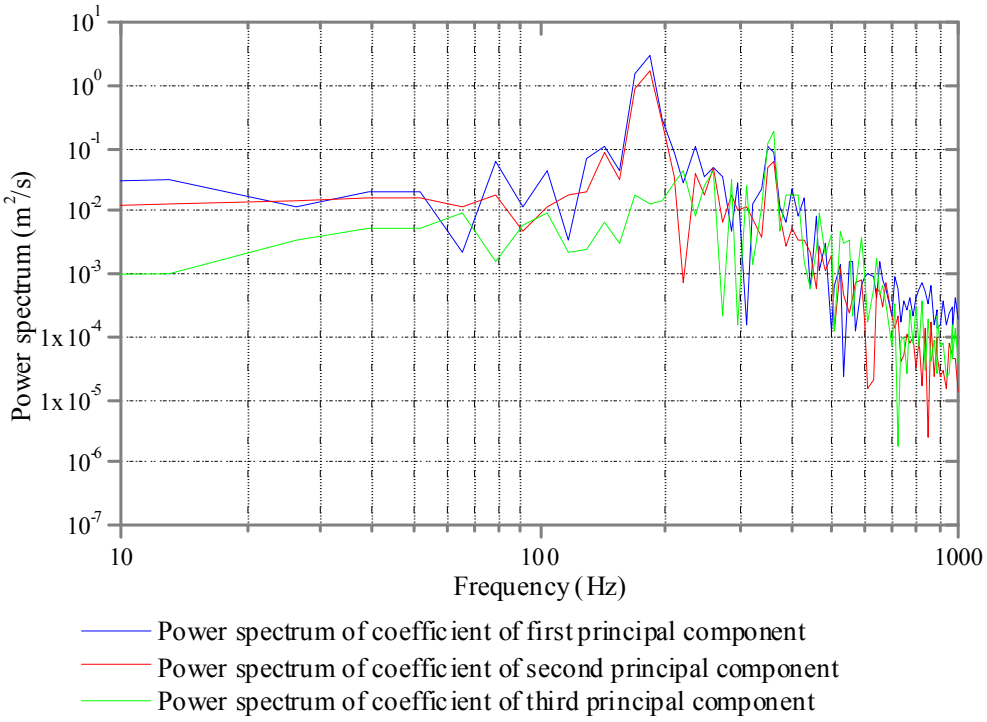

Figure 5.41 Power spectrum of the coefficients of the principal components of a *B/H=4* cylinder (DES).

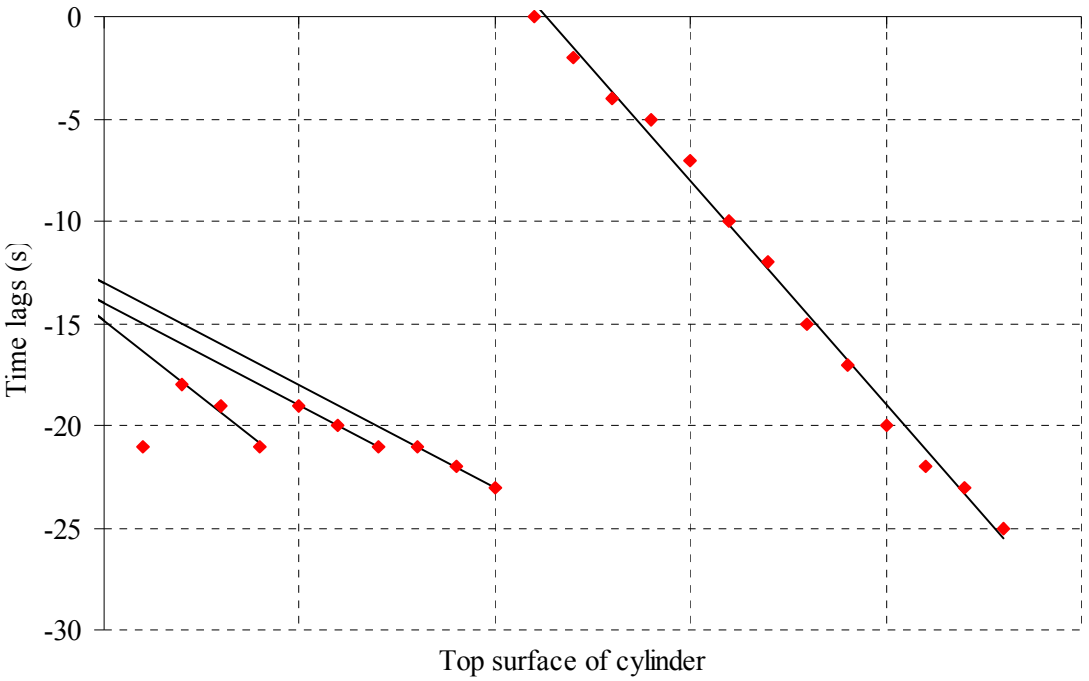

Figure 5.42 Time lags of pressure points along the top surface of a *B/H=4* cylinder (LES).

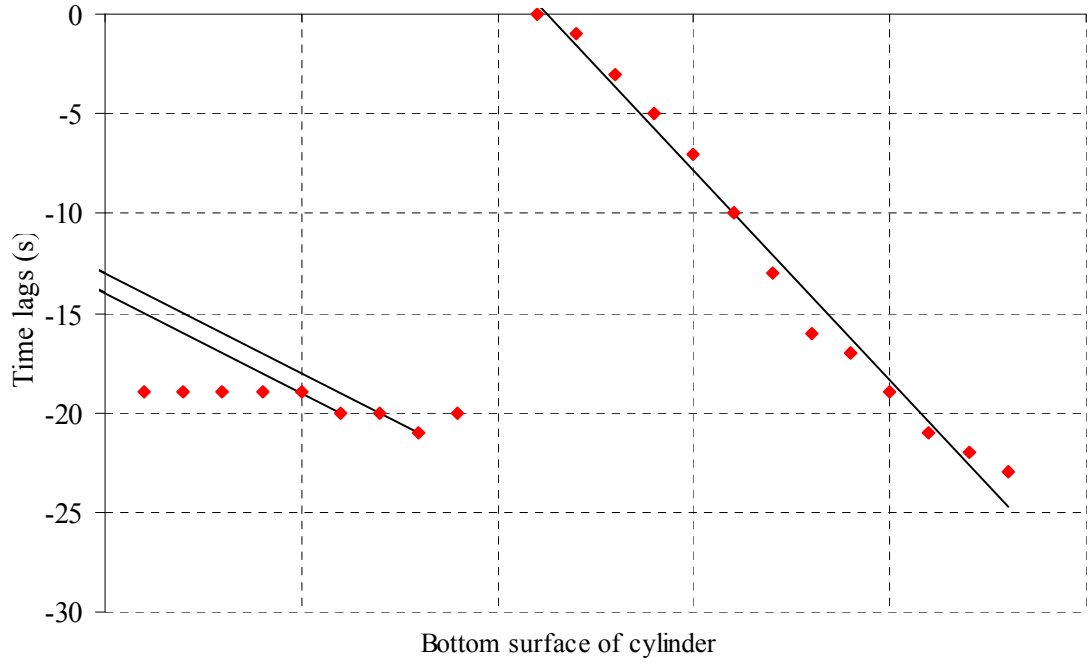

Figure 5.43 Time lags of pressure points along the bottom surface of a *B/H=4* cylinder (LES).

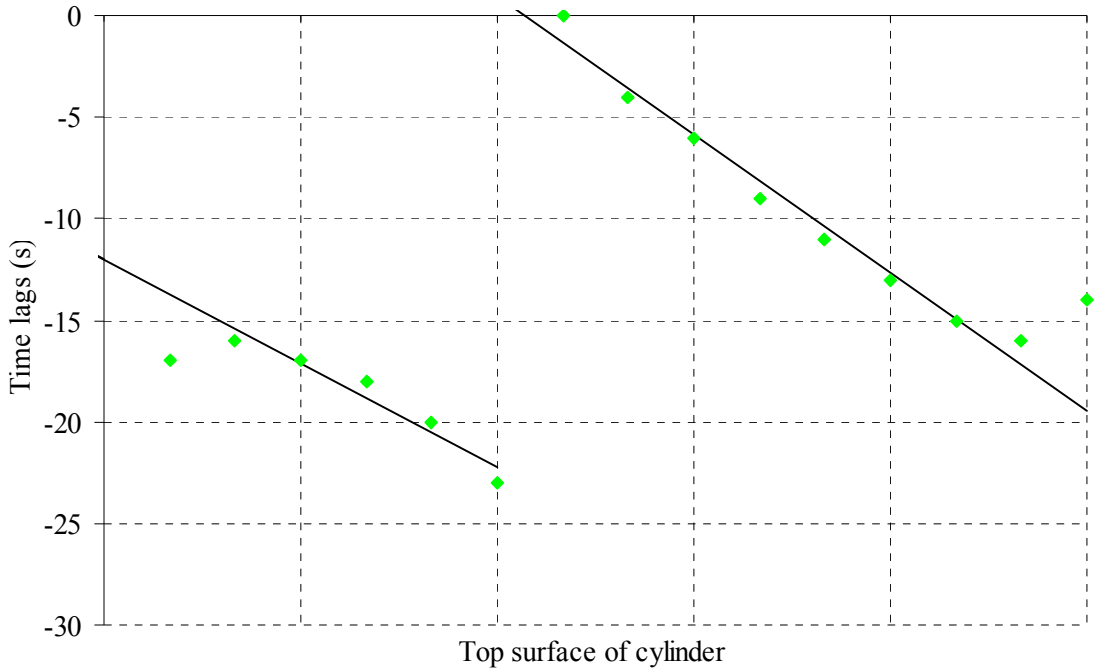

Figure 5.44 Time lags of pressure points along the top surface of a *B/H=4* cylinder (DES).

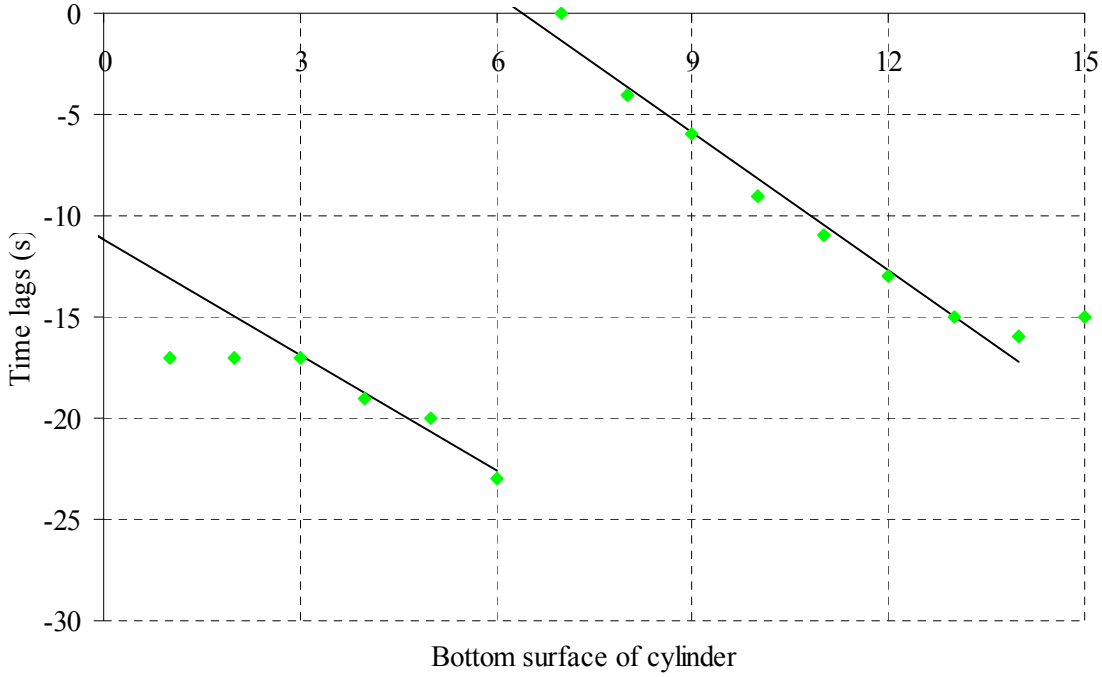

Figure 5.45 Time lags of pressure points along the bottom surface of a *B/H=4* cylinder (DES).

6 WIND TUNNEL TEST AND CFD STUDY OF KESSOCK BRIDGE

The work in this chapter aims to study the flow around the Kessock Bridge in response to wind excitation. To begin with, a *1:40* scale sectional wind tunnel test of the bridge deck section has been conducted to measure the force coefficients and to observe the vortex shedding instability of the deck section in response to wind. Pressure measurement has also been conducted around the middle section of the model. Surface pressure distribution provides information on the flow separation and vortex formation around the bridge deck section.

The second part of the chapter discusses the simulation of the flow around a static bridge deck section (*1:40* scale) of the Kessock Bridge using DES. DES has been chosen based on the findings of previous studies on the flow around the circular cylinder and rectangular sections, which showed that the model is suitable for the simulation of flow at higher Reynolds number compared to LES. DES is capable of capturing the unsteady nature of flow such as the vortex shedding phenomenon and yet less computer power and simulation time is needed compared to LES. Simulations done on the previous two chapters demonstrated that DES predicted result very close to LES. Although LES gives better prediction of flow details compared to DES, its application on the simulation of the flow around a bridge deck section is impractical due to the high computer power requirement.

6.1 KESSOCK BRIDGE

The Kessock Bridge (Figure 6.1) is a cable stay bridge on the *A9* road over the Beauly Firth to the north of Inverness in Scotland (Figure 6.2). The bridge was opened in July *1982* and spans *1052m* across the firth with a main span of *240m* (Figure 6.3). The main span is supported by *64* cables in harp arrangement extending from four main *45m* pylons with reinforced concrete piers. The geographical location of Kessock Bridge makes it vulnerable to the uneven westerly wind blowing over mountainous terrain and an industrial area and the smoother easterly wind blowing from the open water of Moray Firth [98].

The fully continuous all-steel deck has an open cross section (Figure 6.4) of *21.9m* wide and a girder depth of *3.29m*. Upon the completion of the structure, significant vibration of the mid-span (up to *100mm*) occurred [98]. The shape of the bridge explains why it is susceptible to wind excitation. Sharp corners of the deck encourage

flow separation, which results in the formation and progression of vortices around the deck section. Vortical flow induces significant aerodynamic forces on the enveloped structures.

Owen *et al.* (1996) [98] investigated the dynamic response of the Kessock Bridge between October *1991* and May *1992* by recording the full-scale data of the response of the bridge at several locations along the structure. During the period of recording, three significant responses were observed with amplitude in excess of *110mm* in response to wind speed of *23-25m/s*. The collected data were analyzed and it was concluded that the oscillation of the bridge was caused by vortex shedding. Earlier investigation on the bridge response to wind excitation has been carried out at the University of Glasgow using the sectional wind tunnel model during the design stage of the bridge. A large vibration amplitude due to vortex shedding has been observed for a wind speed of around *20m/s* [138].

6.1.1 Study of the flow around the Kessock Bridge

Several research works [32, 52, 60, 81, 105, 135] have been conducted on the computational modelling of the flow around long span bridges. It is crucial that the turbulence models employed for the simulation are capable of predicting the more complex flow features around the deck sections compared to the flow around bluff bodies such as rectangular cylinders. These studies provide background and guidelines for the current investigation of the flow around the Kessock Bridge. Most of the work above involved both experimental and numerical investigation of the bridge such that comparative studies can be carried out. For the study on the Kessock Bridge, experimental work has been conducted but not numerical simulation before the investigation of the current work. Observation on the full scale Kessock Bridge [98] under wind excitation showed that the bridge is susceptible to vortex induced vibration. The capability of advanced turbulence models such as LES and DES in capturing complex vortical flow (as discussed in the previous three chapters) encourages the modelling of the flow around the Kessock Bridge deck section.

The investigation of the response of the Kessock Bridge to wind excitation in the current work includes the sectional wind tunnel test of the bridge and the investigation on the vortex shedding phenomenon around the bridge deck section using CFD techniques. Discussion on the comparison study between the wind tunnel measurement and the CFD results of the flow around the bridge deck section in this chapter focuses

on the static case. The moving mesh simulation software (Chapter Eight) has been developed by Sun *et al.* (2004) [124] as part of the overall project on the modelling of bridge aeroelasticity. Earlier study of the developed software on the flow around bridge deck section only involved RANS models due to the restriction of computer power. Upgrade of the parallel computing system used for the CFD study on the flow around the deck section in this project allows the simulation of a moving mesh using more advanced turbulence models such as DES, this will be discussed in the next chapter.

6.2 WIND TUNNEL TEST

As discussed, current work involved a sectional wind tunnel test of the Kessock Bridge. The test has been conducted as a collaborative research work between the School of Civil and Environmental Engineering of the Nanyang Technology University (NTU) and the School of Civil Engineering of the University of Nottingham.

The team from the NTU was responsible for the building of the *1:40* sectional scale model of the Kessock Bridge for the wind tunnel test. The team was led by Professor C. Choi, with Dr. X. Zhang in charge of the test procedure throughout the experiment. The setting up and equipment calibration of the test were performed by technicians Mr. L. Tay and Mr. Ong.

The team from the University of Nottingham was led by Dr J. Owen and Dr N Wright who supervised the design of the *1:40* scale model of the bridge deck section, in which the calculation was done by the author (details are outlined in section 6.2.2). Also, Dr. D Sun and Miss X. Gu from the University of Nottingham were involved in the test conducted in the wind tunnel in the NTU.

6.2.1 Experimental studies on wind tunnel test of bridges

Sectional model tests are employed to extract loads and aerodynamic forces exerted on structures enveloped in flow such as long span bridges. The results are then used for comparative studies with the numerical solutions and the full-scale measurement. The following reviewed various sectional wind tunnel tests on long span bridges to study the behaviour of the structures in response to wind excitation.

Wardlaw and Ponder (1969) [139] performed a *1:30* scale sectional wind tunnel test on the Longs Creek cable stayed bridge to investigate the aerodynamic behaviour of the bridge. The bridge is geometrically very similar to the Kessock Bridge, with an

open cross section deck and sharp corners. Vortex excited flexural vibration has been observed on the bridge at ranges of wind speed similar to the observation of the large amplitude vibration of the Kessock Bridge. The wind tunnel measurement has shown reasonably good agreement compared to the observations of the prototype response to wind. Efforts have been made to modify the aerodynamic shape of the bridge deck by adding soffit plating and fairings on the bridge which reduced the amplitudes of vibration by up to *40%*. This work provided general ideas for the investigation of the flow behaviour around the open cross section bridge deck shape of the Kessock Bridge.

Brownjohn and Choi (2001) [19] carried out a sectional model wind tunnel test on the Ting Kau cable stayed bridge in Hong Kong to extract the aerodynamic derivatives of the bridge deck. The work also investigated the stability of the deck under different turbulence conditions and angles of attack of wind. A section length scale of *1:80* was chosen to represent *121m* of the actual bridge. Both static and dynamic tests have been carried out and the study concluded that the deck is stable except for torsional vibration which depends very much on the angle of attack of the incoming wind.

Sectional wind tunnel test has been chosen rather than the full scale bridge model for the test in this work. Based on the previous study of the behaviour of the Kessock Bridge in response to wind flow, a vortex shedding mechanism has been identified as the major cause of the large amplitude response of the bridge. Irwin [51] pointed out that a full aeroelastic model test is not a suitable approach for evaluating vortex excitation compared to a sectional model. This is due to the fact that a full aeroelastic model is usually built to a much smaller scale (*1:100* to *1:300*) than a section model, introducing difficulty in retaining the prototype Reynolds number. Furthermore, it demands a larger wind tunnel due to the length of the model and thus is not economical, as a wind tunnel with working section several times larger is needed. On the other hand, sectional wind tunnel testing provides more control over establishing the ranges of velocity when vortex shedding occurs. The following section outlines the scaling rules for the design of a scale model for wind tunnel test.

6.2.1.1 Scaling rules for wind tunnel model

Ideally, a sectional wind tunnel model of a bridge is a stiff, shape-wise representative segment of the full scale structure. For a bridge model, apart from building a geometrically similar scale model to the prototype, the behaviour of the model in response to wind has to match the prototype characteristics aerodynamically to allow

the full scale behaviour of the bridge to be predicted from the wind tunnel test. To achieve this, certain scaling rules need to be satisfied in the design of the wind tunnel model. These rules scale down the important non dimensional parameters of a flow corresponding to the reduced size of the model. Normally, these parameters include:

i) Reynolds number -ratio of inertia force to viscous force,

$$\frac{\rho u B}{\mu} \qquad \text{Eq. 6.1}$$

(Symbols used are explained at the end of this section)

ii) Froude number -ratio of inertia force to gravity force,

$$\frac{gB}{u^2} \qquad \text{Eq. 6.2}$$

iii) Cauchy number or reduced velocity -ratio of elastic force to inertia force,

$$\frac{E}{\rho u^2} \text{ or } \frac{u}{nB} \qquad \text{Eq. 6.3}$$

iv) Mass ratio -ratio of structural density to air density,

$$\frac{m}{\rho B^2} \qquad \text{Eq. 6.4}$$

v) Damping ratio -ratio of actual damping to critical damping.

ρ	Density of air
g	Gravitational acceleration
m	Mass per unit length
u	Mean velocity
B	Representative length
E	Modulus of Elasticity
n	Frequency

The above mentioned parameters need to be satisfied to match the dynamic behaviours of the model and prototype. Practically, it is difficult to match all the parameters especially the Reynolds number scaling. But for the case of the Kessock

Bridge, the Reynolds number scaling is not that crucial since the separation points of the flow are fixed at the sharp corners. If a more streamlined shape deck was considered, Reynolds number matching would be important since it can change the position of the separation points and thus change the flow characteristics around the bridge. Consequently, it is necessary to relax some of the parameters to some extent depending on the nature of the scaling problem.

Whitbread (1963) [140] investigated the similarity requirement for sectional model scaling and he concluded the three important parameters that need to be matched in the sectional test are the Cauchy number (or the reduced velocity), the mass ratio and the damping ratio. Work done by Wardlaw and Ponder (1969) [139] on the sectional wind tunnel test of the Long Creeks Bridge considered the same dimensionless parameters for the test. Also, Hjorth-Hansen (1992) [46] studied various wind tunnel tests method for bridges performance and he reminded that the above three parameters are the major concerns in sectional wind tunnel test of bridges. The above mentioned investigations showed agreement on the scaling rules for a sectional wind tunnel test. Consequently, the *1:40* scale model of Kessock Bridge has been designed with the scaling of the reduced velocity, the mass ratio and the damping ratio.

6.2.2 *1:40* scale wind tunnel model of Kessock Bridge

The following section briefs the reader on the design of the *1:40* scale model of the Kessock Bridge. The design procedure is outlined below:

- Calculate the cross sectional area of the actual bridge so that the mass per unit length of the prototype can be evaluated to decide the corresponding density ratio for the model.
- Choose a length scale of the model. This scale is chosen based on the size of the wind tunnel available.
- Decide a material to build the model, this is normally chosen based on the density ratio requirement as calculated in the first step in this procedure.
- Produce a details drawing of the model geometry.

A *1:40* scale model has been chosen based on the size of the available wind tunnel located in the NTU. The section has a breadth to length ratio of *1:3*, measuring *1.8m* in length and *0.55m* in breadth. If the model is too small, the deck section (only *2mm* thick at *1:40* scale, the prototype deck section measured *80mm* (averaged)) will not be stiff enough and the model might deform during the test. If the section is made too large (with *1:2* or *1:1.5* breadth to length ratio), it might fail to represent the three dimensional nature of the flow correctly.

To build the sectional model, higher density material is preferred to maintain the stiffness and the rigidity of the model during the test. Aluminium was first chosen as the design material but the resulting model was several times heavier than the theoretical mass per unit length value of the model based on the similarity requirement of Eq. 6.4 (assuming equal air density in the wind tunnel and site of the Kessock Bridge). The density ratio similarity cannot be matched accurately due to the thin deck section of the prototype. Thus, the deck section and the diaphragm of the model (separators underneath the deck for stiffening purpose, see Figure 6.5) have been substituted with plywood, which successfully reduced the weight. But the thin deck section suggested that the plywood would not be stiff enough to maintain the rigidity and might cause unwanted deformation of model during the test. So the design needed to be modified with an increase in the stiffness of the deck section but at the same time trying to minimise the total weight of the model.

In the light of this, the NTU wind tunnel team suggested replacing the plywood deck with aluminium deck and diaphragm in order to increase the stiffness of the deck section for the model. At the same time, balsa wood is used to substitute the plywood part of the sectional model. Balsa wood is lighter compared to plywood but still provides the necessary geometric representation of the prototype. Also, some of the diaphragms have been replaced by balsa wood rather than all aluminium diaphragms. Table 6.1 shows the mass per unit length of the designs for the sectional model with the combination of aluminium with plywood or balsa wood.

Table 6.1 Mass per unit length of the designs of the Kessock Bridge sectional model.

Description of material (Aluminium & plywood)	Mass per unit length (*kg/m*) (Eq. 5.4)	Mass per unit length (*kg/m*) Actual design
Plywood main deck	*3.4*	*3.2*
Balsa wood main deck	*3.4*	*2.7*
Aluminium main deck	*3.4*	*6.2*

The design with aluminium and balsa wood (denoted as aluminium main deck in table 6.1) has been chosen as the final design of the sectional model. In this case, the mass ratio of the model has been relaxed (extra mass allowed) to ensure no under deformation happens, the extra mass of the model might alter the characteristics of the prototype such as the frequencies of the vertical and torsional vibration. Since the rotational inertia was not s scaled in the design of the wind tunnel model, some adjustments need to be made while mounting the model onto the rigs in the wind tunnel. This will be discussed in the setting up of the experiment later in this section.

If the scaling of the similarity requirement is appropriately done, the wind tunnel model of the bridge should show similar response to wind as the prototype. From the observation of the response of Kessock Bridge, large amplitude vibration occurred when the wind speed is around *22 m/s* [98]. The study also indicated that the first vertical vibration mode of the bridge is at *0.51 Hz* and it is the main mode of vibration. From these data, we are able to predict the wind speed and the frequency of vibration of the wind tunnel model based on Eq. 6.2 and Eq. 6.3. From Eq. 6.3, assuming equal gravitational force of the wind tunnel and at the site of the Kessock Bridge:

$$\frac{u_p}{u_m} = \frac{B_p}{B_m} \times \frac{N_p}{N_m} \qquad \text{Eq. 6.5}$$

where subscript *p* and *m* represent the values for the prototype and the model respectively. From Figure 6.4 and 6.5,

$B_p=21.9m,\ B_m=0.55m$ and $u_p=22m/s$ as mentioned

Eq. 6.2 gives a *3.5m/s* model wind speed when the vibration should occur in the wind tunnel test. Applying the same analysis on Eq. 6.5, a vibration frequency of *3.2Hz* is obtained for the model (assuming that the model vibrates at *3.5m/s*). These predictions will be discussed in Section 6.3.1.

6.2.2.1 Setting up of the model in the wind tunnel

The *1:40* scale sectional model of the Kessock Bridge measures *0.55m* in breadth and *1.8m* in length. Figure 6.5 shows the dimension of the cross section of the model and the three-dimensional view of the model. The figure also depicts the materials used for individual parts of the model.

Prior to the wind tunnel test, modifications were made to the model [21]. The major concern was the stiffness of the main deck to withstand any flexing or bending during the test, since a section model test is supposed to represent a rigid section of the prototype. Thus, extra bracing using aluminium plates were added at the under side of the bridge, with cross wires tied diagonally between the aluminium plates (Figure 6.6 and 6.7). Geometrically, from the observation of the prototype cross section details (Figure 6.4), top flanges (eaves) have been added onto the model using balsa wood (Figure 6.8) to simulate the geometry of the prototype. These flanges, located near to the top corner of the bridge deck, are important because they could result in significant changes to the separation of the flow and thus the vortical structures on the deck surface, which in turn affects the aerodynamic forces.

The *1:40* scale model is then mounted between the wind tunnel walls in a cross flow situation onto two rigs supported on coil springs attaching at the corners of the model (Figure 6.9). The springs are connected to the model using sliding brackets (Figure 6.10) which can be adjusted accordingly to achieve the vibration frequencies of the prototype. The distance between the springs controls the torsional stiffness of the model to match the prototype torsional frequency.

6.2.2.2 Force measurement

For the study of the static wind loading on the model, load cells (Figure 6.11 to Figure 6.13) have been mounted around the section to measure the drag, lift and moment of the model. Lift force and moment have been measured using four load cells (load cell 1 to load cell 4 in Figure 6.11) fixed vertically at corners of the section (Figure 6.12). Two other cells (load cell 5 and load cell 6 in Figure 6.11) were attached horizontally on the

ends of the model section for the drag force measurement (Figure 6.13). The lift, drag and moment coefficients are calculated as follow,

$$C_L = \frac{F_L}{1/2\,\rho u^2 LB} \quad \text{Eq. 6.6}$$

$$C_D = \frac{F_D}{1/2\,\rho u^2 LB} \quad \text{Eq. 6.7}$$

$$C_M = \frac{F_M}{1/2\,\rho u^2 LB^2} \quad \text{Eq. 6.8}$$

where F_L, F_D and F_M are the lift force, the drag force and the moment measured from the load cells respectively. ρ and u are the density of the air and the speed of the flow in the wind tunnel. The characteristic lengths L and B refer to the span length and the chord length of the model respectively.

For pressure measurement, pressure taps have been set up around the middle section of the model. Figure 6.14 and 6.15 show the position of the pressure taps. Tap *1* to tap *4* are on the top surface of the model, while tap *5* to tap *7* are underneath the deck section. The pressure taps are connected to the pressure sensors through short tubing. Each of the taps is equipped with pressure sensor to record the data.

6.3 RESULT AND DISCUSSION

In section 6.3.1, the observation on the response of the sectional model test to wind excitation has been compared to the full scale measurement of the prototype. The next section (section 6.4) compares the simulated result (DES) of the sectional model and the result of the wind tunnel test.

6.3.1 Wind tunnel sectional model and prototype

To capture the wind excitation response of the wind tunnel model of the Kessock Bridge, wind is slowly increased in the test to investigate the changes of the behaviour of the model. From the observation, the model started to show vibration at around *3m/s*, which corresponds to the prototype wind speed of *19m/s*. Based on Eq. 6.2, the theoretical wind speed for the test at which the excitation should occur is about *3.5m/s* (as calculated in section 6.2.2). Lower wind speed has been predicted from the wind

tunnel test. This might be due to the measurement of gross wind speed (considering wind from all directions) from the full scale measurement.

As reported by Gu (2004) [41], slightly lower wind speed when the vibration happened is observed if the full scale wind speed is normalized (only the normal wind component acting on the bridge is considered, similar to the setting of the wind tunnel test). In this case, comparison of the normalized full scale wind speed and the wind tunnel model measurement is more appropriate leading to a better agreement. Table 6.2 shows the comparison of the prototype gross wind speed and the normalised wind speed (with reference to [41]) with the measured wind speed of the model at which the excitation of the Kessock Bridge occurs.

Table 6.2 Comparison of prototype wind speeds and wind tunnel measurement when vibration occurs [21, 98].

Gross wind speed (Prototype)	Normalised wind speed (Prototype)	Wind tunnel speed
22.0m/s	*19.8m/s*	*19.0m/s*

From the observation of Owen *e. al.* (1996) [98] on the wind response of the Kessock Bridge in the spring of *1992*, it was reported that the bridge vibrated (with peak displacement of *±110mm*) with a vertical mode of *0.51Hz* at wind speed of about *22m/s*. The measurement of the wind tunnel model produced similar situation. From the time history of the fluctuating component of the wind tunnel measurement, the frequencies of the vibration modes can be obtained. Table 6.3 shows the value of the vibration frequencies of the prototype and model during the wind excitation. Notice that there exist some rotational mode of vibration as well, but the vertical mode is the main vibration according to the observation [98]. Discrepancy observed in the rotational frequency could be attributed to the lack of consideration of the scaling of the rotational inertia during the design of the wind tunnel model.

Table 6.3 Frequencies of vibration of prototype and wind tunnel model [21, 98].

	Vertical mode	Rotational mode
Prototype	*0.51Hz*	*0.70Hz*
Model	*0.60Hz*	*0.98Hz*

More measurement data and analysis of the wind tunnel test of the Kessock Bridge model has been covered in the reports produced by Choi *et al.* (2004) [20, 21]. The reports summarise the force measurement, the instability test and the pressure distribution study of the wind tunnel test.

6.4 DES OF FLOW AROUND THE KESSOCK BRIDGE DECK SECTION

In the previous two chapters, DES has been applied on the study of the flow around a circular cylinder and rectangular cylinders. Observation on the solutions of LES and DES concluded that DES is more suitable for the simulation of the flow around a bridge deck section, mainly due to its computational efficiency and the capability of DES to capture the dynamic characteristics of flow similar to LES prediction.

DES of flow at Reynolds number of *33,000* with incoming wind speed of *6.5m/s* has been simulated for the Kessock Bridge deck section. The wind tunnel test includes measurement of wind speed from *2m/s* to *13m/s*, *6.5m/s* has been chosen in between the maximum and the minimum wind speed measured. If all of the wind speeds are to be simulated, very long computational time is needed based on the findings of the previous chapters. A refined mesh is needed around the deck section to resolve the flow profiles where separation and reattachment points of the flow occur. In the DES of flow around the bridge deck section, a hexahedral mesh has been built by Sun *et al.* (2004) [125] for the simulation of flow around the *1:40* scale deck section (Figure 6.17). The mesh employed gives satisfactory y^+ (section 3.2.1.1) values near the wall, which has an average value of *1.87* (Figure 6.16).

The DES turbulence model used in the simulation of the flow around the bridge deck section employed the SST model (section 2.2.2) near the wall and the LES model (section 2.2.1) in the wake region of the flow. Similar to previous applications, the LES is based on a second order central difference scheme for spatial discretisation and a second order backward Euler time differencing scheme for temporal discretisation. For the SST turbulence model, a second order upwind discretisation scheme has been employed.

6.4.1 Mesh sensitivity analysis

For the simulation of the flow around the *1:40* scale bridge deck at wind speed of *6.5m/s*, three different meshes have been used for the mesh independence test. The numbers of element used in each mesh is *1.9 million*, *2.7 million* and *3.1 million* elements which correspond to mesh I, mesh II and mesh III respectively in Figure 6.18. Figure 6.17 shows the mesh around the bridge deck section for mesh I. Mesh II and mesh III have similar mesh structure but are gradually refined in the spanwise direction. The spanwise resolution changes from *20, 28* to *32* seeds for mesh I, mesh II and mesh III respectively.

Basic flow parameters have been compared for the mesh sensitivity analysis. The time history of the lift, drag and moment coefficients predicted from the simulations are compared in Figure 6.18 to ensure that different meshes employed predict consistent result. Good agreement of the coefficients is observed, implying that mesh independence has been achieved.

Figure 6.19 plots the power spectrum of the lift coefficient of the three different meshes. All the simulations predicted the same frequency of lift, which corresponds to the frequency at which vortices are shed from the trailing edge of the bridge deck section. This suggests that the three different meshes employed actually predicted very similar vortex structures around the section.

As well as the above, the pressure distribution on the surface of the deck section has been compared for the three meshes employed. Figures 6.20 to 6.22 show the pressure distribution for the simulations. It can be seen that the pressures predicted show a consistent distribution as the meshes are refined.

6.4.2 Computational time

Obviously, computational time is one of the major considerations in CFD simulations. This section discusses the simulation time for the flow around the deck section based on the comparison with previous simulations of the flow around rectangular cylinders. In the simulation of the flow around the bridge deck section, a time step of *0.0015* has been used, corresponding to *70* time steps (calculated based on the Strouhal number from the wind tunnel experiment) for one complete vortex shedding cycle. This time step is used to make sure that the vortices are properly resolved. A time step that is too large leads to inaccurate results. On the other hand, very long computational times will be needed if the chosen time step is too small.

Figure 6.23 compares the computational time needed for the simulation on the bridge deck section and rectangular cylinders. The *x*-axis represents different aspect ratios for the rectangular cylinders cases. In the figure, the low Reynolds number cases refer to Reynolds numbers ranging from *1,000* to *3,000* while the high Reynolds numbers are close to the wind tunnel test speed (between *Re 33,000* to *Re 100,000*) of the Kessock Bridge. Comparatively, computational time of the flow around rectangular cylinders provides an idea of the magnitude of the simulation of the bridge deck section. Generally, the DES of flow around the bridge deck section required about *2.5* times the computational time of the flow around rectangular cylinders at high Reynolds number (comparing green diamond marks to green triangular marks in Figure 6.23).

To provide an idea on the CPU time used in Figure 6.23 with respect to normal wall clock time, a *30* CPU minute means *30* minutes is needed to compute one time step in a simulation on a single PC. All the simulations have been done on a parallel computing system with multi processors. From the simulated result (Figure 6.23), a *30* CPU minute simulation is equivalent to *21* days of simulation time with *12* processors running for a simulation of about *10,000* time steps at a Reynolds number of *33,000*. Based on the time taken for simulations of flow around rectangular cylinders (LES and DES), the estimated time for the LES on the flow around the bridge deck section for the three different meshes has been plotted. From the prediction, it is obvious that the application of LES on the flow around a bridge deck section is not practical in this project at the moment, bearing in mind that *48* days (estimated) of computational time is needed for simulation on the *1.9* million element case (mesh I) compared to *21* days of DES.

Figure 6.24 shows the number of elements used for each simulation shown in Figure 6.23. Generally, increasing the number of elements for the simulation proportionately increases the computational time. No huge difference on the number of elements is noticed between DES and LES at cases with low Reynolds number (*1,000* to *3,000*) simulations but this went up to *1.7* times different for high Reynolds number (*33,000* to *100,000*) simulations. It is estimated that LES needed *5* million elements for similar case as the DES (mesh III) with *100* days of simulation time. Again, the prediction concluded that LES on the flow around a bridge deck section is not practical for the current work for the time being.

6.4.3 Force coefficients

Table 6.4 compares the prediction of the lift, drag and moment coefficients of the Kessock Bridge deck section between DES and the measurement of the wind tunnel test at a wind speed of *6.5m/s* with zero angle of attack. Angle of attack of the wind significantly affects the force coefficients. Due to restricted time for the current work, only zero angle of attack has been simulated for the time being. The force coefficients from all the three different meshes have been included in the table. From the observation, DES predicted generally close drag force and moment coefficients compared to the wind tunnel measurement.

However, the lift force computed from DES is a lot more negative than the wind tunnel observation. One of the reasons for the discrepancy is the presence of the top flange (eaves) in the wind tunnel model (Figure 6.8), which significantly changed the vortical structures at the separation point of the flow. This feature (top flange) is not simulated in the DES of the flow around the deck section. This is because the simulation was conducted during the design stage of the wind tunnel model and the top flange of the model was added right before the wind tunnel test begun. The top flange enhances flow separation and results in more intense vortices downstream of the separation point. This creates a larger suction region on the top surface of the deck and thus results in an overall less negative lift, which would lead to a better agreement with the wind tunnel observation. The discrepancy of the lift coefficient observed could be due to the performance of the SST model around the deck section too. SST is a RANS model but the flow around the deck section is characterised by large degree of unsteadiness in particular on the lower part of the deck.

Table 6.4 Comparison of lift, drag and moment coefficients of Kessock Bridge deck section between wind tunnel test and DES prediction.

	Lift coefficient (C_L)	Drag coefficient (C_d)	Moment coefficient (C_M)
Wind tunnel Test [21]	*-0.0525*	*0.1813*	*-0.10742*
DES Mesh I	*-0.3075*	*0.1510*	*-0.0722*
DES Mesh II	*-0.2982*	*0.1505*	*-0.0727*
DES Mesh III	*-0.3006*	*0.1501*	*-0.0726*

Apart from the comparison between the wind tunnel test and DES for lift coefficients, the following discusses some other sources for the lift coefficient measurement as references. It is worth mentioning the investigation of Hay (1992) [44] on the lift coefficients of different bridge deck section. Refer to [44] for details on the measurement technique of the force coefficients of the Kessock Bridge. He reported that the full scale lift coefficient of Kessock Bridge is around *-0.25*, which is closer to the DES prediction compared to the wind tunnel test in the NTU. In his study on the wind tunnel test on bridges, a series of *1:50* scale model of box and plate girder bridges has been tested in the wind tunnel. In this measurement, the open cross section deck shape (very similar to the Kessock Bridge deck section) has a lift coefficient ranges from *-0.06* to *-0.39*, depends on the barriers type and position as well as the live loads such as the vehicles on the bridge. DES currently employed predicted lift coefficient within the experimental work of Hay (1992) [44]. Also, the SST simulation of Sun *et al.* (2004) [125] on the moving mesh of a *1:40* scale sectional model of Kessock Bridge predicted a lift coefficient of *-0.15*. This is more negative than the wind tunnel observation, which is closer to the prediction of DES.

6.4.3.1 Vortex shedding

Figure 6.25 shows the vector plot of the velocity coloured by the streamwise component of the DES of flow around the bridge deck section. The diagram depicts the capability of DES to capture the vortex shedding mechanism of the flow. Based on the frequency of the fluctuating lift coefficient (Figure 6.19), the Strouhal number of the flow is calculated using Eq. 3.2. DES predicted a Strouhal number of *0.097*, which agreed well with the wind tunnel measurement of *0.105* [20].

The simulation also demonstrated proper application of the DES for the flow around the bridge deck section. DES successfully captured the unsteady nature of the flow and yet used less computational time compared to LES. Figure 6.26 shows the region where LES and SST are active during the simulation. LES (blue) is active in the wake region of the flow where unsteadiness of flow is found. The rest of the region is covered by SST (red) in order to save computational effort, which resulted in the difference in the computational time needed between LES and DES as observed in Figure 6.23. This is because SST model requires significantly less simulation time compared to LES (as discussed in Chapter Three).

6.4.4 Pressure distribution

The pressure distribution around the middle section of the *1:40* scale sectional Kessock Bridge model has been measured in the wind tunnel test [20]. As part of the validation of the DES model in the study on the flow around the bridge deck section, the computed pressure distribution from DES has been compared to the measurement of the wind tunnel test.

Figure 6.27 shows the comparison of the surface pressure distribution on the top and the bottom deck of the wind tunnel test and the computed result from DES. The multiple lines of the simulated results represent pressure distribution at successive time steps during a simulation. DES managed to capture changes of the pressure from the leading edge to the trailing edge similar to experimental observation. However, the simulated results show discrepancies at the bottom surface of the deck compared to the wind tunnel test. DES predicted a more negative result compared to the wind tunnel measurement but general trend of the pressure distribution has been captured.

The different magnitude observed could be attributed to the changes of the flow structures caused by the diaphragms and the web and deck stiffeners underneath the

deck section. These details were not simulated in the DES. Another reason is the difference between the simulation of a fixed deck case on DES and the moving deck case in the wind tunnel test. Notice also the scattered result observed from the wind tunnel test, which is caused by the changes of the wind velocity from time to time. It is not easy to maintain a constant wind speed in the test, perhaps normalisation of the test data may help to reduce this variation to some extent.

6.4.4.1 Fluctuating frequency of pressure changes

In the wind tunnel test, the peak frequency at which the pressure fluctuates at each pressure point has been identified. Table 6.5 shows the pressure fluctuation frequencies of the measured wind tunnel test and the predictions from DES at point *7* on the bridge deck (Figure 6.14). Notice that two frequencies have been observed from the wind tunnel measurement, with *8.5Hz* as the main fluctuating frequency and *16.1Hz* as a secondary fluctuation, which corresponds to a lower peak observed on the plot of the power spectrum [20].

Table 6.5 Peak frequencies of pressure fluctuation at point *7* of Figure 6.14.

	Peak frequency (main)	Peak frequency (secondary)
Wind tunnel test	*8.5Hz*	*16.1Hz*
DES	*7.8Hz*	*15.5Hz*

DES managed to predict the fluctuating frequencies close to the experimental measurement [20]. As the point of comparison (point *7* on Figure 6.14) is located near to the trailing edge of the deck section, the fluctuating pressure is associated with the vortices shed into the wake region of the flow. This suggests that the Strouhal number of the flow can be calculated using Eq. 3.2 by taking the frequency term in the equation as *7.8Hz* (DES prediction). From the DES prediction, the pressure fluctuation frequency at point *7* showed a Strouhal number of *0.093*, which agreed well with the

wind tunnel measurement of *0.105* [20]. This indicated the ability of DES to resolve the vortex structures correctly around the trailing edge of the deck section.

6.4.5 PCA and pressure analysis

Aerodynamic forces exerted around a body enveloped in a flow are caused by the fluctuating pressure around the body. Knowledge of the statistical characteristics of the pressure distribution allows interpretation of the related physical mechanisms of the flow to be made. As mentioned in the previous chapter (section 5.4.1), the principal component analysis (PCA) technique has been applied to study the pressure distribution around rectangular cylinders for the identification of the major features of the pressure changes during the flow. From the study, it is noticed that, physically, PCA relates each different principal components to a particular mechanism of excitation. For instance, the first principal component corresponds to the lift effect while the second principal component is associated with the drag component of the flow.

Grenet and Ricciardelli (2004) [40] applied a similar mathematical technique called the spectral proper transformation (SPT) to analyse the pressure changes around a square cylinder and a bridge deck section. Mathematically, the concept of SPT is similar to PCA applied in the previous chapter, except that PCA analyses the pressure distribution based on the covariance matrix eigenvectors while SPT uses the spectral density matrix eigenvectors. In SPT, the computed modes are uncoupled in all frequencies and time lags and thus provide more information on the physics of the changes in the flow. This indicates that SPT is more sensitive to situation where variation of the frequency introduces significant effect on the flow parameters. For example, the first principal component in an SPT might represent the lift mode caused by the vortex shedding while the second principal component indicates also lift mode but from buffeting. The PCA applied in the previous chapter did not identify this difference.

However, the downside of SPT is that more computer power is needed for the analysis compared to the PCA due to the extra information provided. Grenet and Ricciardelli (2004) [40] concluded that SPT allows more accurate and detail separation of the modes associate with certain physical excitation at different frequencies.

6.4.5.1 PCA and pressure distribution around the bridge deck section

Figure 6.28 shows the first principal component of the pressure distribution around the Kessock Bridge deck section based on the PCA. From the figure, it is noticed that the pressure on the top and bottom deck surfaces of the bridge distributed mainly on one side of the *x*-axis of the graphs. This suggests that significant vertical force is induced on these surfaces compared to the less influence pressure forces have on the front and rear surfaces of the bridge (where a more even pressure distribution is observed on the graphs). The observation agrees with the plot of the pressure force on Figure 6.30, where the first principal component contributes to the lift force exerted on the bridge deck section.

Distribution of the pressure trend from the second principal component of the PCA is shown on Figure 6.29. Compared to the first principal component, this shows a more even pressure distribution (total area on both sides of the *x*-axis of the graphs nearly cancel each other out) on the top and bottom deck surfaces of the bridge. On the other hand, the one-sided pressure distribution on the front and the rear surfaces of the bridge introduces drag forces on the structure. This can be seen from the pressure force calculated in Figure 6.30.

The eigenvalues of the principal components of the PCA are shown on Figure 6.31 and 6.32. As mentioned in the previous chapter, the highest eigenvalue corresponds to the principal component that contains the most variation of the pressure changes, thus representing the most dominant mode among the distribution. The figures indicate that the first and second principal components of the pressure distributions around the deck section consist of at least *99%* of the total variation of the pressure. This suggests that the application of the PCA on the pressure distribution analysis around the bridge deck section successfully reduces the complexity of the data to give a compact and optimal description of the overall pressure distribution.

6.5 CONCLUSION

The sectional wind tunnel test of the *1:40* scale Kessock Bridge deck section provides useful data for the comparative study with the numerical solution as well as the full scale observation of the flow around the bridge. Similar response of the deck section to wind excitation as the prototype has been noticed in the wind tunnel test including the vortex shedding vibration of the bridge.

In the numerical study of the flow around the bridge deck section, DES managed to simulate the vortex shedding phenomenon well, obtaining a Strouhal number very close to the wind tunnel measurement. The computed static loads of the DES show good agreement with the measured wind tunnel test solution apart from the lift coefficient, which differs significantly. However, the value is close to the finding of the SST simulation and earlier wind tunnel measurement of an open cross section deck.

Application of the PCA on the study of the pressure distribution around the bridge deck section provides further understanding of the flow features around the deck section. It is known that the angle of attack of the flow significantly affects the force distribution around the deck section. Only zero angle of attack case has been investigated in the current work due to restricted time, further work should cover range of angles of attack.

In terms of the performance of DES in the wake region, a more constant vortex street in the wake region is predicted. This can be solved by replacing DES with LES, LES is capable of predicting more complex and turbulence nature of flow (based on the investigation on the previous chapters). But this implies that more powerful computer is needed.

All in all, provided that enough computer resources are available, DES is recommended as one of the most suitable approach to study the bridge aeroelasticity responses. It is more efficient than LES when simulation is at higher wind speed such as the Reynolds number at the level of the wind tunnel test.

Figure 6.1 The Kessock Bridge, to the left of the photo is the Beauly Firth while Moray Firth is to the far right [27].

Figure 6.2 Location of Kessock Bridge [83].

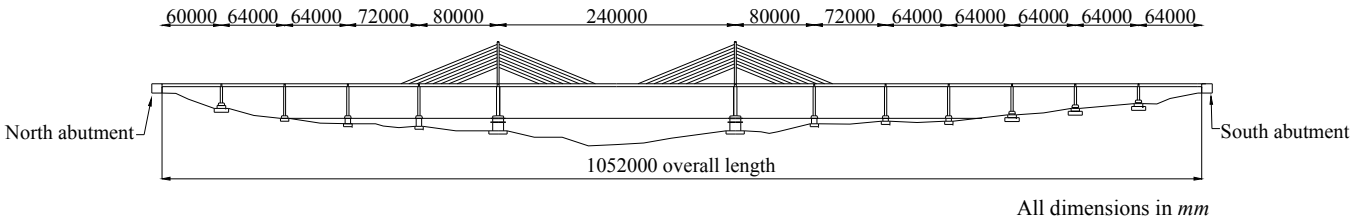

Figure 6.3 Elevation of Kessock Bridge.

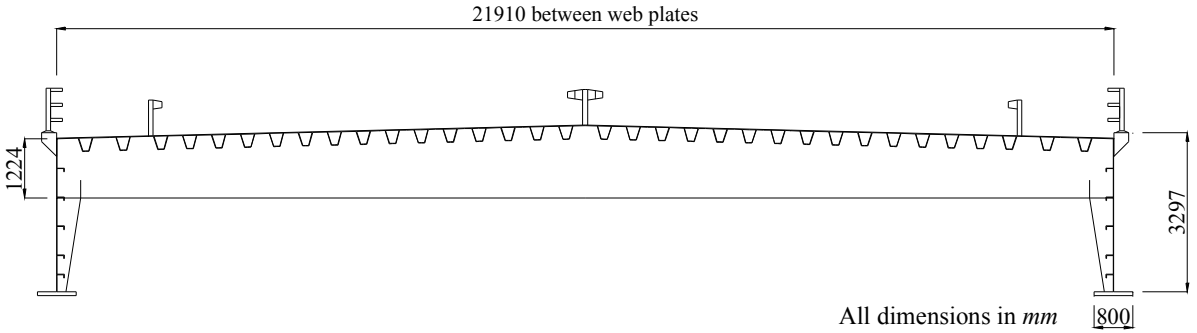

Figure 6.4 Cross section of Kessock Bridge.

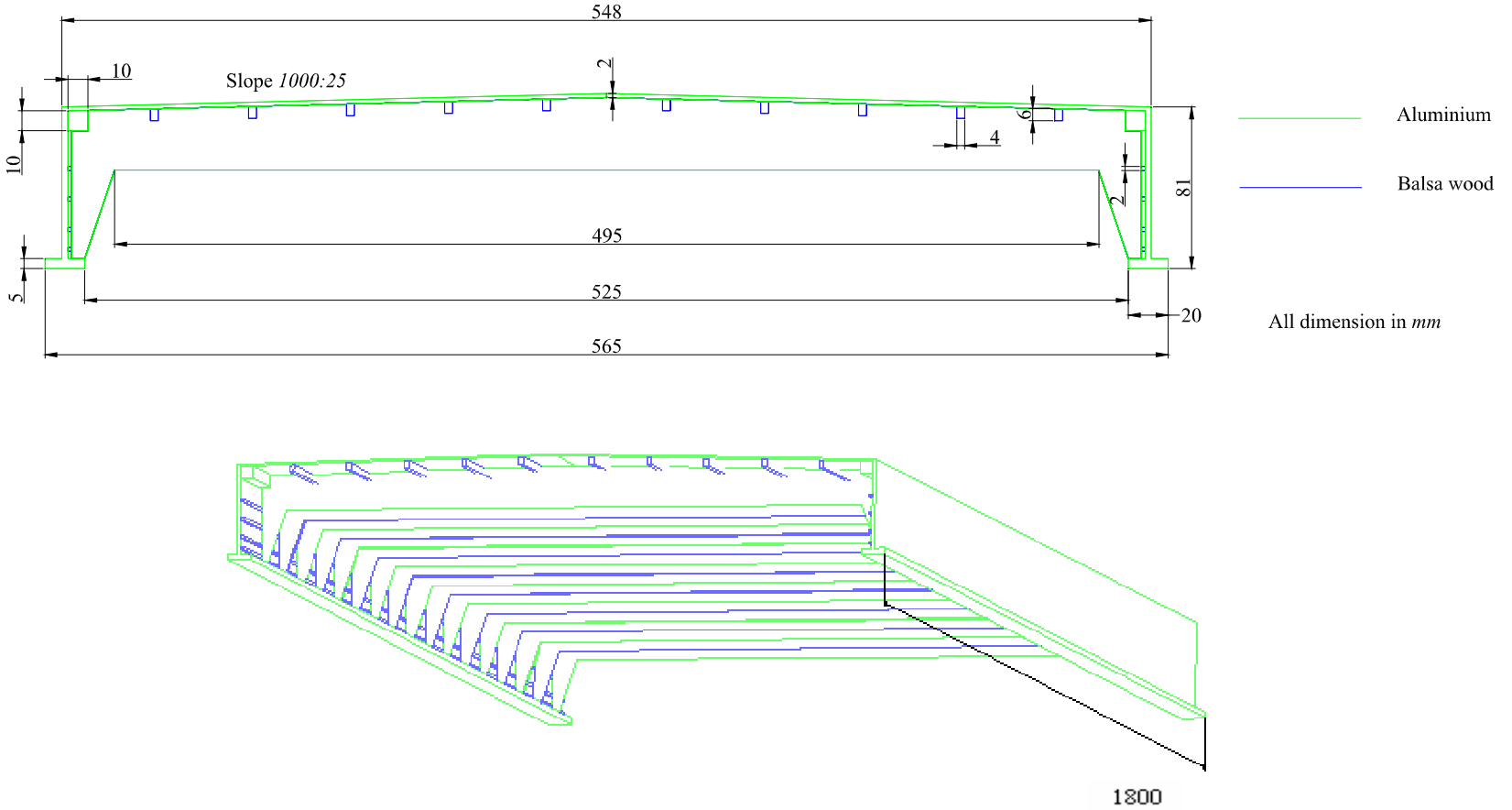

Figure 6.5 Dimensions of a *1:40* scale section wind tunnel model of Kessock Bridge.

Figure 6.6 Aluminium bracing underneath the bridge deck.

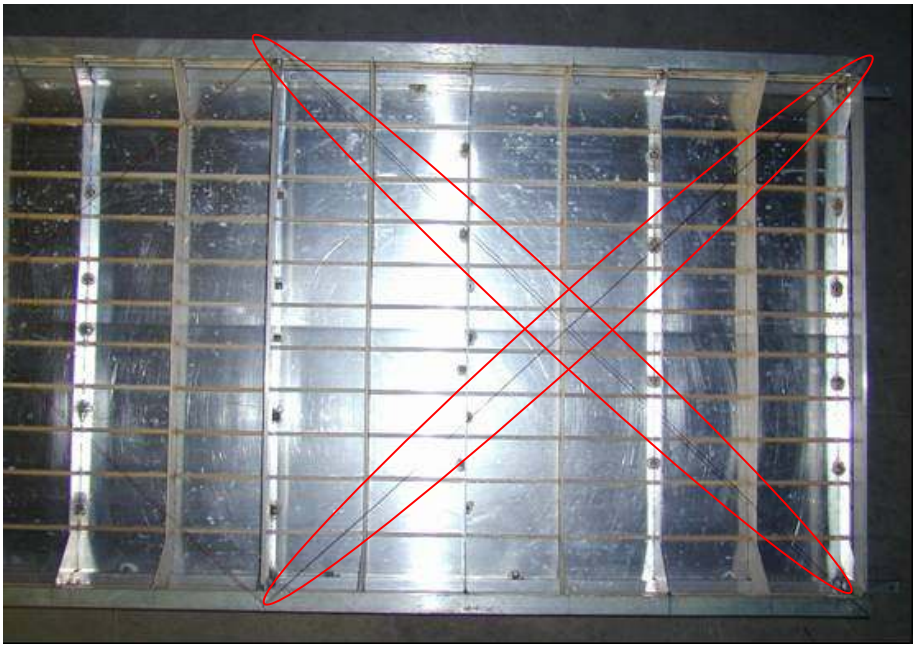

Figure 6.7 Steel wires bracing at the underside of the model to increase stiffness of the section.

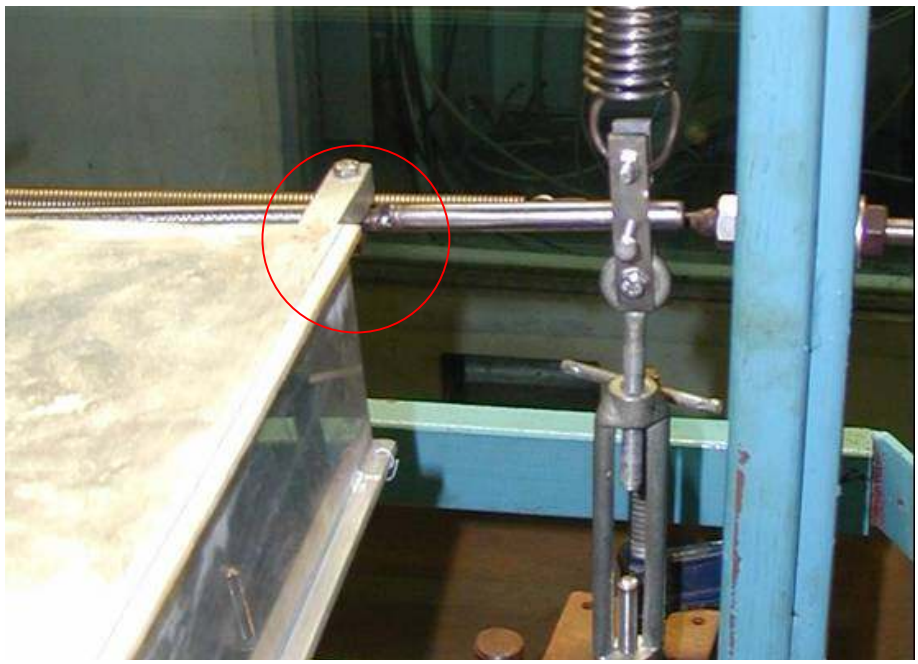

Figure 6.8 Top flange (eaves) to maintain the physical geometry of the prototype.

Figure 6.9 *1:40* scale sectional model of Kessock Bridge on the mounting rigs.

Figure 6.10 Sliding brackets attached to the springs for adjustment of the frequency of vibration of the model.

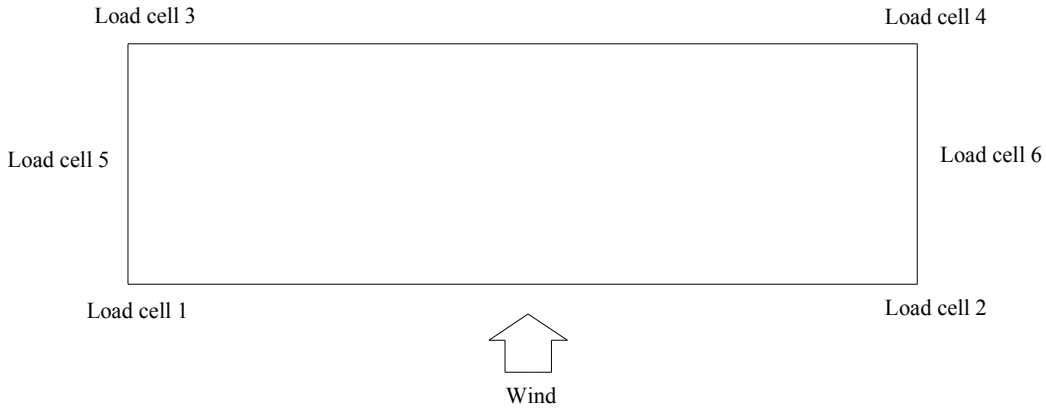

Figure 6.11 Location of load cells around the sectional model (plan view).

Figure 6.12 Load cell for lift measurement.

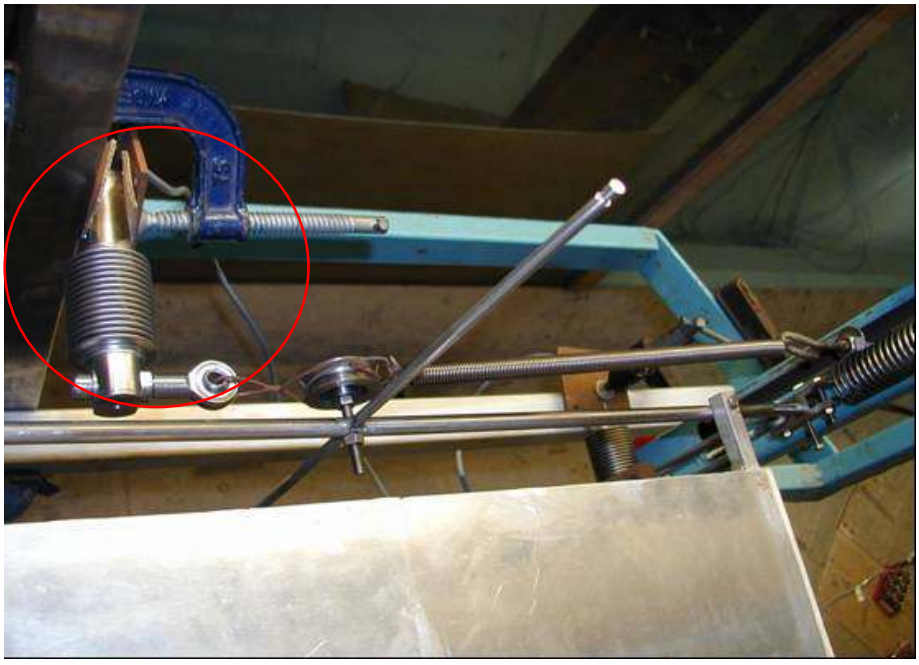

Figure 6.13 Load cell for drag measurement.

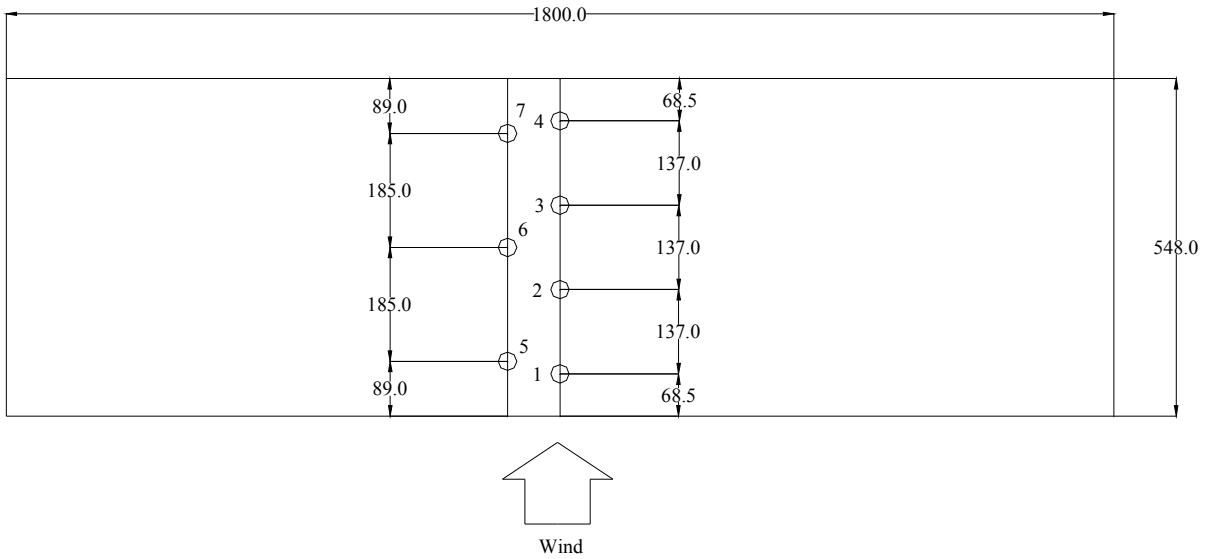

Figure 6.14 Position of pressure taps around the model (plan view), all dimension in *mm*.

Figure 6.15 Pressure taps *5, 6* and *7* underneath the deck section of the model.

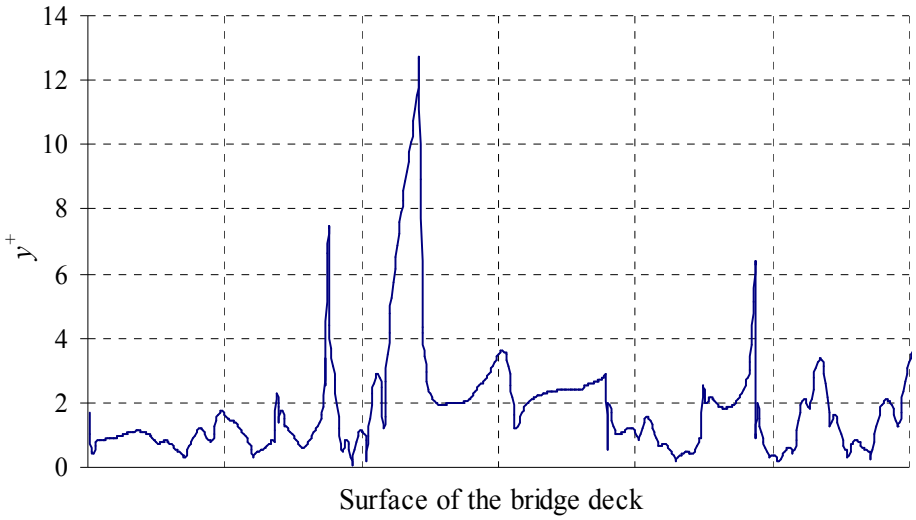

Figure 6.16 y^+ values around the bridge deck section (average=*1.87*).

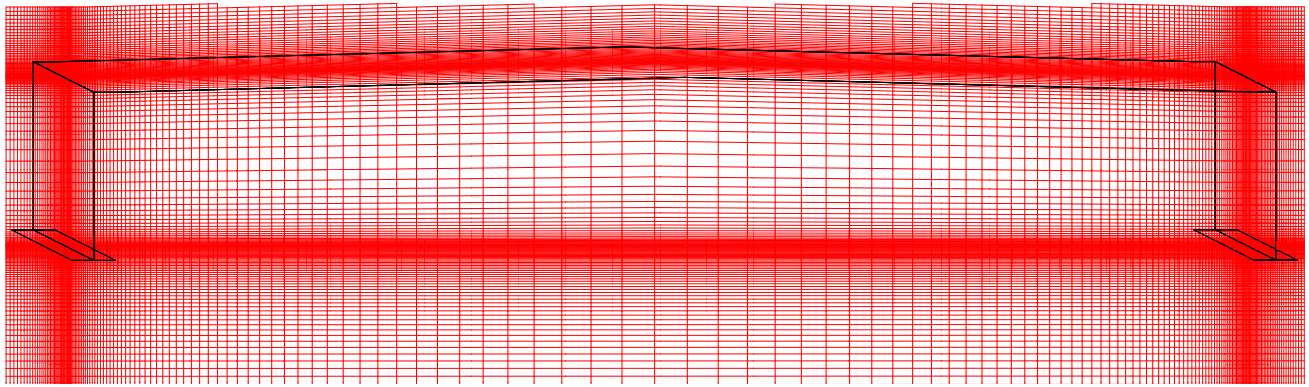

Figure 6.17 A hexahedral mesh around Kessock Bridge deck section [125].

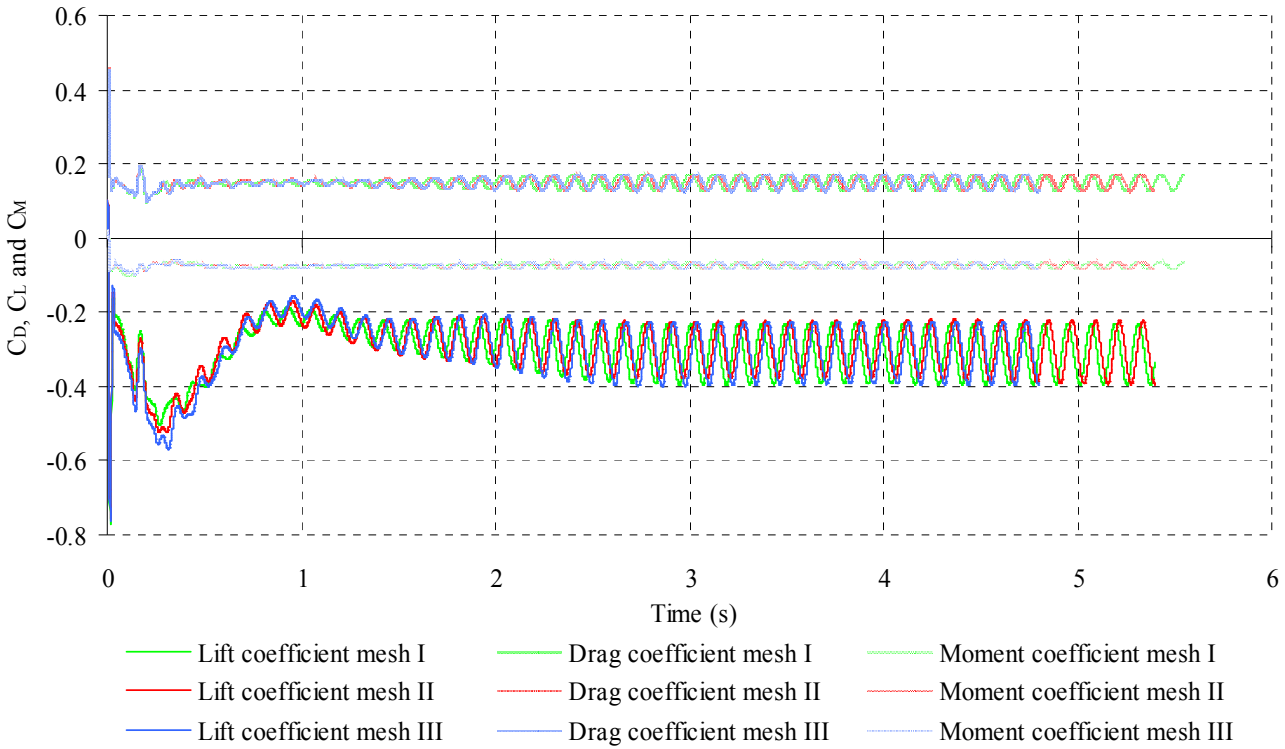

Figure6.18 Lift, drag and moment coefficients for mesh independence test.

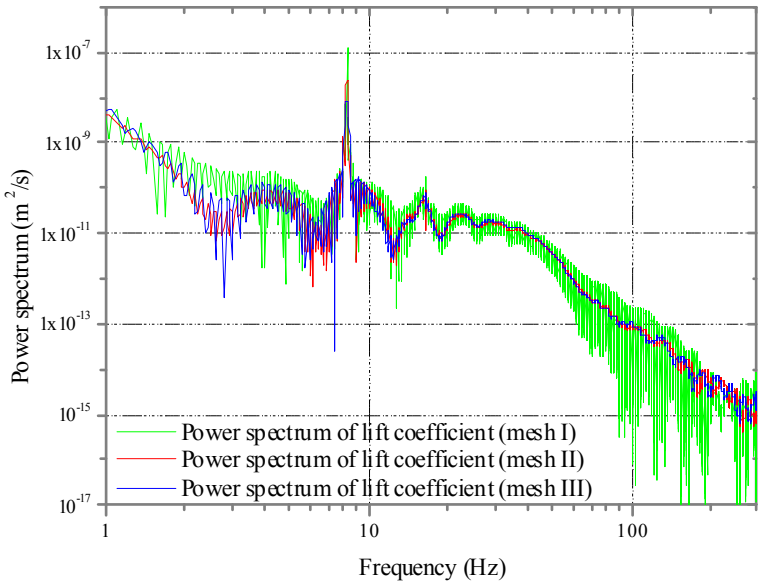

Figure 6.19 Power spectrum of lift coefficients of mesh I, mesh II and mesh III.

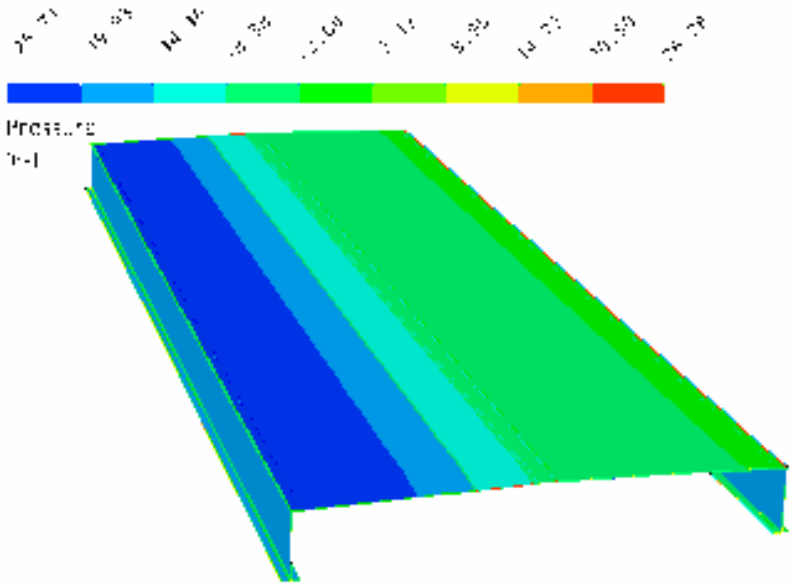

Figure 6.20 Pressure distribution on the surface of Kessock Bridge of mesh I.

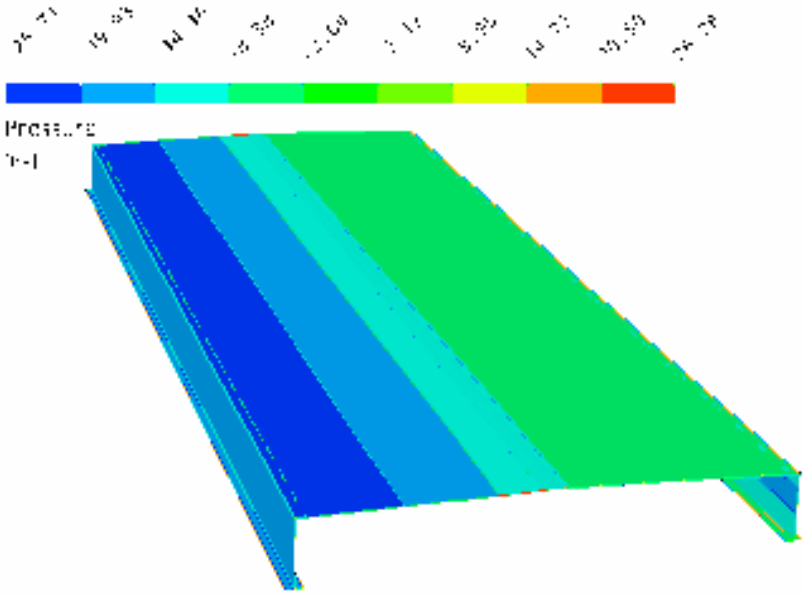

Figure 6.21 Pressure distribution on the surface of Kessock Bridge of mesh II.

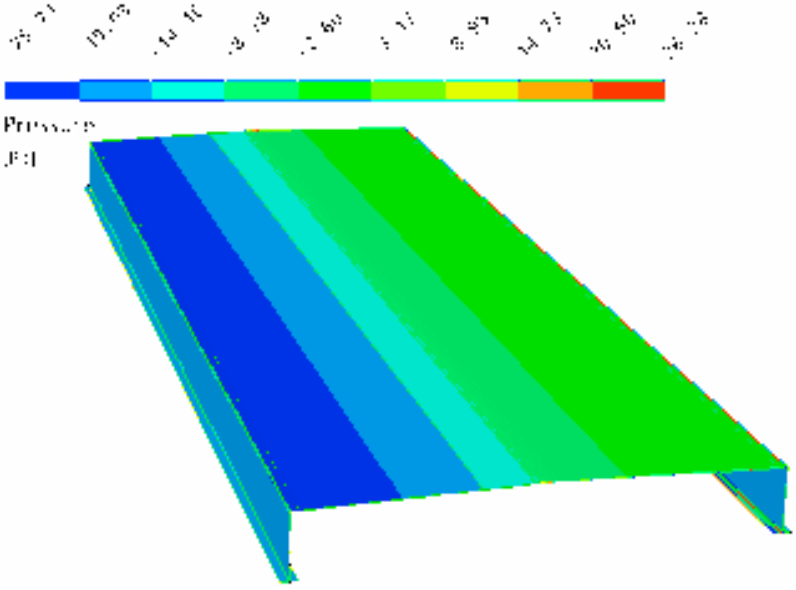

Figure 6.22 Pressure distribution on the surface of Kessock Bridge of mesh III.

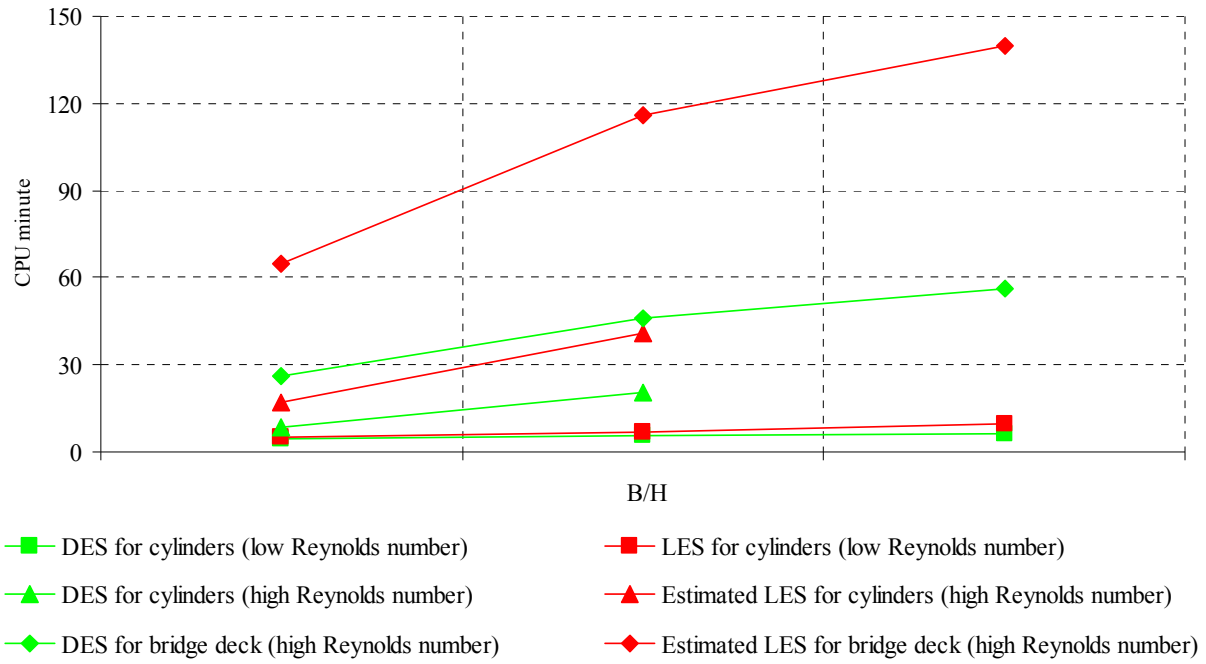

Figure 6.23 Computational time for bridge deck section and rectangular cylinders.

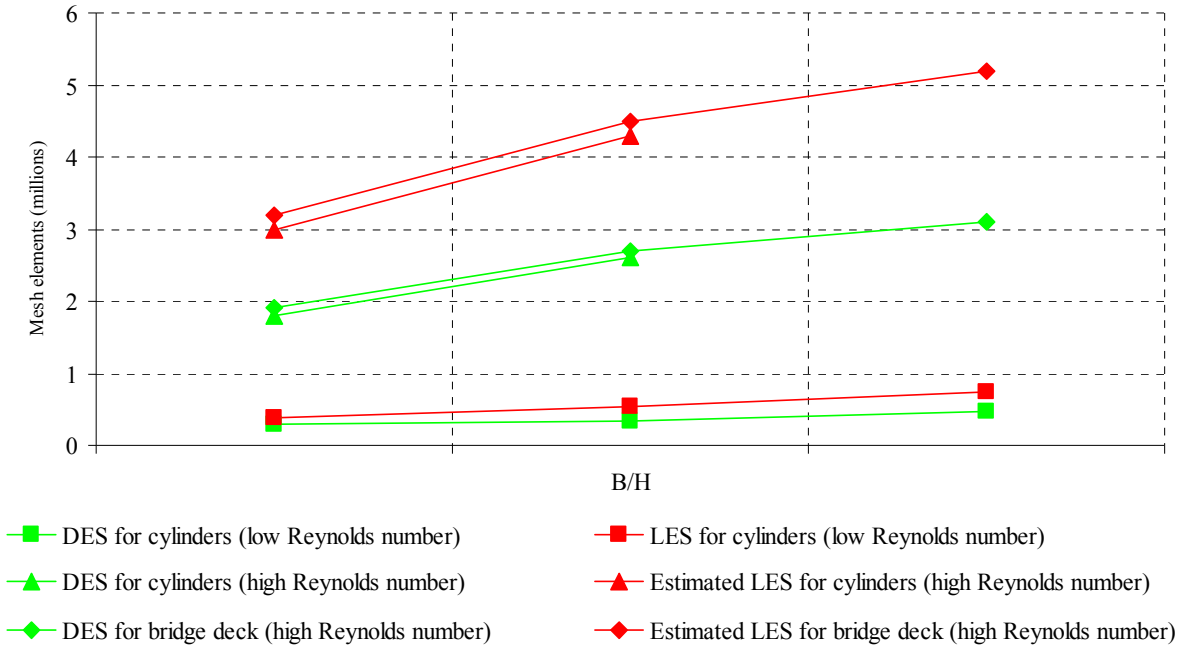

Figure 6.24 Number of elements used in the simulation of cylinders and bridge deck.

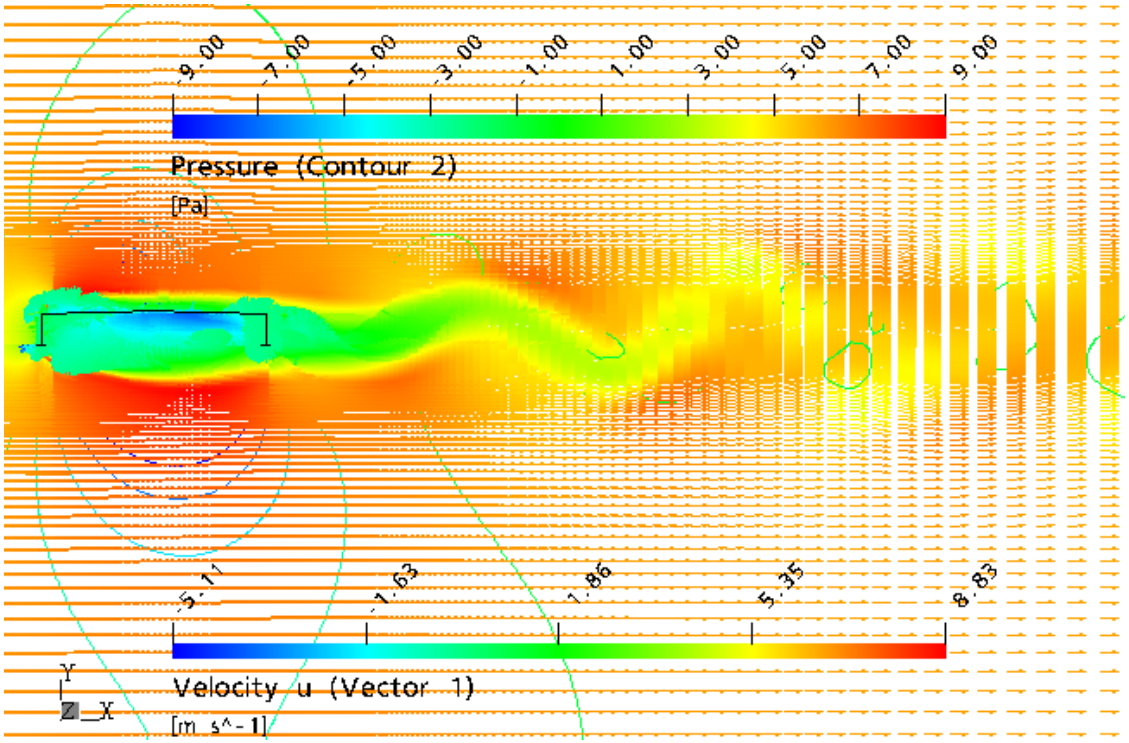

Figure 6.25 Vortex shedding in the wake region of the Kessock Bridge deck section (DES).

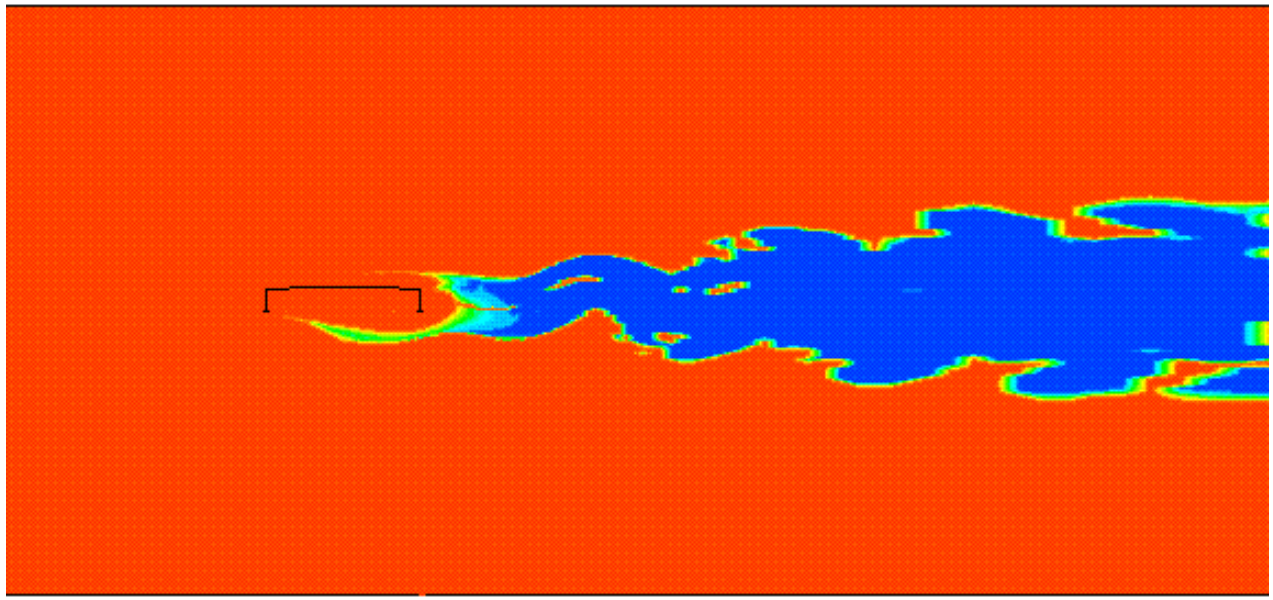

Figure 6.26 Region of SST (red) and LES (blue) in the DES of flow around the Kessock Bridge.

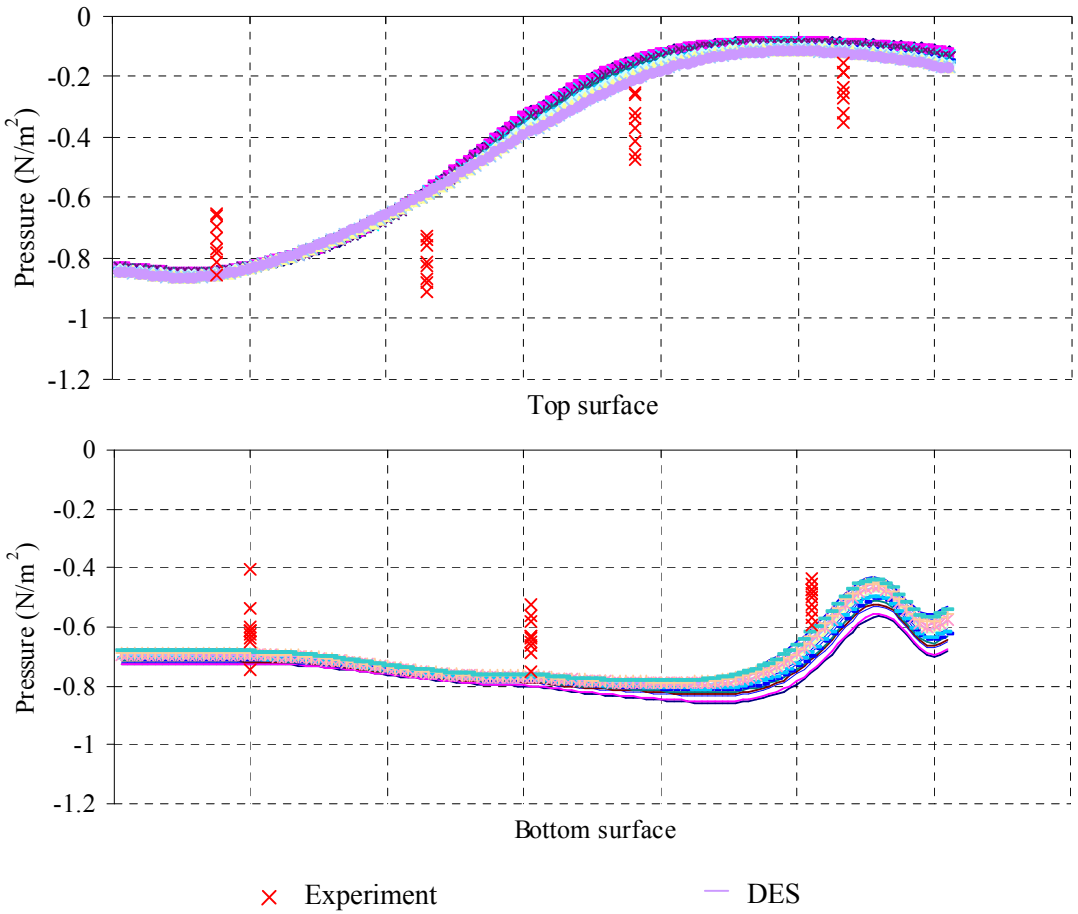

Figure 6.27 Pressure distribution on top and bottom surface of the Kessock Bridge deck section.

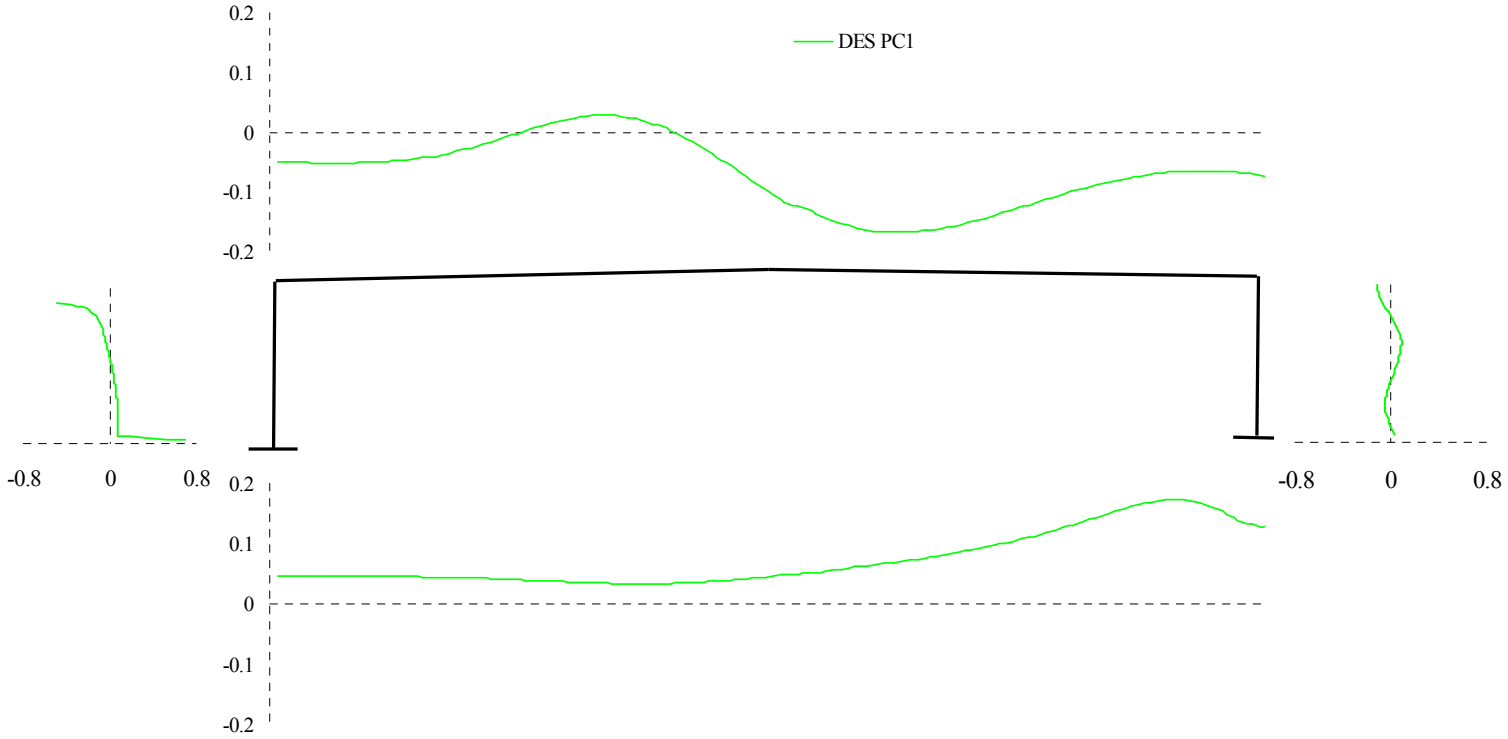

Figure 6.28 First principal component of pressure distribution (N/m^2) around deck section.

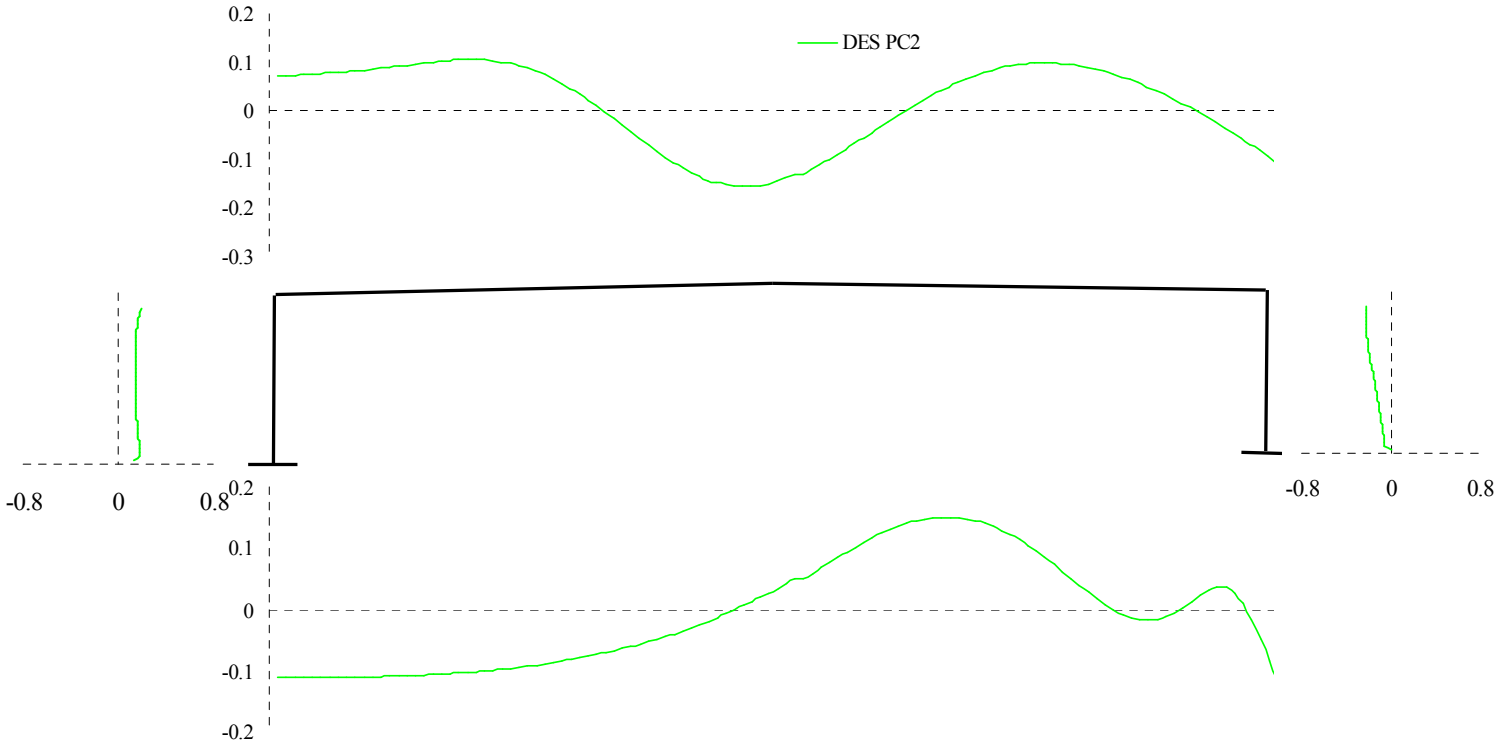

Figure 6.29 Second principal component of pressure distribution (N/m^2) around deck section.

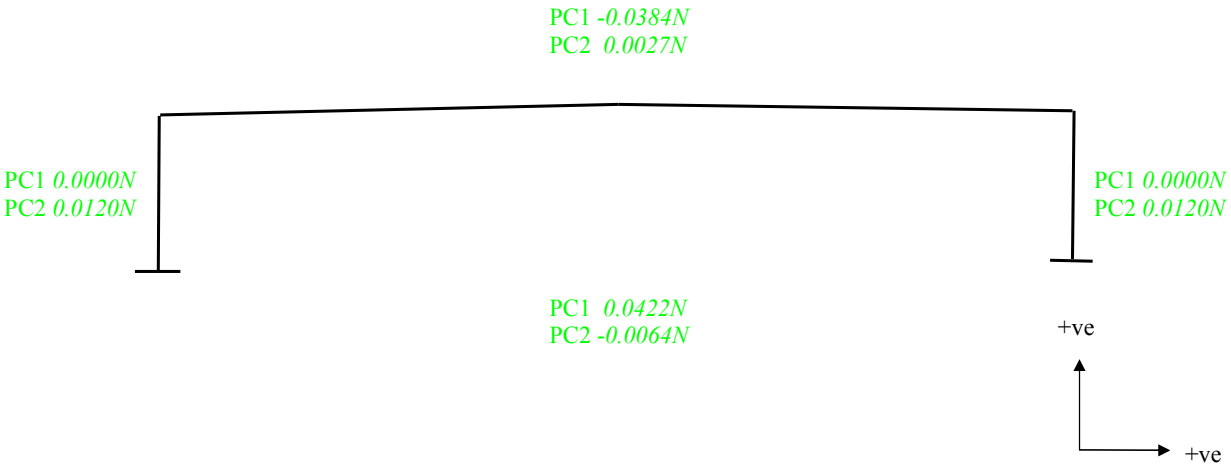

Figure 6.30 Pressure force of the first and second principal components of deck section.

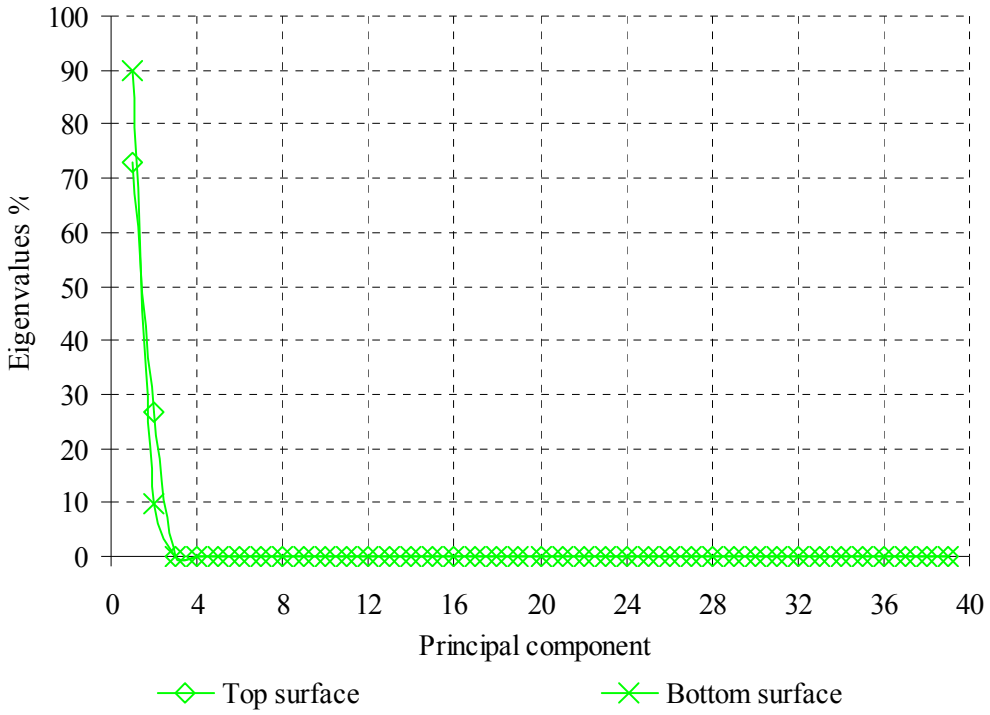

Fgiure 6.31 Eigenvalues of top and bottom surface of the bridge deck section.

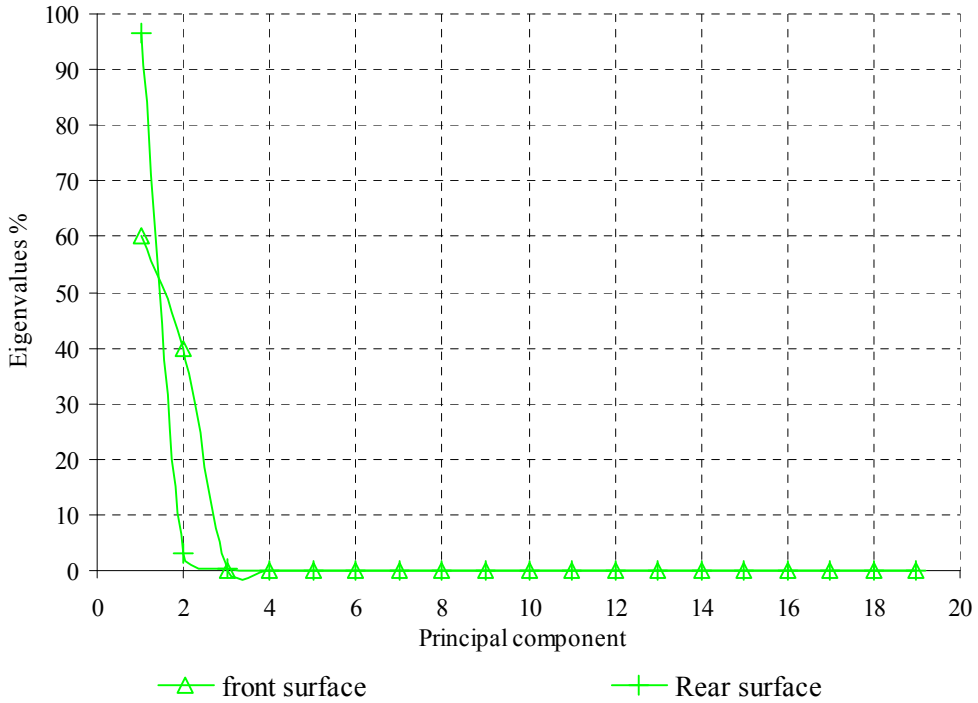

Figure 6.32 Eigenvalues of front and rear surface of the bridge deck section.

7 FLUID STRUCTURE INTERACTION

This chapter is a short discussion chapter relating the fluid structure interaction (FSI) study on the flow around bridge deck sections to the work done in this thesis. This is to provide a link of the involvement of the simulation of the flow around bluff bodies and a static bridge deck section to the simulation of a moving bridge deck case, which is the purpose of the project on modelling bridge response to wind.

Experimentally, investigation of the response of bridges to wind can be easily achieved by wind tunnel test as discussed in the previous chapter. Computationally, simulation of the flow around a moving bridge deck needs to consider both the flow and the flexible structure, known as the fluid structure interaction (FSI). Literally, this method combines the structural analysis technique with the fluid dynamic theory to solve the coupled system. FSI usually involves a third coupler solver which acts as a control centre for the concurrent execution of the solution from the fluid solver and the structure solver.

7.1 MODELLING BRIDGE AEROELASTICITY

As mentioned, the work done in this thesis aims to simulate the flow around the Kessock Bridge deck section using proper modelling techniques developed based on the study of the flow around bluff bodies and static bridge deck sections. In order to achieve the purpose of the project on the modelling of bridge aeroelastic response, FSI appears as the next objective following the three main objectives set at the beginning of this thesis. Aeroelasticity is the study of the effects of the aerodynamic and elastic forces on a flexible solid body immersed in moving fluid. Elasticity deals with the deformation of a flexible body under load induced by moving fluid. Aeroelastic phenomena which commonly occur in daily life include the swaying of tall building or vibration of long span bridges under wind excitation.

To ensure proper modelling of aeroelastic response of long span bridges to wind using FSI, work done in this thesis is important. The work equips the author with proper modelling techniques and provides fundamental knowledge on the flow characteristics around a bridge deck section, especially the knowledge gained on the understanding of the vortex shedding phenomenon and its influence on structures. The

study in this thesis serves as a basis for the FSI study of bridge aeroelasticity. The following section describes FSI studies on the flow around bridge deck conducted by other researchers.

7.1.1 Review

FSI simulation is becoming more common in the study of engineering applications involving flow induced instability of structures. Due to the advances of computer technology in recent decades, computational modelling of bridge aeroelasticity behaviour has become an important tool alongside wind tunnel techniques. This method enables the comparison and investigation of various design solutions without the need of full scale tests. Various investigations have been done on the study of flow around a bridge deck section involving aeroelastic response of the structure.

Jenssen *et al.* (1998) [53] predicted the wind-induced motion of suspension bridges based on the estimated aerodynamic derivatives parameters. These derivatives are functions of the geometrical shape of the bridge deck as well as the wind speed of the flow. These parameters allow the prediction of the behaviour of the bridge under wind excitation such as the estimation of the critical flutter velocity of the flow. Arbitrary Lagrangian-Eulerian (ALE) [4, 49] method has been employed by Jenssen and Jakobsen for the moving mesh in the FSI simulation, with the LES model as the fluid solver. Smagorinsky model has been used in the modelling of the subgrid scale turbulence. Only *2D* simulation has been carried out due to the restriction of computer power. The estimated derivatives and critical flutter wind velocity showed some discrepancies with wind tunnel test results but similar trend of the flow has been observed.

Another similar application of FSI on the flow around a bridge deck section has been conducted by Jenssen and Kvamsdal (1999) [54]. Both *2D* and *3D* simulations have been conducted, the *3D* simulation is based on the finite volume method (FVM) using LES turbulence model. FVM allows treatment of *3D* mesh. Comparison with experimental results showed that LES predicted close agreement with experimental work, especially in capturing the pressure distribution, lift and moment coefficients. But the downside of *3D* simulations is the high demand of computer resources.

Frandsen (1999) [32] employed the transient ALE finite element formulation to model the vortex-induced vibration of the Great Belt East Bridge (GBEB). This fluid-structure formulation is based on the Finite Element code *Spectrum* [117]. Lock-in

phenomenon was modelled successfully. Also, flutter analysis successfully predicted a flutter boundary close to results from other researchers.

Vezza and Taylor (2001) [135] employed the discrete vortex method (DVM) to study the aerodynamic response of the GBEB. DVM is slightly different from conventional CFD methods (explained in section 4.1.2). Qualitatively, this method successfully predicted the mean force coefficients of the GBEB at a range of angles of attack. Besides, the calculated flutter derivatives of the bridge agreed well with experiment data and also with other numerical methods.

Selvam and Govindaswamy (2001) [105] looked into the aeroelastic analysis of bridge girder section of the GBEB using LES turbulence model based on the finite element method (FEM). An ALE coordinate system is used to describe the computational domain. The rigid body motion method is employed for the moving mesh required for FSI. The flow around the GBEB deck section has been simulated successfully for both the fixed and the moving conditions. The vortex shedding phenomenon has been well predicted, as well as the flow separation and vortex structure in the wake region of the flow.

Morgenthal (2000) [81] adopted a numerical code NEWT to study bridge aerodynamics. The code is based on the FVM which features moving mesh and adaptive solution in time and space. An algorithm for moving meshes is incorporated in the NEWT for the bridge deck analysis. Morgenthal successfully applied the adopted code on the study of the flow around bridge deck section with good result.

A recent review on the subject of the injection/suction boundary conditions study shows some advances in FSI simulation [73]. The approach considers the effects of cross section movement in FSI by changing the boundary conditions rather than moving the mesh as in traditional ALE method. This modification of the flow solver considerably reduces the computing cost with respect to the ALE formulations. Various implementations of the injection/suction boundary conditions have been tested on an airfoil flow and a rectangle profile with prescribed motion. Good agreement has been observed between the experimental results and the ALE simulations.

7.2 BLOCK ITERATIVE COUPLING METHOD

Most studies of FSI mentioned above involved direct coupling of the fluid and structure solvers, in which huge computer resources are needed. Also, majority of the studies on

the aeroelastic response of bridges to wind excitation are *2D* in nature due to the restricted computer resources. Hence, sequential coupling technique has been introduced. This method enables the usage of existing software, which means the solvers for the fluid, structures and mesh can be solved separately.

The discussion of DES on the flow around the Kessock Bridge in the previous chapter involved only a fixed deck simulation. In order to investigate the dynamic behaviour of the bridge to wind excitation, FSI plays an important role. As part of the current project on the modelling of bridge response to wind excitation, the block iterative coupling method has been developed by Sun *et al.* (2004) [124] for the FSI study of the flow around the Kessock Bridge deck section. This method is based on the LES model for the fluid solver and the modal analysis technique for the structure part. This sequential coupling method uses subiteration technique to synchronise the fluid and the structure field.

The code has been applied on the simulation of flow around bluff bodies as a pilot study for the flow around a bridge deck section. Flow around a circular cylinder and a *B/H=4* rectangular cylinder has been studied using the developed FSI code. In the study of the flow around a *B/H=4* rectangular cylinder, the flutter derivatives were extracted and compared to the experimental result (Figure 7.1). Slightly different values have been observed from the comparison, this could be caused by the difference in the Reynolds number simulated. However, the general trend of the parameters with respect to the changes of reduced wind velocity has been well captured. This suggests that the block iterative method is capable of predicting the vortex shedding and the aeroelastic behaviour of the flow around bluff bodies.

Prior to the FSI code with the LES model, earlier version of the code using SST as the fluid solver has been tested and basic result has been obtained for the flow around the Kessock Bridge deck section [125]. The simulation managed to predict significant wind induced vibration of the bridge deck section, corresponded to the observation of the wind tunnel test. The predicted wind speed at which the vibration occurred agreed well with the wind tunnel measurement. Also, analysis of the simulated result concluded that the distribution of pressure on top and bottom surfaces of the bridge deck section influences the lift force significantly.

The developed FSI code is to be applied to the flow around the bridge deck section using more advances LES or DES models as the fluid solver. Pilot study on the developed FSI code demonstrated its capability to capture the wind induced response of

the flow around the circular and rectangular section. This suggested that the FSI code is potentially suitable for the study of the aeroelastic response of the bridge deck section with a more advanced fluid solver, provided that enough computer power is available.

7.3 SUMMARY

Promising observation on the simulation of the flow around a fixed deck section of the Kessock Bridge encourages further exploration of the simulation of a moving deck section in the FSI study. The progress on the FSI simulation of the current project has been discussed in this chapter. With the developed *3D* FSI code employing LES as the fluid solver, more complex situation could be simulated in terms of the effects of turbulence on the flow. Also, advances in computer technology allows higher wind speed to be simulated, in which the flow in the wake region is fully turbulent.

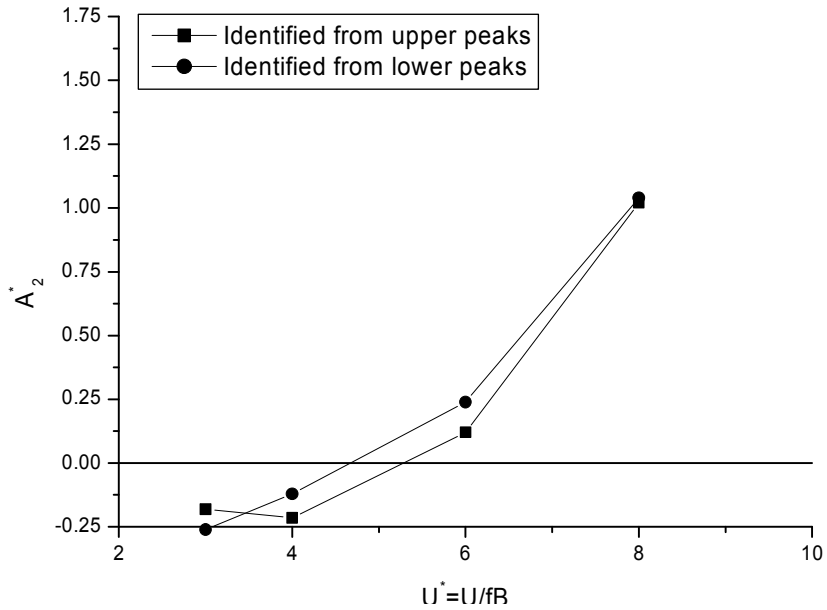

Figure 7.1 Flutter derivative of a *B/H=4* cylinder extracted from the FSI code developed by Sun *et al.* (2004) [124]

8 CONCLUSIONS AND FUTURE WORK

The work done in this thesis has validated the application of LES and DES turbulence models on the flow around bluff bodies through comparison study with experimental results. The study equips the author with proper modelling skills for the simulation of flow around bridge deck sections. The following concludes the findings and achievements on the study of the flow around bluff bodies and bridge deck sections, with some suggestions and recommendations on the future work upon the completion of the thesis.

8.1 CONCLUSIONS

From the study of the flow around bluff bodies, it is concluded that the DES is a suitable turbulence model for the simulation of the flow around a static bridge deck section and should be implemented in the FSI code mentioned in section 7.2 for the modelling of the bridge aeroelasticity. The work conducted in this research is very subject orientated in achieving the aim and objectives of the thesis. All simulations ranging from the basic RANS models to the advanced LES and DES, have provided the necessary skills and knowledge for the investigation of the bridge response to wind using CFD.

Apart from the main conclusion, three findings corresponding to the objectives of the work have been concluded from the study of the flow around bluff bodies and bridge deck sections:

i) Satisfactory results have been observed for the simulation of the flow around a circular cylinder using SST, LES and DES models but not the k-ε and RSM models. The SST model predicted good pressure distribution at the leading edge and flow separation region of the circular cylinder but not the unsteady flow features in the wake region of the flow. On the other hand, vortex shedding phenomenon has been successfully captured by LES and DES models for the flow around a circular cylinder. From the comparative study with experimental work, LES and DES have been successfully validated at Reynolds number of *3,900*.

ii) Flow around a square cylinder at Reynolds number of *14,000* using LES and DES has been validated through comparison study with experimental data. For the simulation of the flow around rectangular sections (*B/H=2, 3, 4, 5, 6, 7,* and *8*),

good agreement of the Strouhal number and the drag coefficient of the flow with experimental findings has been observed. Analysis on the vortical structures of the flow showed that LES and DES are capable of representing flow structures close to experimental observations. LES successfully captured the stepwise increment of the Strouhal number (calculated based on the width of the rectangle sections) with respect to the increase of aspect ratio of the sections.

iii) Sectional wind tunnel test performed on the *1:40* scale model of the Kessock Bridge successfully measured flow parameters such as the Strouhal number and the force coefficients of the deck section. Also, the vortex shedding mechanism which caused the instability observed on the full scale bridge has been identified in the wind tunnel measurement. DES study on the flow around the fixed bridge deck section successfully computed Strouhal number close to the wind tunnel test measurement and managed to capture the vortex shedding phenomenon well. Generally, force coefficients predicted showed good comparison to the wind tunnel result apart from the lift coefficient. But the prediction did agree with experimental data and full scale measurement of other researchers.

Also, several minor conclusions have been drawn:

- The profiles of the streamwise and spanwise velocity components in the wake regions of the flow have been well predicted from both LES and DES for the flow around a circular cylinder and a square cylinder. This resulted in good agreement of the recirculation bubbles and the size of the wake compared to experimental results, with LES predicting closer agreement than DES.

- LES predicted a more complex flow and vortex structure in the wake region of the flow compared to DES. This is attributed to the fact that the SST model in DES averages out part of the unsteadiness of the flow, with LES representing a more realistic vortex shedding in complex flow situation.

- DES predicted slightly different velocity distribution near the ‘grey area’ (where transition from the SST to the LES model takes place) of the flow around a square cylinder compared to experimental data. LES predicted closer agreement comparatively but DES managed to capture the trend of the flow well. The

performance of DES in the 'grey area' depends on how efficient LES is in creating the necessary turbulence and unsteadiness of the flow immediately after the transition of the turbulence models happens.

- Generally, DES saved about *1.5* to *2.5* times of computational time compared to LES in the simulations of the flow around bluff bodies within lower (*Re<22,000*) Reynolds number. At higher Reynolds number (*Re 33,000 to 100,000*) of the level of wind tunnel test of the Kessock Bridge deck section, reasonable computational time is needed for DES running on a parallel computing system.

- PCA analysis on the pressure distribution of the flow around the rectangular sections and the bridge deck section from both LES and DES has successfully identified the related modes of pressure distribution to the physical mechanism causing it. Also, prediction of the progression of the vortices along the side surfaces of the rectangular sections based on PCA agreed well with experimental measurement.

8.2 FUTURE WORK

In this section some recommendations for further research on the work performed on this thesis are listed. The work particularly focuses on the CFD aspect.

i) Drag crisis simulation of flow around a circular cylinder

The simulation of the flow around a circular cylinder in this thesis covered only subcritical flow with Reynolds number of less than *3,900*. As Reynolds number increases, the laminar boundary layer tends to turn turbulent at the transition point. Near Reynolds number of 2×10^5, the transition point and separation point of the flow coincide causing mixing of flow and delay the flow separation. This is associated with narrower wake region and significant reduction in the drag coefficient and base suction of the flow resulting in drag crisis. Numerically, Singh and Mittal (2005) [108] managed to capture this phenomenon using a two dimensional finite element formulation but the three dimensional effect were neglected. In the light of this, more advanced three dimensional turbulence models such as LES and DES should be employed to simulate the drag crisis phenomenon.

ii) Dynamic model in LES

The constant C_s in the Smagorinsky model (section 2.2.1.2) in LES varies according to the flow. It takes a value of zero in laminar flow and shows different values near a wall and in regimes with turbulent flow [101]. C_s is fixed in the standard Smagorinsky model. Consequently, some of the flow may not be accurately resolved using this model, particularly the backscattering of flow. In the dynamic model, C_s changes accordingly (with different filter width) and it takes the place of C_s^2 in Eq. 2.13 of the Smagorinsky model. This allows the possibility of negative values in the dynamic model to account for the backscatter of flow [30]. Research investigations reveal that the dynamic model can outperform the Smagorinsky model in highly complex and turbulent flow. Applications of the dynamic model in the flow around the Kessock Bridge deck section could lead to even more accurate solutions, in which the Reynolds number considered is high (*Re 33,000* to *Re 100,000*) with complex and turbulent flow features.

iii) Investigation of the flow around rectangular sections a higher Reynolds numbers

The simulations of the flow around rectangular sections in this thesis mostly involved flow at lower Reynolds number ($Re<22,000$). Only two cases of Reynolds number at wind tunnel speed have been simulated. More cases of simulations at this level are needed for further understanding of the flow characteristics around the bridge deck section, especially simulations at similar aspect ratio. The simulations particularly refer to the study on the stepwise increment of the Strouhal number with the increase in aspect ratios of the flow around the rectangular sections. From the observation of the simulated results, certain aspect ratios (near to aspect ratio of the bridge deck section) show two shedding frequencies at the same wind speed. Applying this finding on the observation of the wind tunnel test of the bridge deck section, the sudden change of the vibration from heaving to pitching modes of the deck could be explained, in which two shedding frequencies contribute to the different modes of vibration respectively. Further investigation on the flow around rectangular sections at high Reynolds number aids in the study of the responses of the bridge deck section under wind induced forces.

iv) Investigation on the flow around a moving bridge deck section

Only the fixed deck section of the Kessock Bridge has been simulated in this thesis. The moving mesh block iterative [124] FSI code (section 7.2) developed as part of the project on modelling the bridge aeroelasticity has been applied on the study of the flow around the bridge deck section using the SST model as the fluid solver. Satisfactory results have been obtained on the prediction of the wind induced vibration. For the simulation of the moving bridge deck section using more advanced turbulence models, the fluid solver in the FSI code should be substituted with LES or DES. Simulations results presented in this thesis demonstrated the capability of LES and DES in capturing the dynamic features and vortex shedding phenomenon of the flow around bluff bodies. Thus, a similar observation is expected for the applications of the flow around the moving mesh deck section. Also, aeroelastic response of the flow related to vortex shedding instability will be investigated. Parameters such as the flutter derivatives and the critical wind speed of flutter will be estimated from the simulations with respect to the changes of angles of attack of the wind. However, the increase in computer requirement needs to be taken into consideration for these moving mesh simulations. Eventually, these numerical solutions will be compared to the full scale measurement data.

9 REFERENCES

[1] ADPAC sample case: Vortex shedding over a circular cylinder in crossflow, www.grc.nasa.gov/WWW/5900/5940/code/adpac/sample.

[2] Al-Jamal H, Dalton C, Vortex induced vibrations using Large Eddy Simulation at a moderate Reynolds number, Journal of Fluids and Structures, 2004, Vol.19, p. 73-92.

[3] ANSYS, Innovative turbulence modelling: SST model in ANSYS CFX, http://www.ansys.com/assets/tech-briefs/PDF0072.pdf, 2004.

[4] Askes H, Arbitrary Lagrangian-Eulerian formulations in computational solid mechanics, in Numerical Methods of Structural Mechanics, 2000, Delft University of Technology, Faculty of Civil Engineering and Geosciences, www.sd.ruhr-uni-bochum.de/academics-students/lehre/lehrveranstaltungen/ numerische-strukturmechanik/askes.pdf.

[5] Baitis B, Large Eddy Simulation of gravity currents: A finite element analysis, Undergraduate research, Virginia Tech Mathematics Department, 2005.

[6] Baker C, Aspect of the use of proper orthogonal decomposition of surface pressure field, Journal of Wind and Structures, 2000, Vol.3, p. 97-115.

[7] Baker C, Unsteady wind loading on a wall, Journal of Wind and Structures, 2001, Vol.4, p. 413-440.

[8] Bearman P, Near wake flows behind two and three-dimensional bluff bodies, Journal of Wind Engineering and Industrial Aerodynamics, 1997, Vol.69-71, p. 33-54.

[9] Bearman P, Obasaju E, An experimental study of pressure fluctuations on fixed and oscillating square section cylinders, Journal of Fluid Mechanics, 1982, Vol.119, p. 297-321.

[10] Bearman P W, Investigation of the flow behind a two-dimensional model with a blunt trailing edge and fitted with splitter plates, Journal of Fluid Mechanics, 1965, Vol.21, p. 241-255.

[11] Beaudan P, Numerical experiments on the flow past a circular cylinder at subcritical Reynolds number, Technical Report TF-62, Dept. of Mechanical Engineering, Stanford University, 1994.

[12] Biswas R, Strawn R, Tetrahedral and hexahedral mesh adaption for CFD problems*, *To appear in Applied Numerical Mathematical Journal.

[13] Blazek J, Computational Fluid Dynamics: Principles and Applications, Elsevier Science Ltd, Oxford England, 2001.

[14] Bloor M S, The transition to turbulence in the wake of a circular cylinder, Journal of Fluid Mechanics, 1964, Vol.19, p. 290-304.

[15] Boussinesq J, Théorie de l'écoulement tourbillant (Theories of swirling flow), Mém. prés. par div. savants à l'Acad. Sci. Paris, 1877, Vol.23.

[16] Braza M, Chassaing P, Ha Minh H, Prediction of large scales transition features in the wake of a circular cylinder, Phys. Fluids, 1990, Vol.A2, p. 1461-1471.

[17] Breuer M, Large eddy simulation of the subcritical flow past a circular cylinder:Numerical and modelling aspects, International Journal for Numerical Methods in Fluids, 1998, Vol.28, p. 1281-1302.

[18] Breuer M, Bernsdorf J, Zeiser T, Durst F, Accurate computations of the laminar flow past a square cylinder based on two different methods: lattice-Boltzmann and finite volume, International Journal of Heat and Fluid Flow, 2000, Vol.21, p. 186-196.

[19] Brownjohn J M W, Choi C C, Wind tunnel section model study of aeroelastic performance for Ting Kau Bridge deck, Wind and Structures, 2001, Vol.4, (5) p. 367-382.

[20] Choi C C, Brownjohn J, Zhang X, Pressure measurement on Kessock Bridge section model, Collaborative research project of the University of Nottingham and the Nanyang Technological University, 2004.

[21] Choi C C, Brownjohn J, Zhang X, Report on wind tunnel study on the aerodynamic derivatives of the Kessock Bridge, Collaborative research project of the University of Nottingham and the Nanyang Technological University, 2004.

[22] Corner B, The Corner connection, http://doppler.unl.edu/~bcorner/ University of Nebraska-Lincoln, Environmental Remote Sensing Lab.

[23] Courschesne J, Laneville A, A comparison of correction methods used in the evaluation of drag coefficient measurements for 2D rectangular cylinders, Journal of Fluid Engineering, 1979, Vol.11, p. 506-510.

[24] Davenport W, Experiment#3 Flow past a circular cylinder, http://www.aoe.vt.edu/~devenpor/aoe3054/manual/expt3/text.html#F1, 2002.

[25] Davidson L, An introduction to turbulence models, Department of Thermo and Fluid Dynamics, Chalmer University of Technology, Publication 97/2, Sweden, 2003.

[26] Deardroff, James W, A Numerical study of the 3-Dimensional Turbulent Channel flow at Large Reynolds Numbers, Journal of Fluids Mechanics, 1970, Vol.41, (2).

[27] Dexer I, http://website.lineone.net/~indexer/kessockbridge.html.

[28] Durao D G, Heitor M V, Pereira J F, Measurement of turbulent and periodic flows around a square cylinder, Experiments in Fluids, 1988, Vol.6, p. 298-304.

[29] Espeyrac L, Pascaud S, Physics Knowledge, http://www.enseeiht.fr/hmf/travaux/CD0102/travaux/optmfn/gpfmho/01-02/grp1/presenta.htm.

[30] Ferziger J, Subgrid scale modelling, Large Eddy Simulation of Complex Enginering and Geophysical Flows, Cambridge University Press., 1993.

[31] Ferziger J, Peric M, Computational Methods for Fluid Dynamics, Springer-Verlag, Berlin Heidelberg, 1999.

[32] Frandsen B, Computational Fluid-Structure Interaction Applied to Long-Span Bridge Design, PhD Thesis, University of Cambridge, 1999.

[33] Franke J, Frank W, Large eddy simulation of the flow past a circular cylinder at Re=3900, Journal of Wind Engineering and Industrial Aerodynamics, 2002, Vol.90, p. 1191-1206.

[34] Franke R, Rodi W, Schonung B, Analysis of experimental vortex shedding data with respect to turbulence model, in 7th Symposium on Turbulence Shear Flows, Stanford University, 1989.

[35] Franke R, Rodi W, Schonung B, Numerical calculation of laminar vortex-shedding flow past cylinders, Journal of Wind Engineering and Industrial Aerodynamics, 1990, Vol.35, p. 237-257.

[36] Frohlich J, Rodi W, Introduction to large eddy simulation of turbulent flow, Institute of Hydromechanics, University of Karlsruhe, Germany, p. 1-19.

[37] Frohlich J, Rodi W, Kessler Ph, Parpais S, Bertoglio J, Laurence D, Large Eddy Simulation of flow around circular cylinders on structured and unstructured grids, Notes on Numerical Fluid Mechanics, 1998, Vol.66, p. 319-338.

[38] Germano M, Piomelli U, A dynamic subgrid scale eddy viscosity model, Proc. Summer Workshop, Center for turbulence Research, Stanford, CA., 1990.

[39] Gerrard J, The wakes of cylindrical bluff bodies at low Reynolds number, Philosophical Transactions Royal Society, 1978, Vol.288, p. 351-382.

[40] Grenet E T, Ricciardelli F, Spectral proper transformation of wind pressure fluctuations: application to a square cylinder and a bridge deck, Journal of Wind Enginnering and Idustrial Aerodynamics, 2004, Vol.92, p. 1281-1297.

[41] Gu X H, Aeroelasticity in bridges-State of the art review, University of Nottingham, School of Civil Engineering, First year report for Degree of PhD, 2004.

[42] Hama F, Streaklines in a perturbed shear flow, Physics Fluids, 1962, Vol.5, p. 644-650.

[43] Hansen R, Long L, Large eddy simulation of a circular cylinder on unstructured grids, in AIAA Aerospace Science Meeting and Exhibit, Reno, NV, 2002.

[44] Hay J, Response of Bridges to Wind, Transport Research Laboratory, Department of Transport, UK (Published by HMSO Publication Center), 1992.

[45] Hedges L, Travin A, Spalart P, Detached eddy simulations over a simplified landing gear, Journal of Fluid Engineering, 2002, Vol.124, p. 413-423.

[46] Hjorth-Hansen E, Section model tests, in Aerodynamics of Large Bridges, Rotterdam, 1992. p. 95-112.

[47] Holmes J D, Analysis and synthesis of pressure fluctuations on bluff bodies using eigenvetors, Journal of Wind Engineering and Industrial Aerodynamics, 1990, Vol.33, p. 219-230.

[48] Honji H, Ishii K, Wake shedding from a distorted cylinder, Journal of Physical Socity Japan, 1976, Vol.41, p. 1089-1090.

[49] Hughes T, Liu K, Zimmerman K, Lagrangian-Eulerian Finite Element method for Incompressible viscous flows, Comp. Meth. Apll. Mech. Eng., 1981, Vol.29, (1) p. 329-349.

[50] Igarashi T, Fluid flow and heat transfer around rectangular cylinders, International Journal of Heat and Mass Transfer, 1987, Vol.30, p. 893-901.

[51] Irwin P A, The role of wind tunnel modelling in the prediction of wind effects on bridges, in Proc. of the international symposium on advances in bridge aerodynamics, Copenhagen, Rotterdam, 1998. p. 99-117.

[52] Jakobsen J B, Hjorth-Hansen E, Determination of the aerodynamic derivatives by a system identification method, Journal of Wind Engineering and Industrial Aerodynamics, 1995, Vol.57, p. 295-305.

[53] Jenssen C B, J B Jakobsen, I Enevoldsen, Hansen S O, Predicting wind induced motion of suspension bridges using parallel CFD, in Fourth European CFD Conference, Special Technological Sessions, Greece, Athens, 1998.

[54] Jenssen C B, Kvamsdal T, Computational methods for fsi-simulations of slender bridges on high performance computers, in Computational Methods for Fluid-Structure Interactions, Tapir Forlag, Trondheim, Norway, 1999. p. 31-40.

[55] Johnson R, Wichern D, Applied multivariate statistical analysis, 4th Ed., Prentice Hall, New Jersey 07458, 1998.

[56] Kalro V, Tezduyar T, Parallel 3D computation of unsteady flows around circular cylinders, Parallel Computing, 1997, Vol.23, p. 1235-1248.

[57] Kato M, Launder B E, The modelling of turbulent flow around stationary and vibrating cylinders, in Ninth Symposium on Turbulent Shear Flows, Kyoto, Japan, 1993.

[58] Knisely C, Strouhal number of rectangular cylinder at incidence, Journal of Fluid and Structures, 1990, Vol.4, p. 371-393.

[59] Komatsu S, Kobayashi H, Vortex-Induced Oscillation of Bluff Cylinders, Journal of Wind Engineering and Industrial Aerodynamics, 1980, Vol.6, p. 335-362.

[60] Larsen A, Esdahl S., Jacob Anderson, Vejrum T., Storebælt Suspension Bridge-Vortex Shedding Excitation and Mitigation by Guide Vanes, Journal of Wind Engineering and Industrial Aerodynamics, 2000, Vol.88.

[61] Launder E, Rodi W, Progress in the development of a Reynolds stresses Turbulence Closure, Journal of Fluid Mechanics, 1975, Vol.68, p. 537-566.

[62] Liaw K, Wright N, Owen J, Sun D, Large eddy simulation of flow past a circular cylinder, in 11th International Conference on Wind Engineering, Texas, 2003. p. 1919-1926.

[63] Lin H, Vezza M, Galbraith R, Discrete vortex method for simulating unsteady flow around pithching aerofoils, AIAA, 1997, Vol.35, p. 494-499.

[64] Lourenco L, Shih C, Characteristics of the plane turbulent near wake of a circular cylinder, a particle image velocimetry study (Data published in Beaudan P. (1998)), 1993.

[65] Lubcke H, Schmidt St., Rung T, Thiele F, Comparison of LES and RANS in bluff body flows, Journal of Wind Engineering and Industrial Aerodynamics, 2001, Vol.89, p. 1471-1485.

[66] Lyn D, Rodi W, Park J, A laser doppler velocimetry study of ensemble-averaged characteristics of the turbulent near wake of a square cylinder, Journal of Fluid Mechanics, 1995, Vol.304, p. 285-319.

[67] Ma S, Karamanos G-S, Karniadakis, Dynamics and low-dimensionality of the turbulent near-wake, Journal of Fluid Mechanics, 1999, Vol.410, (29-65).

[68] Maajnder P, Siikonen T, Evaluation of Smagorinsky based SGS models in a Finite Volume Computation, International Journal for Numerical Methods in Fluids, 2002, Vol.40, p. 735-774.

[69] Majumdar S, Rodi W, Numerical calculation of turbulent flow past circular cylinders, in Third Symposium on Numerical and Physical Aspect of Aerodynamic Flows, Long Beach, CA, 1985.

[70] MATLAB Documentation, MATLAB 6.5.1, The language of Technical computing, 2003.

[71] Matsumoto M, Vortex shedding of bluff bodies: A review, Journal of Fluids and Structures, 1999, Vol.13, p. 791-811.

[72] McMullen M, Vortex shedding in low Reynolds number flows past cylinders, Aero/Astro Department, Stanford University, http://aero-comlab.stanford.edu/mcmu/cylinder.html, 2003.

[73] Medic G, Mohammadi B, Injection/Suction boundary conditions for fluid-structure interaction simulations in incompressible flow, International Journal for Numerical Methods in Fluids, 2002, Vol.40, p. 875-901.

[74] Menter F R, Two-Equation Eddy-viscosity Turbulence Models for Engineering Applications, AIAA Journal, 1994, Vol.32, (8).

[75] Menter F R, Grotjans H, Application of Advanced Turbulence Models to Complex Industrial Flows, AEA Technology GmbH, Germany.

[76] Menter F R, Kuntz M, Development and application of a zonal DES turbulence model for CFX-5, ANSYS CFX Validation Report, 2001, Vol.CFX-VAL17/0703, p. 1-34.

[77] Menter F R, Thomas E, Advance turbulence modelling in CFX, CFX Update, AEA Technology, 2001.

[78] Mills R, Sheridan J, Hourigan K, Response of base suction and vortex shedding from rectangular prisms to transverse forcing, Journal of Fluid Mechanics, 2002, Vol.461, p. 25-49.

[79] Mizota T, Okajima A, Experimental studies of unsteady flows around rectangular prisms, Japan Soc. of Civil Engrs., 1981, Vol.312, p. 39-47.

[80] Morgans B, Dally B, Nathan G, Lanspeary P, Fletcher D, Application of the revised Wilcox (1998) k-omega turbulence model to a jet in co-flow, Second International Conference on CFD in the Mineral and Process Industries, Melbourne, Australia., 1999.

[81] Morgenthal G, Comparison of Numerical Methods for Bridge Deck Aerodynamics, Thesis submitted for the degree of Mphil, University of Cambridge, 2000, http://www2.eng.cam.ac.uk/~gm249/tr.pdf.

[82] Morris P, Long L, Bangalore A, Wang Q, A parallel three-dimensional computational aeroacoustics method using nonlinear disturbance equations, Journal of Comp. Phys., 1997, Vol.133.

[83] Multimap 2002, Multimap 2002, www.multimap.com.

[84] Murakami S, Mochida A, Hayashi Y, Examining the k-epsilon model by means of wind tunnel test and large eddy simulation of the turbulence structure around a cube, Journal of Wind Engineering and Industrial Aerosynamics, 1990, Vol.35, p. 87-100.

[85] Nakaguchi H, Hashimoto K, Muto S, An experimental study on aerodynamics drag of rectangular cylinders, J. Japan Soc. of Aeronautical and Space Sci.,, 1968, Vol.16, p. 1-5.

[86] Nakamura Y, Ohya Y, Tsuruta H, Experiments on vortex shedding from flat plates with square leading and trailing edges, Journal of Fluid Mechanics, 1991, Vol.222, p. 437-447.

[87] Nakayama A, Vengadesan S, On the influence of numerical schemes and subgrid-stress models on large eddy simulation of turbulent flow past a square cylinder, International Journal for Numerical Methods in Fluids, 2002, Vol.38, p. 227-253.

[88] NASA, Vortex shedding behind a circular cylinder in crossflow, ADPAC sample case, NASA CR-195468, p. 107-119.

[89] Nishioka M, Sato Hiroshi, Measurement of velocity distributions in the wake of a circular cylinder at low Reynolds numbers, Journal of Fluid Mechanics, 1974, Vol.65, p. 91-112.

[90] Noda H, Nakayama A, Free stream turbulence effects on the instanteneous pressure and forces on cylinders of rectangular cross section, Experiments in Fluids, 2003, Vol.34, p. 332-344.

[91] Norberg C, Effects of Reynolds number and a low-intensity free-stream turbulence on the flow around a circualt cylinder, Publication No. 87/2, Department of Applied Thermodynamics and Fluid Mechanics, Chalmer University of Technology, 1987.

[92] Norberg C, Flow around rectangular cylinders: Pressure forces and wake frequencies, Journal of Wind Engineering and Industrial Aerodynamics, 1993, Vol.49, p. 187-196.

[93] Ohya Y, Nakamura Y, Ozono S, Tsuruta H, Nakayama R, A numerical study of vortex shedding from flat plates with square leading and trailing edges, Journal of Fluid Mechanics, 1992, Vol.236, p. 445-460.

[94] Okajima A, Flow around a rectangular cylinder with a section of various depth/breath ratios, Journal of Wind Engineering, 1983, Vol.17, p. 79-80.

[95] Okajima A, Strouhal number of rectangular cylinders, Journal of Fluid Mechanics, 1982, Vol.123, p. 379-398.

[96] Ong L, Wallace J, The velocity field of the turbulent very near wake of a circular cylinder, Experiments in Fluids, 1996, Vol.20, p. 441-453.

[97] Otsuki Y, Washizu K, Tomizawa H, Oya A, A note on the aeroelastic instability of a prismatic bar with square section, Jurnal of Sound and Vibration, 1974, Vol.34, p. 233-248.

[98] Owen J, Vann M, Davies J, Blakeborough A, The prototype testing of Kessock Bridge: response to vortex shedding, Journal of Wind Engineering and Industrial Aerodynamics, 1996, Vol.60, p. 91-108.

[99] Philips A, The intensity of Aeolian tones, Journal of Fluid Mechanics, 1956, Vol.41, p. 137-145.

[100] Pope S, Ten questions concerning the large-eddy simulation of turbulent flows, New Journal of Physics, 2004, Vol.6.

[101] Pope S, Turbulent flow, Cambridge University Press, 2000.

[102] Roshko A, On the development of turbulent wakes from vortex streets, NACA Report 1191, 1954.

[103] Roshko A, On the drag and shedding frequency of two-dimensional bluff bodies, *NACA Tech. Note no.* 3169, 1954.

[104] Rumsey L, Biedron R, Computation of flow over a drag prediction workshop wing/body transport configuration using CFL3D, NASA, Langley Research Center, 2001.

[105] Selvam R P, Govindaswamy S, Aeroelastic analysis of bridge girder section using computer modelling, Report for Mack Blackwell Transportation Center, University of Arkansas, 2001, http://www.mackblackwell.org/research/finals/arc1095/1095.pdf.

[106] Shimada K, Ishihara T, Application of a modified k-epsilon model to the prediction of aerodynamic characteristics of rectangular cross-section cylinders, Journal of Fluids and Structures, 2002, Vol.16, (4) p. 465-485.

[107] Shimada K, Ishihara T, Prediction of aeroelastic vibration of rectangular cylinders by k-epsilon model, Journal of Aerospace Engineering, 1999, Vol.12, (4) p. 122-135.

[108] Singh S P, Mittal S, Flow past a cylinder: shear layer instability and drag crisis, Int. J. Numer. Meth. Fluids, 2005, Vol.47, p. 75-98.

[109] Sitch W, Effective shapes and turbulent wake, http://fur-o-dynamic.org/theory/.

[110] Sohankar A, Davidson L, Norberg C, Large eddy simulation of flow past a square cylinder: Comparison of different subgrid scale models, Journal of Fluids Engineering, 2000, Vol.122, p. 39-47.

[111] Sohankar A, Norberg C, Davidson L, Numerical simulation of flow past a square cylinder, in 3rd ASME/JSME Joint Fluids Engineering Conference, California, 1999.

[112] Sohankar A, Norberg C, Davidson L, A numerical study of unsteady 2D flow around rectangular cylinders at incidence, Internal report Nr. 96/25, Department of Thermo and Fluid Dynamics, Chalmers University of Technology, Sweden, 1996, p. 1-42.

[113] Sohankar A, Norberg C, Davidson L, Simulation of three-dimensional flow around a square cylinder at moderate Reynolds numbers, Phys. of Fluids, 1999, Vol.11, (2) p. 288-306.

[114] Son J, Hanratty T, Velocity gradients at the wall for flow around a cylinder at Reynolds number from 5,000 to 100,000, Journal of Fluid Mehanics, 1969, p. 353-368.

[115] Spalart P R, Strategies for turbulence modelling and simulations, International Journal of Heat and Fluid Flow, 2000, Vol.21, p. 252-263.

[116] Spalart P R, Allmaras S R, A one-equation turbulence model for aerodynamic flows, La Recherche Aerospatiale, 1994, Vol.1, p. 5-21.

[117] Spectrum, Spectrum Solver (ver 2.0) Command reference and Theory Manual, Centric Engineering System Inc., California, 1993.

[118] Squires K, Forstyhe J R, Spalart P R, Detached Eddy Simulation of the separated flow around a forebody cross-section, Mechanical and Aerospace Engineering Department, Arizona State University, Tempe, AZ 85287-6106, USA., 2000.

[119] Stangroom P, Computational fluid dynamics for wind farm optimisation, First year report for the degree of PhD, School of Civil Engineering, University of Nottingham, 2001.

[120] Stoesser T, Development and Validation of a CFD-Code for Turbulent Open-Channel flows, Dissertation Submitted for the degree of Doctor of Philosophy (PhD), University of Bristol, 2001.

[121] Stokes A, Welsh C, Flow resonant sound interaction in a duct containing a plate, Part II, Journal of Sound and Vibrations, 1986, Vol.104, p. 55-73.

[122] Strelets M, Detached eddy simulation of massively separated flow, AIAA, Paper 2001-0879, 2001, Washington: Am. Inst. Aeronaut. Astronaut.

[123] Stroud K A, Further engineering mathematics, Macmillan Press Ltd., 1996.

[124] Sun D, Wright N, Owen J, Liaw K, Fluid structure interaction of prismatic line-like structures using LES and block-iterative coupling, The 5th International Colloquium on Bluff Body Aerodynamics & Applications, July, Ottawa, Canada, 2004, p. 133-136.

[125] Sun D, Wright N, Owen J, Liaw K, Vortex induced vibrations of Kessock Bridge using CFD, Proceeding of the 6th UK conference on wind engineering, Cranfield University, Sept 2004, 2004, (paper 28).

[126] Tamura T, Ito Y, Aerodynamic characteristics and flow structures around a rectangular cylinder with a section of various depth/breath ratios, Journal of Structural and Construction Engineering (Transactions of Architectural Institute of Japan), 1996, (No. 486) p. 153-162.

[127] Tan B, Thompson M, Hourigan K, Simulated flow around long rectangular plates under cross flow perturbations, http://elecpress.monash.edu.au/ijfd/1998_vol2/paper1/Tan.Results.html#table2, Journal of Fluid Dynamics, 1998, Vol.2, (Article 1).

[128] Taneda S, Experimental investigations of the wakes behind cylinders and plates at low Reynolds numbers, Journal of Physical Society Japan, 1956, Vol.11, p. 302-307.

[129] Travin A, Shur M, Strelets M, Spalart P R, Detached-eddy simulations past a circular cylinder, Flow, Turbulence and Combustion, 2000, Vol.63, p. 293-313.

[130] Travin A, Shur M, Strelets M, Spalart P R, Physical and numerical upgrades in the detached eddy simulation of complex turbulent flows, in 412 EUROMESH Colloquium on LES of Complex transitional and turbulent flows, 2000.

[131] Tremblay F, Direct and large-eddy simulation of flow around a circular cylinder at subcritical Reynolds numbers, Dissertation submitted for the degree of PhD, Technical university of Munich, 2001, http://www.software.aeat.com/cfx/european_projects/alessia/papers/D5.17_6_Thesis_Tremblay.pdf.

[132] Tremblay F, Manhart M, Friedrich R, LES of flow around a circular cylinder at a subcritical Reynolds number with cartesian grids, in Proceedings of the EUROMECH Colloquim 412 on LES of complex transional and turbulent flows, 2000.

[133] Tritton D, Experiements on the flow past a circular cylinder at low Reynolds numbers, Journal of Fluid Mechanics, 1959, Vol.6, p. 547-567.

[134] Versteeg H K, Malalasekera W, An Introduction to Computational Fluid Dynamics, Longman Group Limited, Longman House, England, 1995.

[135] Vezza M, Taylor I, Application of a discrete vortex method for the analysis of suspension bridge deck sections, Journal of Wind and Structure, 2001, Vol.4, p. 333-352.

[136] Vezza M, Taylor I, Prediction of unsteady flow around square and rectangular section cylinders using a discrete vortex method, Journal of Wind Engineering and Industrial Aerodynamics, 1999, Vol.82, p. 247-269.

[137] Vieser W, Thomas E, Menter F, Improving heat transfer predictions using advanced turbulence models, CFX Community website, 2003.

[138] Wallace C, Nissen J, Kessock Bridge:Joint Engineer Role, Proc. I.C.E., 1984, Vol.76, p. 67-80.

[139] Wardlaw R L, Ponder C A, An example of the use of wind tunnels for investigating the aerodynamic stability of bridges, in Canadian Good Roads Association Convention, Alberta, Canada, 1969.

[140] Whitbread R E, Model simulation of wind effects on structures, in Symposium of wind effects on buildings and structures, 1963. p. 284-301.

[141] Wilcox D C, Turbulence Modelling for CFD, DCW Industries Inc., California, 1993.

[142] Williamson C, Advances in our understanding of vortex dynamics in bluff body wakes, Journal of Wind Engineering and Industrial Aerodynamics, 1997, Vol.69-71, (3) p. 1-32.

[143] Yu D, Kareem, A two-dimensional simulation of flow around rectangular prisms, Journal of Wind Engineering and Industrial Aerodynamics, 1996, Vol.62, p. 131-161.

[144] Yu D, Kareem A, Parametric study of flow around rectangular prisms using LES, Journal of Wind Engineering and Industrial Aerodynamics, 1998, Vol.77, p. 653-662.

[145] Yuan S, Foundation of fluid mechanics, Prentice Hall, Inc., New, Jersey, 1967.

[146] Zdravkovich M, Flow Around Circular Cylinders, Fundamental Vol. 1, Oxford University Press., Oxford, England, 1997.